

SANDIA REPORT

SAND2013-2650P

Unlimited Release

Printed May 2014

Phase Two of Standard Problem Exercise #3 to Determine Containment Vessel Performance under Severe Accident Conditions

Lili Heitman, Christopher Jones, Robert Dameron, Herman Graves, and Madhumita Sircar

Prepared by
Sandia National Laboratories
Albuquerque, New Mexico 87185 and Livermore, California 94550

Sandia National Laboratories is a multi-program laboratory managed and operated by Sandia Corporation, a wholly owned subsidiary of Lockheed Martin Corporation, for the U.S. Department of Energy's National Nuclear Security Administration under contract DE-AC04-94AL85000.

Approved for public release; further dissemination unlimited.



Sandia National Laboratories

Issued by Sandia National Laboratories, operated for the United States Department of Energy by Sandia Corporation.

NOTICE: This report was prepared as an account of work sponsored by an agency of the United States Government. Neither the United States Government, nor any agency thereof, nor any of their employees, nor any of their contractors, subcontractors, or their employees, make any warranty, express or implied, or assume any legal liability or responsibility for the accuracy, completeness, or usefulness of any information, apparatus, product, or process disclosed, or represent that its use would not infringe privately owned rights. Reference herein to any specific commercial product, process, or service by trade name, trademark, manufacturer, or otherwise, does not necessarily constitute or imply its endorsement, recommendation, or favoring by the United States Government, any agency thereof, or any of their contractors or subcontractors. The views and opinions expressed herein do not necessarily state or reflect those of the United States Government, any agency thereof, or any of their contractors.

Printed in the United States of America. This report has been reproduced directly from the best available copy.

Available to DOE and DOE contractors from
U.S. Department of Energy
Office of Scientific and Technical Information
P.O. Box 62
Oak Ridge, TN 37831

Telephone: (865) 576-8401
Facsimile: (865) 576-5728
E-Mail: reports@adonis.osti.gov
Online ordering: <http://www.osti.gov/bridge>

Available to the public from
U.S. Department of Commerce
National Technical Information Service
5285 Port Royal Rd.
Springfield, VA 22161

Telephone: (800) 553-6847
Facsimile: (703) 605-6900
E-Mail: orders@ntis.fedworld.gov
Online order: <http://www.ntis.gov/help/ordermethods.asp?loc=7-4-0#online>



Phase Two of Standard Problem Exercise #3 to Determine Containment Vessel Performance under Severe Accident Conditions

Lili Heitman and Christopher Jones
Structural and Thermal Analyses
Sandia National Laboratories
P.O. Box 5800
Albuquerque, New Mexico 87185-MS0744

Robert Dameron,
Moffatt & Nichol
1660 Hotel Circle North
San Diego, California 92108

Herman Graves and Madhumita Sircar
United States Nuclear Regulatory Commission
Washington, DC 20555-0001

ABSTRACT

The Nuclear Power Engineering Corporation (NUPEC) of Japan and the US Nuclear Regulatory Commission (NRC) jointly funded a cooperative containment research program at Sandia National Laboratories (SNL) from July 1991-December 2002. As part of the NUPEC/NRC program a 1:4 scale model of a prestressed concrete containment vessel (PCCV) was constructed and pressurized to failure. Six international organizations have participated in the round robin Standard Problem Exercise #3, by using the 1:4 Scale PCCV Model as a starting point. These organizations include:

- Atomic Energy Regulatory Board of India (AERB),
- Électricité de France (EDF)
- FORTUM (Finland)
- Gesellschaft für Anlagen und Reaktorsicherheit (GRS), (German Agency for Reactor Safety)
- Nuclear Power Corporation of India Limited (NPCIL)
- US Nuclear Regulatory Commission (NRC)

The results from the second phase of this exercise are presented. This exercise focused on investigating leakage and thermal effects that have not been studied in previous efforts related to the PCCV 1:4 scale model. Using state-of-the art modeling techniques, local and global models were generated by the participants in order to investigate the response of the structure impacted by combined internal pressure of 150 MPa and temperature loads of 200° C and to predict leak rates as a function of pressure.

ACKNOWLEDGMENTS

The authors would like to thank Herman Graves of the NRC and Michael Hessheimer of SNL for their assistance in setting up these analyses, and their continued input and expertise. In addition, thanks to all the participants for participating in this standard problem exercise, we could not have gotten worthwhile results without you. Finally, thanks to the USNRC and AERB for having the vision to set up this effort, without which none of these analyses would have been completed.

EXECUTIVE SUMMARY

Research into the integrity of containment structures for nuclear power plants has been conducted in multiple international Round Robin analyses. These analyses have contributed to the understanding of the role of containment in ensuring the safe operation of nuclear power plants. One of the most comprehensive experimental efforts, testing of a 1:4 scale prestressed concrete containment vessel (PCCV), was conducted at Sandia National Laboratories (SNL), primarily under the sponsorship of the NRC. Building upon the research efforts made in the pre- and post- test analyses, and the International Standard Problem 48 (ISP 48), the Standard Problem Exercise 3 (SPE -3) has been set up to provide the opportunity for participants to further the state-of-the-art in modeling of prestressed concrete containments. Following the ISP 48 and 1:4 scale PCCV efforts, there was interest in investigating local effects and questions that had been unanswered previously due to modeling and computational limitations at the time and scope limitations of the previous efforts. At the kick off meeting of the SPE-3, held in Mumbai, India, the scope of the first phase of the SPE-3 was agreed upon. There was an interest in investigating the effects of containment dilation on prestressing force, slippage of prestressing cables, steel-concrete interface, failure mechanisms, and the use of nominal versus in-situ conditions.

These areas of investigation, and proposed models to be used in the analyses were determined by those participants who participated in the kick-off meeting. The participants of the kick-off meeting included (in alphabetical order):

- Atomic Energy Regulatory Board of India (AERB)
- Bhabha Atomic Research Center of India (BARC)
- Électricité de France of France (EDF)
- FORTUM of Finland
- Gesellschaft Für Anlagen-und Reaktorsicherheit of Germany (GRS)
- Indira Gandhi Center of Atomic Research of India
- Nuclear Power Corporation Ltd. Of India (NPICL)
- US Nuclear Regulatory Commission, Sandia National Laboratory, and Moffatt & Nichol of The United States of America (NRC/SNL)
- SCANSOT of Sweden

The participants agreed to create three models to investigate the local effects mentioned above. Two of the models were to be local models, and the third was to be a full containment model. The first local model, a fundamental tendon behavior model, consists of two hoop tendons, assumed to be unaffected by penetration stiffness discontinuities in the wall. This model will allow participants to investigate tendon forces as a function of containment dilation and tendon slippage. The second local model investigates the equipment hatch, and allows participants to further investigate tendon force as a function of containment dilation and tendon slippage, while also allowing participants to investigate the steel-concrete interface and failure mechanisms in the liner. The final full 3-D model will allow participants to investigate all of the local effects (phase one), and allow the participants to investigate the response of the structure to combined pressure and temperature loads (phase two), and to predict leak rates as a function of pressure (phase two).

This report provides a comparison of the modeling approaches and results of all of the participants from the second phase of the analyses. Chapter 1 provides a description of the model, as well as a list of the expected results from the participants. Chapter 2 compares the methods used by the participants to create Model 4. Chapter 3 compares results from the Case 1 loading profile (excluding leakage). Chapter 4 compares results from the Case 2 loading profile (excluding leakage). Chapter 5 compares the leakage rate calculations that the participants completed. Chapter 6 compares the different approaches participants used to transition to probabilistic space. Each participant wrote a report summarizing their modeling efforts. Those are included in the appendices, and organized alphabetically.

CONTENTS

Abstract	3
Acknowledgments.....	5
Executive Summary	7
Contents	9
Figures.....	11
Tables	19
Nomenclature.....	21
1 Introduction.....	23
1.1 Background	24
1.2 Phase Two Analysis Definition	25
1.2.1 Introduction.....	25
1.2.2 Phase Two SPE #3 Analyses	25
1.2.3 Assumptions for Heat Transfer Analysis.....	27
1.2.4 Material Properties and Variations Due to Temperature	30
1.2.5 Concrete Strength Degradation Versus Temperature Used in ISP-48.....	30
1.2.6 Required Outputs/Results	39
1.2.7 Estimating Crack Size and Leak Areas.....	43
1.3 Documents of SPE #3 Phase Two	46
1.4 Organizational Schedule	46
2 Model 4	47
2.1 Description of Material and FEM Models	47
2.2 Description of Model Failure Criteria.....	49
3 Case 1: Saturated Steam Results.....	51
3.1 Deformed Shape.....	51
3.2 Liner Strains.....	59
3.2.1 Peak Strains of Entire Liner	59
3.2.2 Average Strains at Selected Locations.....	68
3.3 Tendon Stress Distribution	74
3.3.1 Hoop Tendons	74
3.3.2 Vertical Tendons	88
3.4 Standard Output Location Comparisons	97
3.4.1 Displacements	97
3.4.2 Rebar Strains	105
3.4.3 Liner Strains	109
3.4.4 Tendon Strains	112
3.4.5 Tendon Forces.....	115
4 Case 2: Station Blackout Results	117
4.1 Deformed Shape.....	117
4.2 Liner Strains.....	125
4.2.1 Peak Strains of Entire Liner	125
4.2.2 Average Strains at Selected Locations.....	134

4.3	Tendon Stress Distribution	139
4.3.1	Hoop Tendons	139
4.3.2	Vertical Tendons	153
4.4	Standard Output Location Comparisons	162
4.4.1	Displacements	162
4.4.2	Rebar Strains	170
4.4.3	Liner Strains	174
4.4.4	Tendon Strains	178
4.4.5	Tendon Forces	180
5	Leak Rate Comparison.....	182
5.1	Methods Used To Calculate Leak Rate	182
5.1.1	Leakage Rate Methods Provided by AERB.....	182
5.1.2	Comparison of Methods Used by Participants.....	184
5.2	Comparison of Model 3 Liner Strains and Leak Rates.....	185
5.3	Comparison of Model 4, Case 1 and 2 Leak Rates.....	192
6	Transition To Probabilistic space.....	194
7	Conclusions.....	195
8	References.....	197
	Distribution	198

FIGURES

Figure 1: Model 4 – Case 1 Saturated Steam Pseudo- Time History [1].....	26
Figure 2: Model 4 – Case 2 Station Black-Out Time History	27
Figure 3: Axisymmetric Model with Thermal Boundary Conditions.....	29
Figure 4: Axisymmetric Model Thermal Gradients.....	30
Figure 5: Thermal Gradient Locations.....	30
Figure 6: Concrete Compression Strength Ratio vs. Temperature (Used for ISP-48	31
Figure 7: Steel yield Strength and Modulus Ratio vs. Temperature (used for ISP -48)	32
Figure 8: Stress-Strain Curves for Typical Hot-Rolled Steel at Elevated Temperature [3]	33
Figure 9: Reduction Factors for the Stress-Strain Relationship of Carbon Steel at Elevated Temperatures	35
Figure 10: Determination of Strain-Hardening of Carbon Steel at Elevated Temperatures [4]	36
Figure 11: A.1 Alternate Stress-Strain Relationship for steel allowing for strain hardening [4].....	37
Figure 12. A.2 Alternate Stress-Strain Relationships for Steel at elevated temperatures, allowing for strain hardening [4]	37
Figure 13: Idealization of Stress-Strain For Concrete at Elevated Temperatures per Eurocode [4].....	38
Figure 14: Liner View Showing SOL Strain Reports – Also Shown for Reference in Planning Global Liner Strain Map.....	42
Figure 15: LST Calculated Leak Rates at 1.5, 2.0, and 2.5 P_d	43
Figure 16: LST – Estimated Leak Rates (2.5-3.1 P_d)	44
Figure 17. Estimated Terminal Leak Rates.....	44
Figure 18: Schematic of a Containment Performance Model.....	46
Figure 19: Deformed Shape after Tendon Anchorage (a) AERB (b) NRC (x500)	51
Figure 20: Deformed Shape at 1.0 x P_d (a) AERB (b) NRC (x100).....	52
Figure 21: Deformed Shape at 1.5 x P_d (a) AERB (b) NRC (x100).....	53
Figure 22: Deformed Shape at 2.0 x P_d (a) AERB (b) NRC (x50)	54
Figure 23: Deformed Shape at 2.5 x P_d for (a) AERB (b) NRC (x50)	55
Figure 24: Deformed Shape at 3.0 x P_d (a) AERB (b) NRC (x20)	56
Figure 25: Deformed Shape at (a) 3.25 x P_d AERB (b) 3.3 x P_d NRC (x20)	57
Figure 26: Deformed Shape at 3.4 x P_d (a) AERB (b) NRC (x20)	58
Figure 27: Deformed Shape at Ultimate Pressure (a) AERB - 3.46 x P_d (b) NRC 3.6 x P_d , Deformation Scale x 20	59
Figure 28: Peak Strain at 0 x P_d (a) AERB (b) NRC	60
Figure 29: Peak Strain at 1.0 x P_d (a) AERB (b) NRC	61
Figure 30: Peak Strain at 1.5 x P_d (a) AERB (b) NRC	62
Figure 31: Peak Strain at 2.0 x P_d (a) AERB (b) NRC	63
Figure 32: Peak Strain at 2.5 x P_d (a) AERB (b) NRC	64
Figure 33: Peak Strain at 3.0 x P_d (a) AERB (b) NRC	65
Figure 34: Peak Strain at (a) 3.25 x P_d AERB (b) 3.3 x P_d NRC	66
Figure 35: Peak Strain at 3.40 x P_d (a) AERB (b) NRC	67
Figure 36: Peak Strain at Ultimate Pressure (a) 3.46 x P_d AERB (b) 3.6 x P_d NRC	68
Figure 37: Liner (E/H) View Showing Locations where Participants are Requested to Provide Liner Strain Results	69

Figure 38: Strain over Gauge Length at Location 1 Near Equipment Hatch.....	70
Figure 39: Strain over Gauge Length at Location 2 Near Equipment Hatch.....	70
Figure 40: Strain over Gauge Length at Location 3 Near Equipment Hatch.....	71
Figure 41: Strain over Gauge Length at Location 4 Near Equipment Hatch.....	71
Figure 42: Strain over Gauge Length at Location 5 Near Equipment Hatch.....	72
Figure 43: Strain over Gauge Length at Location 6 Near Equipment Hatch.....	72
Figure 44: Strain over Gauge Length at Location 7 Near Equipment Hatch.....	73
Figure 45: Strain over Gauge Length at Location 8 Near Equipment Hatch.....	73
Figure 46: Strain over Gauge Length at Location 9 Near Equipment Hatch.....	74
Figure 47: Strain over Gauge Length at Location 10 Near Equipment Hatch.....	74
Figure 48: Tendon Stress Distribution for Tendon #H35 at 0 x P _d	75
Figure 49: Tendon Stress Distribution for Tendon #H35 at 1.0 x P _d	75
Figure 50: Tendon Stress Distribution for Tendon #H35 at 1.5 x P _d	76
Figure 51: Tendon Stress Distribution for Tendon #H35 at 2.0 x P _d	76
Figure 52: Tendon Stress Distribution for Tendon #H35 at 2.5 x P _d	77
Figure 53: Tendon Stress Distribution for Tendon #H35 at 3.0 x P _d	77
Figure 54: Tendon Stress Distribution for Tendon #H35 at 3.3 x P _d	78
Figure 55: Tendon Stress Distribution for Tendon #H35 at 3.4 x P _d	78
Figure 56: Tendon Stress Distribution for Tendon #H35 at Ultimate Pressure.....	79
Figure 57: Tendon Stress Distribution for Tendon #H53 at 0 x P _d	79
Figure 58: Tendon Stress Distribution for Tendon #H53 at 1.0 x P _d	80
Figure 59: Tendon Stress Distribution for Tendon #H53 at 1.5 x P _d	80
Figure 60: Tendon Stress Distribution for Tendon #H53 at 2.0 x P _d	81
Figure 61: Tendon Stress Distribution for Tendon #H53 at 2.5 x P _d	81
Figure 62: Tendon Stress Distribution for Tendon #H53 at 3.0 x P _d	82
Figure 63: Tendon Stress Distribution for Tendon #H53 at 3.3 x P _d	82
Figure 64: Tendon Stress Distribution for Tendon #H53 at 3.4 x P _d	83
Figure 65: Tendon Stress Distribution for Tendon #H53 at Ultimate Pressure.....	83
Figure 66: Tendon Stress Distribution for Tendon #H68 at 0 x P _d	84
Figure 67: Tendon Stress Distribution for Tendon #H68 at 1.0 x P _d	84
Figure 68: Tendon Stress Distribution for Tendon #H68 at 1.5 x P _d	85
Figure 69: Tendon Stress Distribution for Tendon #H68 at 2.0 x P _d	85
Figure 70: Tendon Stress Distribution for Tendon #H68 at 2.5 x P _d	86
Figure 71: Tendon Stress Distribution for Tendon #H68 at 3.0 x P _d	86
Figure 72: Tendon Stress Distribution for Tendon #H68 at 3.3 x P _d	87
Figure 73: Tendon Stress Distribution for Tendon #H68 at 3.4 x P _d	87
Figure 74: Tendon Stress Distribution for Tendon #H68 at Ultimate Pressure.....	88
Figure 75: Tendon Stress Distribution for Tendon #V37 at 0 x P _d	88
Figure 76: Tendon Stress Distribution for Tendon #V37 at 1.0 x P _d	89
Figure 77: Tendon Stress Distribution for Tendon #V37 at 1.5 x P _d	89
Figure 78: Tendon Stress Distribution for Tendon #V37 at 2.0 x P _d	90
Figure 79: Tendon Stress Distribution for Tendon #V37 at 2.5 x P _d	90
Figure 80: Tendon Stress Distribution for Tendon #V37 at 3.0 x P _d	91
Figure 81: Tendon Stress Distribution for Tendon #V37 at 3.3 x P _d	91
Figure 82: Tendon Stress Distribution for Tendon #V37 at 3.4 x P _d	92
Figure 83: Tendon Stress Distribution for Tendon #V37 at Ultimate Pressure.....	92

Figure 84: Tendon Stress Distribution for Tendon #V46 at 0 x P _d	93
Figure 85: Tendon Stress Distribution for Tendon #V46 at 1.0 x P _d	93
Figure 86: Tendon Stress Distribution for Tendon #V46 at 1.5 x P _d	94
Figure 87: Tendon Stress Distribution for Tendon #V46 at 2.0 x P _d	94
Figure 88: Tendon Stress Distribution for Tendon #V46 at 2.5 x P _d	95
Figure 89: Tendon Stress Distribution for Tendon #V46 at 3.0 x P _d	95
Figure 90: Tendon Stress Distribution for Tendon #V46 at 3.3 x P _d	96
Figure 91: Tendon Stress Distribution for Tendon #V46 at 3.4 x P _d	96
Figure 92: Tendon Stress Distribution for Tendon #V46 at Ultimate Pressure.....	97
Figure 93: Displacement Versus Pressure at SOL #1 (Vertical Displacement at Top of Basemat)	98
Figure 94: Displacement Versus Pressure at SOL #2 (Radial Displacement at Base of Cylinder)	98
Figure 95: Displacement Versus Pressure at SOL #3 (Radial Displacement at Base of Cylinder)	99
Figure 96: Displacement Versus Pressure at SOL #4 (Radial Displacement at Base of Cylinder)	99
Figure 97: Displacement Versus Pressure at SOL #5 (Radial Displacement at E/H Elevation)	100
Figure 98: Displacement Versus Pressure at SOL #6 (Radial Displacement at Midheight)	100
Figure 99: Displacement Versus Pressure at SOL #7 (Radial Displacement at Springline)	101
Figure 100: Displacement Versus Pressure at SOL #8 (Vertical Displacement at Springline)	101
Figure 101: Displacement Versus Pressure at SOL #9 (Radial Displacement at Dome 45°)	102
Figure 102: Displacement Versus Pressure at SOL #10 (Vertical Displacement at Dome 45°)	102
Figure 103: Displacement Versus Pressure at SOL #11 (Vertical Displacement at Dome Apex)	103
Figure 104: Displacement Versus Pressure at SOL #12 (Radial Displacement at Midheight of Buttress).....	103
Figure 105: Displacement Versus Pressure at SOL #13 (Radial Displacement at Springline of Buttress).....	104
Figure 106: Displacement Versus Pressure at SOL #14 (Radial Displacement at Center of E/H).....	104
Figure 107: Displacement Versus Pressure at SOL #15 (Radial Displacement at Center of A/L).....	105
Figure 108: Rebar Strain Versus Pressure at SOL #22 (Hoop Strain of Outer Rebar at Midheight and Azimuth 135).....	105
Figure 109: Rebar Strain Versus Pressure at SOL #23 (Meridional Strain of Outer Rebar at Midheight and Azimuth 135).....	106
Figure 110: Rebar Strain Versus Pressure at SOL #24 (Hoop Strain of Outer Rebar at Springline)	106
Figure 111: Rebar Strain Versus Pressure at SOL #25 (Meridional Strain of Inner Rebar at Springline)	107
Figure 112: Rebar Strain Versus Pressure at SOL #26 (Meridional Strain of Outer Rebar at Springline)	107
Figure 113: Rebar Strain Versus Pressure at SOL #27 (Hoop Strain of Outer Rebar at Dome 45°).....	108

Figure 114: Rebar Strain Versus Pressure at SOL #28 (Meridional Strain of Inner Rebar at Dome 45°).....	108
Figure 115: Rebar Strain Versus Pressure at SOL #29 (Meridional Strain of Outer Rebar at Dome 45°).....	109
Figure 116: Liner Strain Versus Pressure at SOL #36 (Meridional Strain of Inside of Liner at Base of Cylinder).....	109
Figure 117: Liner Strain Versus Pressure at SOL #37 (Hoop Strain of Inside of Liner at Base of Cylinder).....	110
Figure 118: Liner Strain Versus Pressure at SOL #38 (Meridional Strain of Inside of Liner at Midheight)	110
Figure 119: Liner Strain Versus Pressure at SOL #39 (Hoop Strain of Inside of Liner at Midheight)	111
Figure 120: Liner Strain Versus Pressure at SOL #40 (Meridional Strain of Inside of Liner at Springline)	111
Figure 121: Liner Strain Versus Pressure at SOL #41 (Hoop Strain of Inside of Liner at Springline)	112
Figure 122: Liner Strain Versus Pressure at SOL #42 (Meridional Strain of Inside of Liner at Dome Apex).....	112
Figure 123: Tendon Strain Versus Pressure at SOL #48 (Hairpin, Tendon V37 at Tendon Apex)	113
Figure 124: Tendon Strain Versus Pressure at SOL #49 (Hairpin, Tendon V46 at Tendon Springline)	113
Figure 125: Tendon Strain Versus Pressure at SOL #50 (Hoop, Tendon H53 at Mid-Tendon)	114
Figure 126: Tendon Strain Versus Pressure at SOL #51 (Hoop, Tendon H53 at ¼ Tendon)	114
Figure 127: Tendon Strain Versus Pressure at SOL #52 (Hoop, Tendon H53 Near Buttress)....	115
Figure 128: Tendon Strain Versus Pressure at SOL #53 (Hoop, Tendon H35 Between E/H and A/L).....	115
Figure 129: Tendon Force Versus Pressure at SOL #54 (Hairpin, Tendon V37 at Tendon Gallery).....	116
Figure 130: Tendon Strain Versus Pressure at SOL #55 (Hoop, Tendon H53 at Buttress)	116
Figure 131: Deformed Shape after Tendon Anchorage (a) AERB (b) NRC (x500)	117
Figure 132: Deformed Shape at 1.0 x P _d (a) AERB (b) NRC (x100).....	118
Figure 133: Deformed Shape at 1.5 x P _d (a) AERB (b) NRC (x100).....	119
Figure 134: Deformed Shape at 2.0 x P _d (a) AERB (b) NRC (x50).....	120
Figure 135: Deformed Shape at 2.5 x P _d for (a) AERB (b) NRC (x50)	121
Figure 136: Deformed Shape at 3.0 x P _d (a) AERB (b) NRC (x20).....	122
Figure 137: Deformed Shape at (a) 3.25 x P _d AERB (b) 3.3 x P _d NRC (x20)	123
Figure 138: Deformed Shape at 3.4 x P _d (a) AERB (b) NRC (x20).....	124
Figure 139: Deformed Shape at Ultimate Pressure (a) AERB - 3.46 x P _d (b) NRC 3.6 x P _d , Deformation Scale x 20	125
Figure 140: Peak Strain at 0 x P _d (a) AERB (b) NRC	126
Figure 141: Peak Strain at 1.0 x P _d (a) AERB (b) NRC	127
Figure 142: Peak Strain at 1.5 x P _d (a) AERB (b) NRC	128
Figure 143: Peak Strain at 2.0 x P _d (a) AERB (b) NRC	129
Figure 144: Peak Strain at 2.5 x P _d (a) AERB (b) NRC	130
Figure 145: Peak Strain at 3.0 x P _d (a) AERB (b) NRC	131

Figure 146: Peak Strain at (a) $3.25 \times P_d$ AERB (b) $3.3 \times P_d$ NRC	132
Figure 147: Peak Strain at $3.40 \times P_d$ (a) AERB (b) NRC	133
errFigure 148: Peak Strain at Ultimate Pressure (a) $3.46 \times P_d$ AERB (b) $3.6 \times P_d$ NRC	134
Figure 149: Strain over Gauge Length at Location 1 Near Equipment Hatch.....	135
Figure 150: Strain over Gauge Length at Location 2 Near Equipment Hatch.....	135
Figure 151: Strain over Gauge Length at Location 3 Near Equipment Hatch.....	136
Figure 152: Strain over Gauge Length at Location 4 Near Equipment Hatch.....	136
Figure 153: Strain over Gauge Length at Location 5 Near Equipment Hatch.....	137
Figure 154: Strain over Gauge Length at Location 6 Near Equipment Hatch.....	137
Figure 155: Strain over Gauge Length at Location 7 Near Equipment Hatch.....	138
Figure 156: Strain over Gauge Length at Location 8 Near Equipment Hatch.....	138
Figure 157: Strain over Gauge Length at Location 9 Near Equipment Hatch.....	139
Figure 158: Strain over Gauge Length at Location 10 Near Equipment Hatch.....	139
Figure 159: Tendon Stress Distribution for Tendon #H35 at $0 \times P_d$	140
Figure 160: Tendon Stress Distribution for Tendon #H35 at $1.0 \times P_d$	140
Figure 161: Tendon Stress Distribution for Tendon #H35 at $1.5 \times P_d$	141
Figure 162: Tendon Stress Distribution for Tendon #H35 at $2.0 \times P_d$	141
Figure 163: Tendon Stress Distribution for Tendon #H35 at $2.5 \times P_d$	142
Figure 164: Tendon Stress Distribution for Tendon #H35 at $3.0 \times P_d$	142
Figure 165: Tendon Stress Distribution for Tendon #H35 at $3.3 \times P_d$	143
Figure 166: Tendon Stress Distribution for Tendon #H35 at $3.4 \times P_d$	143
Figure 167: Tendon Stress Distribution for Tendon #H35 at Ultimate Pressure.....	144
Figure 168: Tendon Stress Distribution for Tendon #H53 at $0 \times P_d$	144
Figure 169: Tendon Stress Distribution for Tendon #H53 at $1.0 \times P_d$	145
Figure 170: Tendon Stress Distribution for Tendon #H53 at $1.5 \times P_d$	145
Figure 171: Tendon Stress Distribution for Tendon #H53 at $2.0 \times P_d$	146
Figure 172: Tendon Stress Distribution for Tendon #H53 at $2.5 \times P_d$	146
Figure 173: Tendon Stress Distribution for Tendon #H53 at $3.0 \times P_d$	147
Figure 174: Tendon Stress Distribution for Tendon #H53 at $3.3 \times P_d$	147
Figure 175: Tendon Stress Distribution for Tendon #H53 at $3.4 \times P_d$	148
Figure 176: Tendon Stress Distribution for Tendon #H53 at Ultimate Pressure.....	148
Figure 177: Tendon Stress Distribution for Tendon #H68 at $0 \times P_d$	149
Figure 178: Tendon Stress Distribution for Tendon #H68 at $1.0 \times P_d$	149
Figure 179: Tendon Stress Distribution for Tendon #H68 at $1.5 \times P_d$	150
Figure 180: Tendon Stress Distribution for Tendon #H68 at $2.0 \times P_d$	150
Figure 181: Tendon Stress Distribution for Tendon #H68 at $2.5 \times P_d$	151
Figure 182: Tendon Stress Distribution for Tendon #H68 at $3.0 \times P_d$	151
Figure 183: Tendon Stress Distribution for Tendon #H68 at $3.3 \times P_d$	152
Figure 184: Tendon Stress Distribution for Tendon #H68 at $3.4 \times P_d$	152
Figure 185: Tendon Stress Distribution for Tendon #H68 at Ultimate Pressure.....	153
Figure 186: Tendon Stress Distribution for Tendon #V37 at $0 \times P_d$	154
Figure 187: Tendon Stress Distribution for Tendon #V37 at $1.0 \times P_d$	154
Figure 188: Tendon Stress Distribution for Tendon #V37 at $1.5 \times P_d$	154
Figure 189: Tendon Stress Distribution for Tendon #V37 at $2.0 \times P_d$	155
Figure 190: Tendon Stress Distribution for Tendon #V37 at $2.5 \times P_d$	155
Figure 191: Tendon Stress Distribution for Tendon #V37 at $3.0 \times P_d$	156

Figure 192: Tendon Stress Distribution for Tendon #V37 at $3.3 \times P_d$	156
Figure 193: Tendon Stress Distribution for Tendon #V37 at $3.4 \times P_d$	157
Figure 194: Tendon Stress Distribution for Tendon #V37 at Ultimate Pressure.....	157
Figure 195: Tendon Stress Distribution for Tendon #V46 at $0 \times P_d$	158
Figure 196: Tendon Stress Distribution for Tendon #V46 at $1.0 \times P_d$	158
Figure 197: Tendon Stress Distribution for Tendon #V46 at $1.5 \times P_d$	159
Figure 198: Tendon Stress Distribution for Tendon #V46 at $2.0 \times P_d$	159
Figure 199: Tendon Stress Distribution for Tendon #V46 at $2.5 \times P_d$	160
Figure 200: Tendon Stress Distribution for Tendon #V46 at $3.0 \times P_d$	160
Figure 201: Tendon Stress Distribution for Tendon #V46 at $3.3 \times P_d$	161
Figure 202: Tendon Stress Distribution for Tendon #V46 at $3.4 \times P_d$	161
Figure 203: Tendon Stress Distribution for Tendon #V46 at Ultimate Pressure.....	162
Figure 204: Displacement Versus Pressure at SOL #1 (Vertical Displacement at Top of Basemat)	163
Figure 205: Displacement Versus Pressure at SOL #2 (Radial Displacement at Base of Cylinder)	163
Figure 206: Displacement Versus Pressure at SOL #3 (Radial Displacement at Base of Cylinder)	164
Figure 207: Displacement Versus Pressure at SOL #4 (Radial Displacement at Base of Cylinder)	164
Figure 208: Displacement Versus Pressure at SOL #5 (Radial Displacement at E/H Elevation).....	165
Figure 209: Displacement Versus Pressure at SOL #6 (Radial Displacement at Midheight)	165
Figure 210: Displacement Versus Pressure at SOL #7 (Radial Displacement at Springline)	166
Figure 211: Displacement Versus Pressure at SOL #8 (Vertical Displacement at Springline)....	166
Figure 212: Displacement Versus Pressure at SOL #9 (Radial Displacement at Dome 45°).....	167
Figure 213: Displacement Versus Pressure at SOL #10 (Vertical Displacement at Dome 45°) .	167
Figure 214: Displacement Versus Pressure at SOL #11 (Vertical Displacement at Dome Apex)	168
Figure 215: Displacement Versus Pressure at SOL #12 (Radial Displacement at Midheight of Buttress).....	168
Figure 216: Displacement Versus Pressure at SOL #13 (Radial Displacement at Springline of Buttress).....	169
Figure 217: Displacement Versus Pressure at SOL #14 (Radial Displacement at Center of E/H).....	169
Figure 218: Displacement Versus Pressure at SOL #15 (Radial Displacement at Center of A/L).....	170
Figure 219: Rebar Strain Versus Pressure at SOL #22 (Hoop Strain of Outer Rebar at Midheight and Azimuth 135).....	170
Figure 220: Rebar Strain Versus Pressure at SOL #23 (Meridional Strain of Outer Rebar at Midheight and Azimuth 135).....	171
Figure 221: Rebar Strain Versus Pressure at SOL #24 (Hoop Strain of Outer Rebar at Springline)	171
Figure 222: Rebar Strain Versus Pressure at SOL #25 (Meridional Strain of Inner Rebar at Springline)	172

Figure 223: Rebar Strain Versus Pressure at SOL #26 (Meridional Strain of Outer Rebar at Springline)	172
Figure 224: Rebar Strain Versus Pressure at SOL #27 (Hoop Strain of Outer Rebar at Dome 45°).....	173
Figure 225: Rebar Strain Versus Pressure at SOL #28 (Meridional Strain of Inner Rebar at Dome 45°).....	173
Figure 226: Rebar Strain Versus Pressure at SOL #29 (Meridional Strain of Outer Rebar at Dome 45°).....	174
Figure 227: Liner Strain Versus Pressure at SOL #36 (Meridional Strain of Inside of Liner at Base of Cylinder).....	174
Figure 228: Liner Strain Versus Pressure at SOL #37 (Hoop Strain of Inside of Liner at Base of Cylinder).....	175
Figure 229: Liner Strain Versus Pressure at SOL #38 (Meridional Strain of Inside of Liner at Midheight)	175
Figure 230: Liner Strain Versus Pressure at SOL #39 (Hoop Strain of Inside of Liner at Midheight)	176
Figure 231: Liner Strain Versus Pressure at SOL #40 (Meridional Strain of Inside of Liner at Springline)	176
Figure 232: Liner Strain Versus Pressure at SOL #41 (Hoop Strain of Inside of Liner at Springline)	177
Figure 233: Liner Strain Versus Pressure at SOL #42 (Meridional Strain of Inside of Liner at Dome Apex).....	177
Figure 234: Tendon Strain Versus Pressure at SOL #48 (Hairpin, Tendon V37 at Tendon Apex)	178
Figure 235: Tendon Strain Versus Pressure at SOL #49 (Hairpin, Tendon V46 at Tendon Springline)	178
Figure 236: Tendon Strain Versus Pressure at SOL #50 (Hoop, Tendon H53 at Mid-Tendon)	179
Figure 237: Tendon Strain Versus Pressure at SOL #51 (Hoop, Tendon H53 at $\frac{1}{4}$ Tendon)	179
Figure 238: Tendon Strain Versus Pressure at SOL #52 (Hoop, Tendon H53 Near Buttress)....	180
Figure 239: Tendon Strain Versus Pressure at SOL #53 (Hoop, Tendon H35 Between E/H and A/L).....	180
Figure 240: Tendon Force Versus Pressure at SOL #54 (Hairpin, Tendon V37 at Tendon Gallery).....	181
Figure 241: Tendon Strain Versus Pressure at SOL #55 (Hoop, Tendon H53 at Buttress)	181
Figure 242: Definition of Crack Length and Crack Width	182
Figure 243: Liner Strains in Model 3 at $1.0 \times P_d$ for (a) FORTUM, and (b) NRC with (c) Scale for NRC	186
Figure 244: Liner Strains in Model 3 at $2.0 \times P_d$ for (a) FORTUM, and (b) NRC with (c) Scale for NRC.....	187
Figure 245: Liner Strains in Model 3 at $3.0 \times P_d$ for (a) FORTUM, and (b) NRC with (c) Scale for NRC.....	188
Figure 246: Liner Strains in Model 3 at $3.3 \times P_d$ for (a) FORTUM, and (b) NRC with (c) Scale for NRC.....	189
Figure 247: Liner Strains in Model 3 at Ultimate Pressure for (a) FORTUM ($3.5 \times P_d$), and (b) NRC ($3.6 \times P_d$) with (c) Scale for NRC	190

Figure 248: Comparison of Model 3 Leak Rates vs Experimental Data for (a) AERB (b) FORTUM and (c) NRC	192
Figure 249: Calculated Model 4 Leak Rates for (a) AERB (case 1) (b) AERB (case 2) and (c) NRC.....	193

TABLES

Table 1: Data Point for Strength Degradation Versus Temperature.....	31
Table 2: Reduction Factors for Stress-Strain Relationship of Carbon Steel at Elevated Temperatures	34
Table 3: Values for the Main Parameters of the Stress-Strain Relationships of Normal Weight Concrete with Siliceous or Calcareous Aggregates Concrete at Elevated Temperatures	39
Table 4: Standard Output Location Definitions.....	41
Table 5: Model Detail Comparison.....	48
Table 6: Boundary Conditions of Note	48
Table 7: Comparison of Material Models	49
Table 8: Tendon failure criteria	50
Table 9: Liner failure criteria.....	50
Table 10: Leakage Rate Formulations Used.....	184
Table 11: Methods Used to Calculate Crack Width	185

NOMENCLATURE

AERB	Atomic Energy Regulatory Board
A/L	Airlock
AMEC	AMEC Power & Process
BARC	Bhabha Atomic Research Center
BWR	Boiling Water Reactor
Δs	Anchorage Slip
E	Young's Modulus
E/H	Equipment Hatch
E_p	Plastic Hardening Modulus
EDF	Électricité de France
FEM	Finite Element Method
f_{gu}	Guaranteed Ultimate Tensile Strength
FY	Fiscal Year
GRS	Gesellschaft Für Anlagen-und Reaktorsicherheit
IGCAR	Indira Gandhi Center of Atomic Research
ISP	International Standard Problem
M&N	Moffatt and Nichol
NPCIL	Nuclear Power Corporation (India) Ltd.
NRC	See USNRC
NUPEC	Nuclear Power Engineering Corporation of Japan
ρ	Density
PCCV	Prestressed Concrete Containment Vessel
P_d	Design Pressure
PWR	Pressurized Water Reactor
SCANSBOT	Scanscot Technology
σ_t	Tensile Yield Strength
SCV	Steel Containment Vessel
SNL	Sandia National Laboratory
SOL	Standard Output Location
SPE	Standard Problem Exercise
T_0	Initial Prestressing Force
μ	Coefficient of Friction
USNRC	United States Nuclear Regulatory Commission
ν	Poisson Ratio

1 INTRODUCTION

Research into the integrity of containment structures for nuclear power plants has been conducted in multiple international Round Robin analyses. These analyses have contributed to the understanding of the role of containment in ensuring the safe operation of nuclear power plants. One of the most comprehensive experimental efforts, testing of a 1:4 scale PCCV, was conducted at SNL, under the sponsorship of the NRC and NUREG. Building upon the research efforts made in the pre- and post- test analyses, and the International Standard Problem 48 (ISP 48), the Standard Problem Exercise #3 (SPE #3) has been set up to provide the opportunity for participants to advance the state-of-the-art in modeling of prestressed concrete containment vessels. Following the ISP 48 and 1:4 scale PCCV efforts, there was interest in investigating local effects and questions that had been unanswered previously due to modeling and computational limitations at the time and scope limitations of the previous efforts. At the kick off meeting of the SPE-3, held in Mumbai, India, the scope of the first phase of the SPE-3 was agreed upon. There was an interest in investigating the effects of containment dilation on prestressing force, slippage of prestressing cables, steel-concrete interface, failure mechanisms, and the use of nominal versus in-situ conditions in modeling.

These areas of investigation, and proposed models to be used in the analyses were determined by those involved who participated in the kick-off meeting. The participants of the kick-off meeting included (in alphabetical order):

- Atomic Energy Regulatory Board of India
- Bhabha Atomic Research Center of India
- Électricité de France of France
- FORTUM of Finland
- Gesellschaft Für Anlagen-und Reaktorsicherheit of Germany
- Indira Gandhi Center of Atomic Research of India
- Nuclear Power Corporation Ltd. Of India
- NRC/SNL/M&N of The United States of America
- SCANSOT of Sweden

The participants agreed to create three models to investigate the local effects mentioned above. Two of the models were to be local models, and the third was to be a full 3-D model. The first local model is a fundamental tendon behavior model, that consists of two hoop tendons, assumed to be unaffected by penetration stiffness discontinuities in the wall. This model will allow participants to investigate tendon forces as a function of containment dilation and tendon slippage. The second local model investigates the equipment hatch, and allows participants to further investigate tendon force as a function of containment dilation and tendon slippage, while also allowing participants to investigate the steel-concrete interface and failure mechanisms in the liner. The final full 3-D model will allow participants to: investigate all of the local effects (phase one); allow the participants to investigate the response of the structure to combined pressure and temperature loads (phase two); and to predict leak rates as a function of just pressure or as a function for both pressure and time (phase two).

This report provides a comparison of the modeling approaches and results of all of the participants from the second phase of the analyses. Chapter 1 provides a description of the model, as well as a list of the expected results from the participants. Chapter 2 compares the methods used by the participants to create Model 4. Chapter 3 compares results from the Case 1 loading profile (excluding leakage). Chapter 4 compares results from the Case 2 loading profile (excluding leakage). Chapter 5 compares the leakage rate calculations that the participants completed. Chapter 6 compares the different approaches participants used to transition to probabilistic space. Each participant wrote a report summarizing their modeling efforts. Those are included in the appendices, and organized alphabetically.

1.1 Background

Research into the integrity of containment structures for nuclear power plants has been conducted in both internal and international Round Robin analyses. While the contributions of each of these efforts to the understanding of the role of containment in ensuring the safe operation of nuclear power plants is important, the most comprehensive experimental effort has been conducted at Sandia National Laboratories, primarily under the sponsorship of the Nuclear Regulatory Commission. NUREG/CR 6906, “Containment Integrity Research at Sandia National Laboratories: An Overview,” summarizes the major results of the experimental efforts, the observations and insights gained from the analytical efforts for more than 25 years of containment integrity research at SNL. Prior to pressure testing the scale models, a number of regulatory and research organizations were invited to participate in a pre-test Round Robin analysis to perform predictive modeling of the response of scale models to over pressurization. Seventeen organizations responded and agreed to participate in the pre-test Round Robin analysis activities. The purpose of the Containment Integrity Research at SNL was to provide a forum for researchers in the area to apply current state-of-the-art analysis methodologies to predicting capacity of steel, reinforced, and pre-stressed concrete containment vessels.

As noted above, this work is related to the NRC-sponsored Containment Integrity Programs at SNL. These programs investigated the behavior of light water reactor (LWR) containment buildings under loadings that exceed the design basis or so-called “severe” accident loads. A combination of experimental and analytical studies was employed in these programs. Initially, over-pressurization tests of several scale model containment buildings were conducted under FIN A1817, “Concrete Containment Experiments,” and FIN A1249, “Experiments on Containment Models under Extreme Loading Conditions.” Separate tests of typical containment penetrations were conducted under FIN A 1375, “Integrity of Containment Penetrations under Severe Accident Loads.” Tests of electrical penetration assemblies (EPAs), a personnel airlock, bellows, a pressure unseating equipment hatch, the seals, and gaskets used in penetrations were included in this program.

In FY91, a cooperative program on containment integrity under severe accident conditions began between the NRC and NUPPEC of Japan. Testing and analyses of a steel containment vessel (SCV) model representative of a boiling water reactor (BWR), Mk-11 containment and a prestressed concrete containment vessel model, as used in some large, dry, pressurized water reactor (PWR) containments, were funded by the NRC.

Efforts were also made to assess the seismic capacity of containment structures. SNL performed pre- and post-test analyses of shaking table tests of a 1:10-scale prestressed concrete containment

model and a 1:8 scale reinforced concrete containment model. These models were constructed and the tests were conducted by NUPEC at Tadotsu Engineering Laboratory. The insights gained from analyzing the response of these test models were used to estimate the seismic capacities of typical US containments. The effects of aging-related degradation on containment capacity to resist severe accident pressures were investigated.

All of the aforementioned research efforts are being used to set the foundation for the current AERB/USNRC sponsored SPE #3. The 1:4 Scale Prestressed Concrete Containment Vessel built and pressure tested to failure by NUPEC, the USNRC, and SNL between 1998 and 2000 is the experimental model which is being used to test the FEM models against in the current SPE #3. Analytical models are meant to improve on modeling techniques developed for the pre- and post-test analyses, and the ISP #48, which also used the 1:4 Scale PCCV as the experimental basis for its FEM models. This exercise was set up as part of the U.S.-India Civil Nuclear Cooperation Agreement, and provides all participants the opportunity to improve the current state-of-the-art modeling of prestressed concrete containment vessels

1.2 Phase Two Analysis Definition

This chapter includes the analysis specification plan for Phase Two of the SPE #3 effort. This problem definition was determined and agreed to at the Phase One Concluding Meeting, held in April of 2011 in Washington, D.C.

1.2.1 *Introduction*

At the SPE Phase 1 Results Discussion Meeting for the Standard Problem Exercise (SPE) on the performance of containment vessels under severe accident conditions (Washington DC, April 13-14, 2011); consensus was reached on some of the details for the Phase 2 SPE program. This chapter is meant to specify the results of discussions held during the meeting, specifying those details of the SPE Phase 2 analyses to be performed, and to identify the results which are requested of the participants. It should be noted that a goal, continuing from discussions held in 2010, is to focus on questions still unanswered by the ISP-48, but to follow most of the temperature and loading definitions of ISP-48.

The current round-robin program consists of two rounds of analyses and three review meetings. Currently, the first round of analysis and the second review meeting have been completed. The primary source of physical test data remains the Sandia/NRC/NUPEC 1:4 Scale PCCV Test [1], but the introduction of other research or published ancillary test data is welcomed in furthering the aims of the SPE work.

This chapter is organized as follows. The work phases and topics of study printed in the original SPE invitation are shown in *italics*. The actual finite element model (FEM) definitions are presented in normal typeface, as Models 1, 2, and 3.

1.2.2 *Phase Two SPE #3 Analyses*

This phase of work has two distinct parts. Following the first phase of the Round Robin Analyses, the participants are asked to examine methods to estimate leakage rate as a function of pressure (and later, pressure and temperature). These methods will be evaluated relative to the PCCV test results, and incorporate lessons learned from the first phase of the Round Robin Analysis. This would constitute the first part. The second part will consist of enumeration of

methods for predicting leakage of prestressed concrete containment vessels as function of pressure and temperature; apply these methods to characterize the performance, in terms of leakage rate, under pressure and temperature; and transition them to probabilistic space.

Phase 2 shall require the participants to re-investigate Model 3 from Phase 1. We will refer to this additional investigation as Model 4. It is, essentially, Model 3, but with all modifications the participant may wish to introduce based on lessons-learned from Phase 1 and modifications suitable to introducing temperature into the solution. The participants will apply two different temperature loading cases to the global Model 4. The loading cases are shown below in Figure 1 and Figure 2. At the initial workshop, the participants agreed to use the ISP-48 [1] temperature cases, but to remove the H₂ burn because of its lack of effect on leak rate [1]. For Case 2, the “simplified” curves are used.

For temperature cases 1 & 2, a heat transfer solution was performed by Dameron et al for the 1:4 Scale PCCV to develop the temperature profiles through the containment wall at different elevations of the containment [1]. This information (and the derivation) is provided herein. (It is the same as was used for the ISP-48 Exercise.) More information about the ISP-48 analyses is available in the reports published from that exercise, and these are available on the SPE website. Nodal point temperatures should be interpolated between the section points given.

Development of a third temperature case was also discussed in Washington, aimed at incorporating recent information becoming available from the last several years of study of Containment Accident Scenarios, however, a third case was not added.

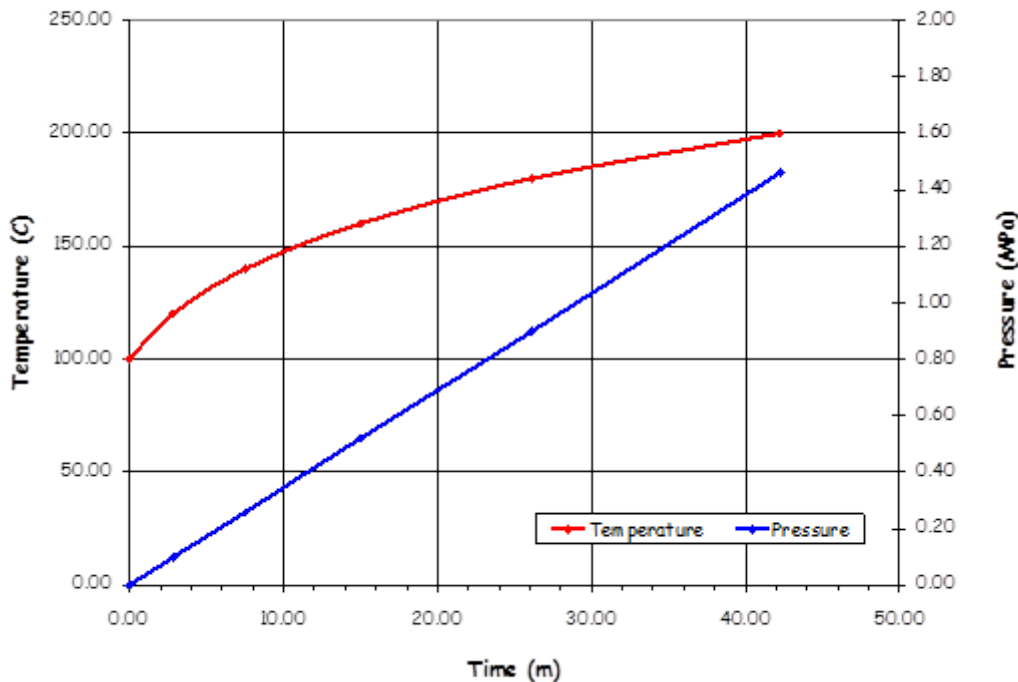


Figure 1: Model 4 – Case 1 Saturated Steam Pseudo- Time History [1]

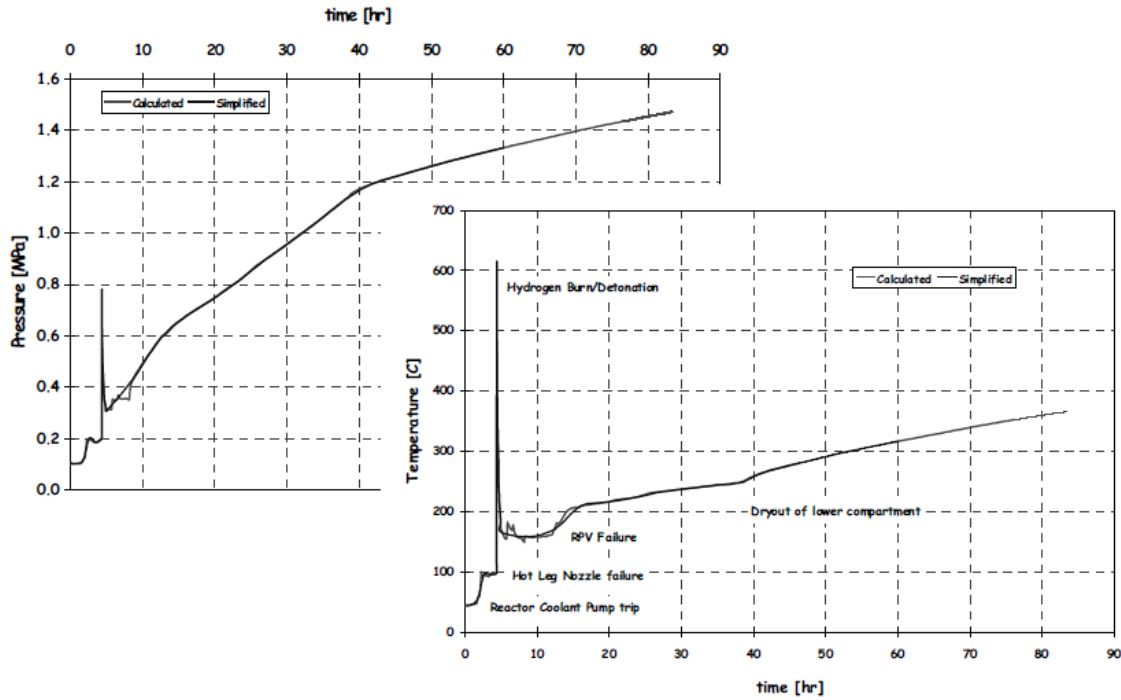


Figure 2: Model 4 – Case 2 Station Black-Out Time History

The thermal and mechanical analyses were de-coupled from the heat transfer calculations that were first performed using a full-scale axisymmetric model and a combination of applied temperature (liner), convection (cylinder wall and dome), and conduction (basemat/soil) boundary conditions. Thermal material properties and temperature dependent mechanical properties were based on handbook data (e.g. [2]).

A set of temperature-dependent concrete and steel mechanical properties were also provided. However these properties only enter into the mechanical (stress) portion of the solution and not into the purely thermal solution. All of these properties were offered as a baseline suggestion and documentation of the source of the thermal gradients, but SPE-3 participants were free to use properties from their own research if desired.

1.2.3 Assumptions for Heat Transfer Analysis

A full scale version of the PCCV 2 dimensional axisymmetric model was used to conduct the thermal analysis since the thermal response does not scale geometrically. The resulting gradients are then scaled and applied to the 1:4-scale models for combined thermal-mechanical analysis.

To conduct the Heat Transfer analysis in ABAQUS, all elements relevant for thermal analysis were changed to diffusive heat transfer element types, which only have temperature degrees of freedom. Thermal boundary conditions were imposed at the outer surface of the PCCV cylinder and dome wall consisting of free convection with air with a sink temperature ($T_{f,\infty}$) of 25°C. For free convection with air, the heat transfer coefficient, h , varies with temperature according to the following relationship:

$$h = 0.00382(\Delta T)^{1/3} \text{ lbf/in-s-}^{\circ}\text{F} \quad (\text{T in } {}^{\circ}\text{F}) \text{ for the full scale PCCV analysis, and}$$

$h = 0.0153(\Delta T)^{1/3}$ lbf/in-s-°F for the 1:4 scale analysis.

(These convert to 1.20 and 4.80 W-m⁻²-°K.)

This is input to ABAQUS as a “non-uniform film coefficient” (FNU) through the User-defined subroutine related to the SFILM option.

The boundary condition on the basemat foundation consists of heat conduction with soil with a sink temperature ($T_{f,*}$) of 25°C. The heat transfer coefficient was developed for the horizontal surface of the foundation in contact with the soil to be:

$h = 5.76 \times 10^{-5}$ lbf/in-s-°F for the full scale PCCV analysis,

$h = 2.30 \times 10^{-4}$ lbf/in-s-°F for the 1:4 scale PCCV.

(These convert to 0.0181 and 0.0724 W-m⁻²-°K)

This is input to ABAQUS as a constant film coefficient using the SFILM option and no User-defined subroutine. The temperature input for the thermal analysis was applied through prescribed temperature boundary conditions on the nodes of the inner surface of the basemat, cylinder wall, and dome (i.e., on the liner). For Case 2, a steady-state heat transfer analysis step preceded the dynamic heat transfer analysis with the time history temperature input. The steady state heat transfer step was used to bring the model up to an ambient/operating temperature of 25°C. Figure 3 shows the location of the prescribed boundary conditions for the axisymmetric model. Figure 4 shows the temperature contours for various steps in the heat transfer analysis. Also shown in Figure 5 are the sections through the containment wall and basemat where the temperature gradients are provided.

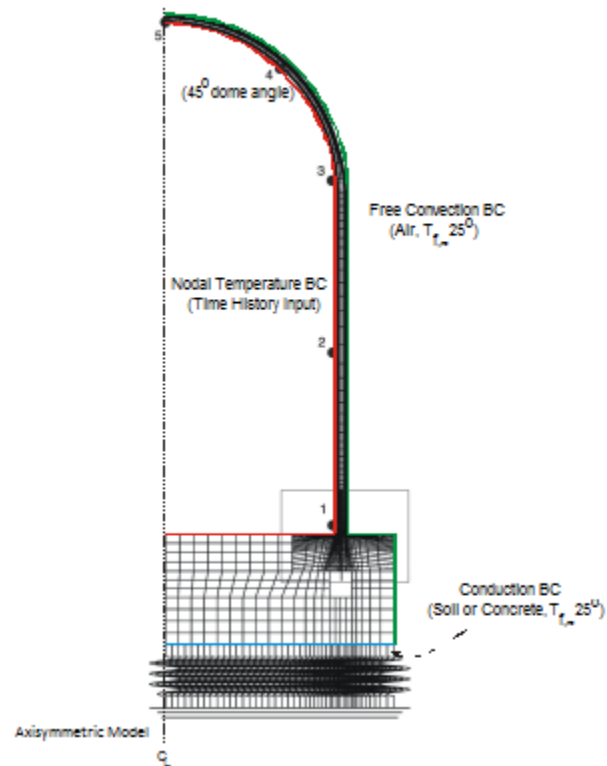
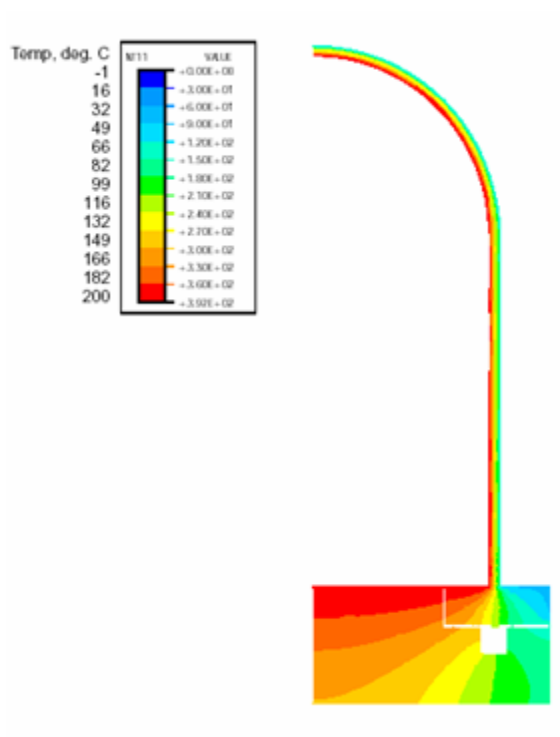
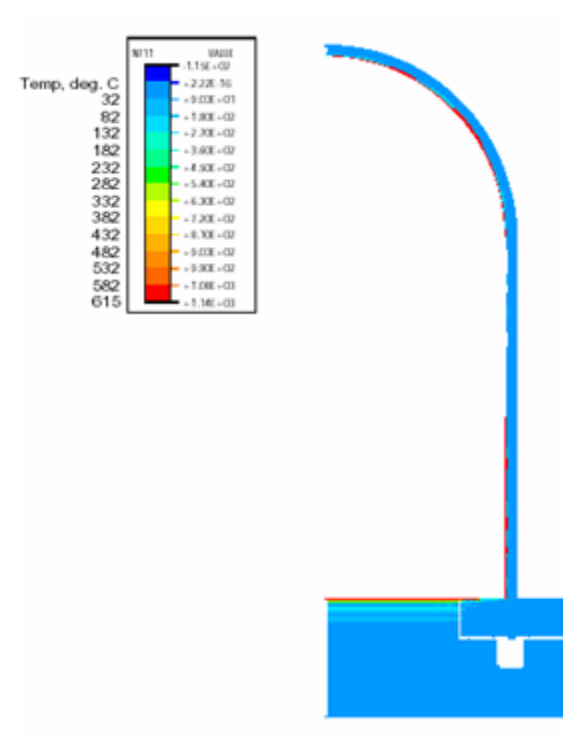


Figure 3: Axisymmetric Model with Thermal Boundary Conditions



Case 1 Thermal Gradients @ T = 200°C



Case 2 Thermal Gradients @ T = 615°C

Figure 4: Axisymmetric Model Thermal Gradients

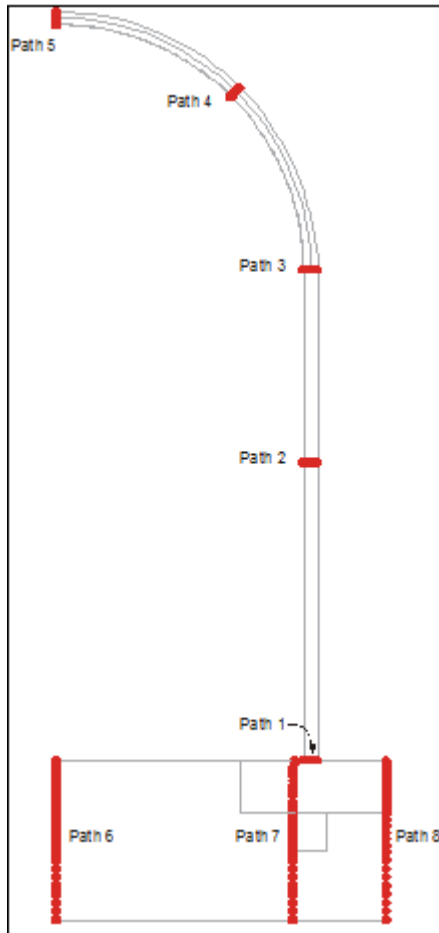


Figure 5: Thermal Gradient Locations

1.2.4 Material Properties and Variations Due to Temperature

A literature review was conducted during the ISP-48 work to choose and substantiate assumptions for concrete thermal properties, and for degradation of concrete and steel material properties. The final outcome of this work is summarized in Figure 6 and Figure 7. However, when the ISP-48 work was published, the literature review was still lacking in stress-strain information for steel at elevated temperature. Since that time, more data has been found, particularly with the research interest in design for fire- resistance conducted in the last decade (for example [3]). In order to consolidate the many research findings, we suggest that SPE participants use the stress-strain property versus temperature relationships published in the 2005 Euro-Code [4]; these are summarized in Figure 8 through Figure 12.

1.2.5 Concrete Strength Degradation Versus Temperature Used in ISP-48

Concrete Strength Ratio, $S_{Rc} = \exp^{-((T / 632)^{1.8})}$ where T is in degrees C.

The derivation of this curve was based on assumption of a basic shape as observed from the data, and then pegging the curve to the following points.

Table 1: Data Point for Strength Degradation Versus Temperature

T (°C)	S _R at 1000°C
0	1.00
200	0.88
600	0.40
1000	1.10

Further, based on the literature, it appears reasonable to base the modulus on the standard ACI formula (English Units) such that a Modulus Reduction Ratio (MR) can be defined as:

$$M_R = \sqrt{S_R} \quad (1.1)$$

It should be noted, however, that the peak strain at which the concrete compressive strength limit is reached also shifts with increasing temperature. While at 25°C, this strain is approximately 0.002, it can reach two to three times this value at high temperatures.

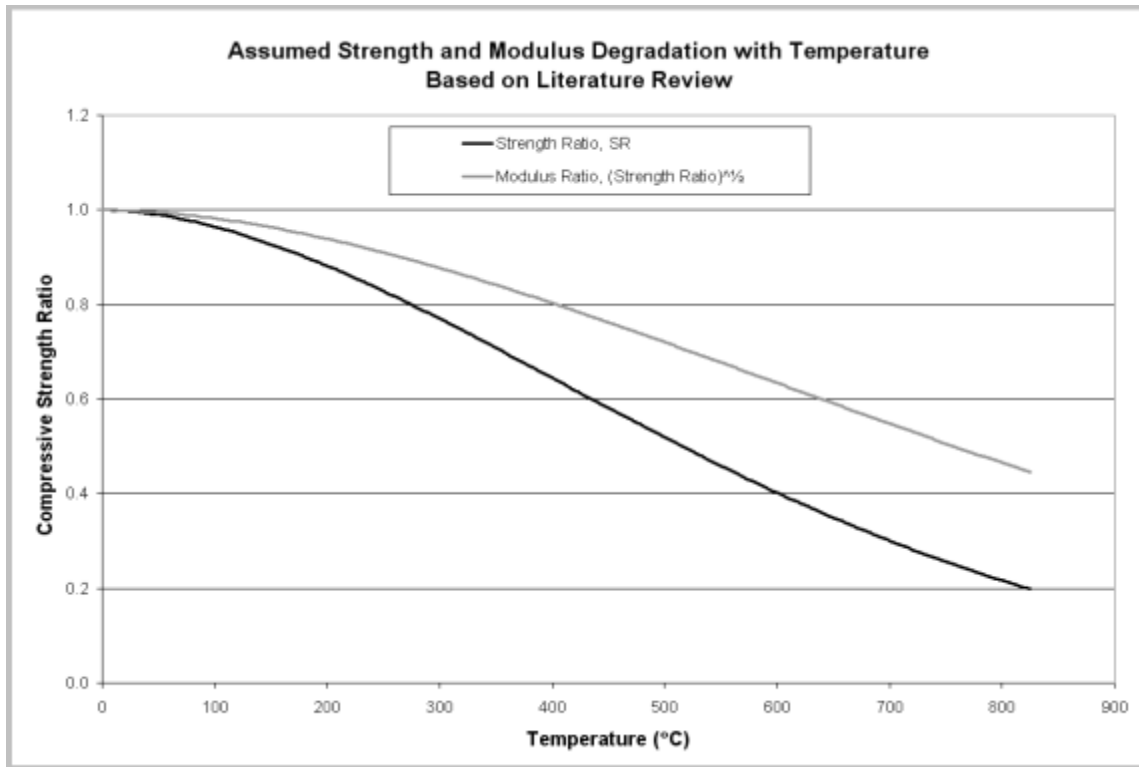


Figure 6: Concrete Compression Strength Ratio vs. Temperature (Used for ISP-48

Temperature variation of steel is also included in the mechanical solution. This variation has been idealized based on curves and trends observed in other texts and papers:

Steel Yield Strength Ratio, $S_{Rs} = \exp^{-((T - 340)/300)^{1.9}}$ where T is in degrees C.

$$S_{Rs} = 1.0, T \leq 340C$$

For steel, the Young's Modulus tends to follow the yield strength one-to-one, rather than the square-root relationship found in concrete.

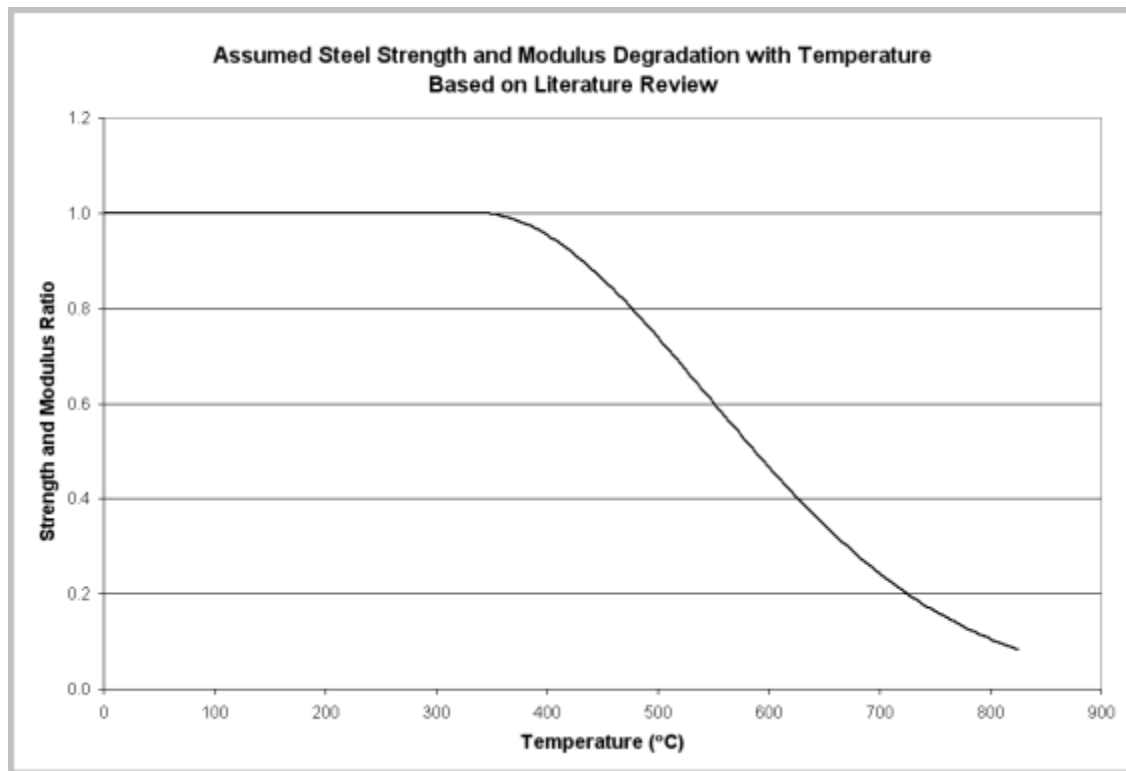


Figure 7: Steel yield Strength and Modulus Ratio vs. Temperature (used for ISP -48)

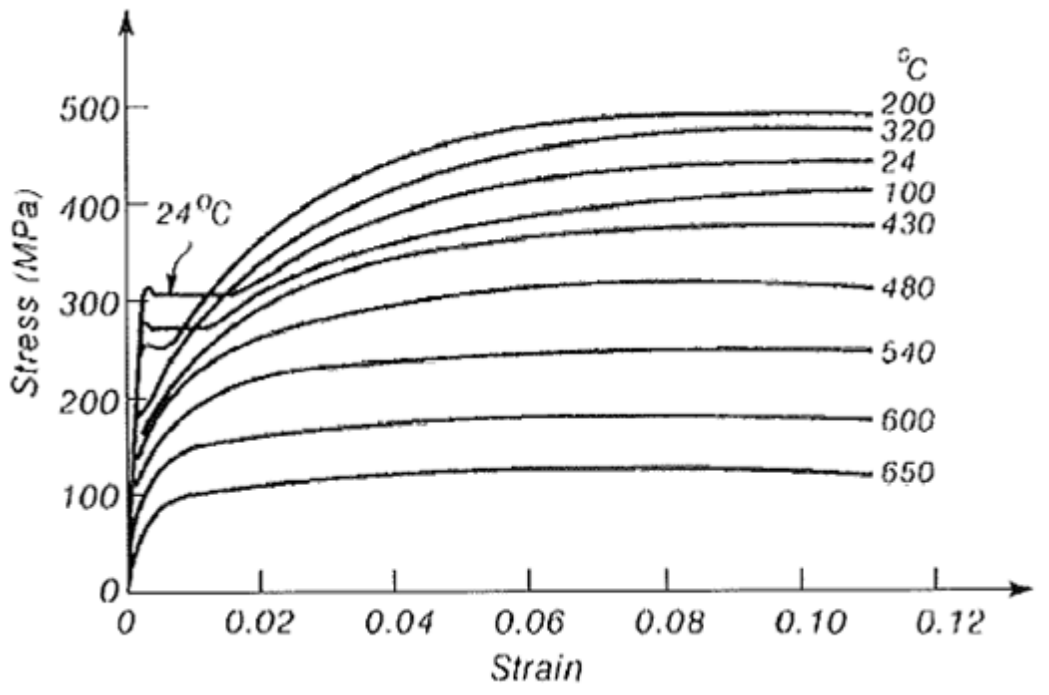


Figure 8: Stress-Strain Curves for Typical Hot-Rolled Steel at Elevated Temperature [3]

Table 2: Reduction Factors for Stress-Strain Relationship of Carbon Steel at Elevated Temperatures

Steel Temperature θ_λ	Reduction factors at temperature θ_λ relative to the value of f_y or E_λ at 20°C		
	Reduction factor (relative to f_y) for effective yield strength $k_{y\theta} = f_{y\theta}/f_y$	Reduction factor (relative to f_y) for proportional limit $k_{v\theta} = f_{v\theta}/f_y$	Reduction factor (relative to E_λ) for the slope of the linear elastic range $k_{e\theta} = E_{\lambda\theta}/E_\lambda$
20°C	1.000	1.000	1.000
100 °C	1.000	1.000	1.000
200 °C	1.000	0.807	0.900
300 °C	1.000	0.613	0.800
400 °C	1.000	0.420	0.700
500 °C	0.780	0.360	0.600
600 °C	0.470	0.180	0.310
700 °C	0.230	0.075	0.130
800 °C	0.110	0.050	0.090
900 °C	0.060	0.0375	0.0675
1000 °C	0.040	0.0250	0.0450
1100 °C	0.020	0.0125	0.0225
1200 °C	0.000	0.0000	0.0000

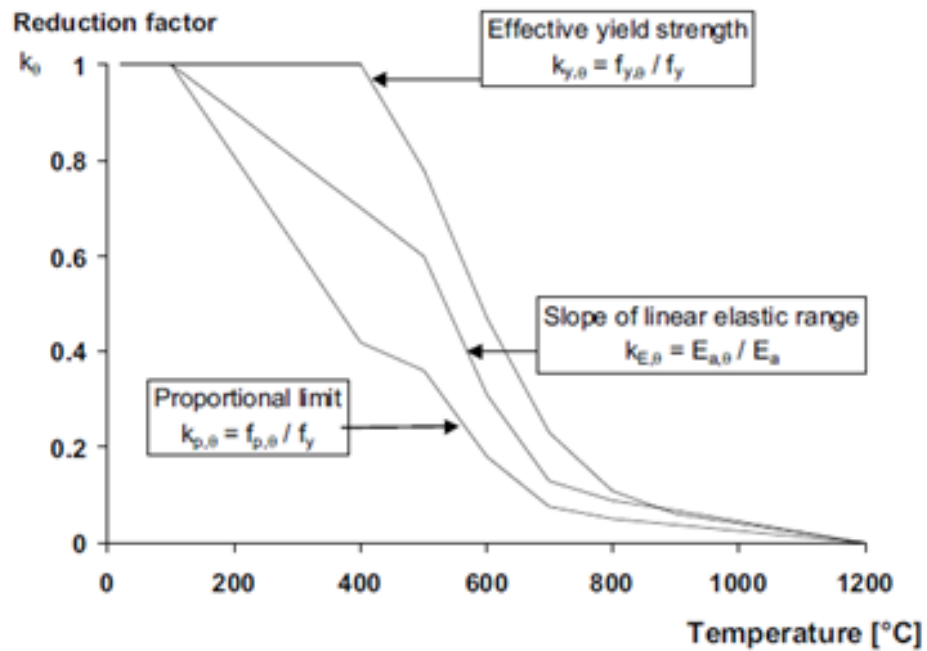


Figure 9: Reduction Factors for the Stress-Strain Relationship of Carbon Steel at Elevated Temperatures

Annex A [normative] Strain-hardening of carbon steel at elevated temperatures

(1) For temperatures below 400°C , the alternative strain-hardening option mentioned in 3.2 may be used as follows:

- for $0,02 < \varepsilon < 0,04$:

$$\sigma_a = 50(f_{u,0} - f_{y,0})\varepsilon + 2f_{y,0} - f_{u,0} \quad (\text{A.1a})$$

- for $0,04 \leq \varepsilon \leq 0,15$:

$$\sigma_a = f_{u,0} \quad (\text{A.1b})$$

- for $0,15 < \varepsilon < 0,20$:

$$[\text{AC2}] \sigma_a [\text{AC2}] = f_{u,0}[1 - 20(\varepsilon - 0,15)] \quad (\text{A.1c})$$

- for $\varepsilon \geq 0,20$:

$$\sigma_a = 0,00 \quad (\text{A.1d})$$

where:

$f_{u,0}$ is the ultimate strength at elevated temperature, allowing for strain-hardening.

NOTE: The alternative stress-strain relationship for steel, allowing for strain hardening, is illustrated in figure A.1.

(2) The ultimate strength at elevated temperature, allowing for strain hardening, should be determined as follows:

- for $\theta_a < 300^{\circ}\text{C}$:

$$f_{u,0} = 1,25f_{y,0} \quad (\text{A.2a})$$

- for $300^{\circ}\text{C} \leq \theta_a < 400^{\circ}\text{C}$:

$$[\text{AC2}] f_{u,0} = f_{y,0}(2 + 0,0025\theta_a) [\text{AC2}] \quad (\text{A.2b})$$

- for $\theta_a \geq 400^{\circ}\text{C}$:

$$f_{u,0} = f_{y,0} \quad (\text{A.2c})$$

NOTE: The variation of the alternative stress-strain relationship with temperature is illustrated in figure A.2.

Figure 10: Determination of Strain-Hardening of Carbon Steel at Elevated Temperatures
[4]

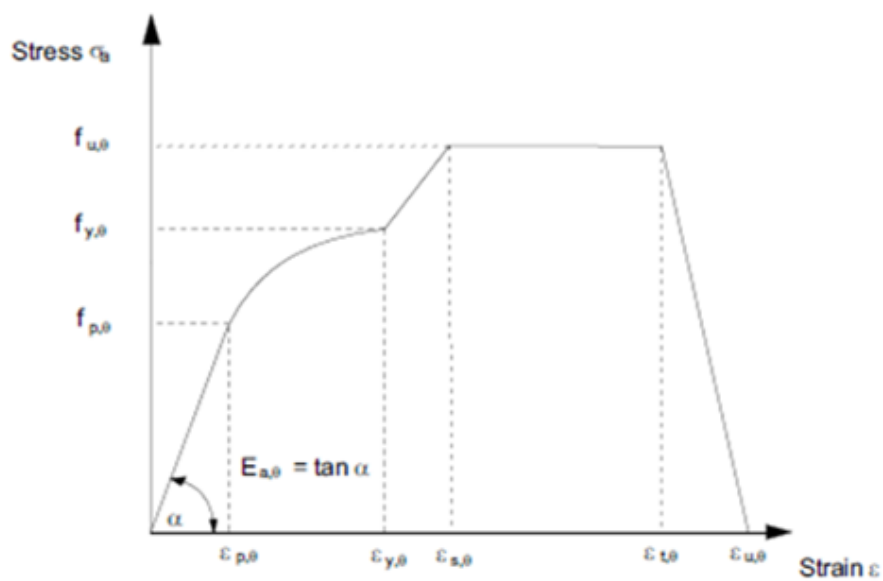


Figure A.1: Alternative stress-strain relationship for steel allowing for strain-hardening

Figure 11: A.1 Alternate Stress-Strain Relationship for steel allowing for strain hardening [4]

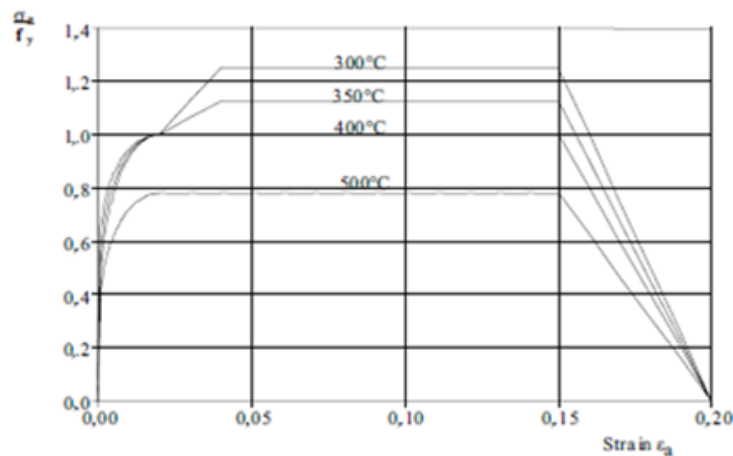


Figure 12. A.2 Alternate Stress-Strain Relationships for Steel at elevated temperatures, allowing for strain hardening [4]

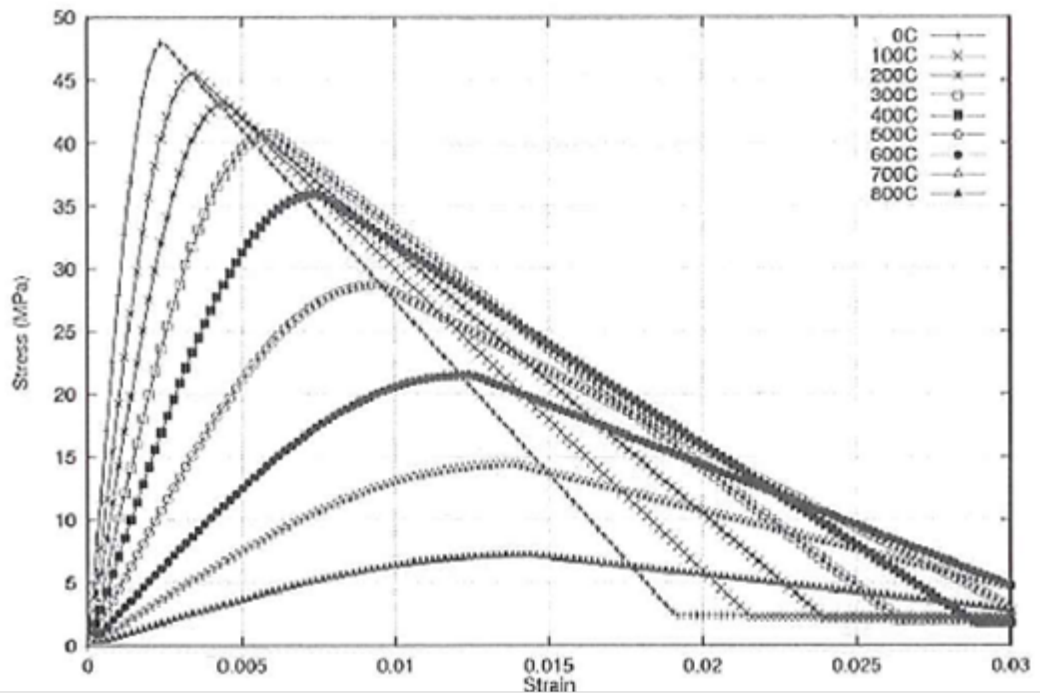


Figure 13: Idealization of Stress-Strain For Concrete at Elevated Temperatures per Eurocode [4]

Table 3: Values for the Main Parameters of the Stress-Strain Relationships of Normal Weight Concrete with Siliceous or Calcareous Aggregates Concrete at Elevated Temperatures

Concrete temp. θ [°C]	Siliceous aggregates			Calcareous aggregates		
	$f_{c,0} / f_{ck}$ [-]	$\varepsilon_{c1,0}$ [-]	$\varepsilon_{cu1,0}$ [-]	$f_{c,0} / f_{ck}$ [-]	$\varepsilon_{c1,0}$ [-]	$\varepsilon_{cu1,0}$ [-]
1	2	3	4	5	6	7
20	1,00	0,0025	0,0200	1,00	0,0025	0,0200
100	1,00	0,0040	0,0225	1,00	0,0040	0,0225
200	0,95	0,0055	0,0250	0,97	0,0055	0,0250
300	0,85	0,0070	0,0275	0,91	0,0070	0,0275
400	0,75	0,0100	0,0300	0,85	0,0100	0,0300
500	0,60	0,0150	0,0325	0,74	0,0150	0,0325
600	0,45	0,0250	0,0350	0,60	0,0250	0,0350
700	0,30	0,0250	0,0375	0,43	0,0250	0,0375
800	0,15	0,0250	0,0400	0,27	0,0250	0,0400
900	0,08	0,0250	0,0425	0,15	0,0250	0,0425
1000	0,04	0,0250	0,0450	0,06	0,0250	0,0450
1100	0,01	0,0250	0,0475	0,02	0,0250	0,0475
1200	0,00	-	-	0,00	-	-

1.2.6 Required Outputs/Results

The ISP-48 instructions can be used to guide the list of deliverables from the analysis related to temperature, but the basic list of Required Outputs/Results for the analysis are the same as for Model 3, as follows:

1. Description of failure prediction model or criteria selected.
2. Assumptions made in geometric modeling, and model description.
3. A subset of the response information defined by the “55 Standard Output Locations”, SOL, of the 1:4 Scale PCCV round-robin exercise; subset is to be determined later, but participants should plan models accordingly. At a minimum, the displacement transducer/data plots are required to consist of portions of the 55 SOLs.
4. Contour plot of peak strains in the liner during the LST at the pressure milestones: $P = 0$ (prestress applied); 1 Pd; 1.5 Pd; 2 Pd; 2.5 Pd; 3 Pd; 3.3 Pd; 3.4 Pd; Ultimate Pressure
5. A subset of the response information defined by the 55 SOLs of the 1:4 Scale PCCV round-robin exercise; see below for the specific list.

6. Liner strain map of entire liner surface was discussed at the April 13-14 Meeting, while an Excel format for this was under development. But participants were asked to plan for outputting this from their Model 4 Analysis. The “map” location format uses the azimuths and elevations of the model as shown in Figure 13. The fine spacing of the data points does not matter, because participants model mesh sizes vary; but participants were asked to plan for a minimum spacing for liner strain data of 450 mm, which corresponds to the liner-anchor spacing.

For direct comparison amongst participants, please also plot (Using Excel):

1. Liner strain magnitudes (hoop direction) at locations indicated in Figure 11 (of SPE problem statement), versus pressure
2. Tendon stress distribution at $P = 0$ (prestress applied); 1 Pd; 1.5 Pd; 2 Pd; 2.5 Pd; 3 Pd; 3.3 Pd; 3.4 Pd; Ultimate Pressure for
 - Hoop tendons # H35, H53, H68
 - Vertical tendon # V37 and V46
3. Plots of response versus pressure for Standard Output Locations:
 - 1-15 (displacements);
 - 22-29 (rebar strains);
 - 36-42 (liner strains);
 - 48-55 (tendon strains and stresses)

(See Table 4 for exact locations and definitions of SOL's)

Table 4: Standard Output Location Definitions

Loc. #	Type	Orientation	Az. (°)	El. (m)	Comments	General Location
1	Displacement	Vertical	135	0.00	Outside Cylinder	Top of Basemat
2	"	Radial	135	0.25	Inside Liner Surface	Base of Cylinder
3	"	Radial	135	1.43	"	"
4	"	Radial	135	2.63	"	"
5	"	Radial	135	4.68	"	E/H elev.
6	"	Radial	135	6.20	"	Approximate Midheight
7	"	Radial	135	10.75	"	Springline
8	"	Vertical	135	10.75	"	"
9	"	Horiz.(Rad)	135	14.55	"	Dome 45 deg
10	"	Vertical	135	14.55	"	"
11	"	Vertical	135	16.13	"	Dome apex
12	"	Radial	90	6.20	"	Midheight @ Buttress
13	"	Radial	90	10.75	"	Springline @ Buttress
14	"	Radial	324	4.675	"	Center of E/H
15	"	Radial	62	4.525	"	Center of A/L
16	Rebar Strain	Meridional	135	0.05	Inner Rebar Layer	Base of Cylinder
17	"	Meridional	135	0.05	Outer Rebar Layer	"
18	"	Meridional	135	0.25	Inner Rebar Layer	"
19	"	Meridional	135	0.25	Outer Rebar Layer	"
20	"	Meridional	135	1.43	Inner Rebar Layer	"
21	"	Meridional	135	1.43	Outer Rebar Layer	"
22	"	Hoop	135	6.20	Outer Rebar Layer	Midheight
23	"	Meridional	135	6.20	Outer Rebar Layer	"
24	"	Hoop	135	10.75	Outer Rebar Layer	Springline
25	"	Meridional	135	10.75	Inner Rebar Layer	"
26	"	Meridional	135	10.75	Outer Rebar Layer	"
27	"	Hoop	135	14.55	Outer Rebar Layer	Dome 45 deg
28	"	Meridional	135	14.55	Inner Rebar Layer	"
29	"	Meridional	135	14.55	Outer Rebar Layer	"
30	"	Meridional	90	0.05	Inner Rebar Layer	Base of Cylinder @ Buttress
31	"	Meridional	90	0.05	Outer Rebar Layer	"
32	"	Hoop	90	6.20	Outer Rebar Layer	Midheight @ Buttress
33	"	Meridional	90	6.20	Outer Rebar Layer	"
34	Liner Strain	Meridional	0	0.010	Inside Liner Surface	Base of Cylinder
35	"	Meridional	0	0.010	Outside Liner Surface	"
36	"	Meridional	135	0.25	Inside Liner Surface	"
37	"	Hoop	135	0.25	"	"
38	"	Meridional	135	6.20	"	Midheight
39	"	Hoop	135	6.20	"	"
40	"	Meridional	135	10.75	"	Springline
41	"	Hoop	135	10.75	"	"
42	"	Meridional	135	16.13	"	Dome apex
43	"	Meridional	90	6.20	"	Midheight @ Buttress
44	"	Hoop	90	6.20	"	"
45	"	Hoop	332	4.675	"	10 mm from thickened plate
46	"	Hoop	59	4.525	"	10 mm from thickened plate
47	Base Liner	Radial	135	0.00	100 mm Inside Cyl.	FF Basemat Liner Strain
48	Tendon Str.	Hairpin	180	15.60	Tendon - V37	Tendon Apex
49	"	Hairpin	135	10.75	Tendon - V46	Tendon Springline
50	"	Hoop	90	6.58	Tendon - H53	Mid Tendon
51	"	Hoop	180	6.58	Tendon - H53	1/4 - Tendon
52	"	Hoop	225	6.58	Tendon - H53	1/8 - Tendon
53	"	Hoop	0	4.57	Tendon - H35	Tendon btwn E/H and A/L
54	Tendon Force	Hairpin	241	-1.16	Tendon - V37	Tendon Gallery
55	"	Hoop	275	6.58	Tendon - H53	@ Buttress

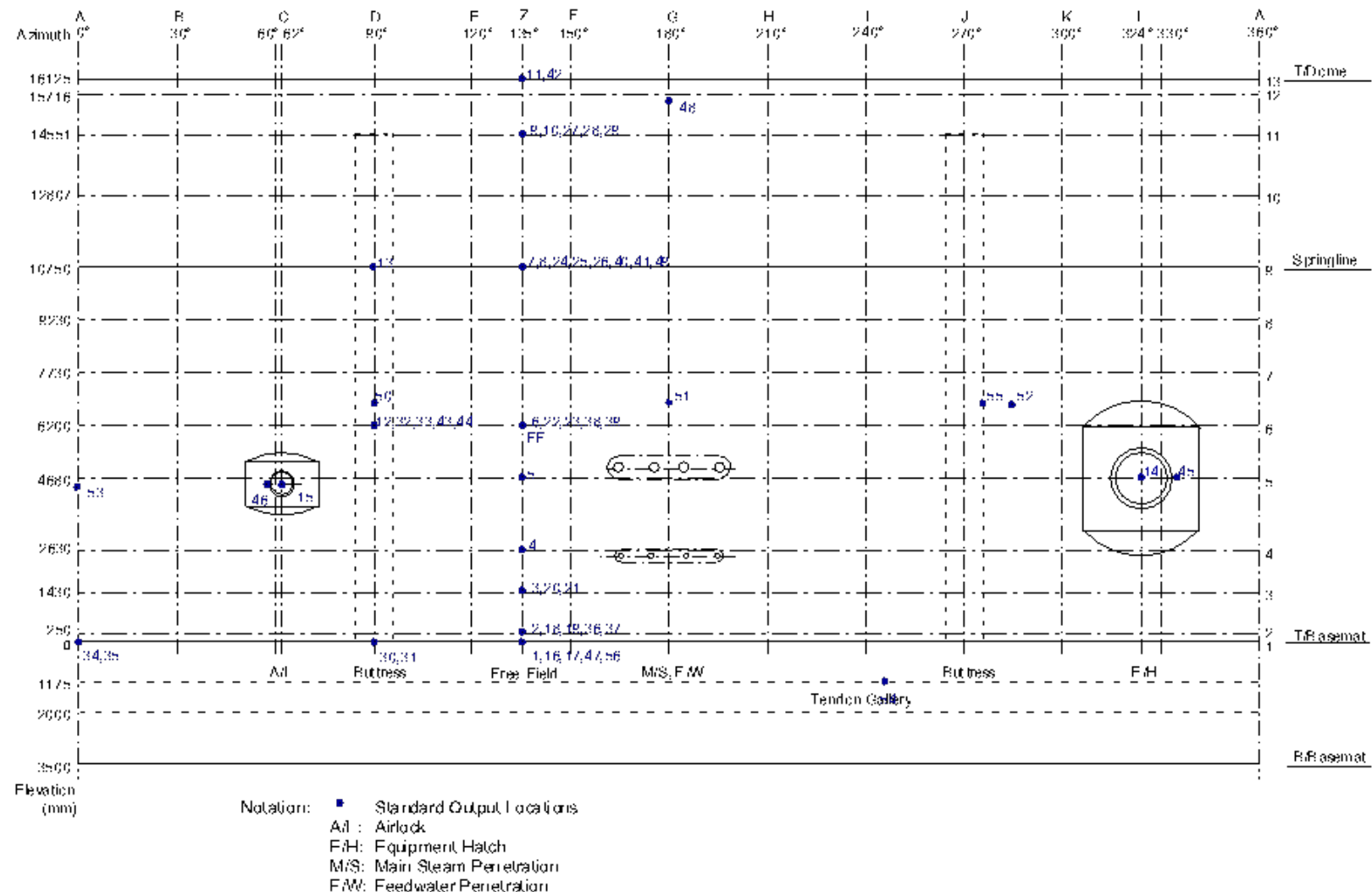


Figure 14: Liner View Showing SOL Strain Reports – Also Shown for Reference in Planning Global Liner Strain Map

1.2.7 Estimating Crack Size and Leak Areas

Model 4 and adjunct submodels should also be planned to estimate crack size and leak area, as this is one of the primary goals of the Phase 2 work. In conjunction with this, India will continue investigating into leak rates as a function of crack size; this will be provided during the execution of Phase 2. A plot of leak-rates at different stages of testing the 1:4 Scale PCCV is provided for reference in Figure 15 through Figure 17. Leak rate estimates from point to point and total time methods are shown. The Point to Point approach estimates leak rate between measurements (spaced at approximately 1 hour for the PCCV Test), while the Total Time method always refers back to the initial condition to estimate leak rate. As such the Total Time method produces a smoothed estimate, while the Point to Point approach captures the peak values. See [5] for more information.

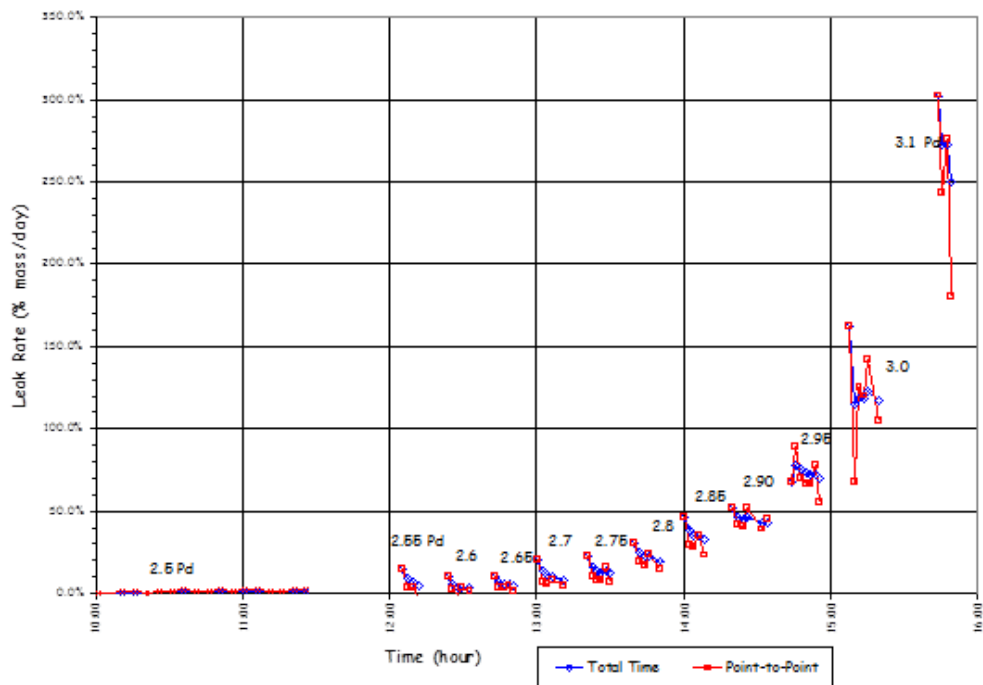


Figure 15: LST Calculated Leak Rates at 1.5, 2.0, and 2.5 P_d

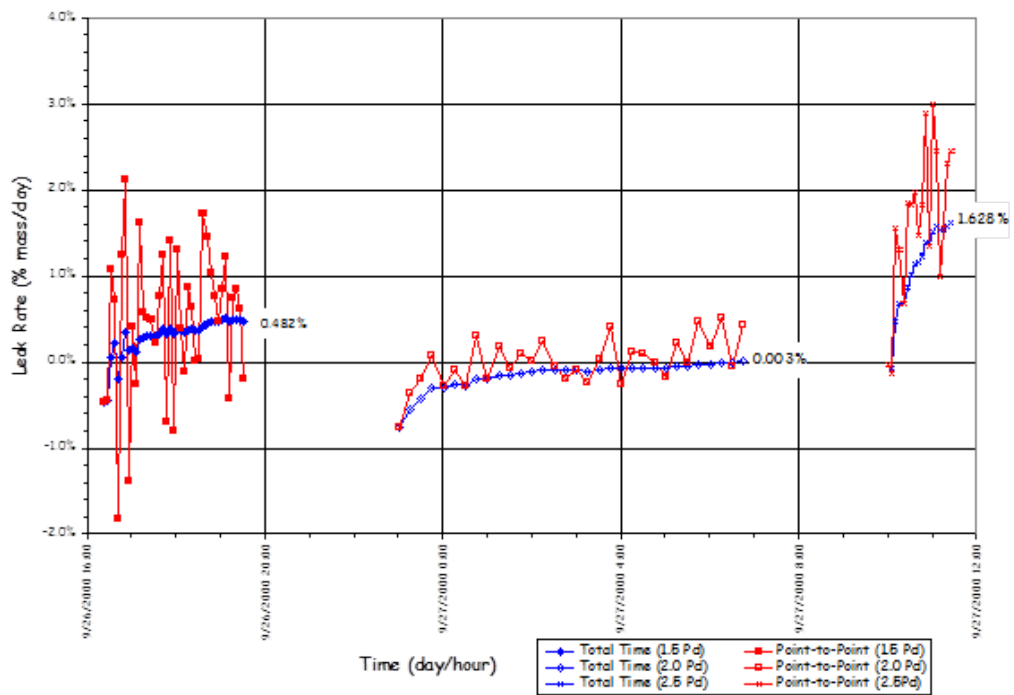


Figure 16: LST – Estimated Leak Rates (2.5-3.1 P_d)

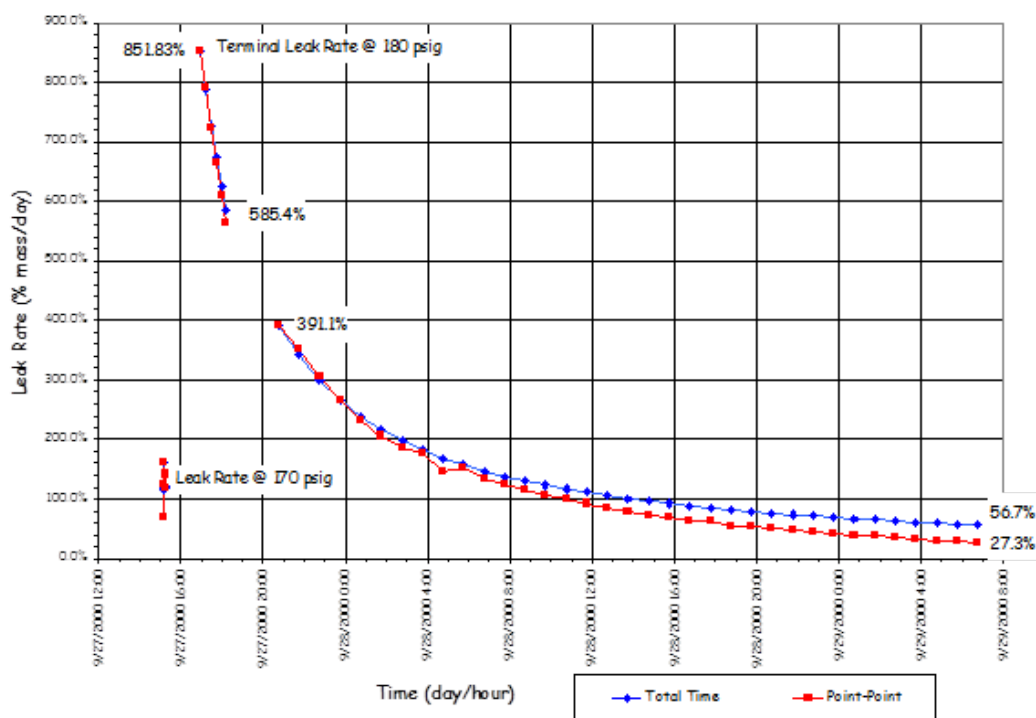


Figure 17. Estimated Leak Rates Following Cessation of Test Pressurization

Since the April 13-14 Meeting, renewed study has been made of the 1:4 Scale Model liner tears, and liner metallurgical properties. The liner and the regions at or near all 26 observed tears were studied in [5]. Some SPE-3 participants may wish to expand on previously used liner failure criterion in their Phase 2 analyses and conclusions about failure and leakage, as for example, a few participants did in Phase 1, considering a fracture mechanics approach. For Phase 1, a fracture J-critical of 350 psi-inch was assumed, without benefit of specific data, but as a “typical” value for mild carbon structural steel. Unfortunately, based on further examination, there are no true measured toughness data values for the 1:4 Scale Model liner. From Ref. [5], Vickers Hardness data (using 100 gram load), helped supply the following ranges:

- Base metal: 160 kgf/mm^2
- Heat Affected Zones (depending on grain size): $151 \text{ to } 164 \text{ kgf/mm}^2$
- Fusion Zone: $173\text{-}180 \text{ kgf/mm}^2$

Based on a brief literature review, hardness testing does provide approximate indication of ultimate-tensile-strength (it is roughly the Vickers hardness divided by 3), and very approximate indication of fracture toughness (K_{Ic} or J_{cr}). In the absence of conducting specific fracture-toughness testing, we recommend using the following based on the aforementioned rule of thumb and engineering judgement.

- Median $J_{cr} = 500 \text{ psi-inch}$
- Median + 1 std deviation $J_{cr} = 800 \text{ psi-inch}$
- Median - 1 std deviation $J_{cr} = 200 \text{ psi-inch}$

Fracture toughness data is often presented as a statistical distribution, so even if these hypothetical values are used for final predictions (in the absence of further data), we believe that framing a tearing criteria in this way can serve to advance the technology of our predictions toward a probabilistic leakage prediction basis. Indeed, the second task of Phase 2 will be to transition the results of Model 4 into probabilistic space. The participants were requested to provide leak rate versus pressure curves for a suite of temperatures. An example of the desired output is shown in Figure 18. The pressure range should vary from 0 to 4 times the design pressure.

One approach to both aspects of this (the estimation of crack size, and the estimation of probabilistic distribution on leakage and crack size versus pressure) is the methodology developed through EPRI research in the 1990's. References for more information on this are [6 and 7]. Ref. [6] provides a general description of the methodology, and is publicly available; Ref. [7] provides more detail, but is only available on a limited basis. Another approach that gained momentum (as presented and discussed by participants in our April 13-14, 2011 meeting) was a modified version of the EPRI approach where uncertainty distributions are still placed on a number of variables, but the fracture occurrence and tear areas could be based on a fracture mechanics approach.

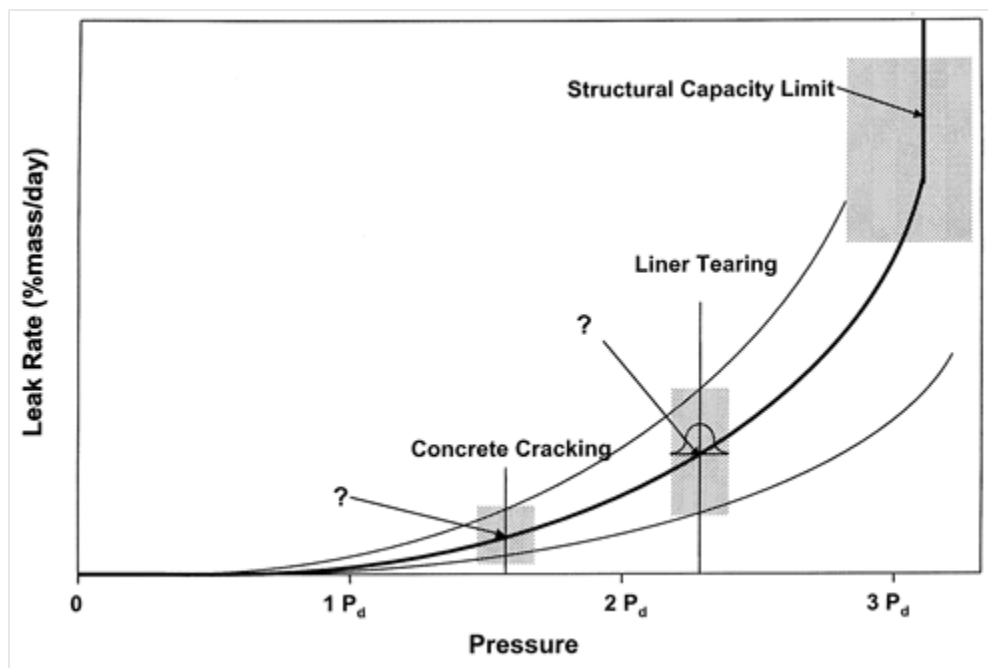


Figure 18: Schematic of a Containment Performance Model

1.3 Documents of SPE #3 Phase Two

In conjunction with completing the aforementioned analyses, participants were asked to document, in the form of a report, results from Phase 2 of the Round Robin Analyses. The reports provided the input for this NUREG, and can be found in the appendices.

1.4 Organizational Schedule

The schedule for the meetings and calculations for the overall SPE program was as follows (as now modified and agreed to at the April, 2011 meeting):

Event	Dates
Initial Workshop (Mumbai, India)	June 30-July 2, 2010
White Paper Finalization	August 6, 2010
Milestone Verification of Tendon and Equipment Hatch	December 1, 2010
Return Results from Milestone Evaluation	December 21, 2010
Phase One Calculations and Documentation Due	March 15, 2011
Phase One Review Meeting (Washington, D.C.)	April 13-15, 2011
Phase Two Calculations and Documentation Due	April 27, 2012
Final Workshop (Washington, D.C.)	March 27-29, 2012

2 MODEL 4

Model 4 uses the same geometry as Model 3, but allows for the use of temperature and pressure loads. Model 4 is a global analysis model aimed at incorporating lessons learned from Model exercises 1, 2, and 3, and at providing PCCV response information at any and all locations of the structure. The participants were asked to provide the following output for direct comparison:

1. Description of failure prediction model or criteria selected
2. Assumptions made in geometric modeling, and model description
3. A subset of the response information defined by the “55 standard output locations” of the 1:4 Scale PCCV round-robin exercise
4. Contour plot of peak strains in the liner during the LST at the pressure milestones: $P = 0$ (prestress applied); $1 \times P_d$; $1.5 P_d$; $2 P_d$; $2.5 P_d$; $3 P_d$; $3.3 P_d$; $3.4 P_d$; Ultimate Pressure
5. A subset of the response information defined by the “55 standard output locations” of the 1:4 Scale PCCV round-robin exercise; see below for the specific list.
6. Liner strain map of entire liner surface

For direct comparison amongst participants, please also plot (Using Excel):

7. Liner strain magnitudes (hoop direction) at locations indicated in Figure 11 (of SPE problem statement), versus pressure
8. Tendon stress distribution at $P = 0$ (prestress applied); $1 \times P_d$; $1.5 P_d$; $2 P_d$; $2.5 P_d$; $3 P_d$; $3.3 P_d$; $3.4 P_d$; Ultimate Pressure for
 - a. Hoop tendons # H35, H53, H68
 - b. Vertical tendon # V37 and V46
9. Plots of response versus pressure for Standard Output Locations:
 - a. 1-15 (displacements);
 - b. 22-29 (rebar strains);
 - c. 36-42 (liner strains);
 - d. 48-55 (tendon strains and stresses)

(see Table 4 for exact locations and definitions of SOLs)

2.1 Description of Material and FEM Models

A comparison of the different modeling software and modeling set-up is listed below in Table 5. Each participant was free to use any FEM software they so chose, and to represent the geometry for Model 3 as needed.

Table 5: Model Detail Comparison

MODELING DETAILS	AERB	NRC
FEM Tool	Abaqus	Abaqus Standard FE
Concrete Element Type	Hex Elements (C3D8R)	Hex Elements (C3D8R)
Rebar Element Type	Rebar Layer	Rebar Layer (SFM3D4R)
Liner Element Type	Linear 4-node Shell Element with Uniaxial Behavior	Shell Elements (S4R)
Tendon Element Type	Linear 2-Node Truss Element	Beam Elements (B31)
Tendon / Concrete Interaction	Embedded	Tendons inside tendon ducts (Friction modeled, $\mu=0.21$)
Concrete / Rebar Interaction	Embedded	Embedded

A comparison of key boundary conditions is provided in Table 6.

Table 6: Boundary Conditions of Note

	AERB	NRC
Basemat	Assumed Fixed at Top of Base Mat (Basemat not Modeled)	Basemat Modeled

A comparison of the material models is provided in Table 7. In general, there is good agreement between the material parameters chosen by the participants.

Table 7: Comparison of Material Models

MATERIAL	AERB	NRC
Concrete Model	Damage Plasticity Concrete	Concrete Damage Plasticity
Concrete Parameters of Note	$E = 26,900 \text{ MPa}$ $\nu = 0.21$ $\sigma_t = 2.4 \text{ MPa}$ $\rho = 2,176 \text{ kg/m}^3$	$E = 33,000 \text{ MPa}$ $\nu = 0.2$
Rebar	Non-Linear Elasto-Plastic	Elasto-Plastic
Rebar Parameters of Note	$E = 185,000 \text{ MPa}$ $\nu = 0.3$ $\sigma_t = 445-460 \text{ MPa}$ $\rho = 7,850 \text{ kg/m}^3$ $E_p = 1,250-1,350 \text{ MPa}$	$E = 200,000 \text{ MPa}$ $\nu = 0.3$ $\sigma_t = 498 \text{ MPa}$
Liner	Metal Plasticity	Elasto-Plastic
Liner Parameters of Note	$E = 210,000 \text{ MPa}$ $\nu = 0.3$ $\sigma_t = 400 \text{ MPa}$ $\rho = 7,850 \text{ kg/m}^3$ $E_p = 700 \text{ MPa}$	$E = 200,000 \text{ MPa}$ $\nu = 0.3$ $\sigma_t = 498 \text{ MPa}$
Tendon	Non-Linear Elasto-Plastic	Elasto-Plastic
Tendon Parameters of Note	$E = 191,000 \text{ MPa}$ $\nu = 0.3$ $\sigma_t = 1,750 \text{ MPa}$ $\rho = 7,850 \text{ kg/m}^3$ $E_p = 3,350 \text{ MPa}$ $f_{gu} = 1,857 \text{ MPa}$ $\mu = 0.21$ $\Delta s = 3.95 \text{ mm}$ $T_0 = 444 \text{ kN}$	$E = 195,000 \text{ MPa}$ $\nu = 0.3$ $\sigma_t = 1875 \text{ MPa}$

2.2 Description of Model Failure Criteria

The critical parameter for predicting tendon failure is the axial strain in the tendon of interest. The participants in the present study were requested to provide the tendon failure criteria used when predicting the failure of the tendons in Model 3 from their simulations. The participants all selected tendon failure criteria in reasonable agreement with one another. Three participants (Fortum, NRC, and SCANSOT) specified the actual ultimate tensile strain to predict failure, while one participant (EDF) specified the ultimate tensile stress as well as the assumed yield stress and the elastic and hardening moduli. The tendon failure strain was calculated from these

parameters. The ultimate strain for the prestressing tendons in Model 1 used by all the participants are presented below in Table 8.

Table 8: Tendon failure criteria

	AERB	NRC
Tendon Failure Criteria (ultimate strain)	3.96%	3.8%

The model failure parameter of interest in Model 2 was liner tearing and this parameter is still of interest in Model 3. This failure criteria is not as straightforward as the dominant failure mechanism in Model 1, tendon rupture. Because the liner experiences a bi-axial state of stress, determining the particular onset of tearing is somewhat complicated. The methods used by the participants for Model 3 are identified in Table 9.

Table 9: Liner failure criteria

	AERB	NRC
Tendon Failure Criteria (ultimate strain)	Biaxial Stress based (Davis Triaxiality Factor)	Biaxial Stress based (Davis Triaxiality Factor)

3 CASE 1: SATURATED STEAM RESULTS

3.1 Deformed Shape

Several participants provided deformed shape plots for Model 3 at the usual pressure milestones. These deformed shape plots can be found in Figure 19 through Figure 24. Similar to the deformed shape plots from Model 1, the different scaling factors used by the various participants limit the initial comparability of the figures. Nonetheless, the general shape of the deformed models does indicate some difference between the participants.

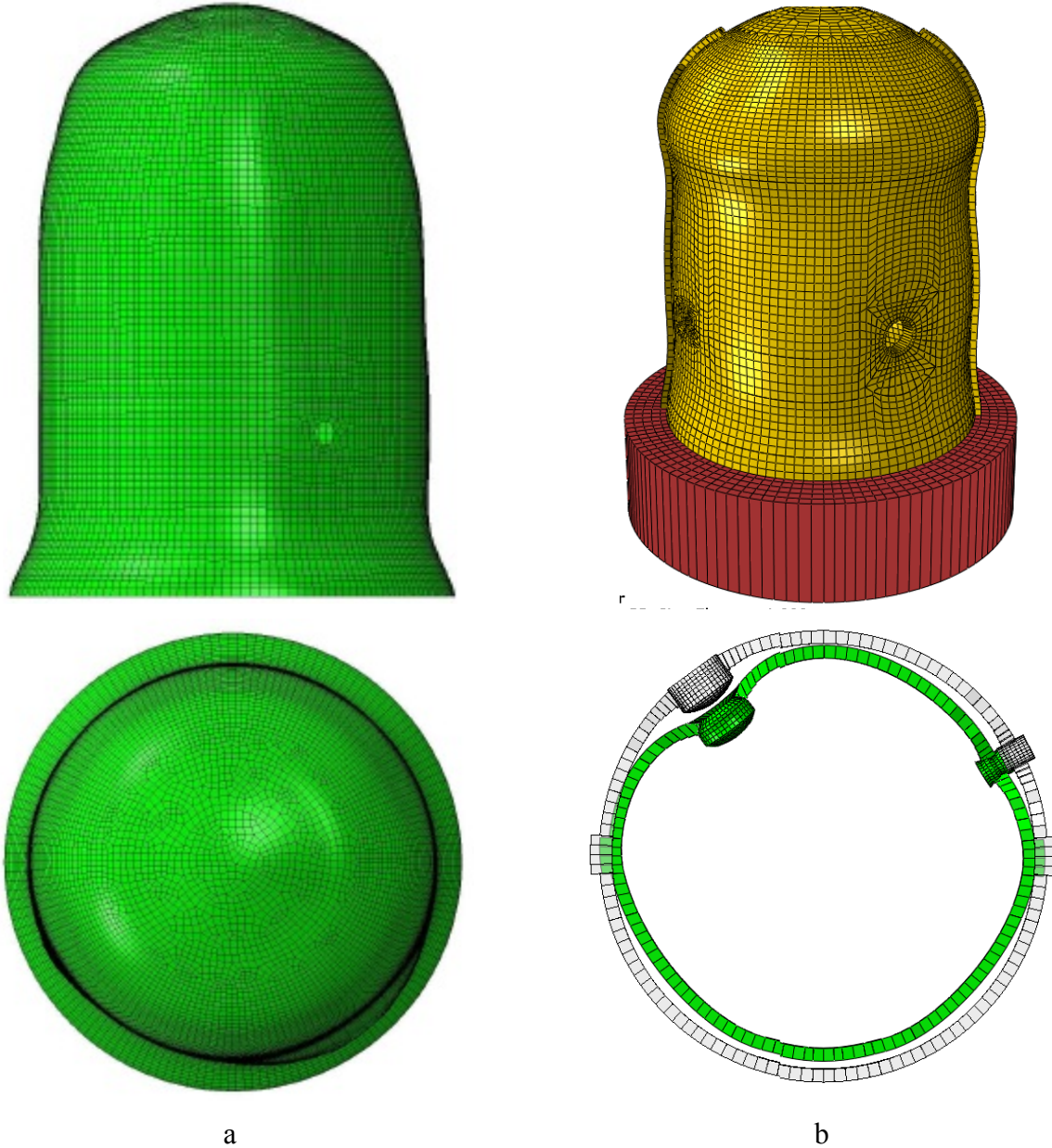


Figure 19: Deformed Shape after Tendon Anchorage (a) AERB (b) NRC (x500)

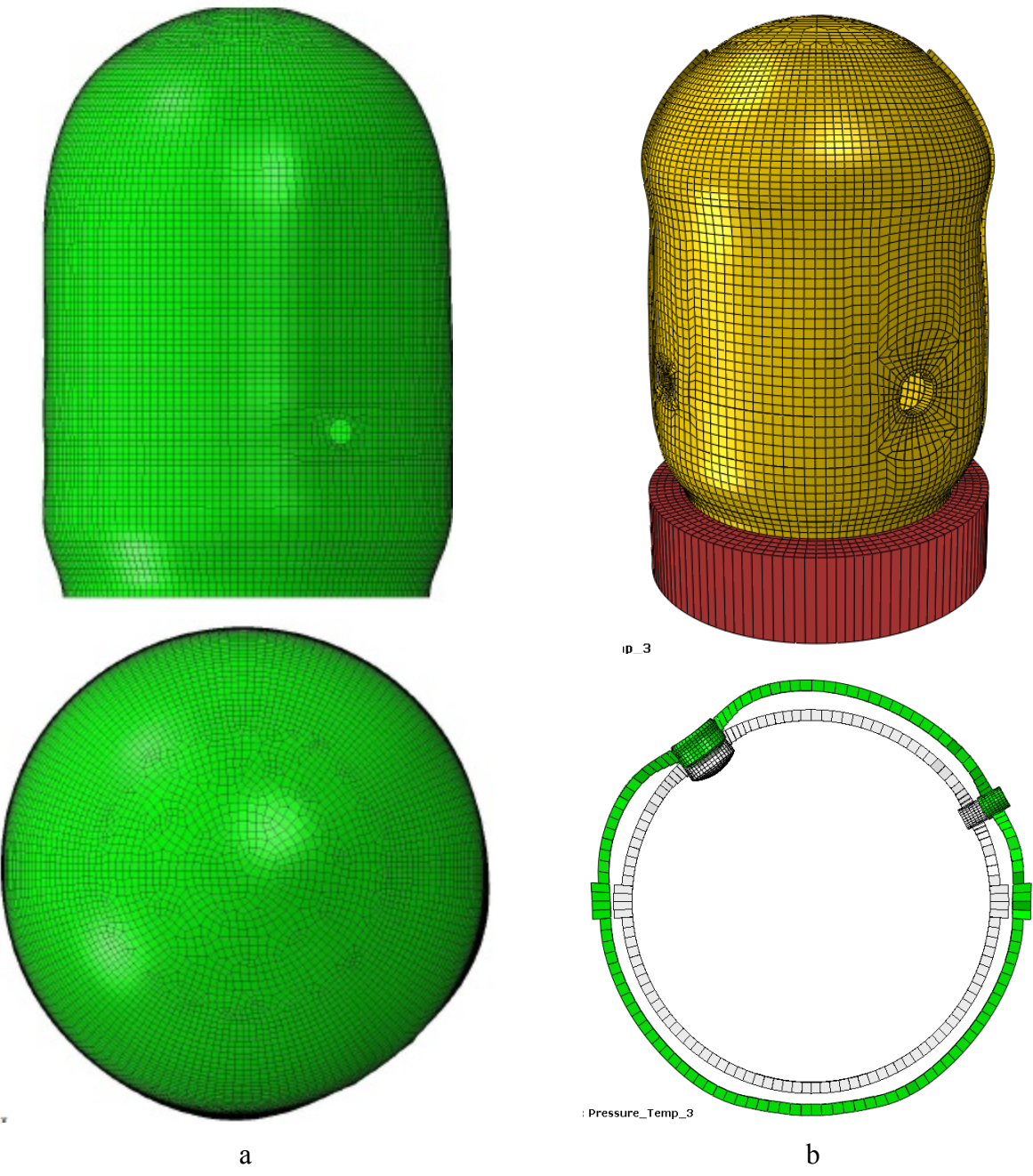


Figure 20: Deformed Shape at $1.0 \times P_d$ (a) AERB (b) NRC (x100)

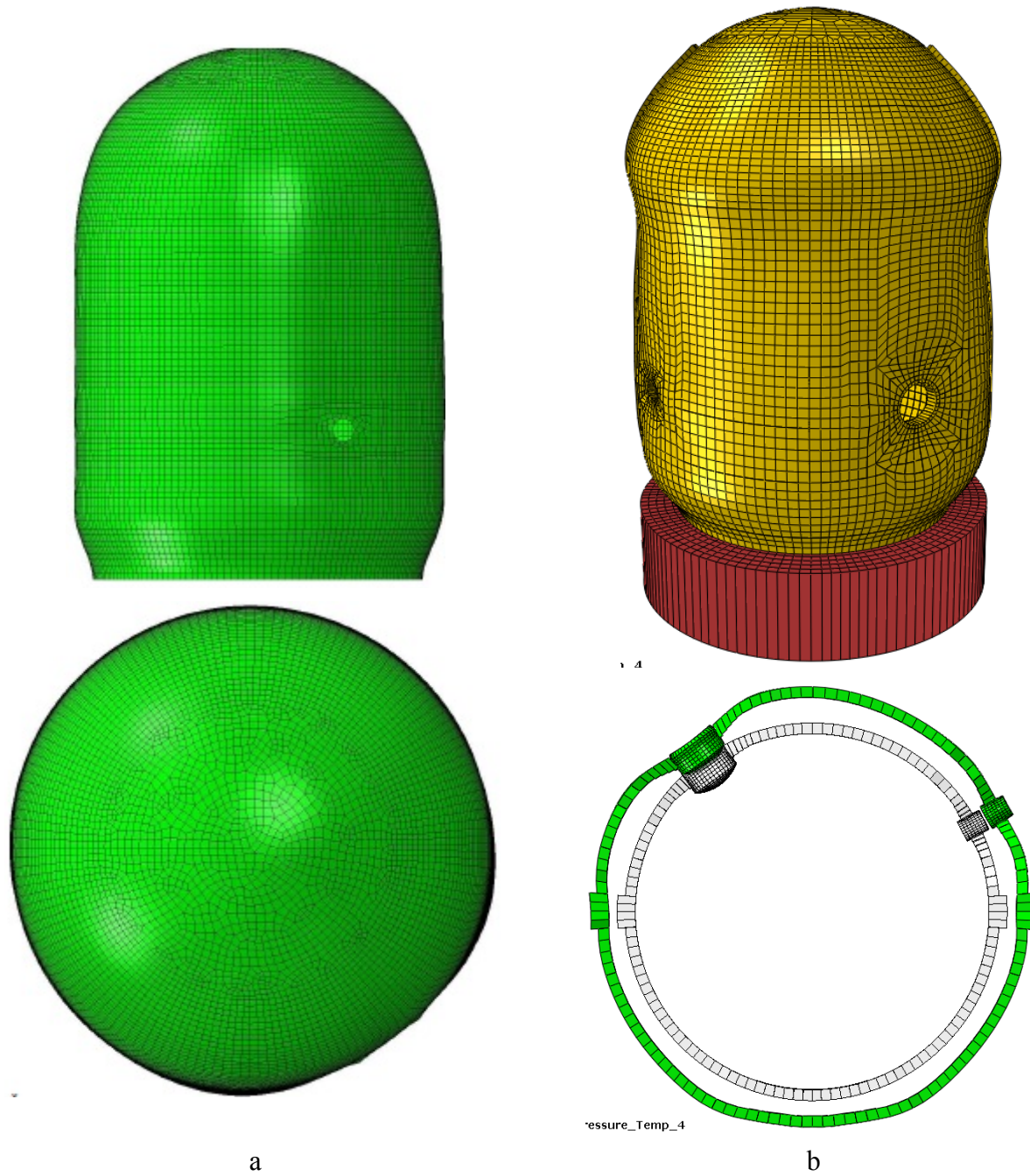
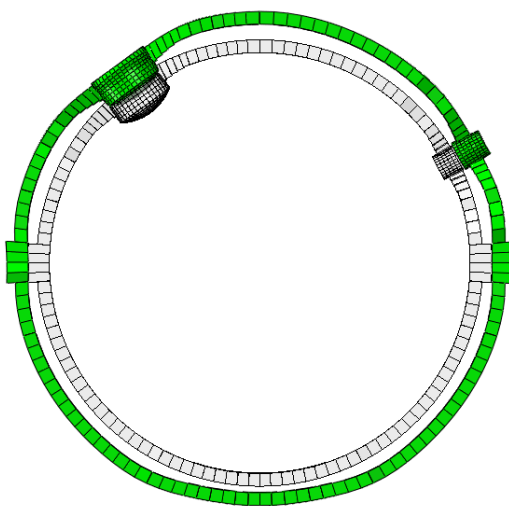
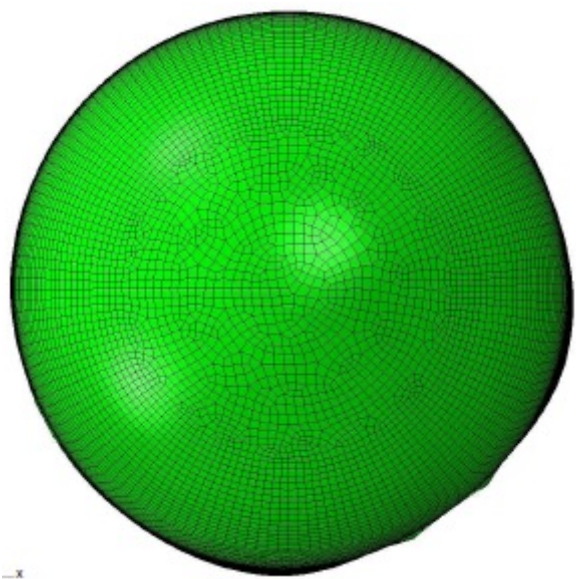
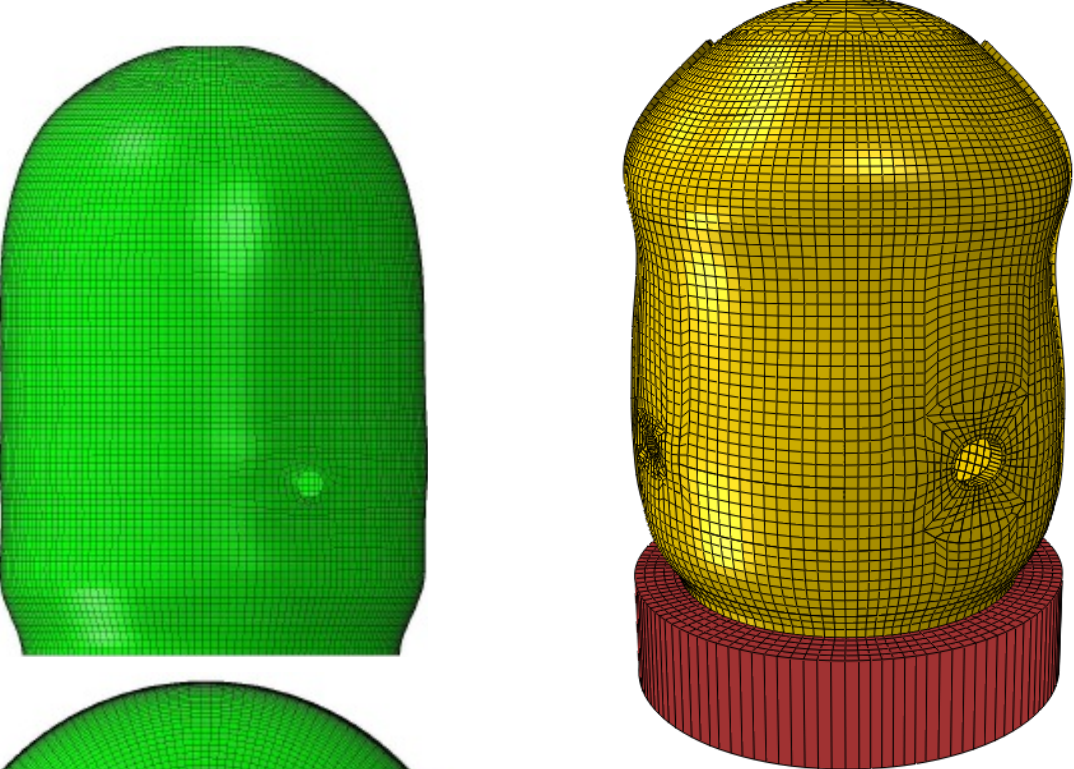


Figure 21: Deformed Shape at $1.5 \times P_d$ (a) AERB (b) NRC (x100)



a

b

Figure 22: Deformed Shape at $2.0 \times P_d$ (a) AERB (b) NRC (x50)

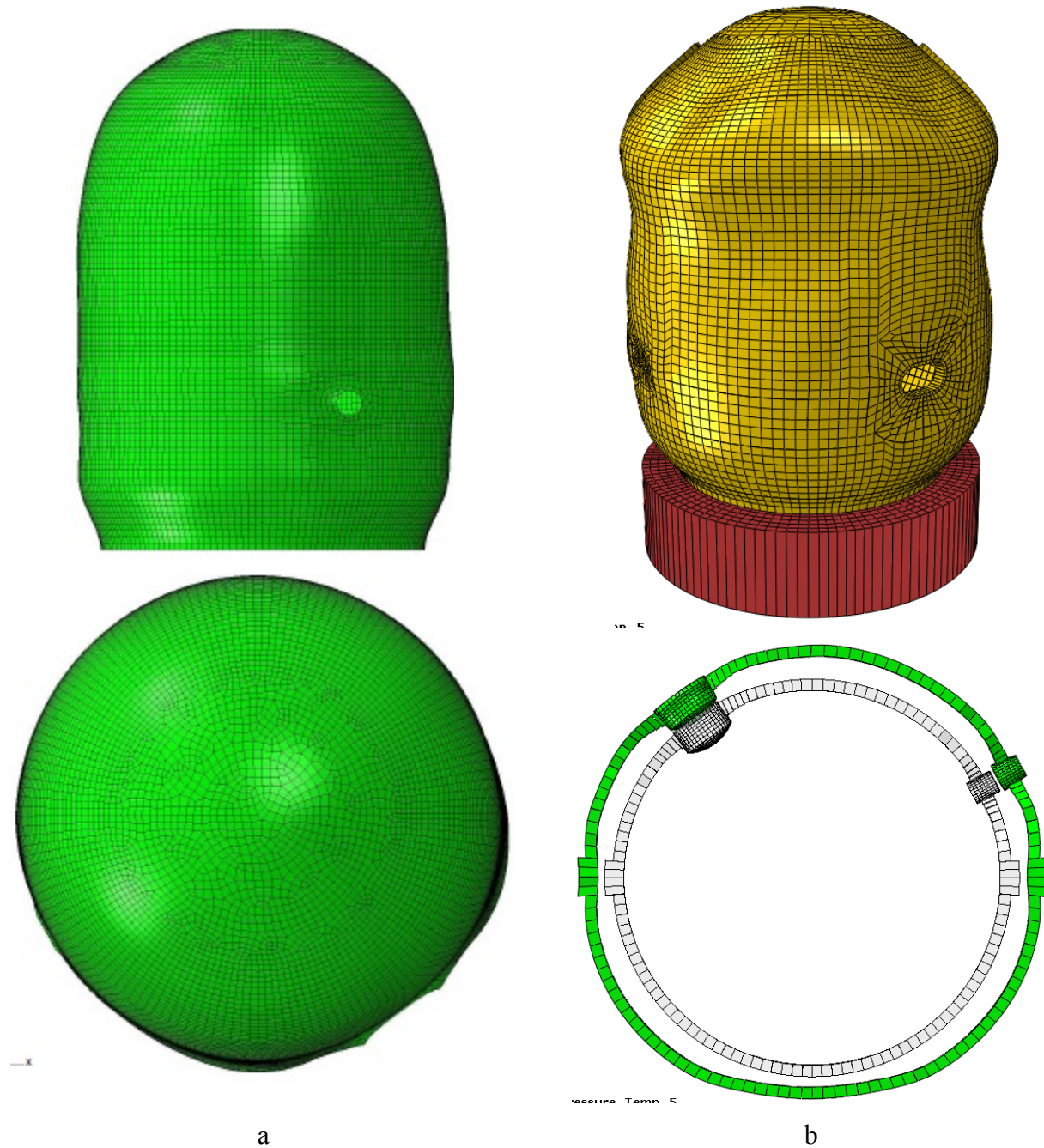


Figure 23: Deformed Shape at $2.5 \times P_d$ for (a) AERB (b) NRC (x50)

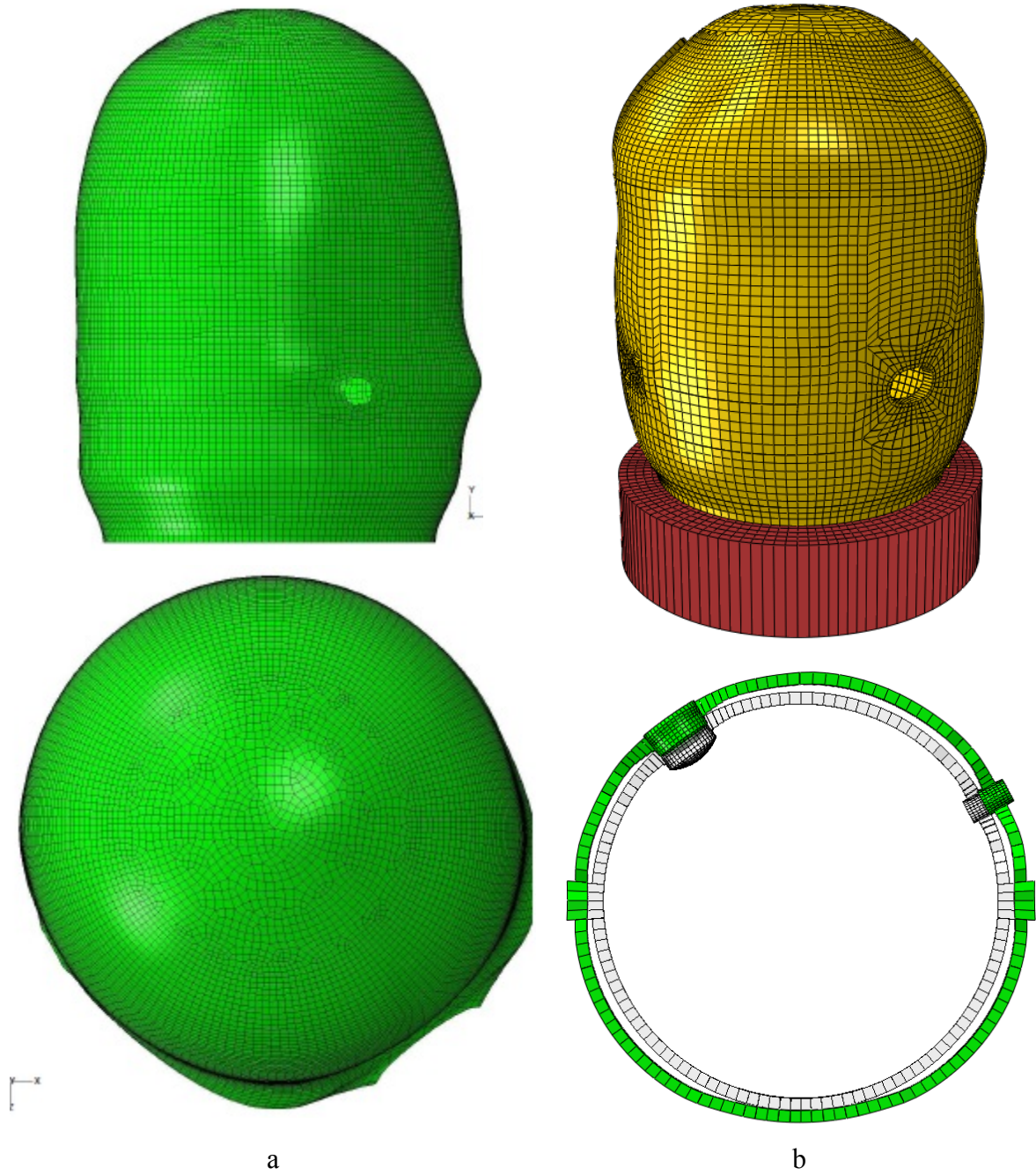


Figure 24: Deformed Shape at $3.0 \times P_d$ (a) AERB (b) NRC (x20)

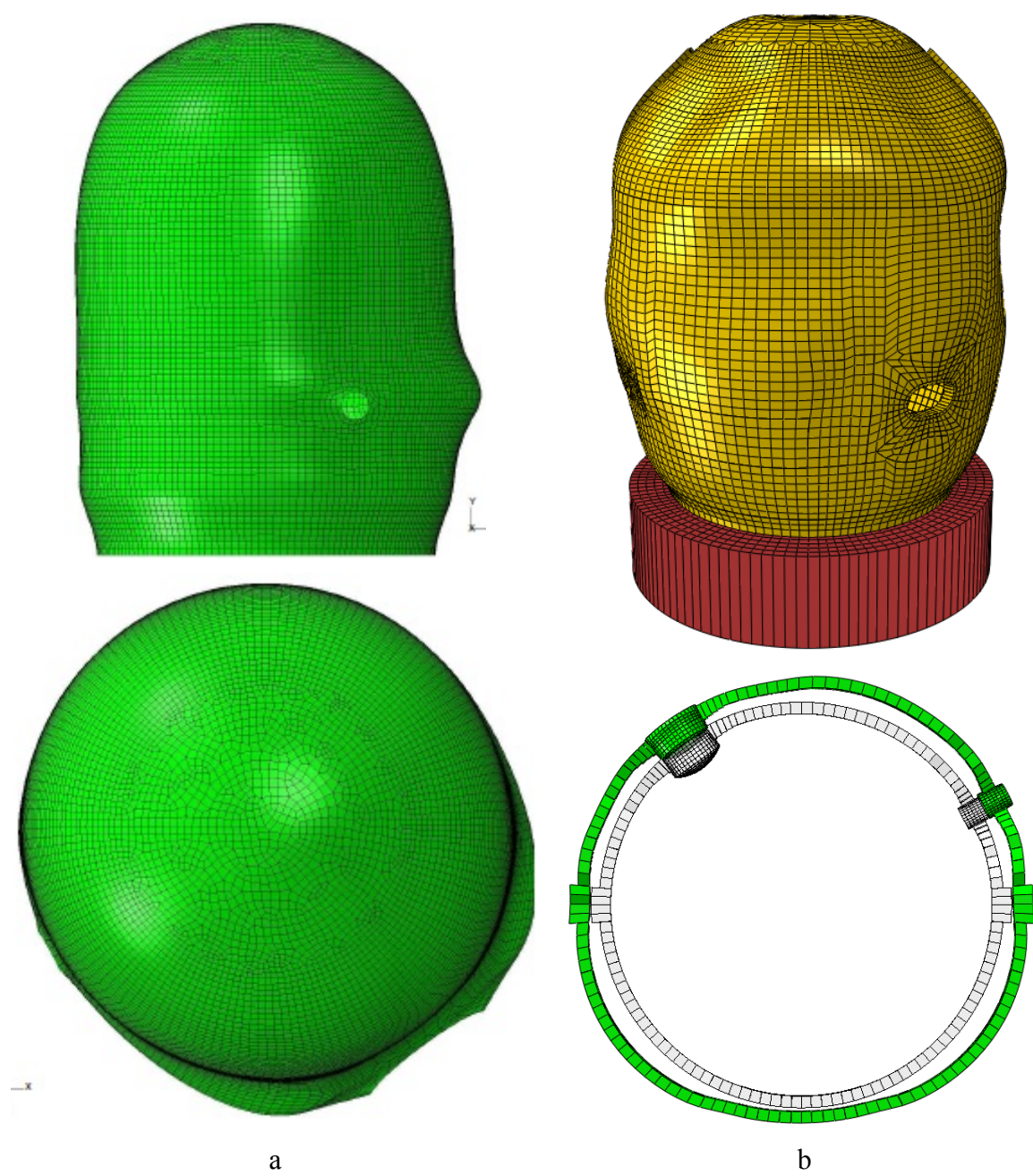


Figure 25: Deformed Shape at (a) $3.25 \times P_d$ AERB (b) $3.3 \times P_d$ NRC (x20)

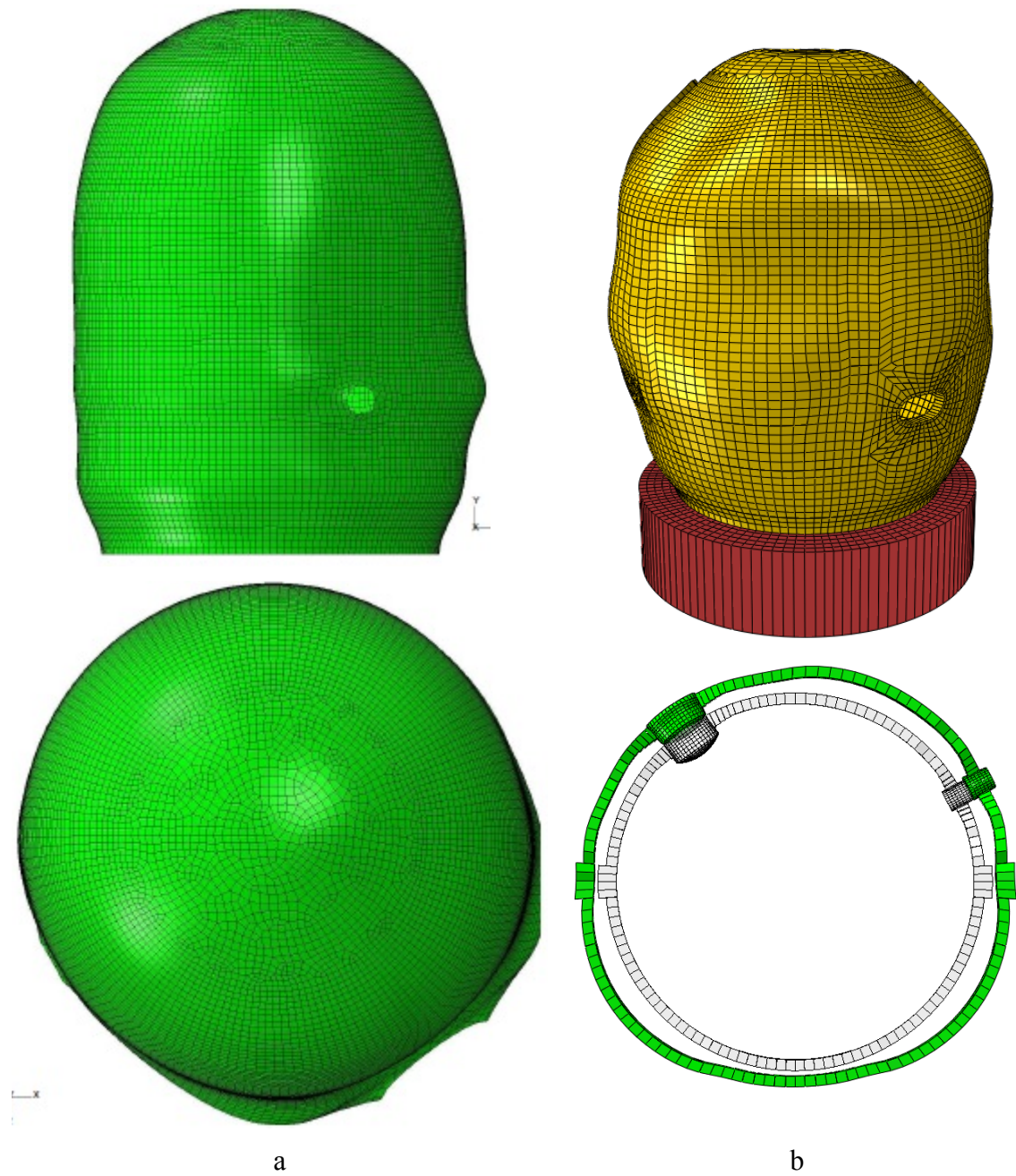


Figure 26: Deformed Shape at $3.4 \times P_d$ (a) AERB (b) NRC (x20)

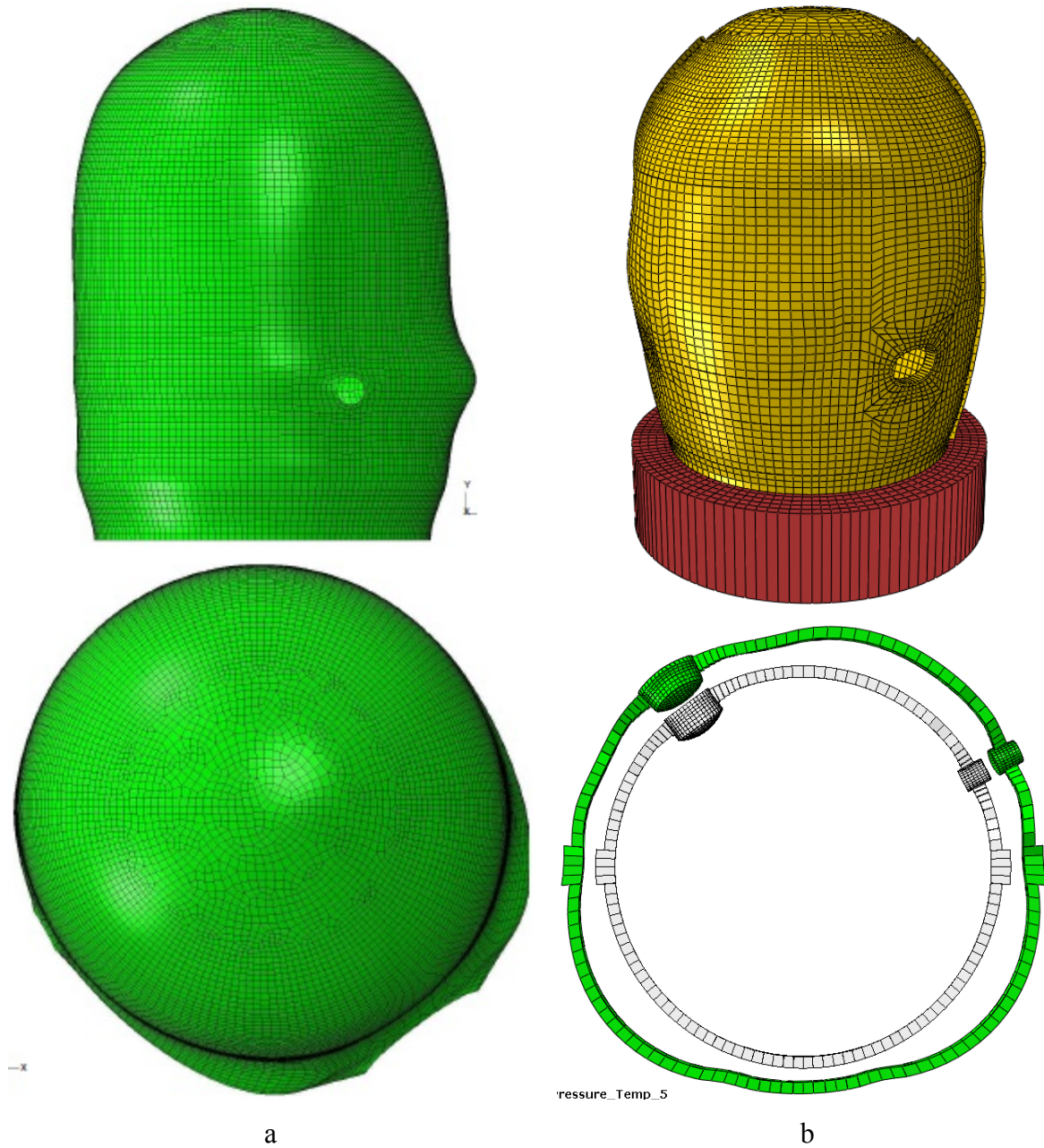


Figure 27: Deformed Shape at Ultimate Pressure (a) AERB - $3.46 \times P_d$ (b) NRC $3.6 \times P_d$, Deformation Scale x 20

3.2 Liner Strains

3.2.1 Peak Strains of Entire Liner

Contour plots of peak strains in the liner at the pressure milestones can be found in Figure 28 through Figure 36. Perhaps of greatest interest in the peak strain plots, are the general frequency and locations of the “hot spots” in the liner. For all participants, the peak strains occur near the

various discontinuities in the model. This is in agreement with the experimental testing from the PCCV test.

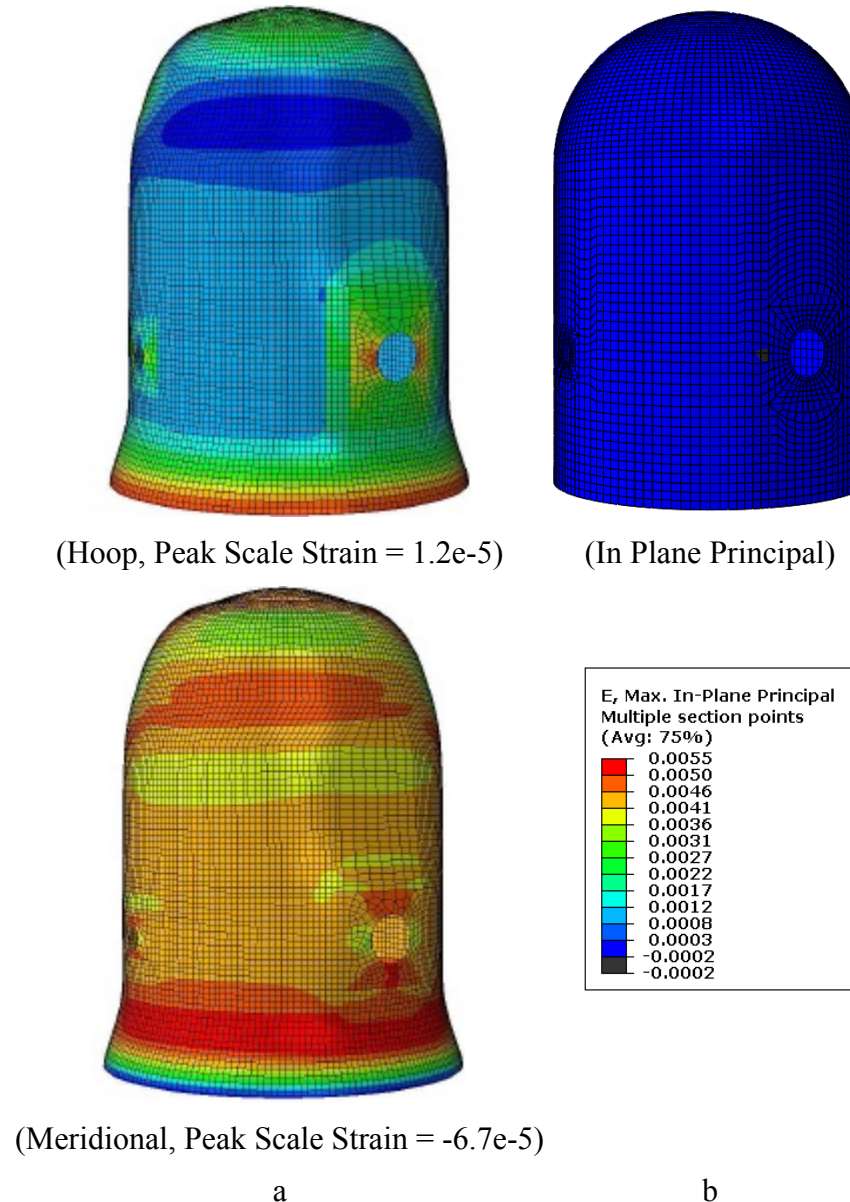
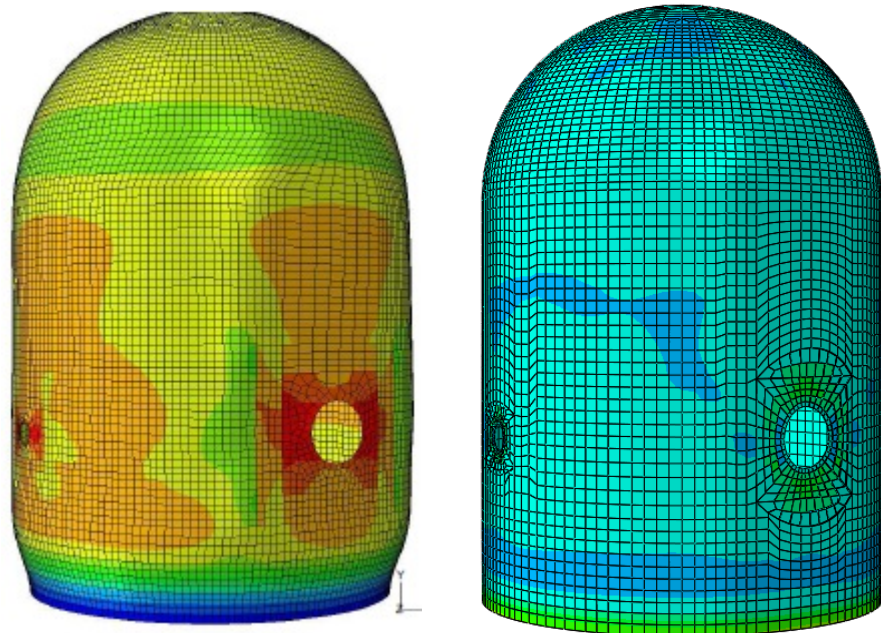
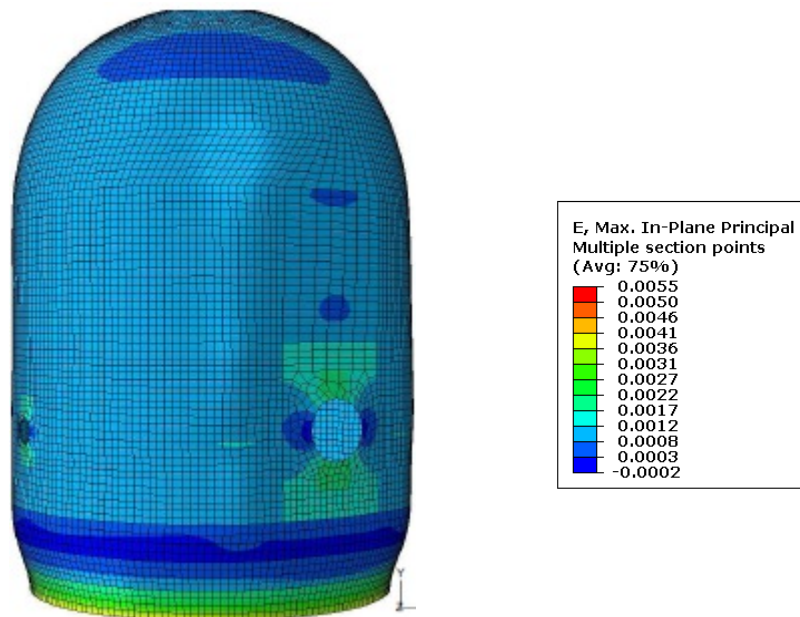


Figure 28: Peak Strain at $0 \times P_d$ (a) AERB (b) NRC



(Hoop, Peak Scale Strain = 1.8e-3)

(In Plane Principal)



(Meridional, Peak Scale Strain = 3.8e-3)

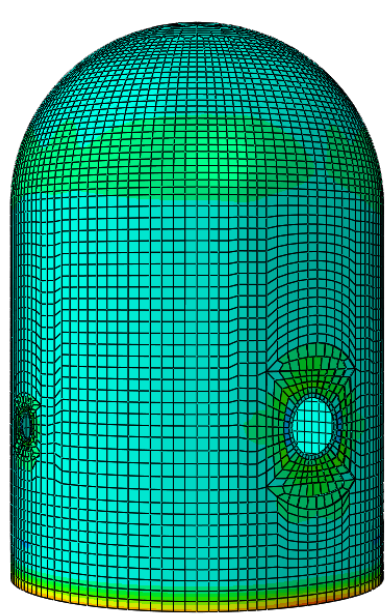
a

b

Figure 29: Peak Strain at $1.0 \times P_d$ (a) AERB (b) NRC



(Hoop, Peak Scale Strain = 2.0e-3)



(In Plane Principal)



(Meridional, Peak Scale Strain = 4.8e-3)

a

b

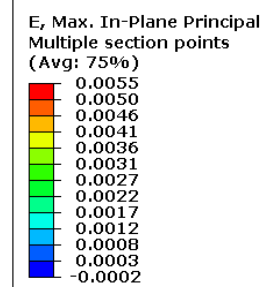
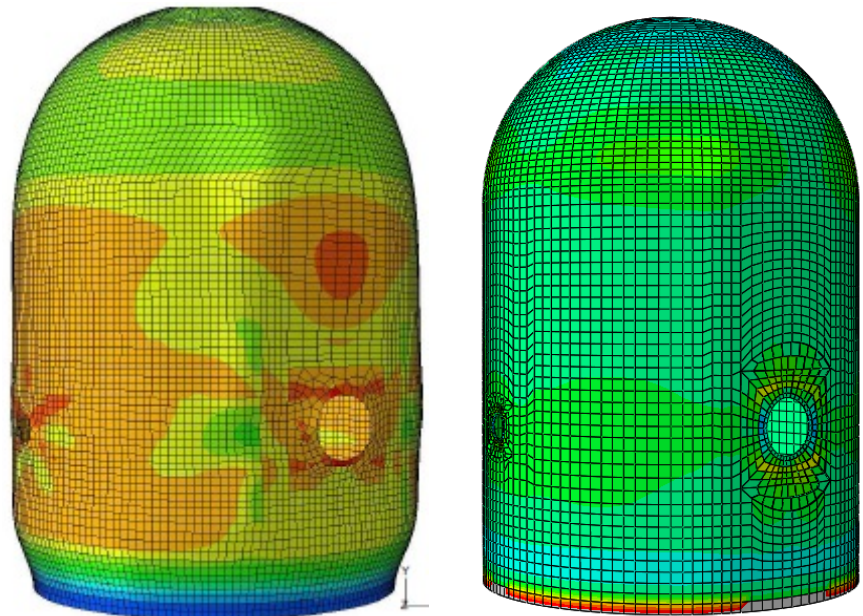
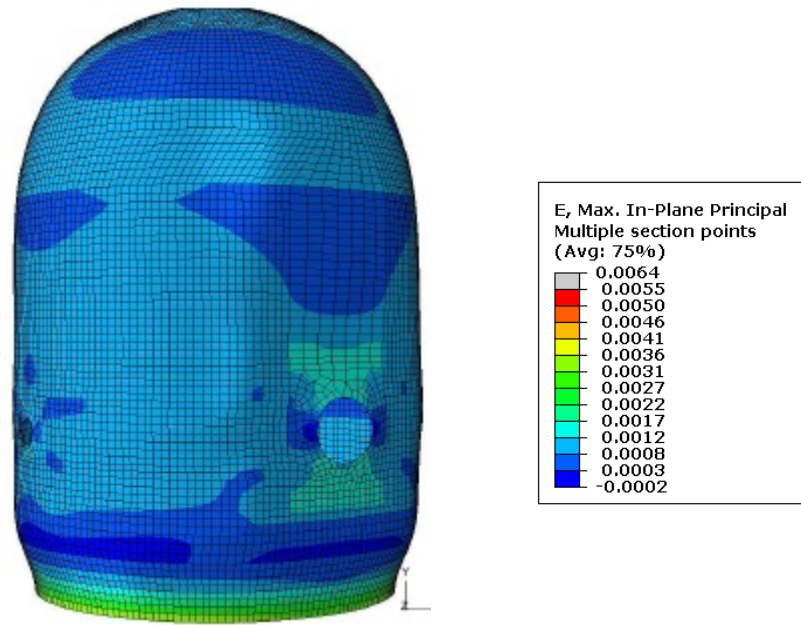


Figure 30: Peak Strain at $1.5 \times P_d$ (a) AERB (b) NRC



(Hoop, Peak Scale Strain = 2.6e-3)

(In Plane Principal)

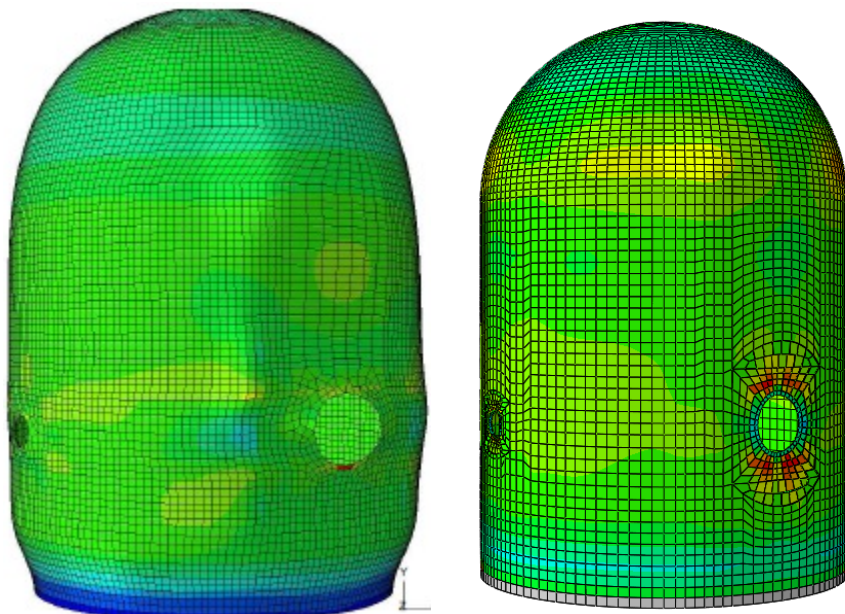


(Meridional, Peak Scale Strain = 5.8e-3)

a

b

Figure 31: Peak Strain at $2.0 \times P_d$ (a) AERB (b) NRC



(Hoop, Peak Scale Strain = 4.7e-3)

(In Plane Principal)



(Meridional, Peak Scale Strain = 7.1e-3)

a

b

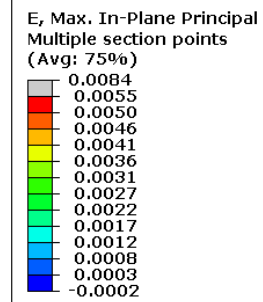
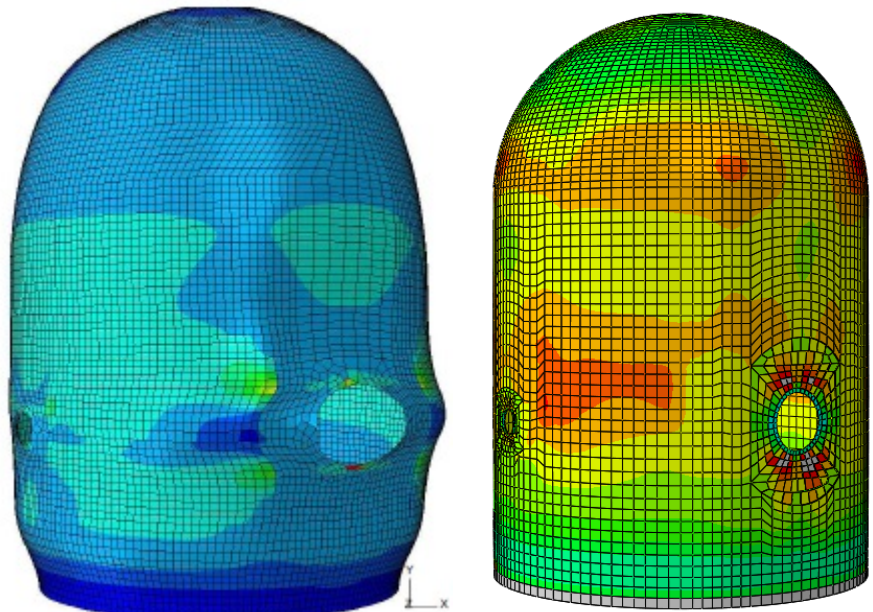
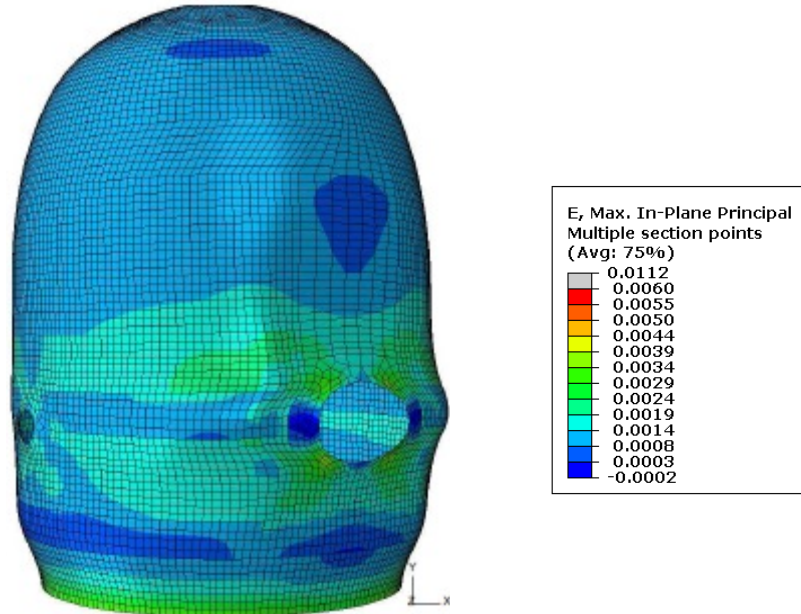


Figure 32: Peak Strain at $2.5 \times P_d$ (a) AERB (b) NRC



(Hoop, Peak Scale Strain = 1.3e-2)

(In Plane Principal)

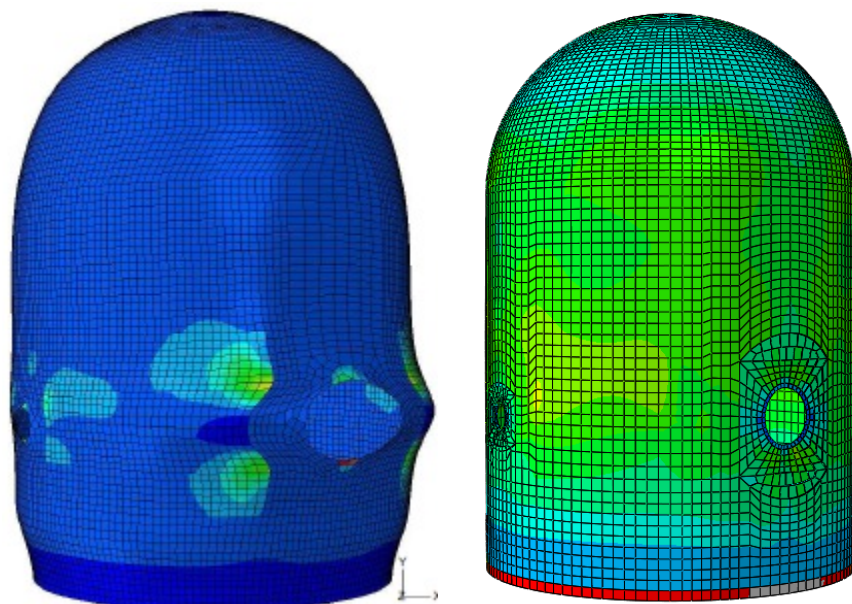


(Meridional, Peak Scale Strain = 8.7e-3)

a

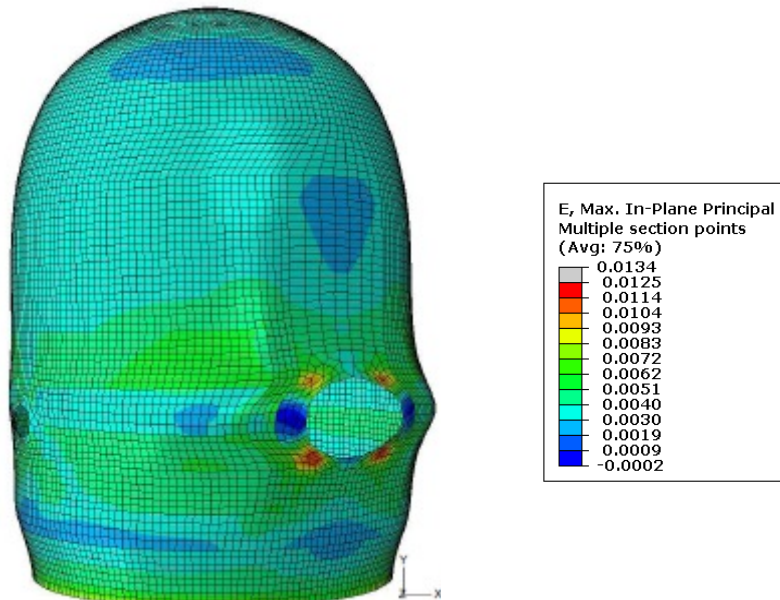
b

Figure 33: Peak Strain at $3.0 \times P_d$ (a) AERB (b) NRC



(Hoop, Peak Scale Strain = 2.7e-2)

(In Plane Principal)

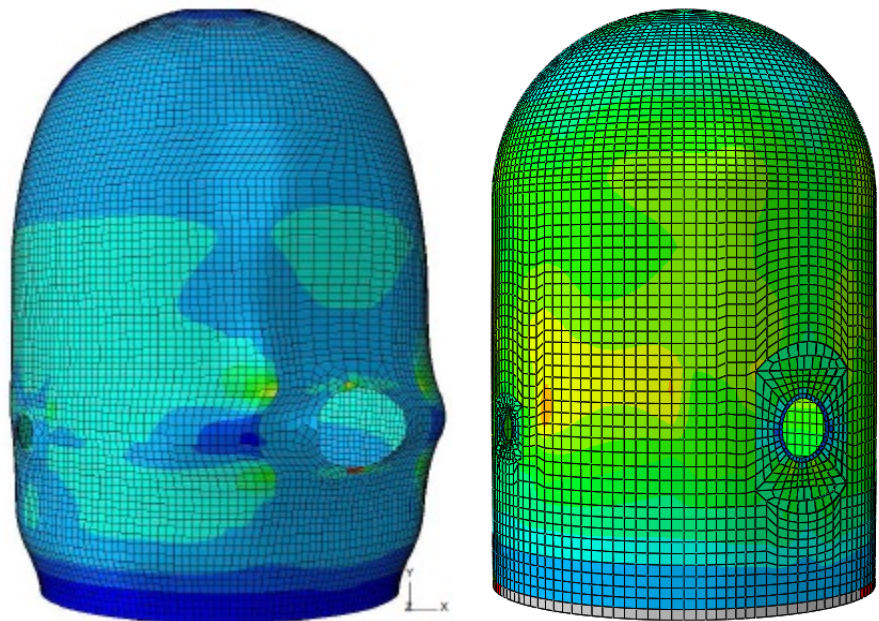


(Meridional, Peak Scale Strain = 1.0e-2)

a

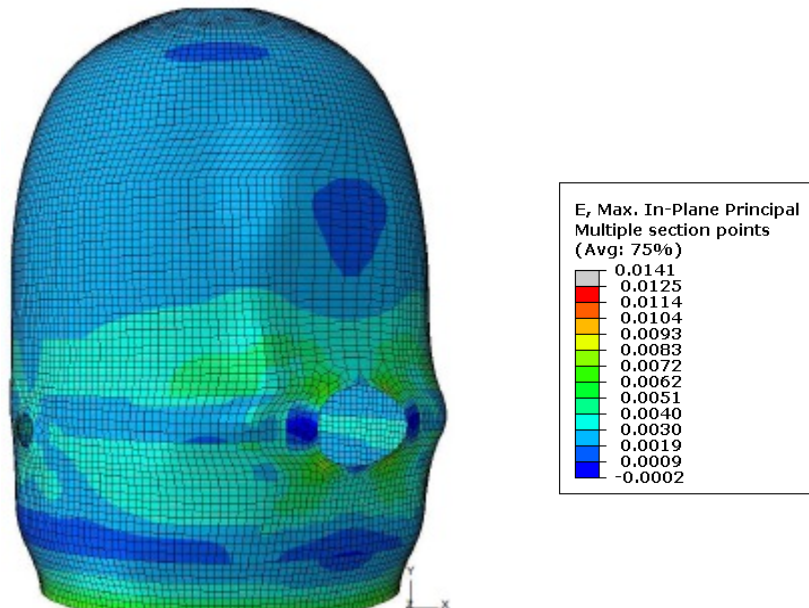
b

Figure 34: Peak Strain at (a) $3.25 \times P_d$ AERB (b) $3.3 \times P_d$ NRC



(Hoop, Peak Scale Strain = 1.3e-2)

(In Plane Principal)

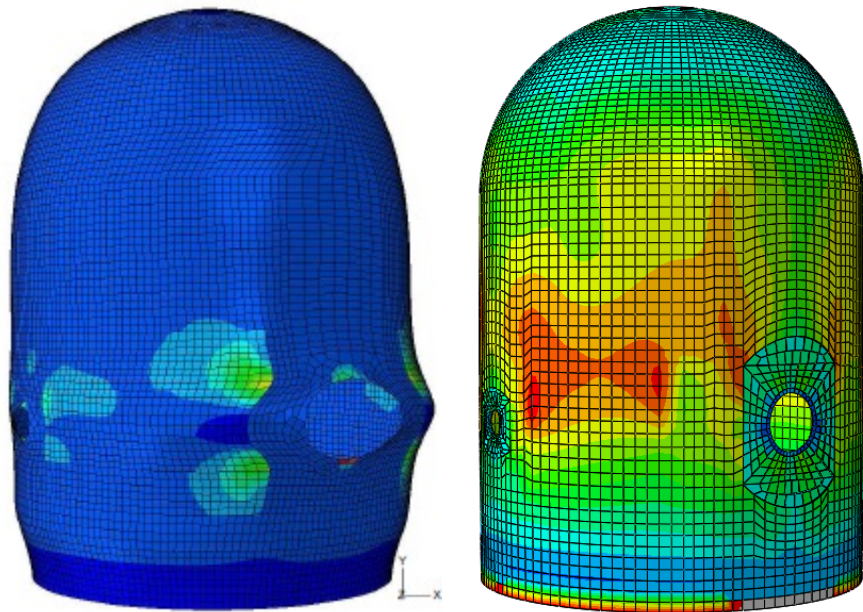


(Meridional, Peak Scale Strain = 8.7e-3)

a

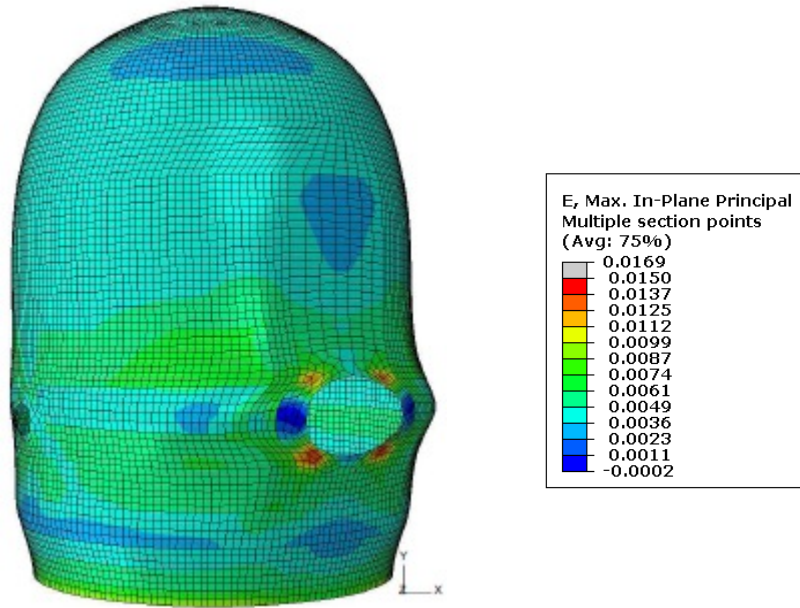
b

Figure 35: Peak Strain at $3.40 \times P_d$ (a) AERB (b) NRC



(Hoop, Peak Scale Strain = 2.7e-2)

(In Plane Principal)



(Meridional, Peak Scale Strain = 1.0e-2)

a

b

Figure 36: Peak Strain at Ultimate Pressure (a) 3.46 x P_d AERB (b) 3.6 x P_d NRC

3.2.2 Average Strains at Selected Locations

The participants were asked to provide strain data at the locations shown in Figure 37. These results are documented in Figure 38 through Figure 47.

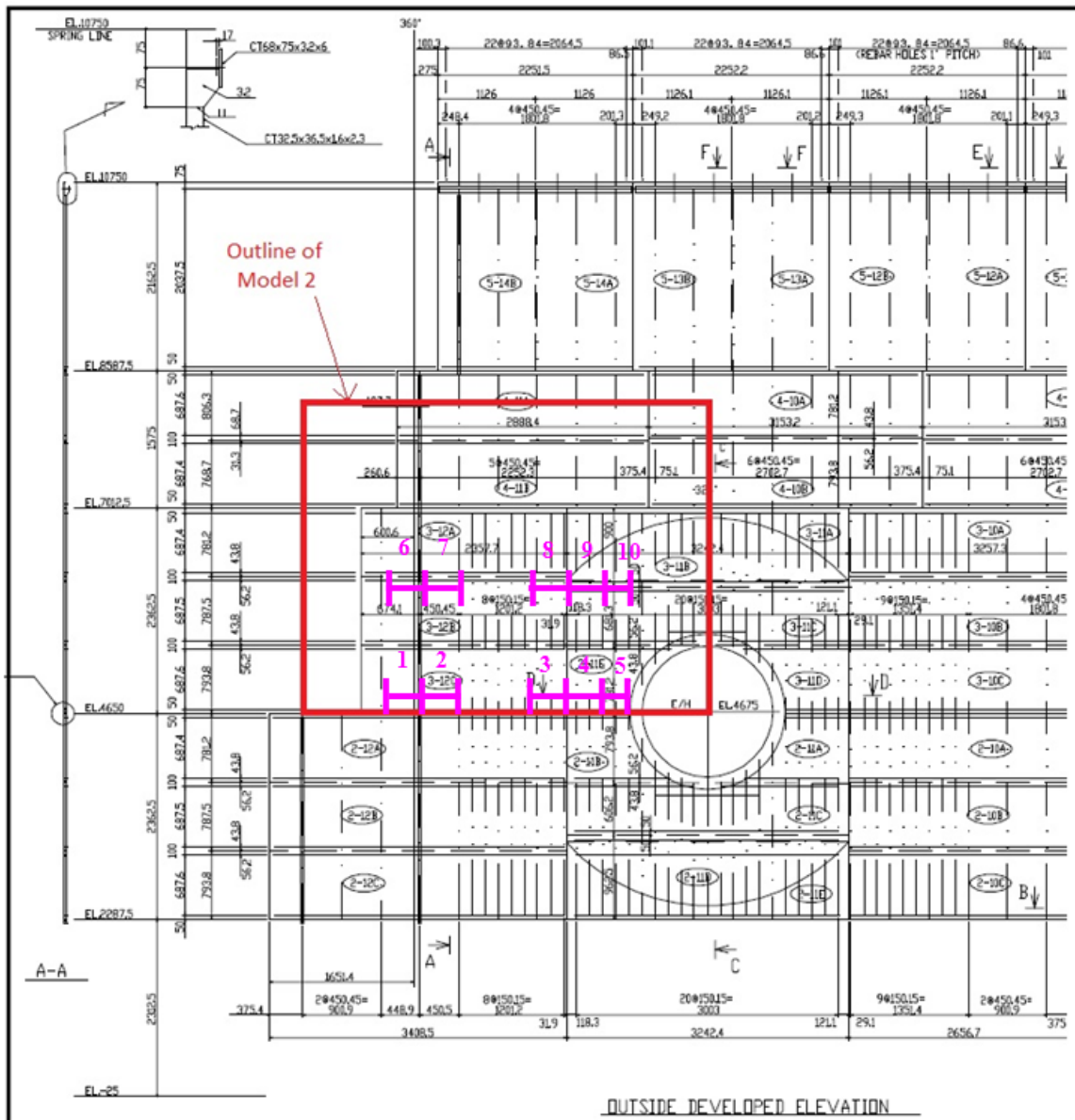


Figure 37: Liner (E/H) View Showing Locations where Participants are Requested to Provide Liner Strain Results

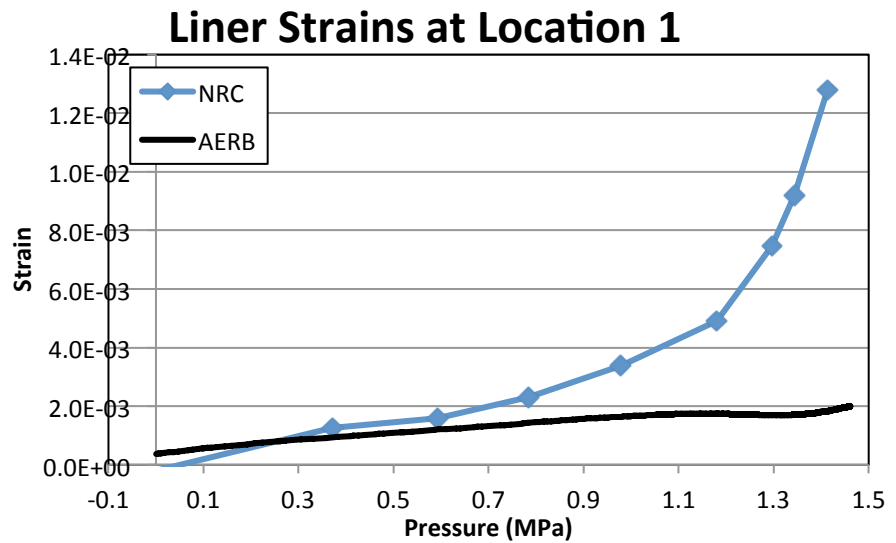


Figure 38: Strain over Gauge Length at Location 1 Near Equipment Hatch

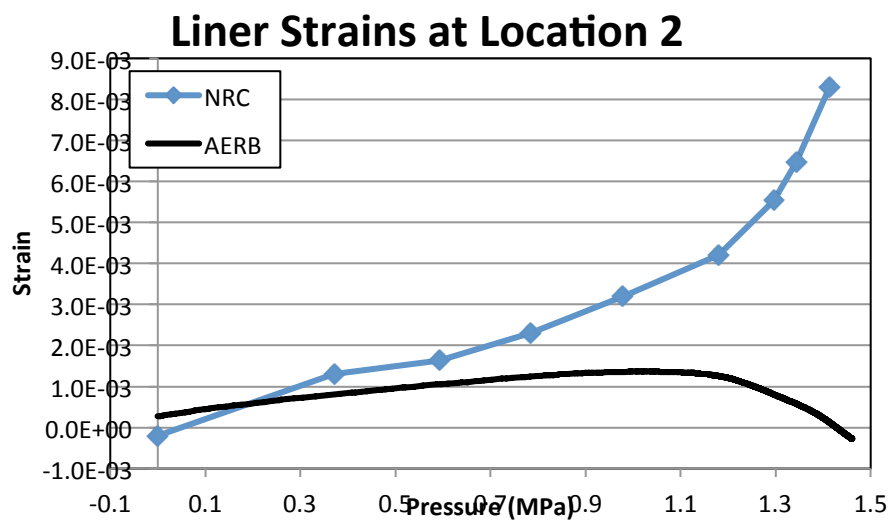


Figure 39: Strain over Gauge Length at Location 2 Near Equipment Hatch

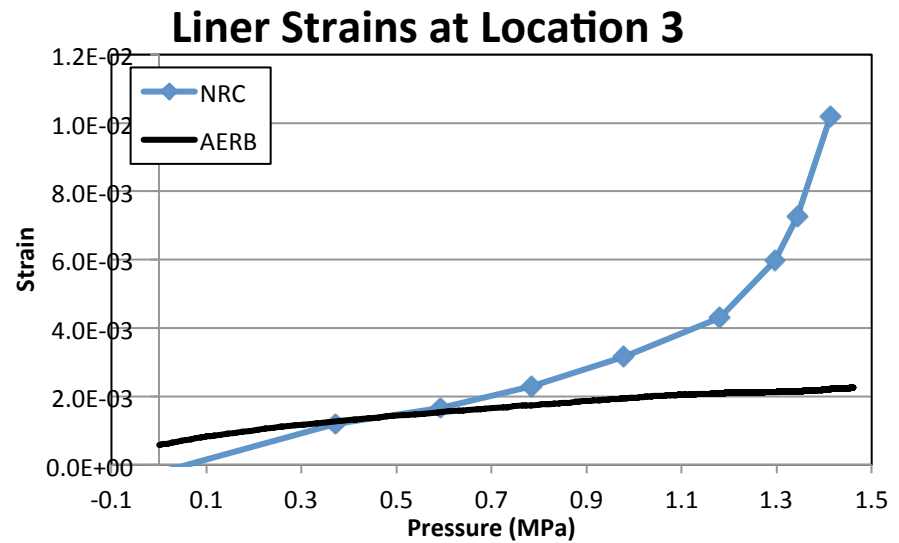


Figure 40: Strain over Gauge Length at Location 3 Near Equipment Hatch

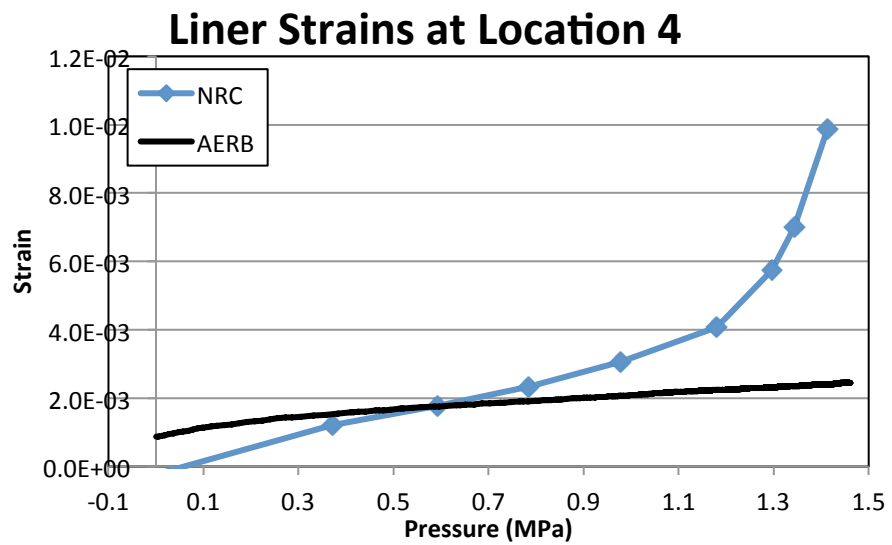


Figure 41: Strain over Gauge Length at Location 4 Near Equipment Hatch

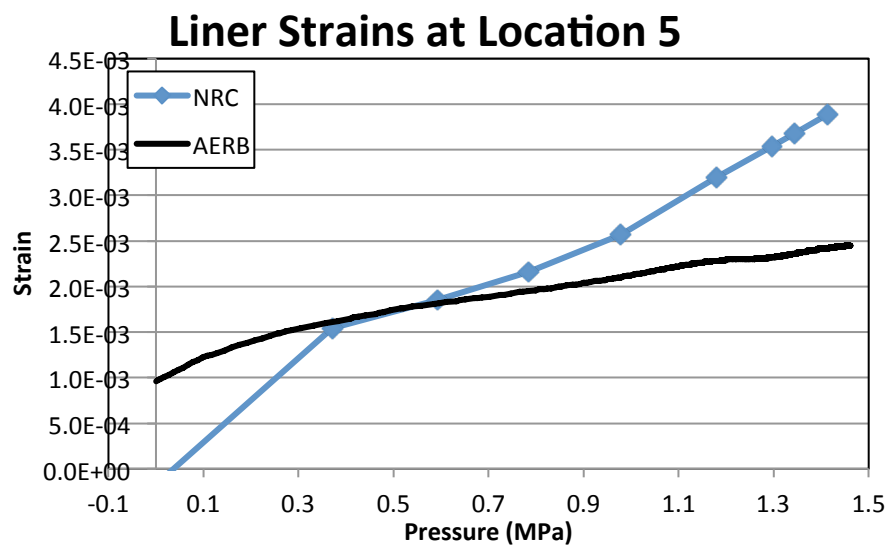


Figure 42: Strain over Gauge Length at Location 5 Near Equipment Hatch

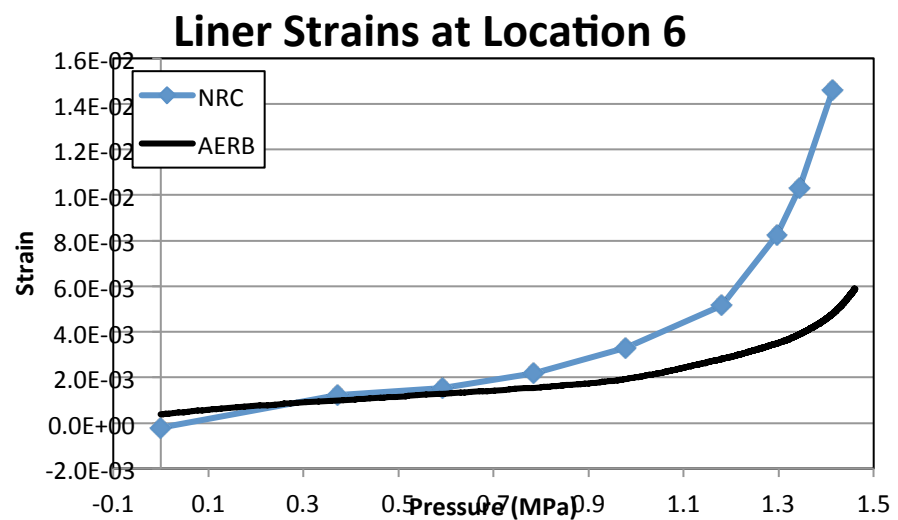


Figure 43: Strain over Gauge Length at Location 6 Near Equipment Hatch

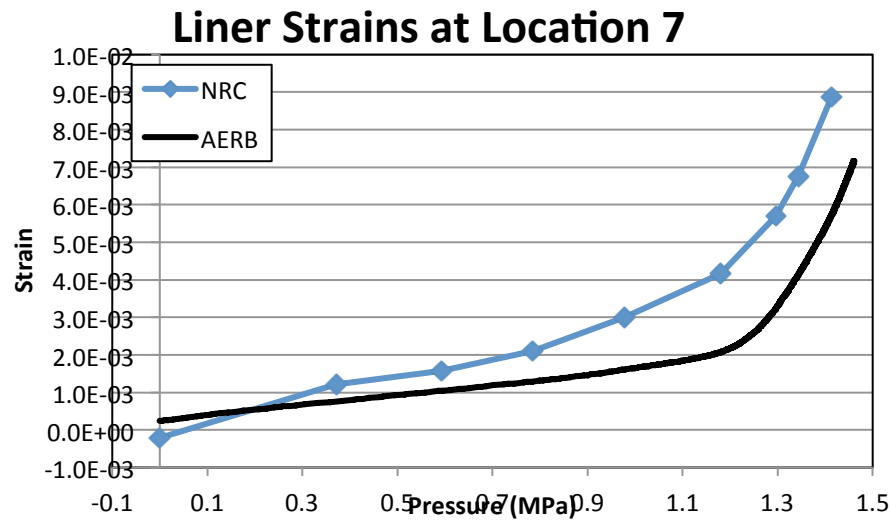


Figure 44: Strain over Gauge Length at Location 7 Near Equipment Hatch

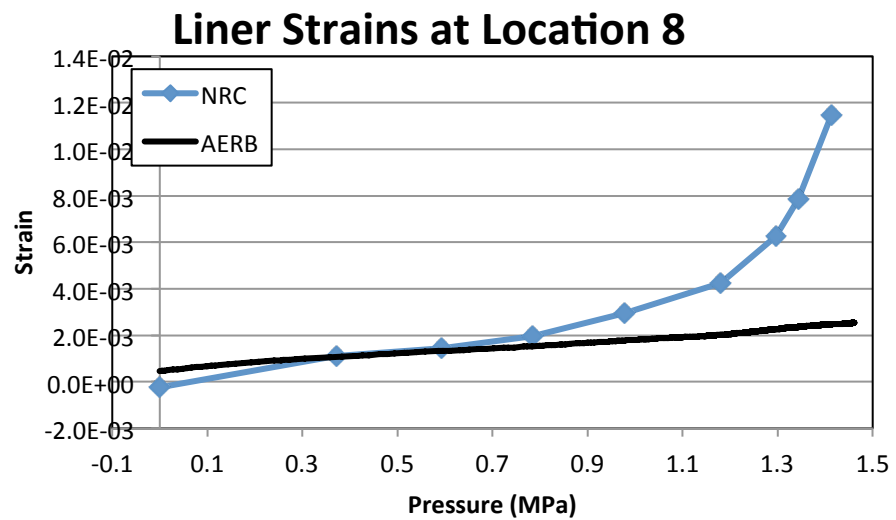


Figure 45: Strain over Gauge Length at Location 8 Near Equipment Hatch

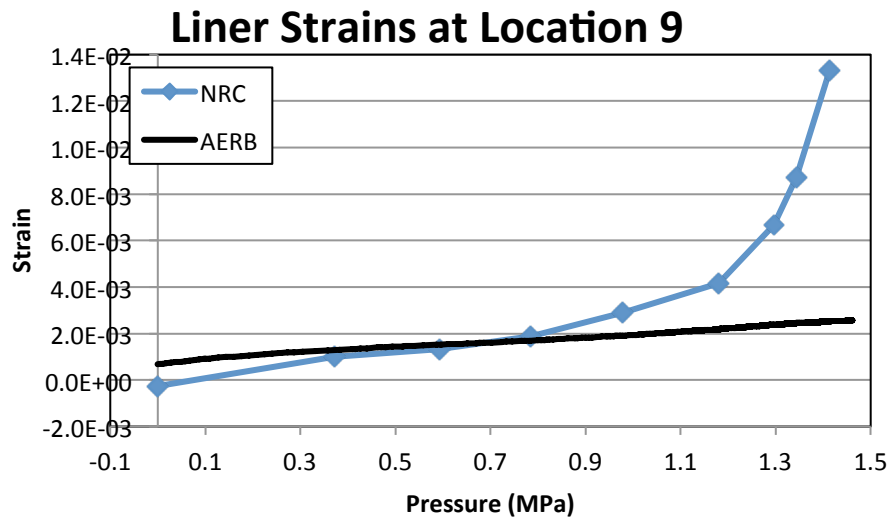


Figure 46: Strain over Gauge Length at Location 9 Near Equipment Hatch

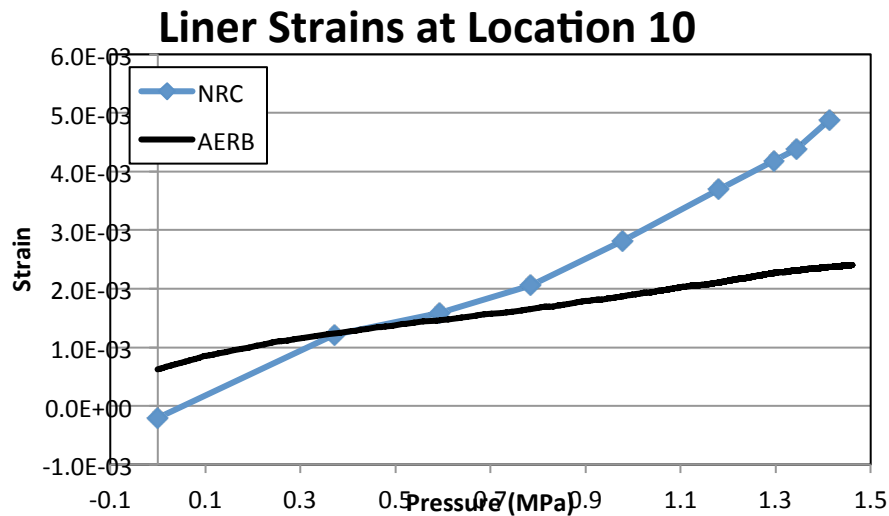


Figure 47: Strain over Gauge Length at Location 10 Near Equipment Hatch

3.3 Tendon Stress Distribution

The tendon stress distribution plots from the participants are presented in Figure 48 through Figure 92. As was the case in previous sections, the abscissa and ordinate are plotted on constant scales through this subsection in order to facilitate comparison between the plots.

3.3.1 Hoop Tendons

The hoop tendons plotted in this subsection correspond to tendons #H35, H53, and H68 from the PCCV test. The selection of these tendons for analysis helped facilitate comparison with the

most instrumented tendons from the 1:4 scale test. The hoop tendon stress profiles can be found in Figure 48 through Figure 74. In general the tendon stress distributions from the participants agree reasonably well with the exception of the AERB provided data which seems to deviate from the shape of the NRC's data.

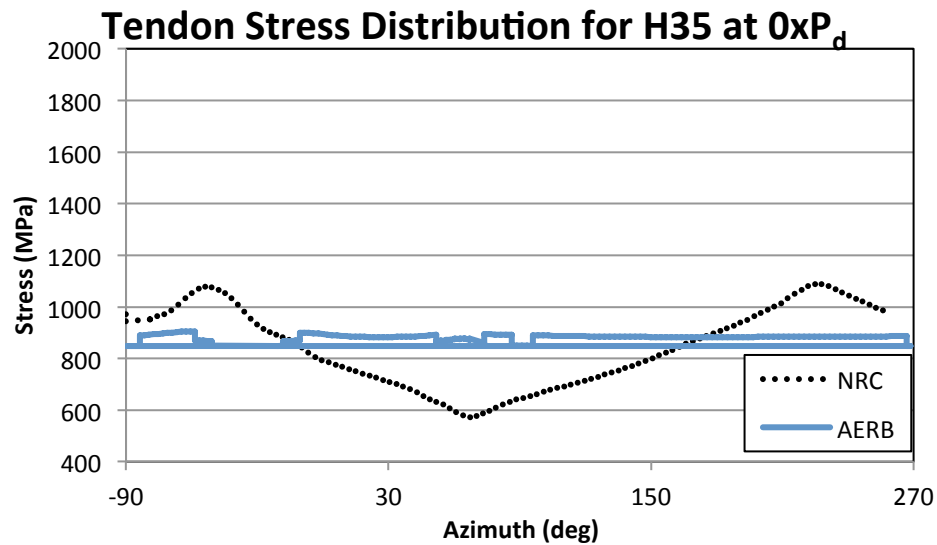


Figure 48: Tendon Stress Distribution for Tendon #H35 at $0 \times P_d$

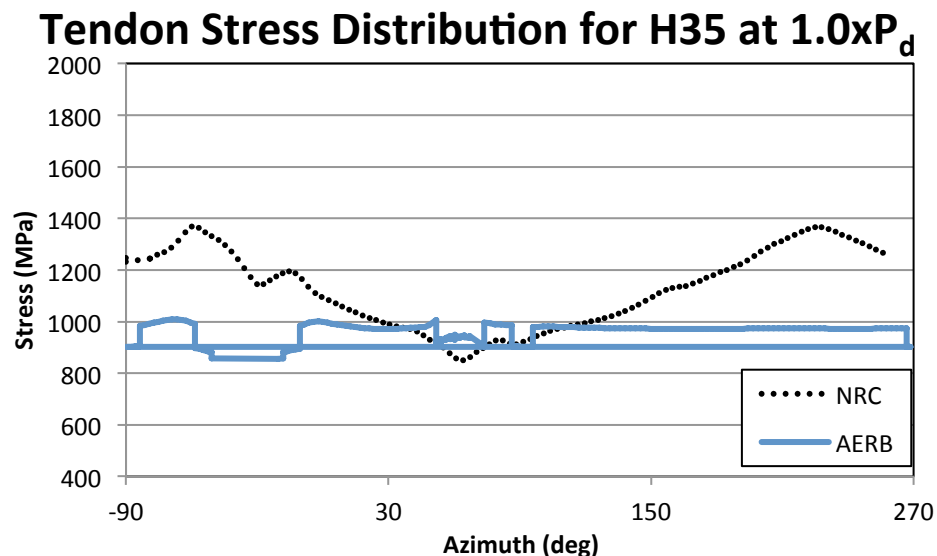


Figure 49: Tendon Stress Distribution for Tendon #H35 at $1.0 \times P_d$

Tendon Stress Distribution for H35 at $1.5 \times P_d$

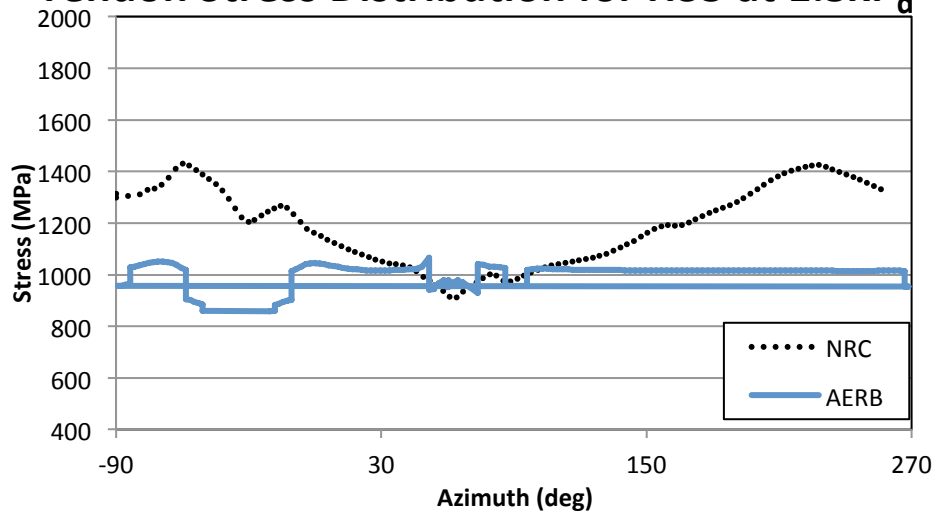


Figure 50: Tendon Stress Distribution for Tendon #H35 at $1.5 \times P_d$

Tendon Stress Distribution for H35 at $2.0 \times P_d$

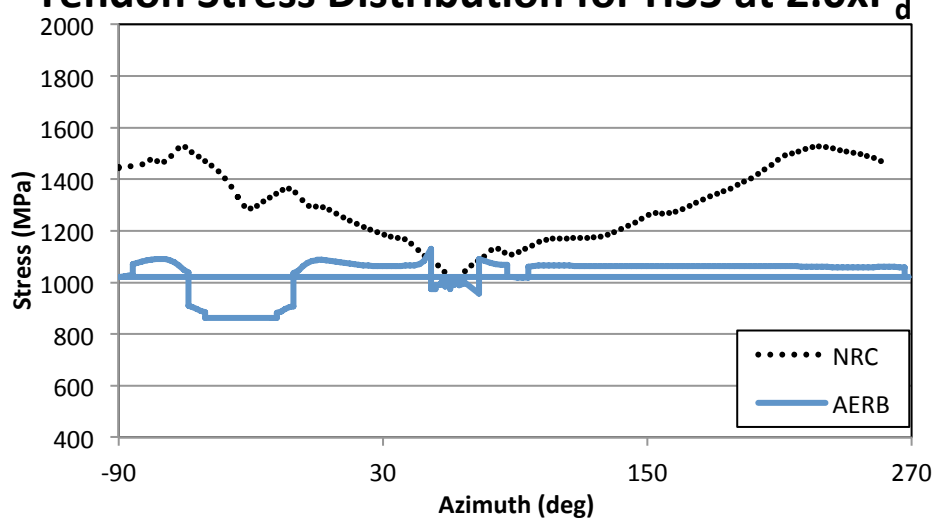


Figure 51: Tendon Stress Distribution for Tendon #H35 at $2.0 \times P_d$

Tendon Stress Distribution for H35 at $2.5 \times P_d$

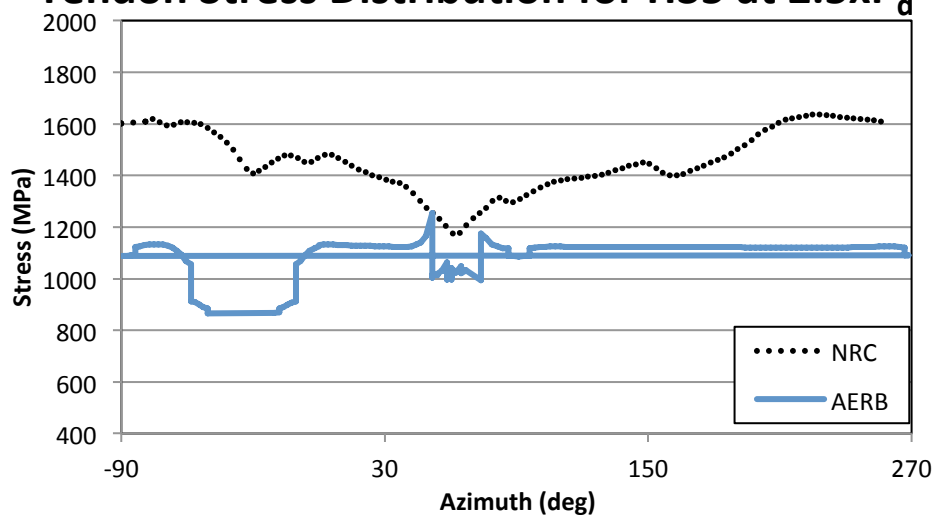


Figure 52: Tendon Stress Distribution for Tendon #H35 at $2.5 \times P_d$

Tendon Stress Distribution for H35 at $3.0 \times P_d$

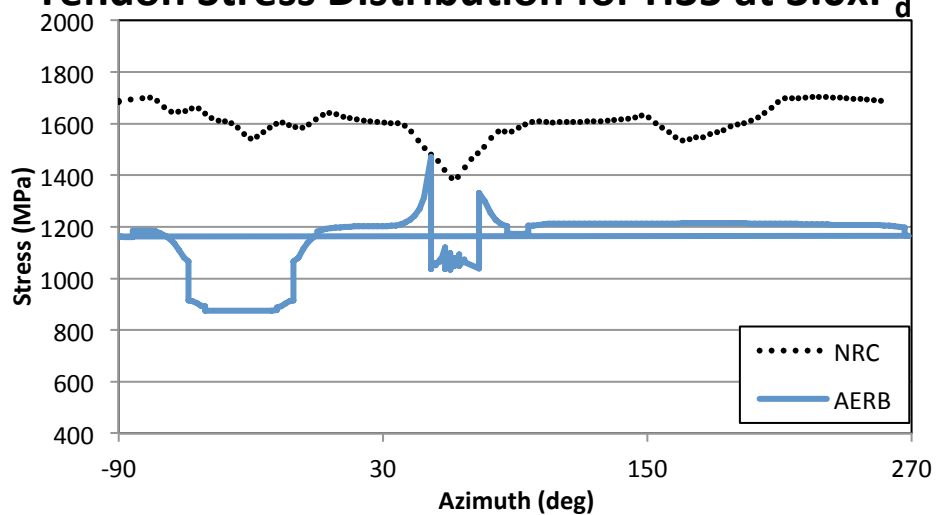


Figure 53: Tendon Stress Distribution for Tendon #H35 at $3.0 \times P_d$

Tendon Stress Distribution for H35 at $3.3 \times P_d$

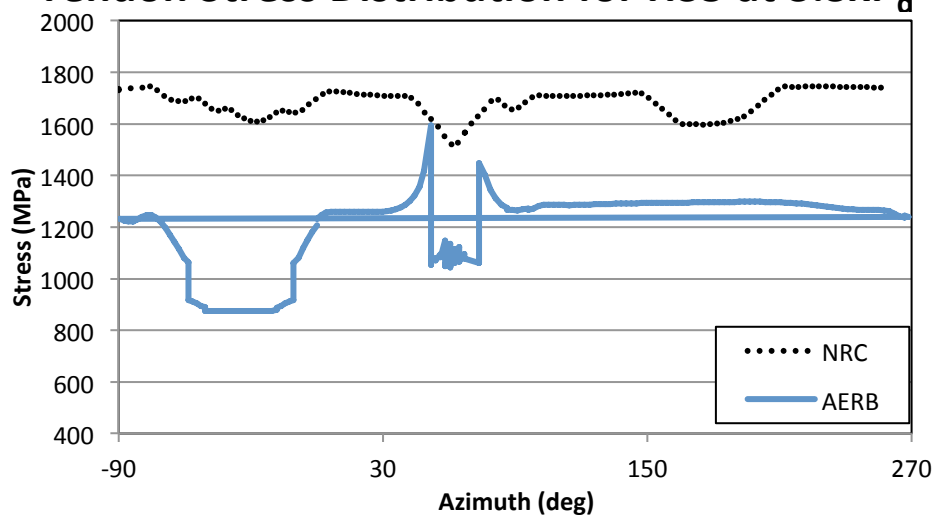


Figure 54: Tendon Stress Distribution for Tendon #H35 at $3.3 \times P_d$

Tendon Stress Distribution for H35 at $3.4 \times P_d$

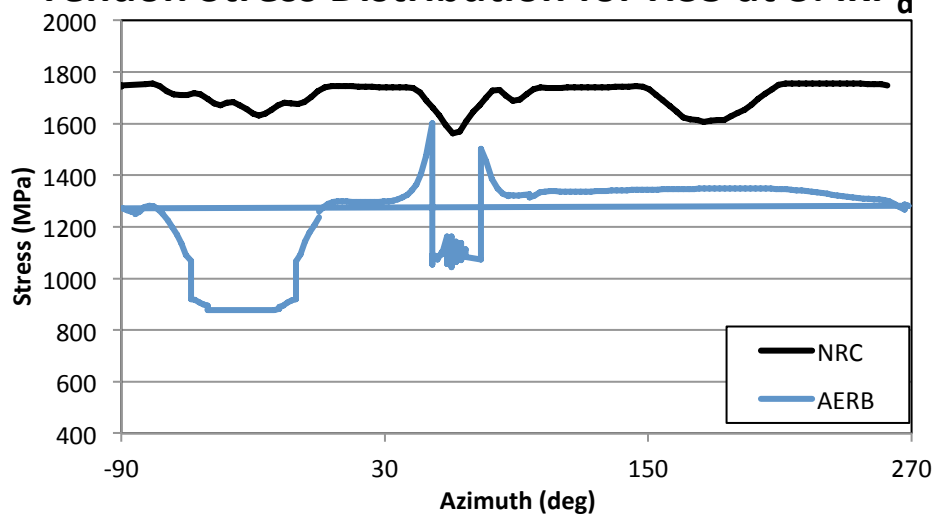


Figure 55: Tendon Stress Distribution for Tendon #H35 at $3.4 \times P_d$

Tendon Stress Distribution for Ultimate Pressure

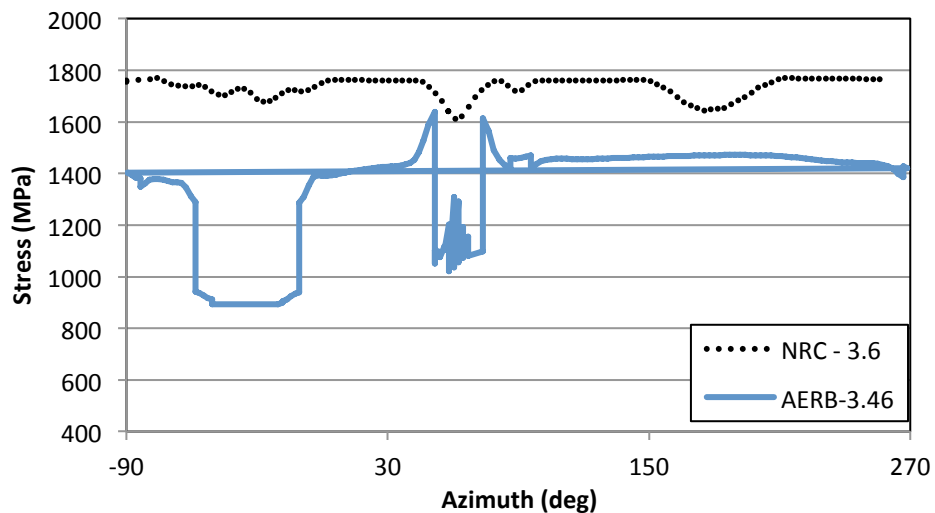


Figure 56: Tendon Stress Distribution for Tendon #H35 at Ultimate Pressure

Tendon Stress Distribution for H53 at $0 \times P_d$

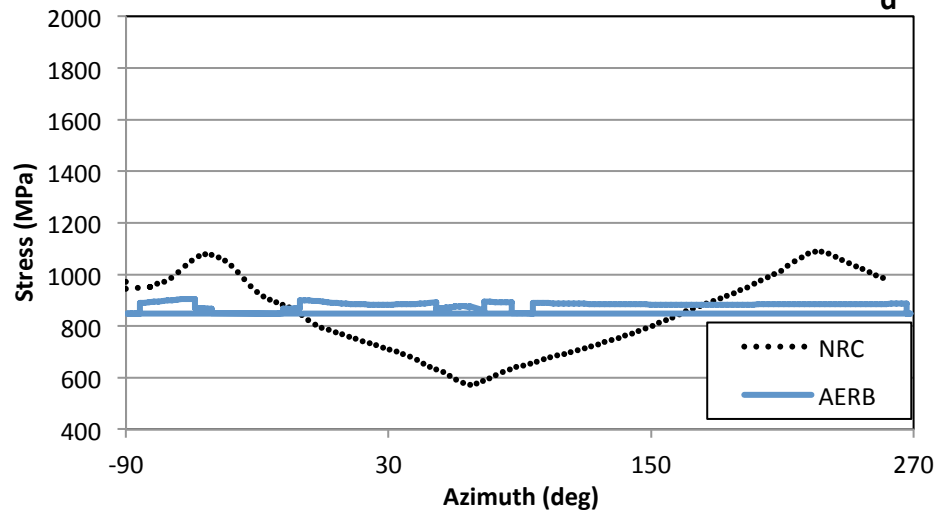


Figure 57: Tendon Stress Distribution for Tendon #H53 at $0 \times P_d$

Tendon Stress Distribution for H53 at 1.0xP_d

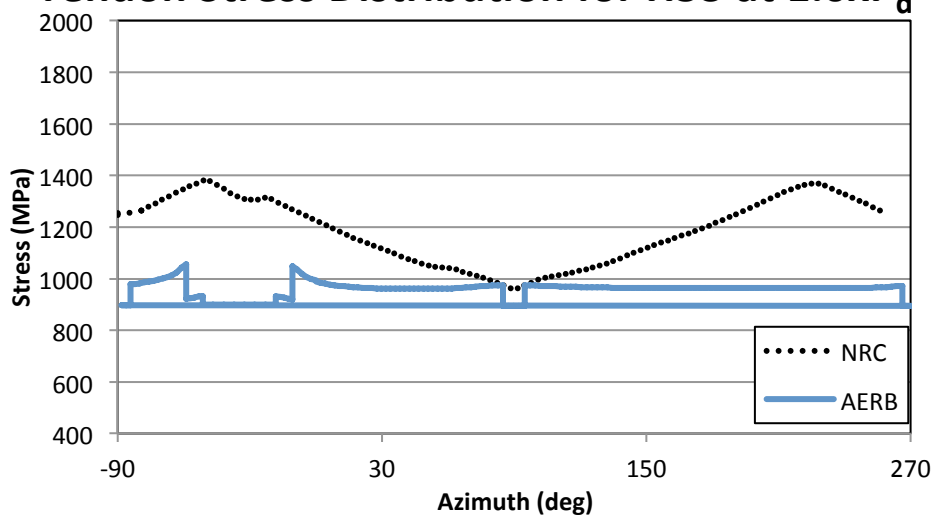


Figure 58: Tendon Stress Distribution for Tendon #H53 at 1.0 x P_d

Tendon Stress Distribution for H53 at 1.5xP_d

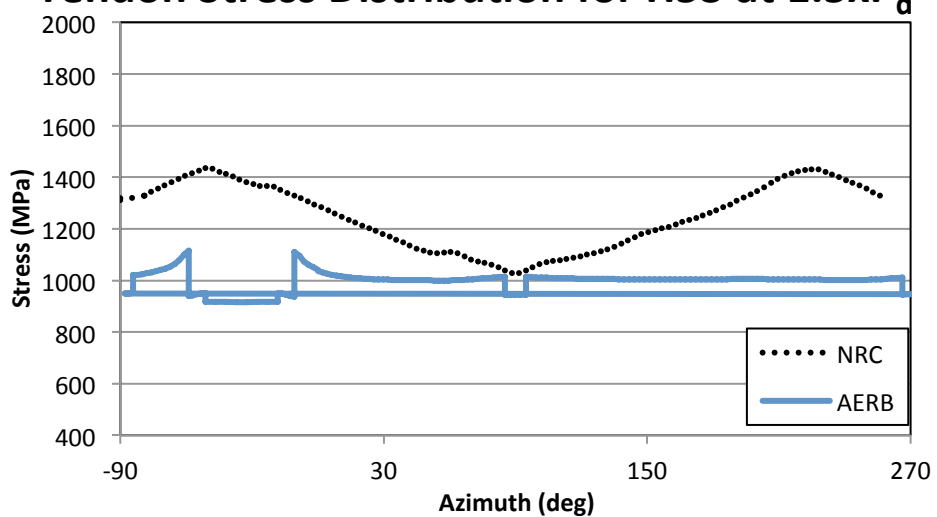


Figure 59: Tendon Stress Distribution for Tendon #H53 at 1.5 x P_d

Tendon Stress Distribution for H53 at $2.0 \times P_d$

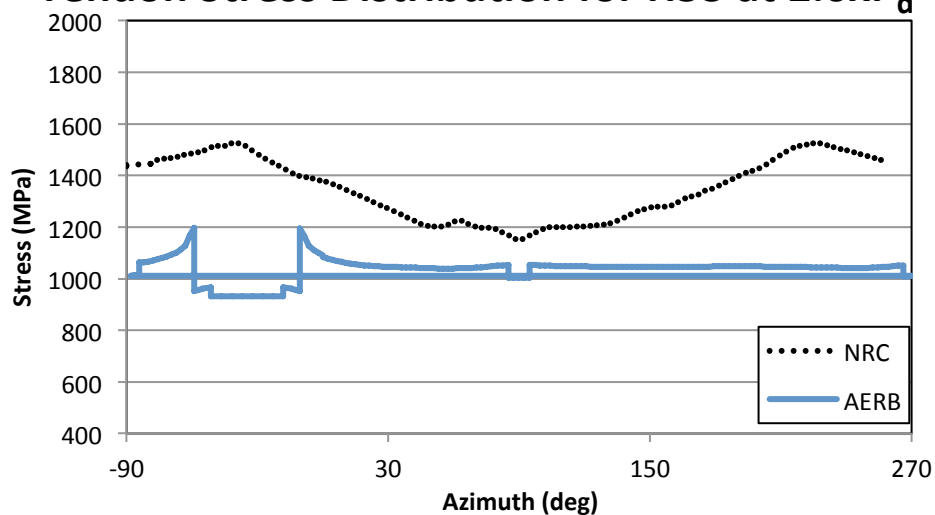


Figure 60: Tendon Stress Distribution for Tendon #H53 at $2.0 \times P_d$

Tendon Stress Distribution for H53 at $2.5 \times P_d$

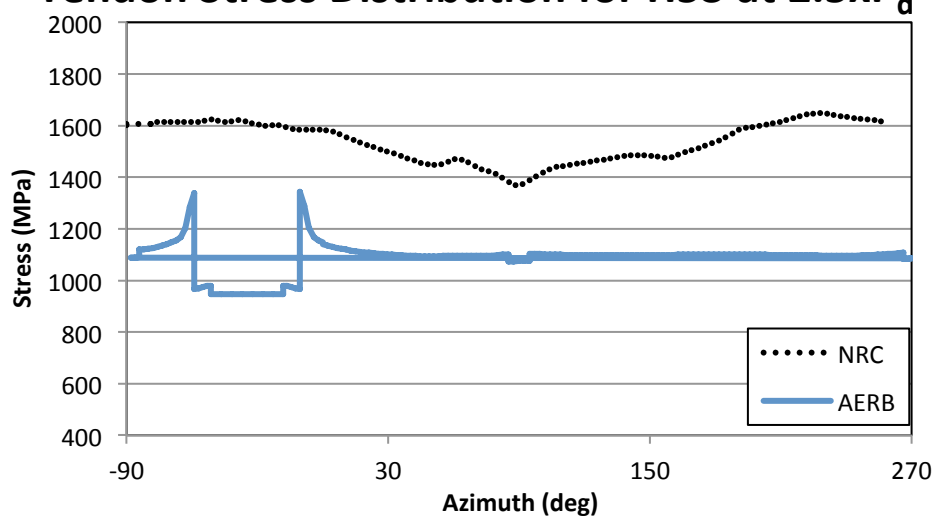


Figure 61: Tendon Stress Distribution for Tendon #H53 at $2.5 \times P_d$

Tendon Stress Distribution for H53 at $3.0 \times P_d$

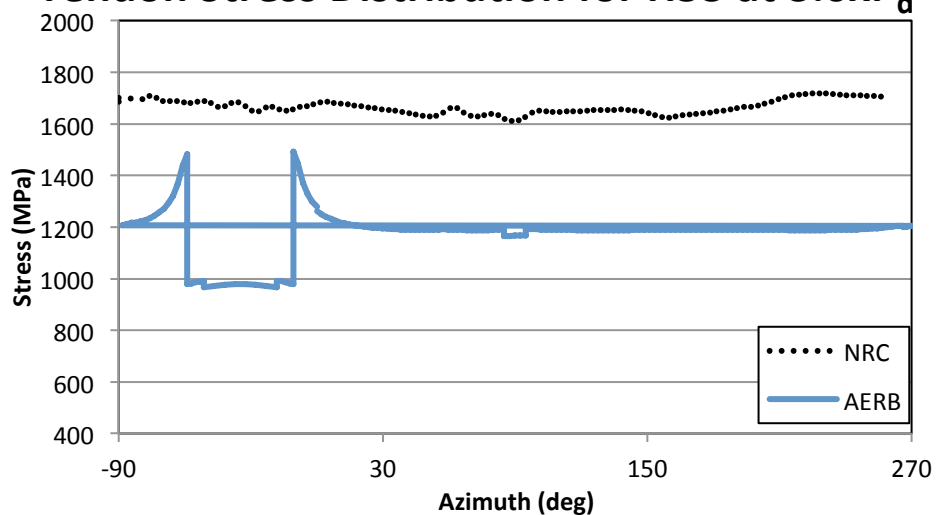


Figure 62: Tendon Stress Distribution for Tendon #H53 at $3.0 \times P_d$

Tendon Stress Distribution for H53 at $3.3 \times P_d$

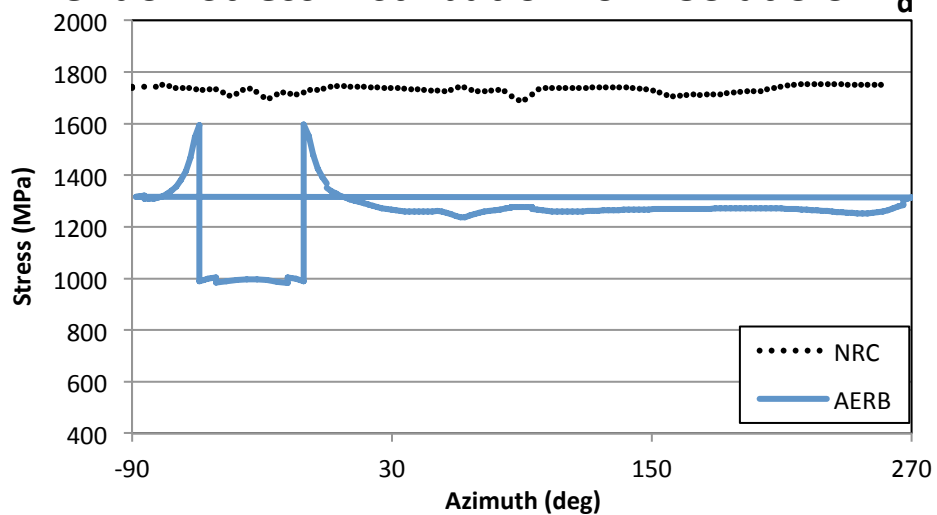


Figure 63: Tendon Stress Distribution for Tendon #H53 at $3.3 \times P_d$

Tendon Stress Distribution for H53 at $3.4 \times P_d$

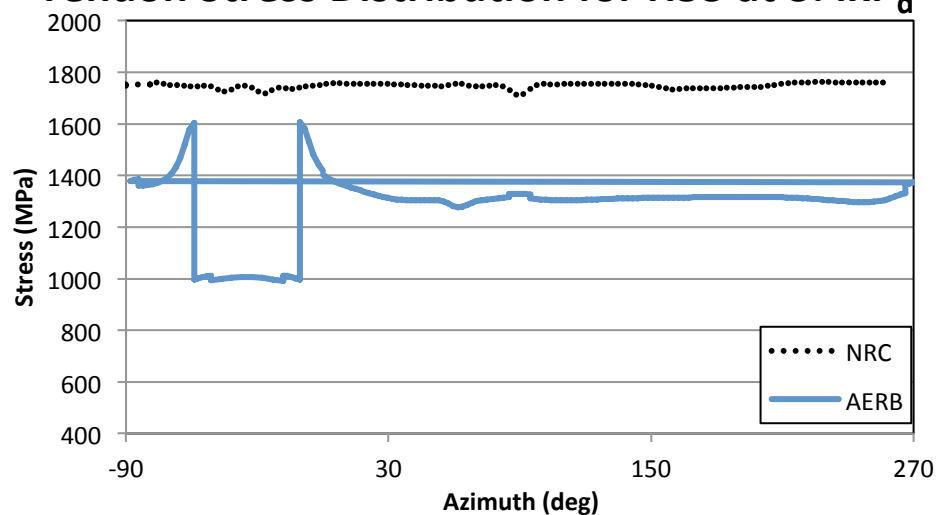


Figure 64: Tendon Stress Distribution for Tendon #H53 at $3.4 \times P_d$

Tendon Stress Distribution for H53 at Ultimate Pressure

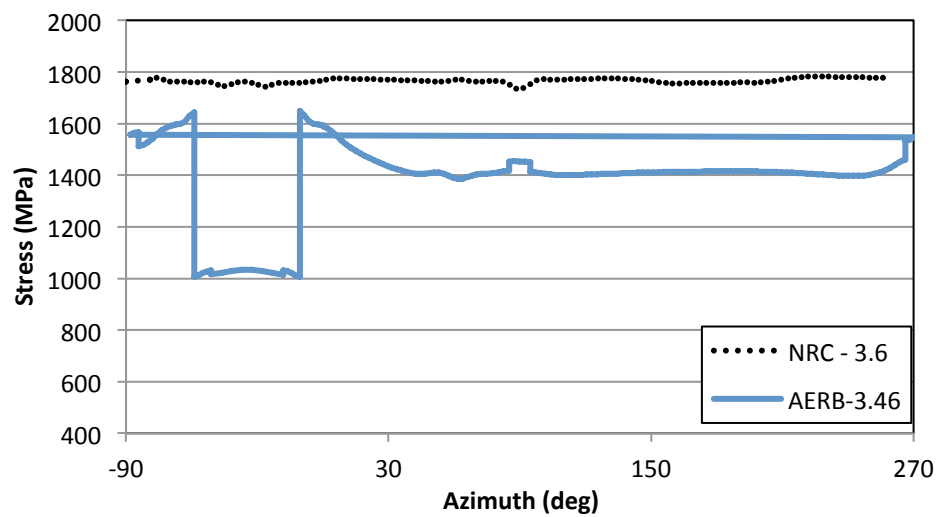


Figure 65: Tendon Stress Distribution for Tendon #H53 at Ultimate Pressure

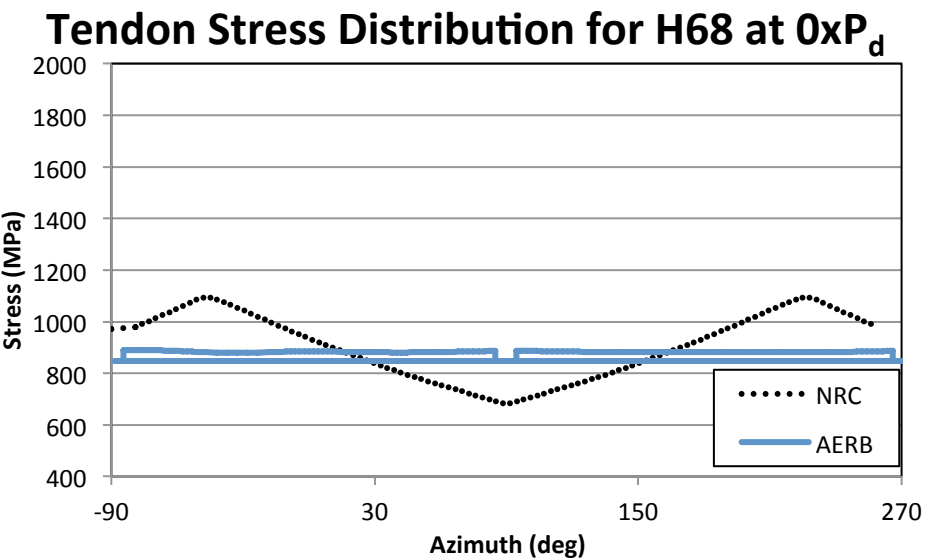


Figure 66: Tendon Stress Distribution for Tendon #H68 at 0 x P_d

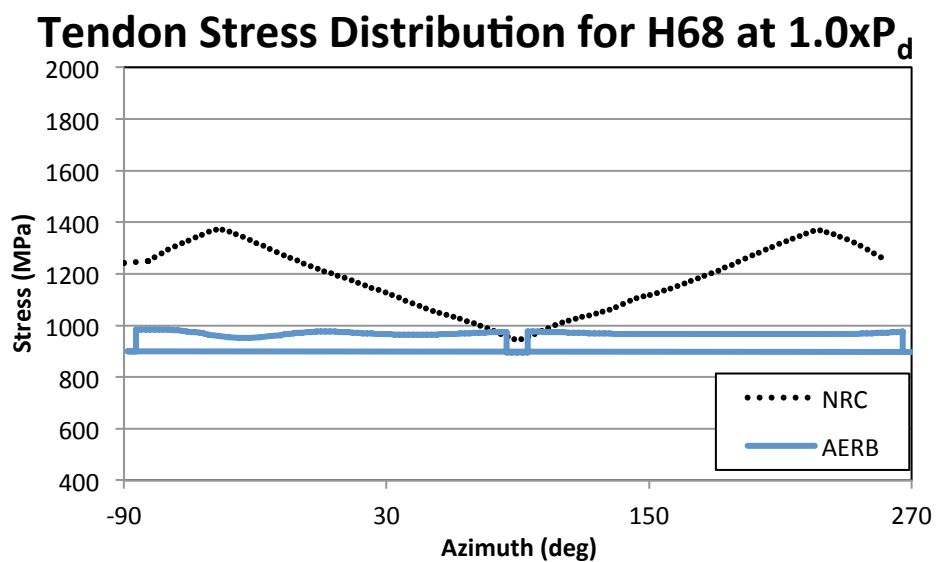


Figure 67: Tendon Stress Distribution for Tendon #H68 at 1.0 x P_d

Tendon Stress Distribution for H68 at $1.5 \times P_d$

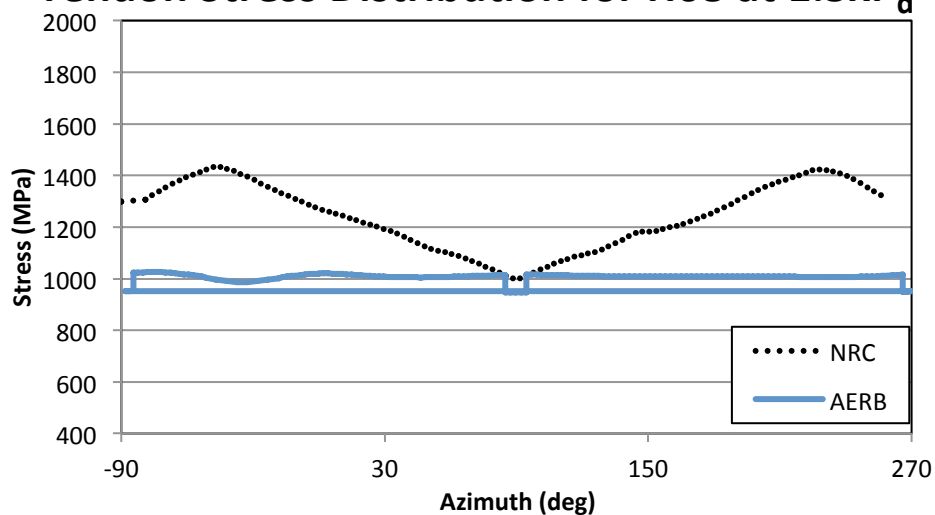


Figure 68: Tendon Stress Distribution for Tendon #H68 at $1.5 \times P_d$

Tendon Stress Distribution for H68 at $2.0 \times P_d$

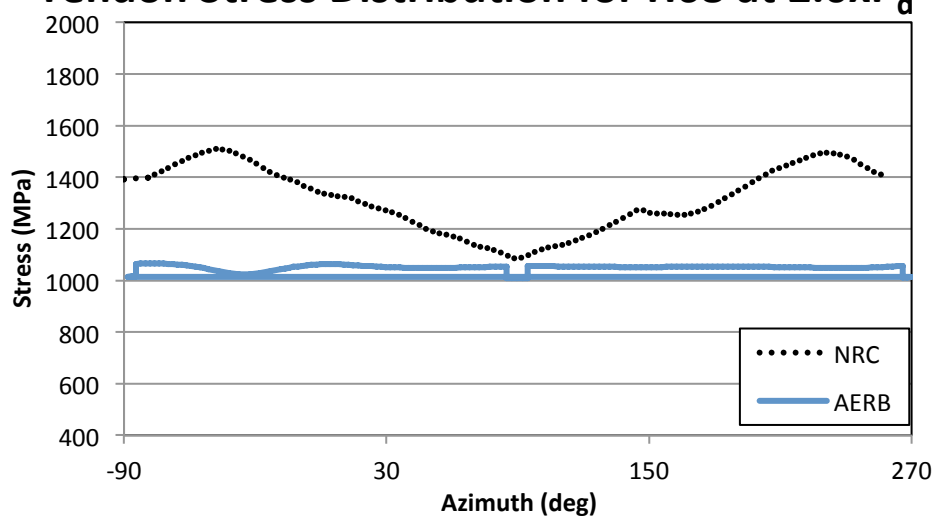


Figure 69: Tendon Stress Distribution for Tendon #H68 at $2.0 \times P_d$

Tendon Stress Distribution for H68 at $2.5 \times P_d$

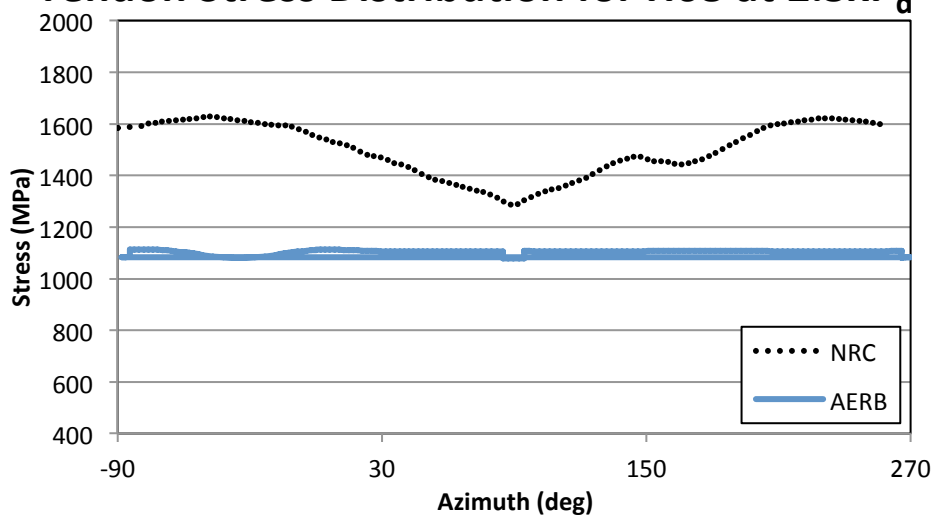


Figure 70: Tendon Stress Distribution for Tendon #H68 at $2.5 \times P_d$

Tendon Stress Distribution for H68 at $3.0 \times P_d$

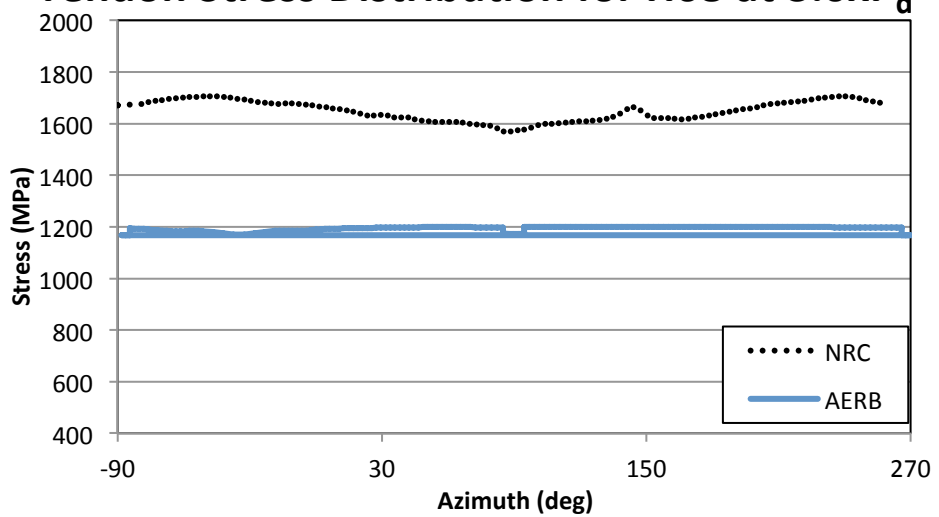


Figure 71: Tendon Stress Distribution for Tendon #H68 at $3.0 \times P_d$

Tendon Stress Distribution for H68 at $3.3 \times P_d$

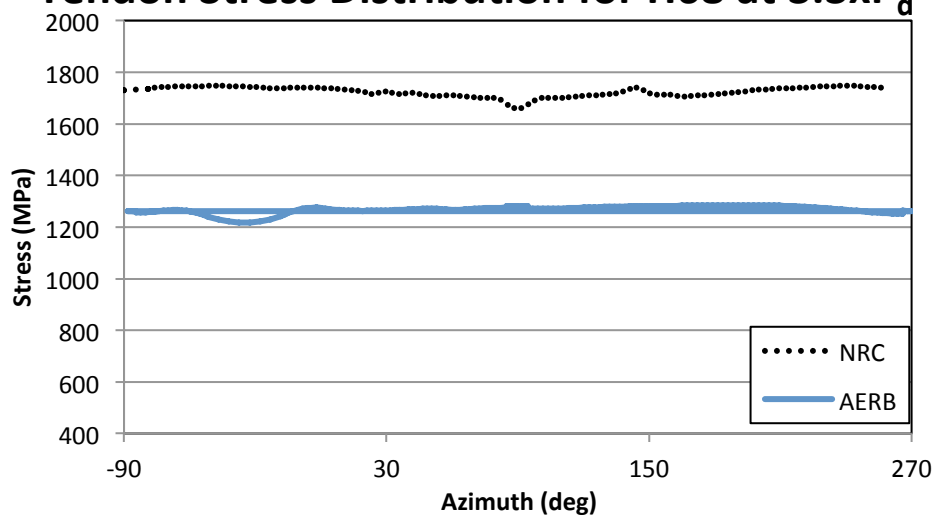


Figure 72: Tendon Stress Distribution for Tendon #H68 at $3.3 \times P_d$

Tendon Stress Distribution for H68 at $3.4 \times P_d$

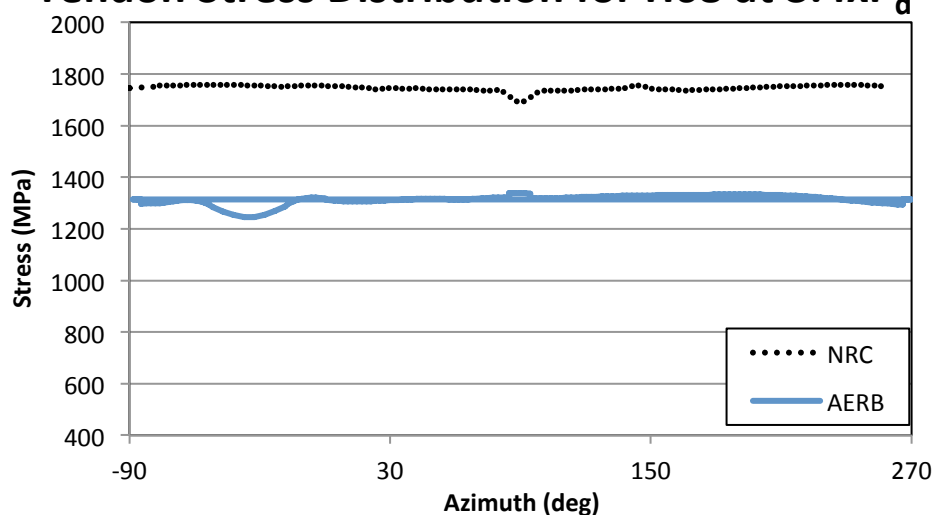


Figure 73: Tendon Stress Distribution for Tendon #H68 at $3.4 \times P_d$

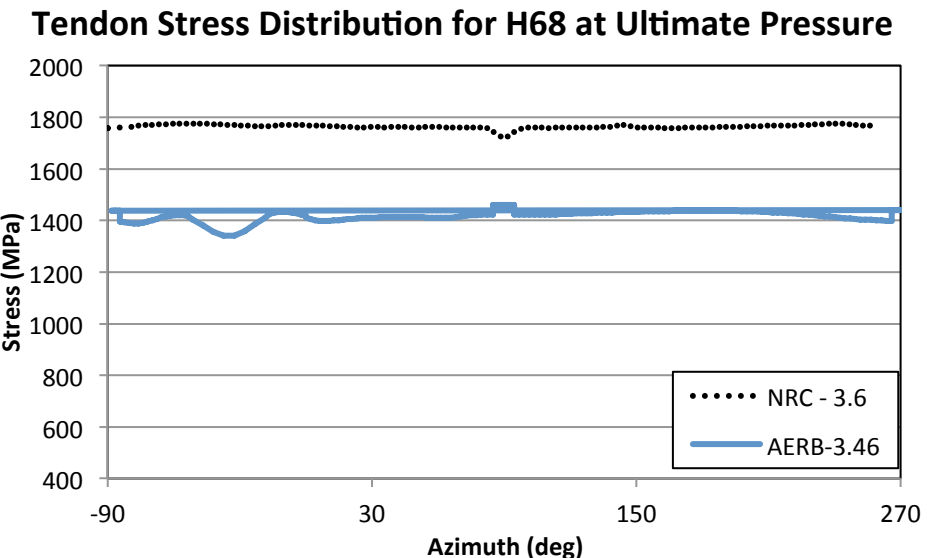


Figure 74: Tendon Stress Distribution for Tendon #H68 at Ultimate Pressure

3.3.2 Vertical Tendons

The vertical tendons selected for analysis correspond with tendons #V37, V46 from the PCCV test, and as stated earlier, this selection facilitates comparison with the most instrumented tendons from the test. There is less agreement between the participants for the vertical tendons when compared with the hoop tendons in the previous section. The source of this deviation is not immediately known. The tendon stress versus location plots for the vertical tendons can be found in Figure 75 through Figure 92.

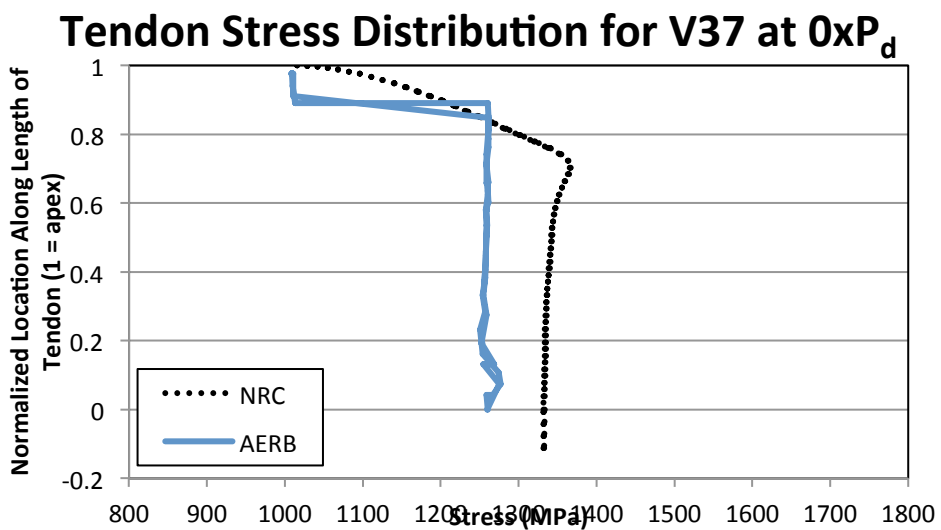


Figure 75: Tendon Stress Distribution for Tendon #V37 at $0 \times P_d$

Tendon Stress Distribution for V37 at $1.0 \times P_d$

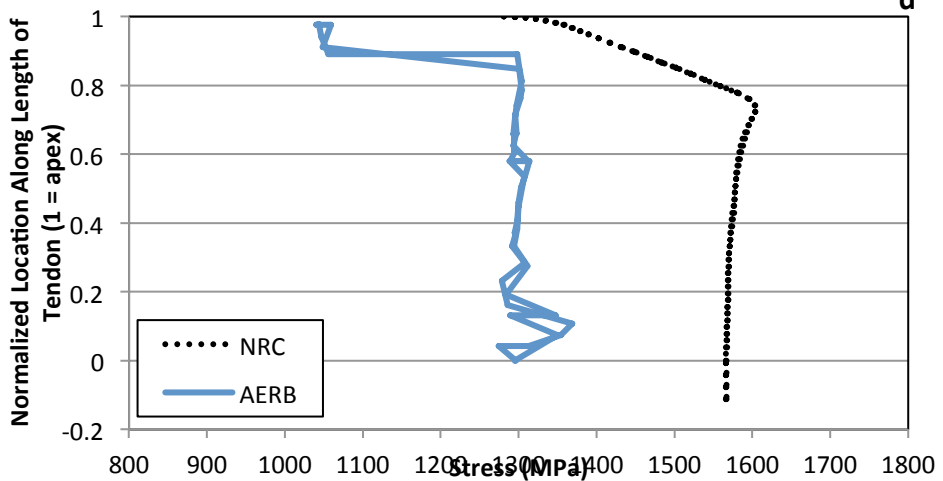


Figure 76: Tendon Stress Distribution for Tendon #V37 at $1.0 \times P_d$

Tendon Stress Distribution for V37 at $1.5 \times P_d$

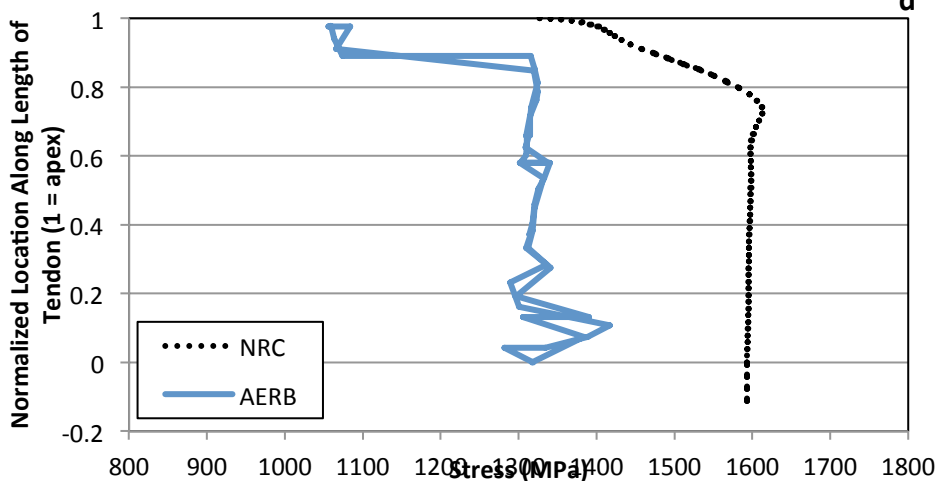


Figure 77: Tendon Stress Distribution for Tendon #V37 at $1.5 \times P_d$

Tendon Stress Distribution for V37 at $2.0 \times P_d$

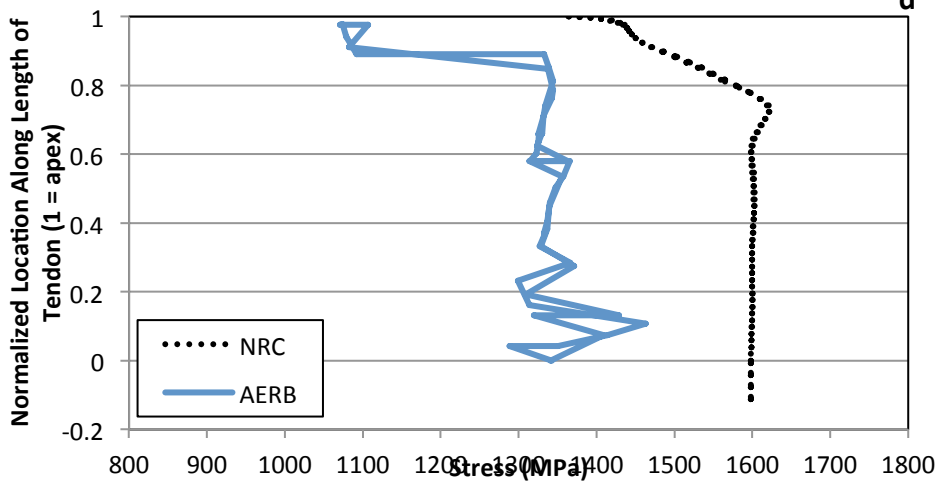


Figure 78: Tendon Stress Distribution for Tendon #V37 at $2.0 \times P_d$

Tendon Stress Distribution for V37 at $2.5 \times P_d$

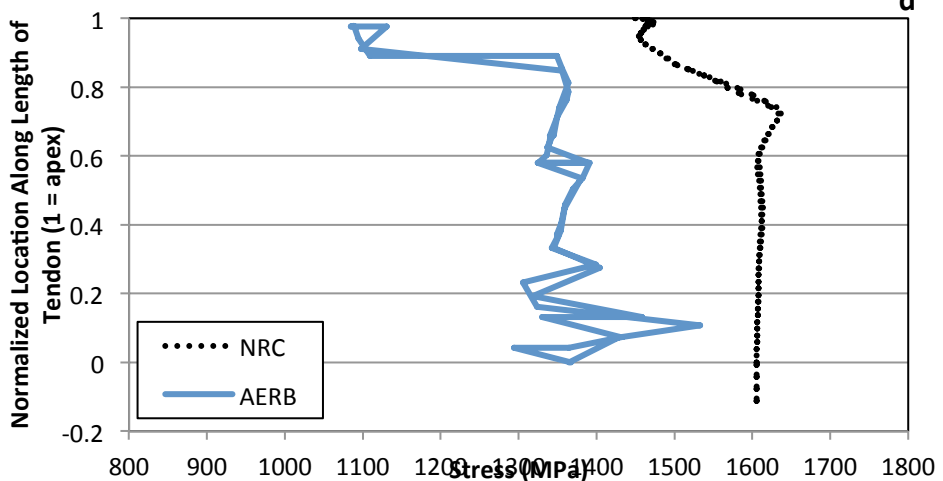


Figure 79: Tendon Stress Distribution for Tendon #V37 at $2.5 \times P_d$

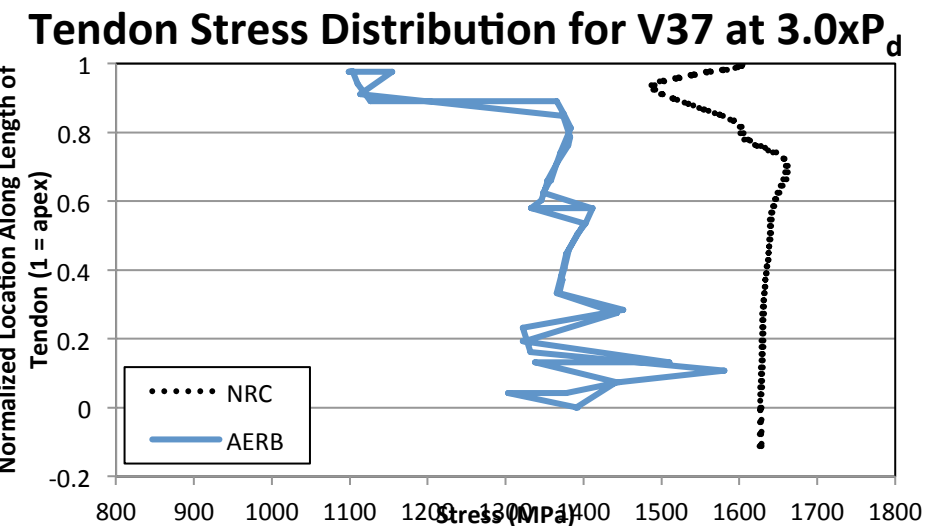


Figure 80: Tendon Stress Distribution for Tendon #V37 at $3.0 \times P_d$

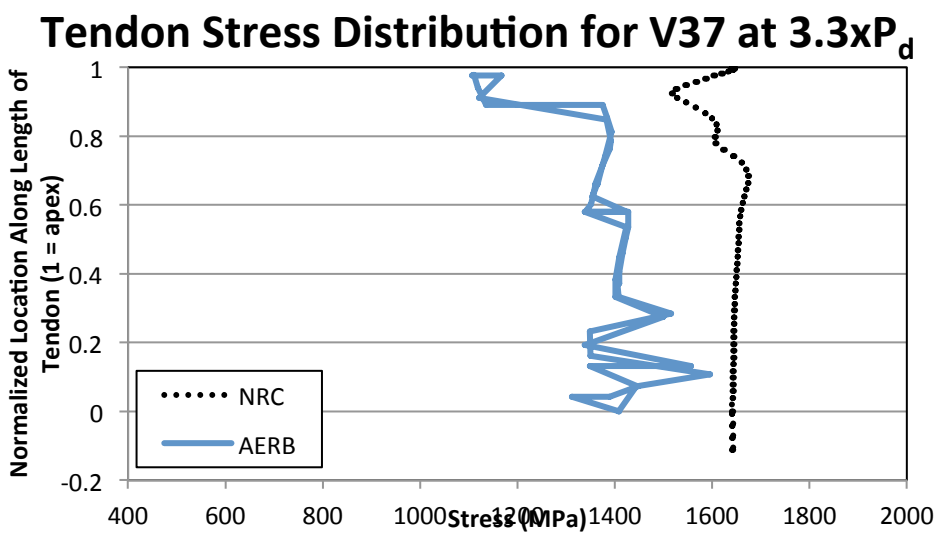


Figure 81: Tendon Stress Distribution for Tendon #V37 at $3.3 \times P_d$

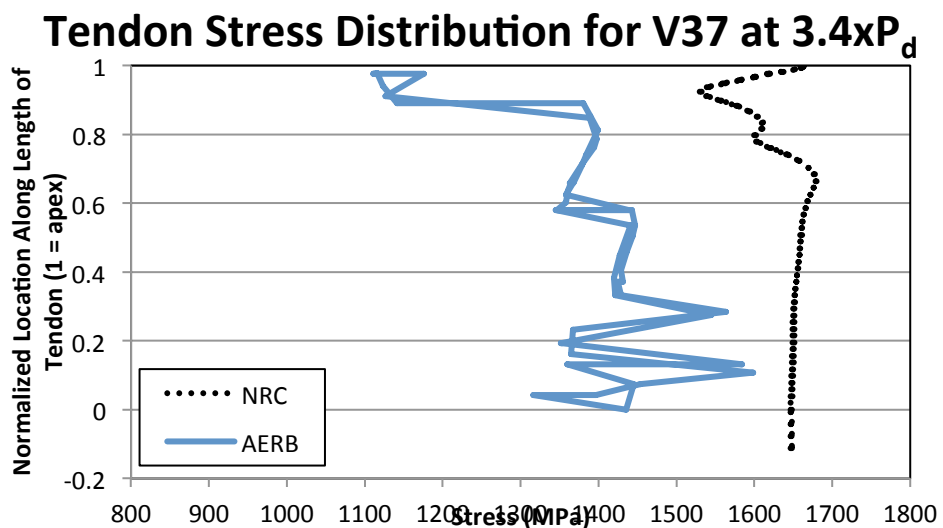


Figure 82: Tendon Stress Distribution for Tendon #V37 at $3.4 \times P_d$

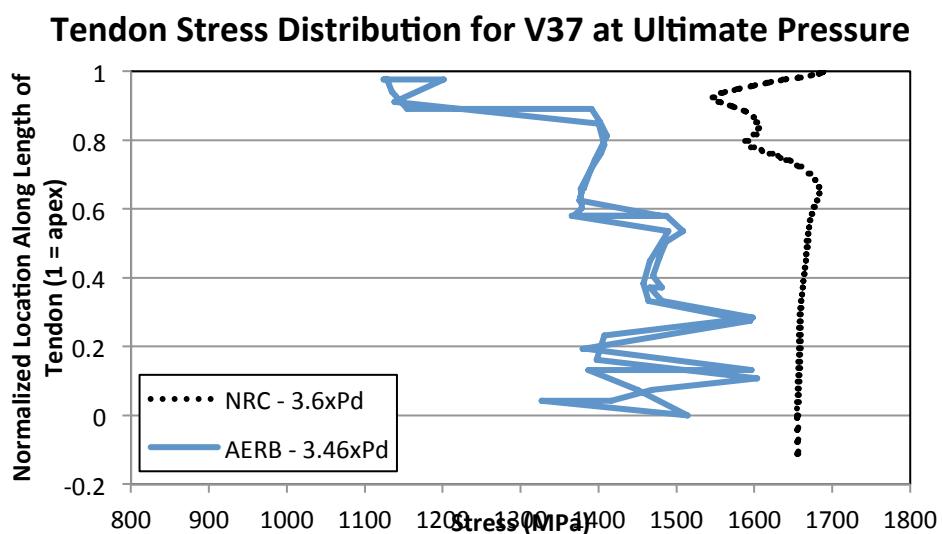


Figure 83: Tendon Stress Distribution for Tendon #V37 at Ultimate Pressure

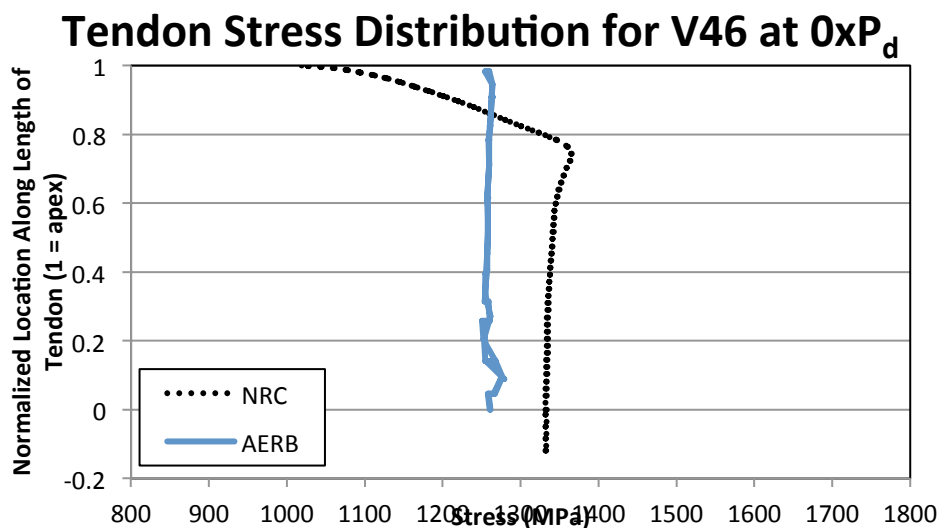


Figure 84: Tendon Stress Distribution for Tendon #V46 at 0 x P_d

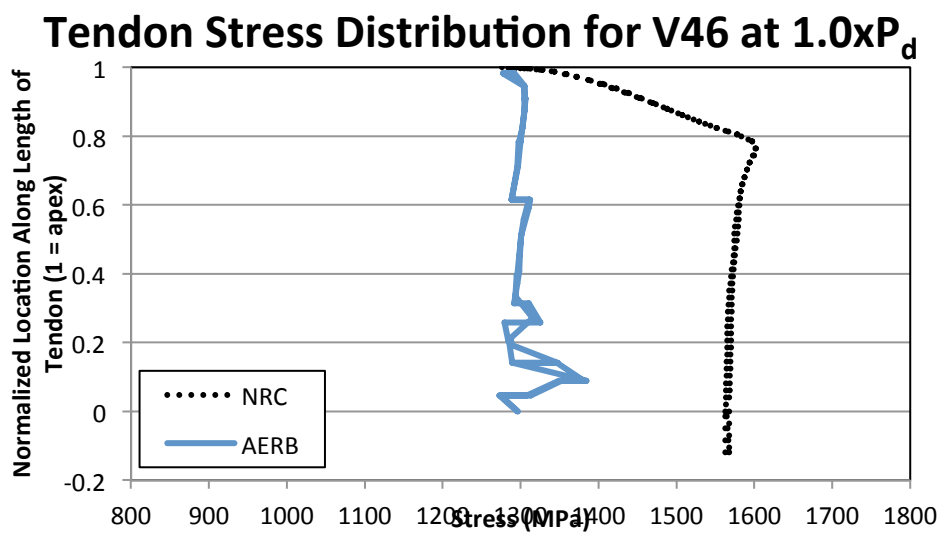


Figure 85: Tendon Stress Distribution for Tendon #V46 at 1.0 x P_d

Tendon Stress Distribution for V46 at $1.5 \times P_d$

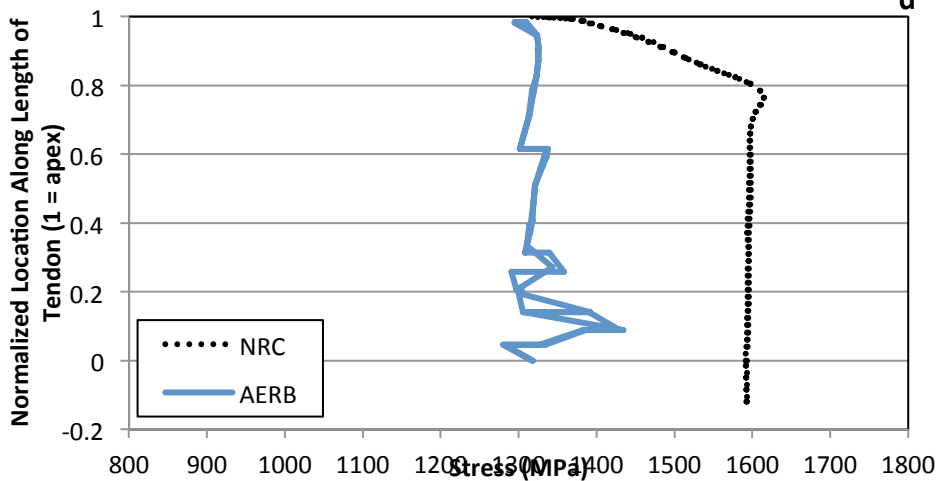


Figure 86: Tendon Stress Distribution for Tendon #V46 at $1.5 \times P_d$

Tendon Stress Distribution for V46 at $2.0 \times P_d$

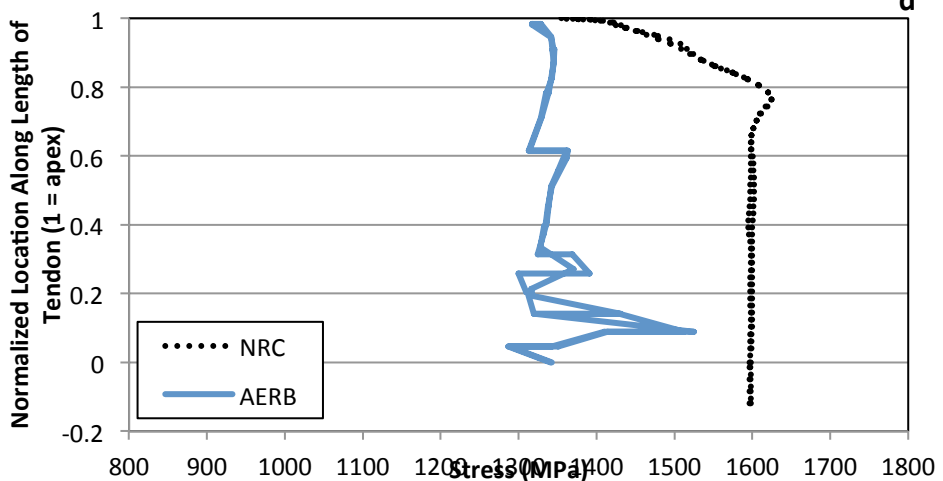


Figure 87: Tendon Stress Distribution for Tendon #V46 at $2.0 \times P_d$

Tendon Stress Distribution for V46 at $2.5 \times P_d$

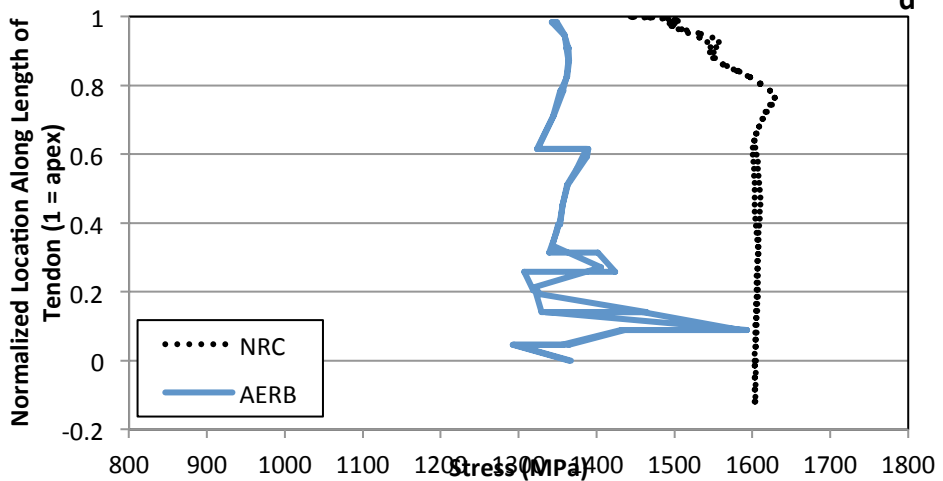


Figure 88: Tendon Stress Distribution for Tendon #V46 at $2.5 \times P_d$

Tendon Stress Distribution for V46 at $3.0 \times P_d$

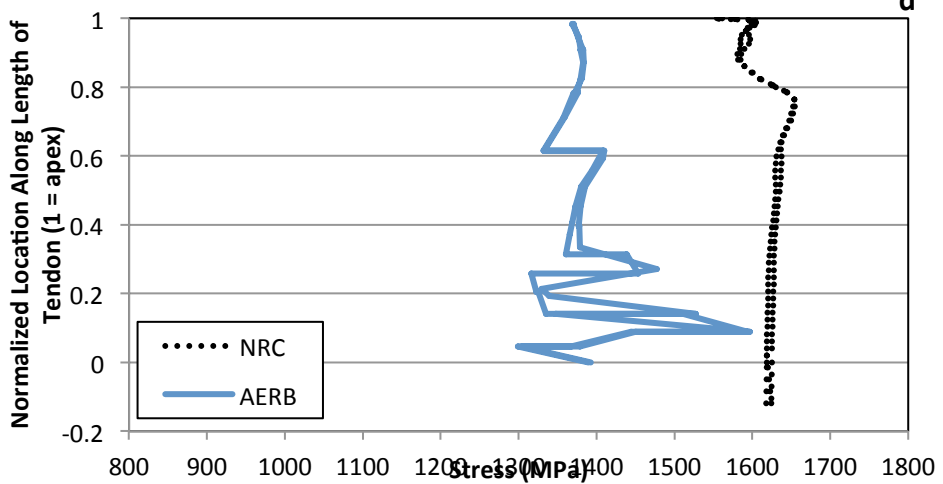


Figure 89: Tendon Stress Distribution for Tendon #V46 at $3.0 \times P_d$

Tendon Stress Distribution for V46 at $3.3 \times P_d$

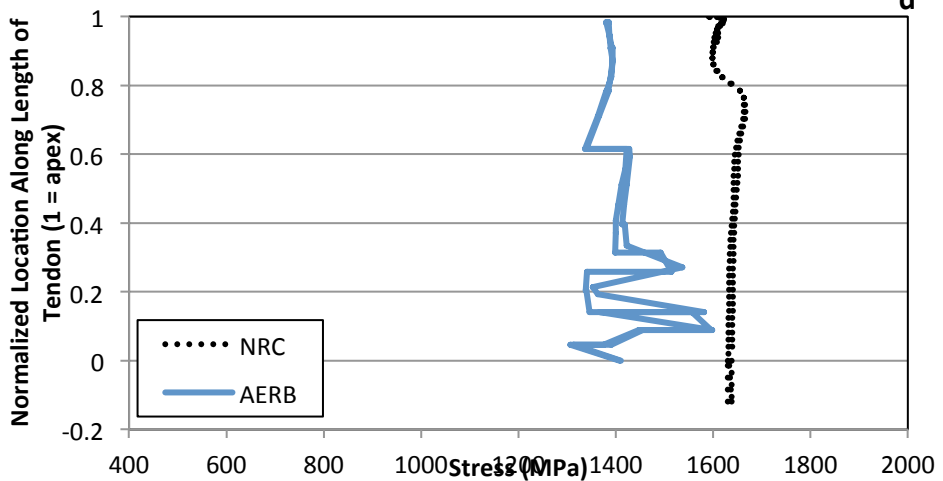


Figure 90: Tendon Stress Distribution for Tendon #V46 at $3.3 \times P_d$

Tendon Stress Distribution for V46 at $3.4 \times P_d$

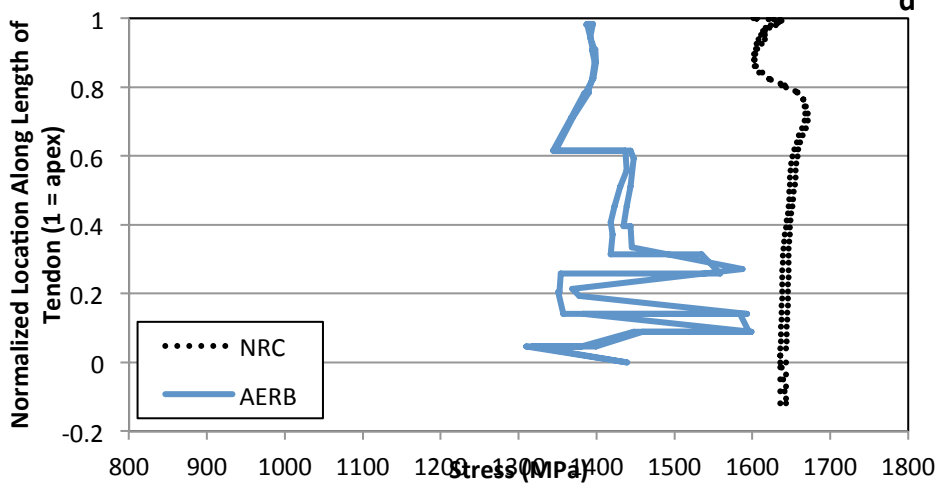


Figure 91: Tendon Stress Distribution for Tendon #V46 at $3.4 \times P_d$

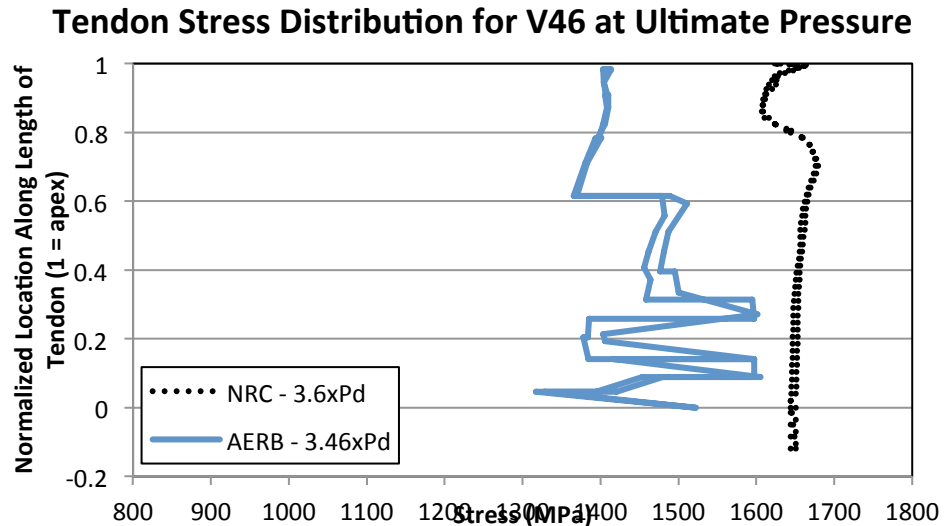


Figure 92: Tendon Stress Distribution for Tendon #V46 at Ultimate Pressure

3.4 Standard Output Location Comparisons

This section of the report compares the modeled results from the participants with the standard output locations (SOLs) from the PCCV test. This section serves to provide the most direct comparison to the experimental results and is therefore considered very valuable for evaluating the modeling of the participants.

3.4.1 Displacements

The first 15 SOLs involve displacement measurements both in the radial and meridional directions. The nature of the displacement is indicated in the figure caption for each figure in this section, namely Figure 93 through Figure 107. As before, the participants' data agree well in some locations and less so in others. In several of the displacement figures, the NRC supplied data shows a bi-linear trend where there is an initial response that terminates at approximately 0.4 MPa, or approximately 12 minutes of accident progression. It is believed that this initial response is caused by thermal effects as the containment warms approximately 50°C. Later in the accident, the rise in pressure dominates the thermal response.

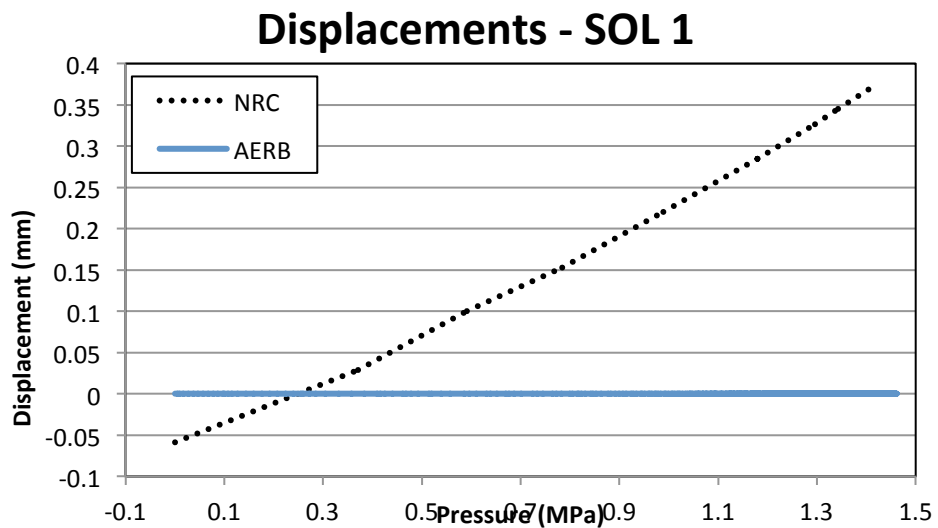


Figure 93: Displacement Versus Pressure at SOL #1 (Vertical Displacement at Top of Basemat)

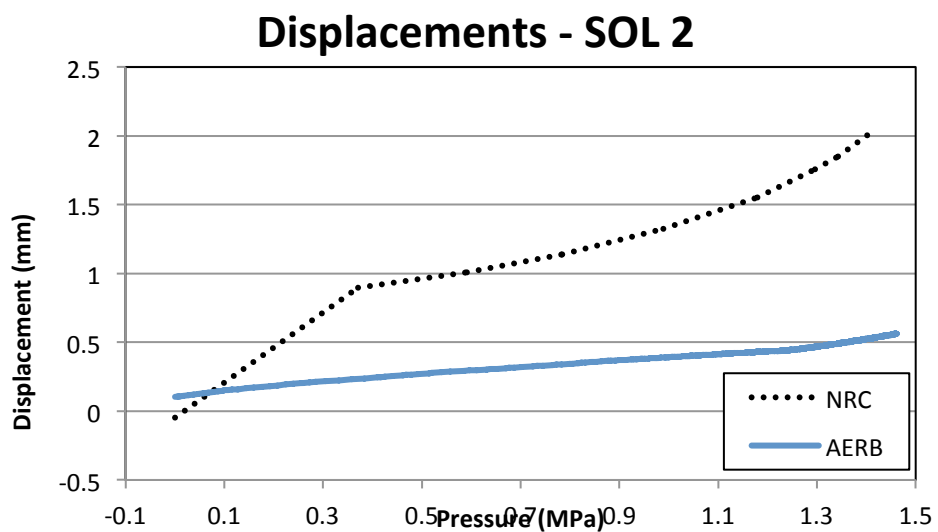


Figure 94: Displacement Versus Pressure at SOL #2 (Radial Displacement at Base of Cylinder)

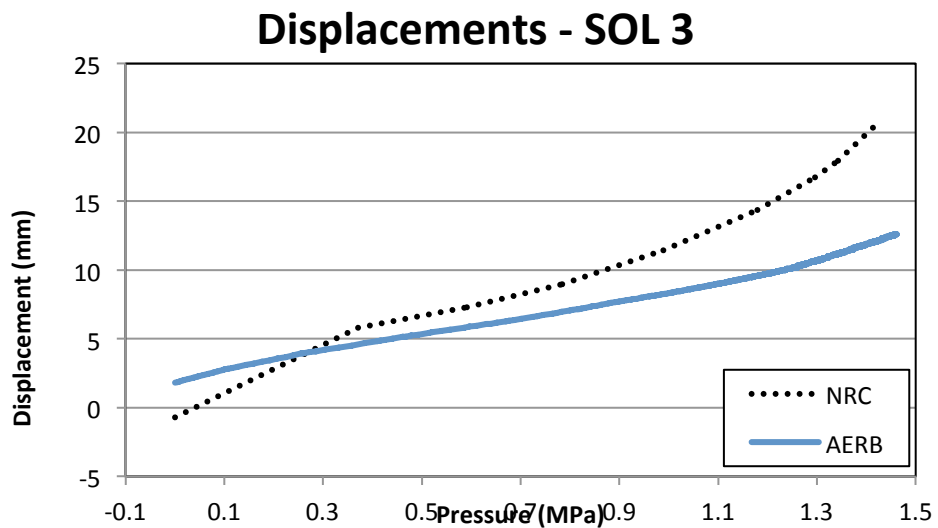


Figure 95: Displacement Versus Pressure at SOL #3 (Radial Displacement at Base of Cylinder)

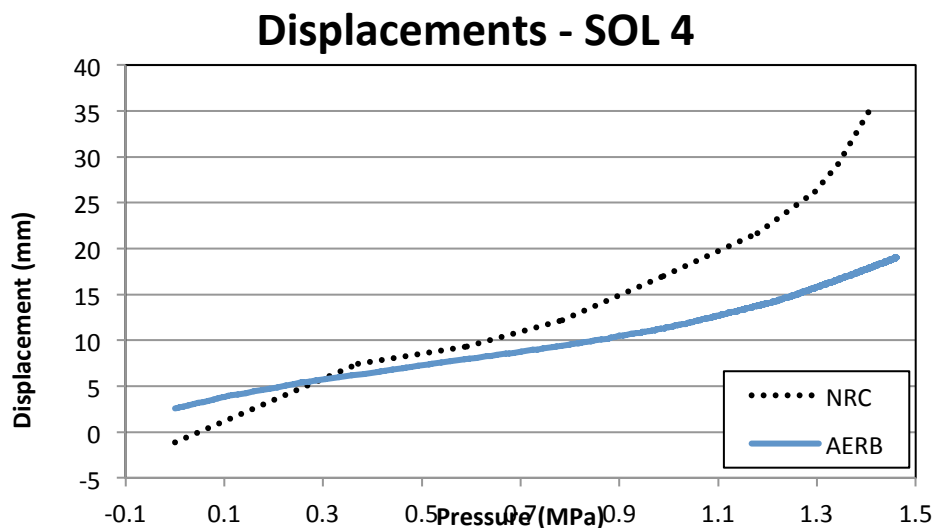


Figure 96: Displacement Versus Pressure at SOL #4 (Radial Displacement at Base of Cylinder)

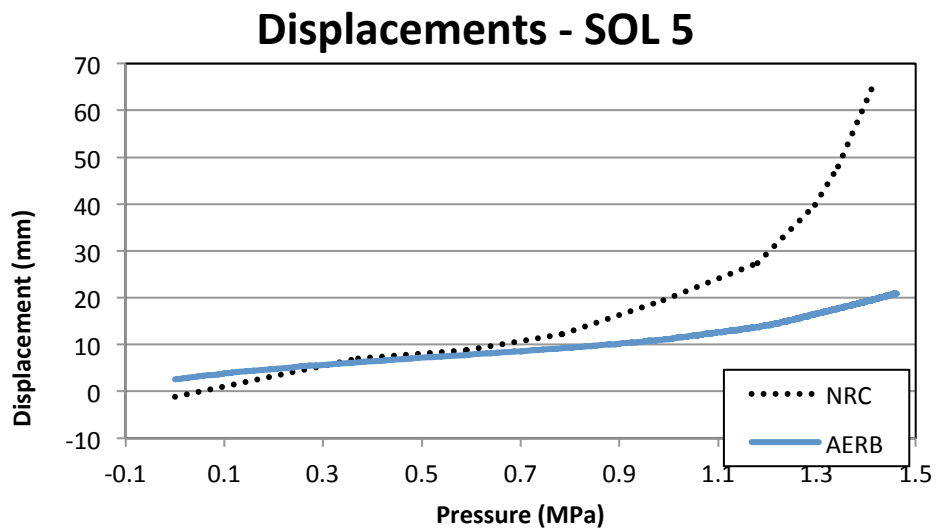


Figure 97: Displacement Versus Pressure at SOL #5 (Radial Displacement at E/H Elevation)

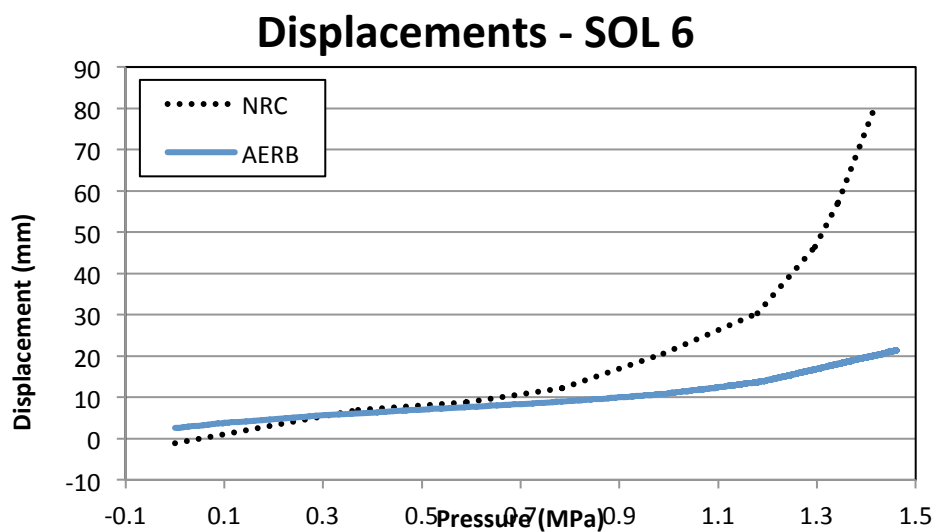


Figure 98: Displacement Versus Pressure at SOL #6 (Radial Displacement at Midheight)

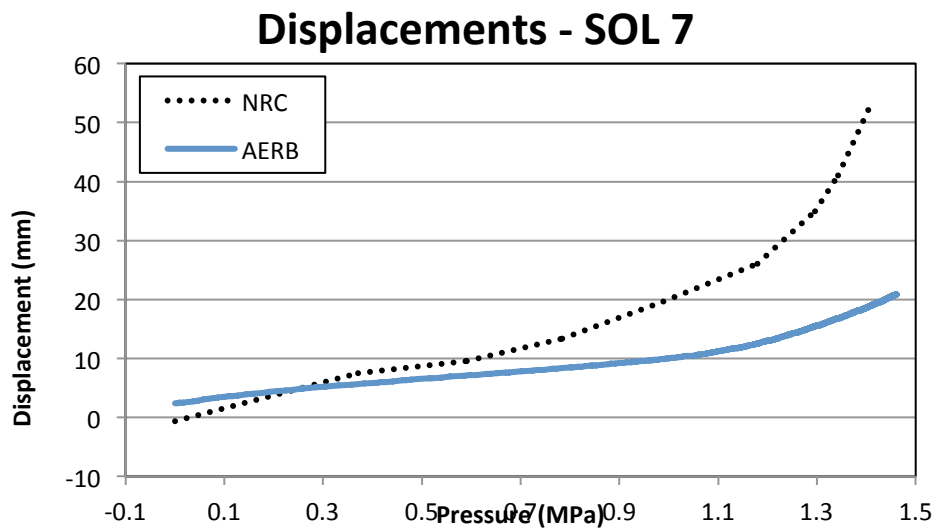


Figure 99: Displacement Versus Pressure at SOL #7 (Radial Displacement at Springline)

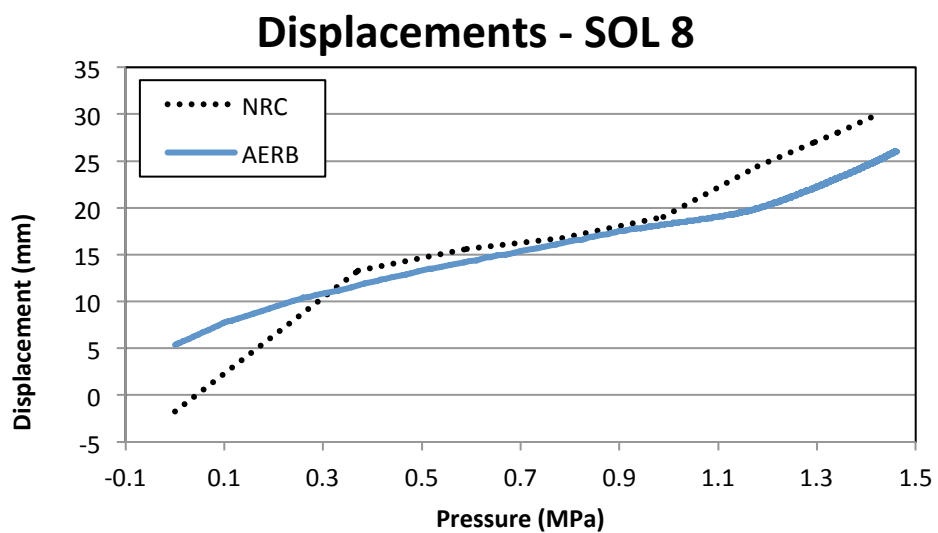


Figure 100: Displacement Versus Pressure at SOL #8 (Vertical Displacement at Springline)

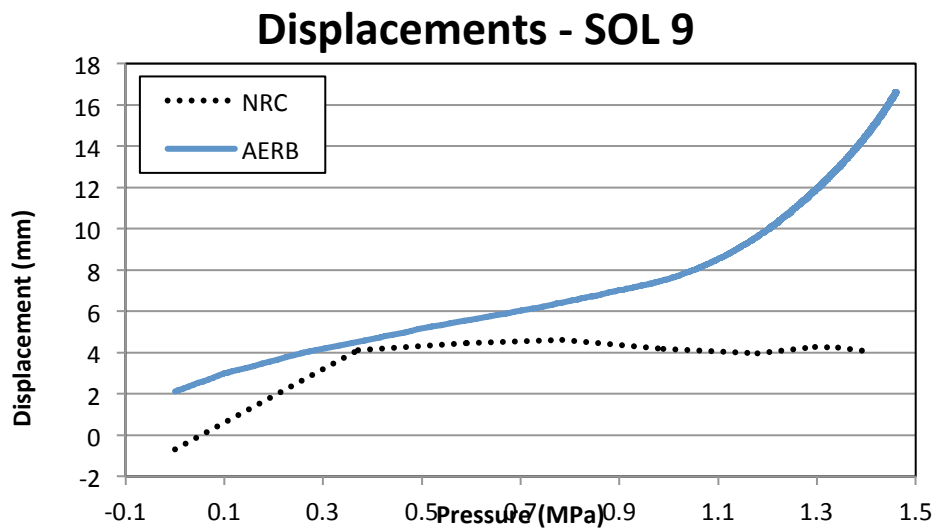


Figure 101: Displacement Versus Pressure at SOL #9 (Radial Displacement at Dome 45°)

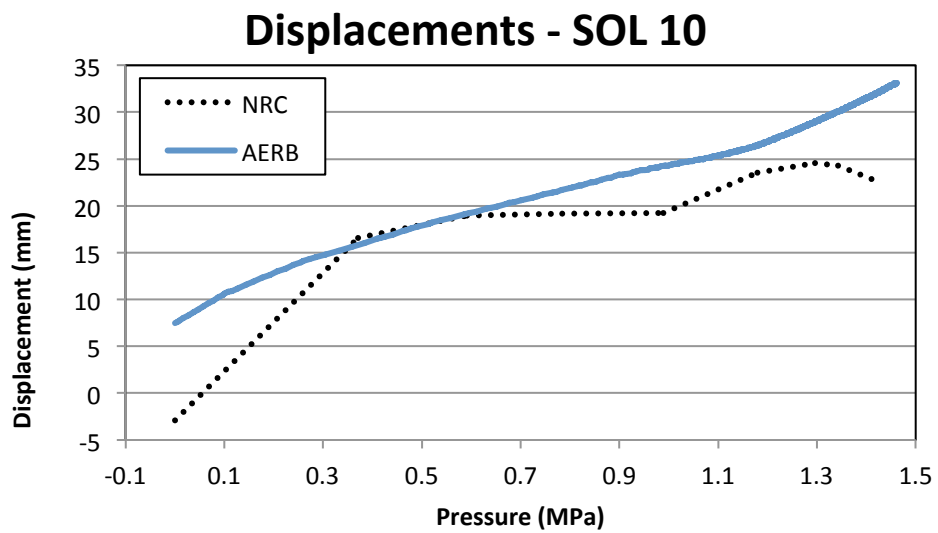


Figure 102: Displacement Versus Pressure at SOL #10 (Vertical Displacement at Dome 45°)

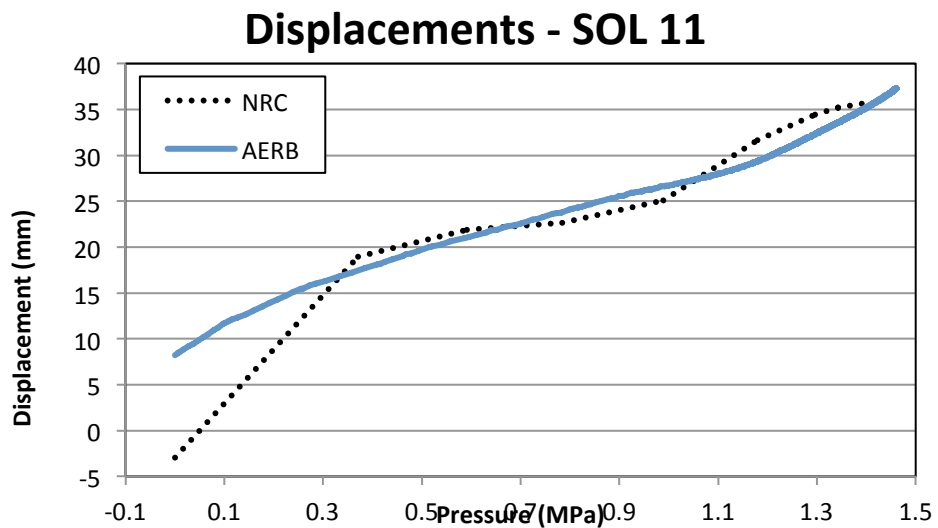


Figure 103: Displacement Versus Pressure at SOL #11 (Vertical Displacement at Dome Apex)

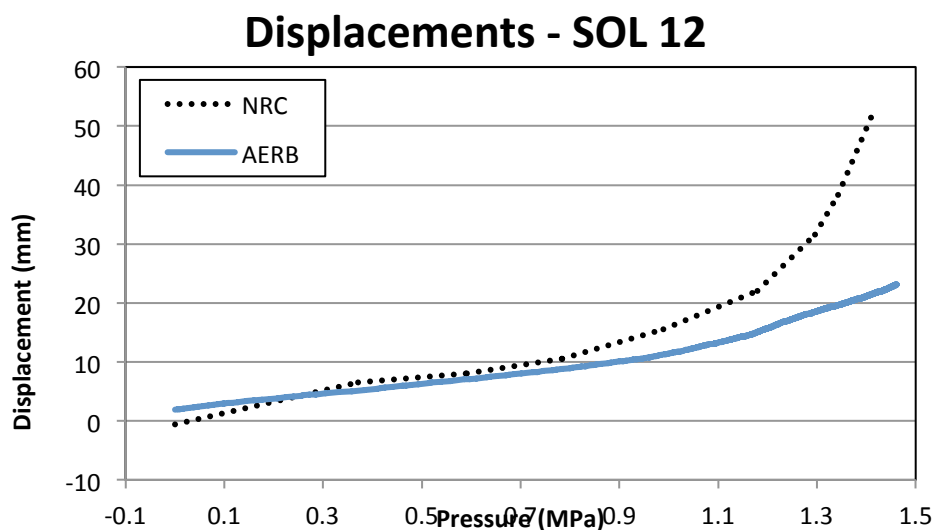


Figure 104: Displacement Versus Pressure at SOL #12 (Radial Displacement at Midheight of Buttress)

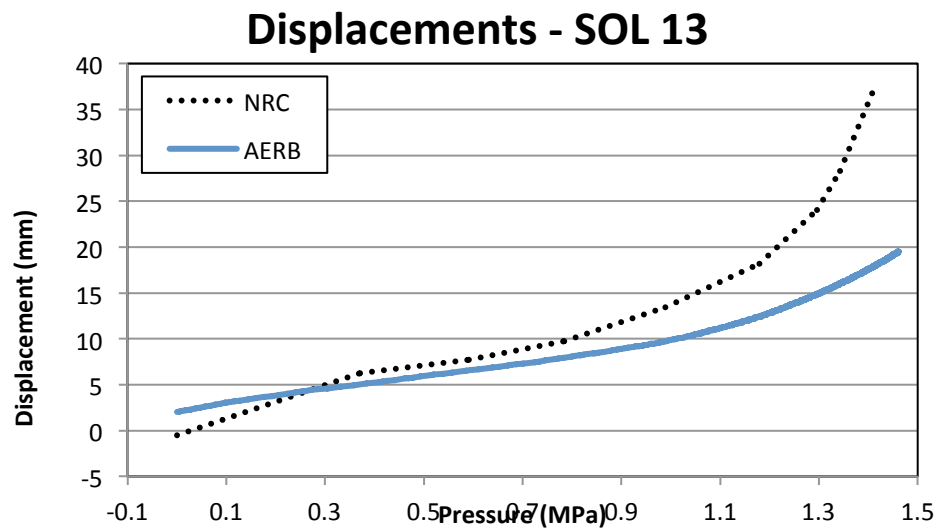


Figure 105: Displacement Versus Pressure at SOL #13 (Radial Displacement at Springline of Buttress)

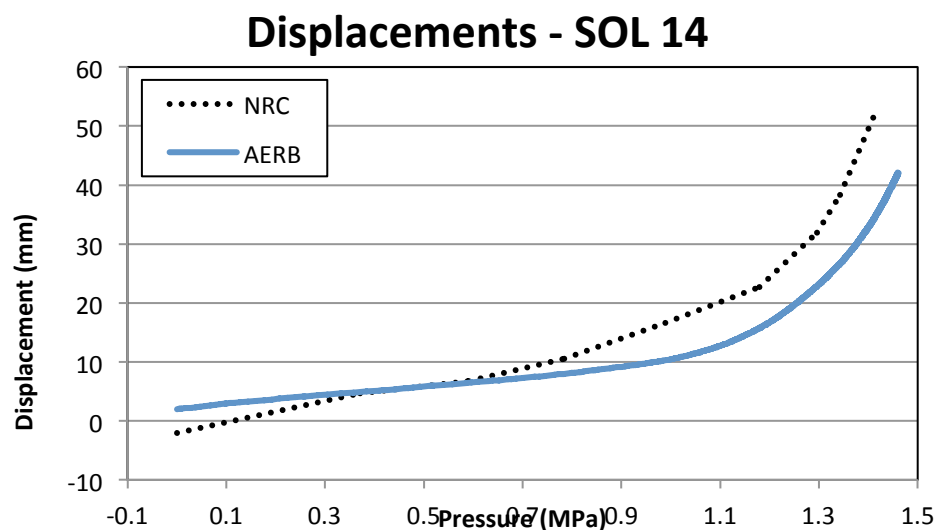


Figure 106: Displacement Versus Pressure at SOL #14 (Radial Displacement at Center of E/H)

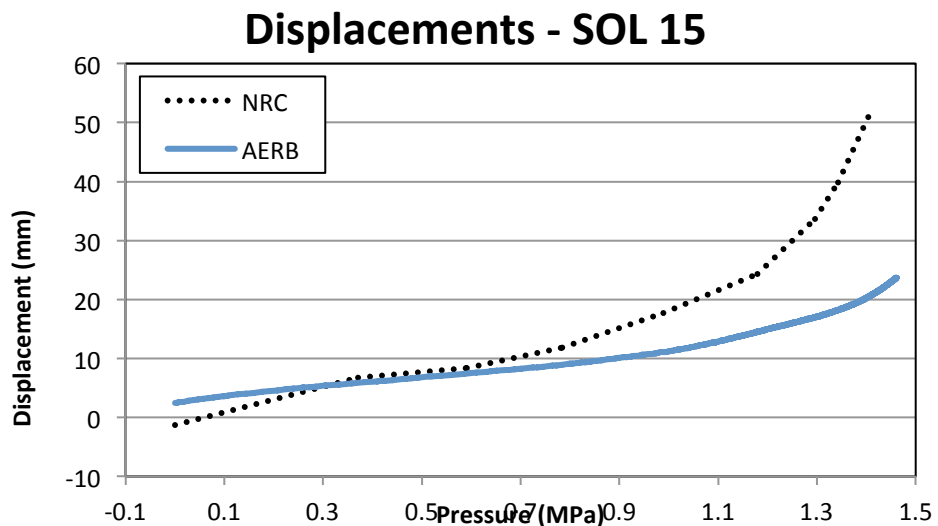


Figure 107: Displacement Versus Pressure at SOL #15 (Radial Displacement at Center of A/L)

3.4.2 Rebar Strains

The participants were asked to report results for rebar strains at locations SOL 22-29. The rebar SOL comparison plots can be found in Figure 108 through Figure 115.

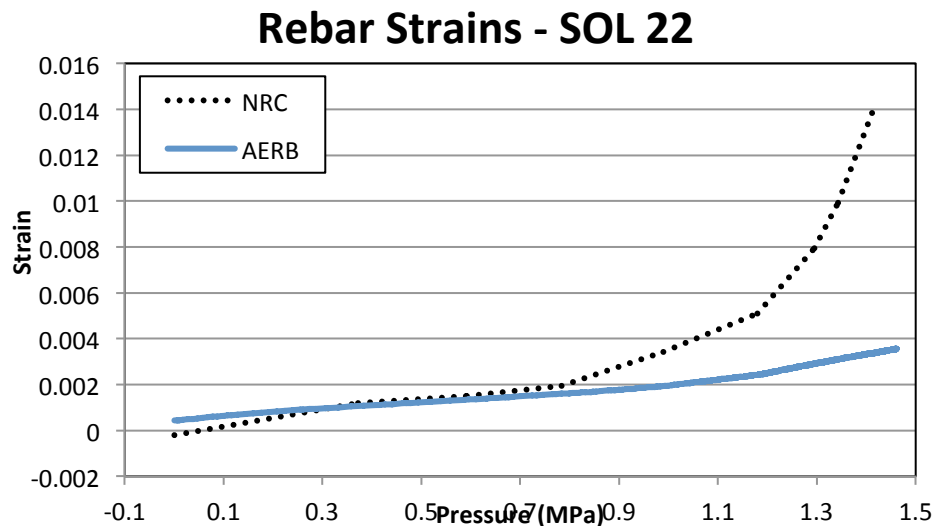


Figure 108: Rebar Strain Versus Pressure at SOL #22 (Hoop Strain of Outer Rebar at Midheight and Azimuth 135)

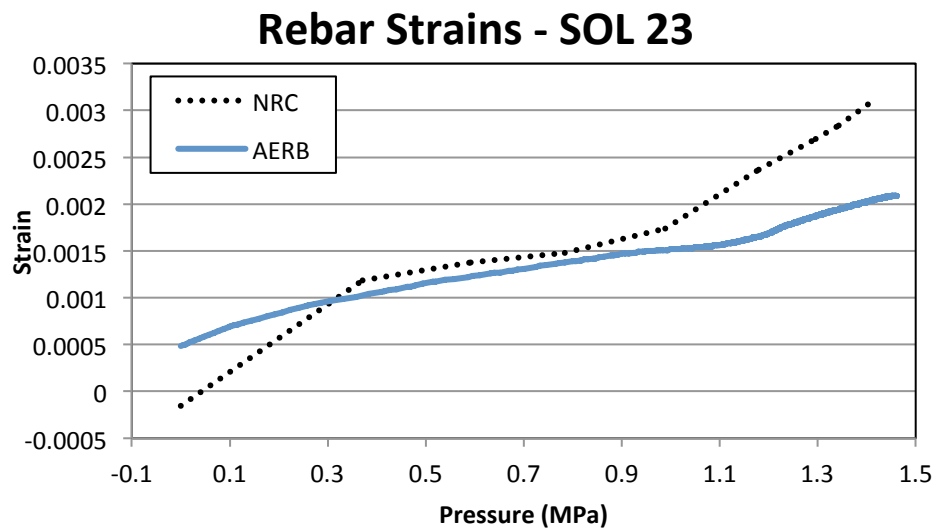


Figure 109: Rebar Strain Versus Pressure at SOL #23 (Meridional Strain of Outer Rebar at Midheight and Azimuth 135)

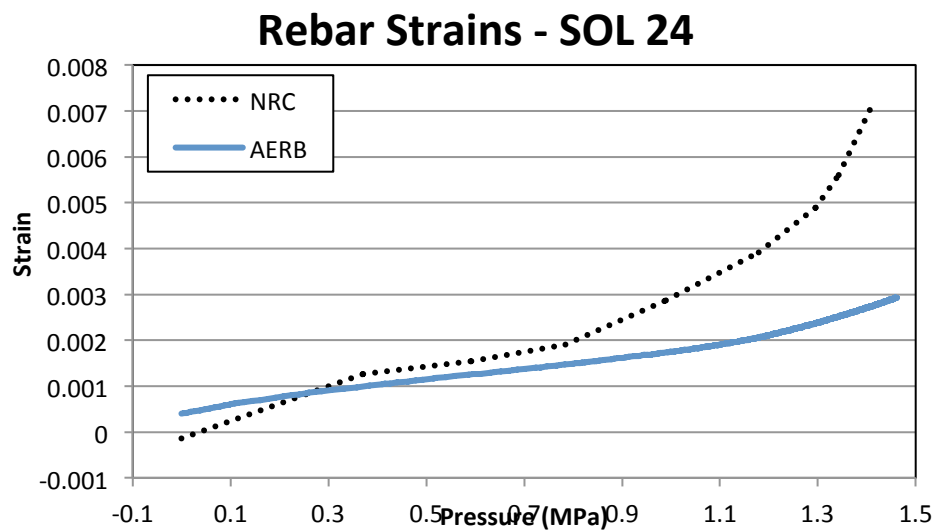


Figure 110: Rebar Strain Versus Pressure at SOL #24 (Hoop Strain of Outer Rebar at Springline)

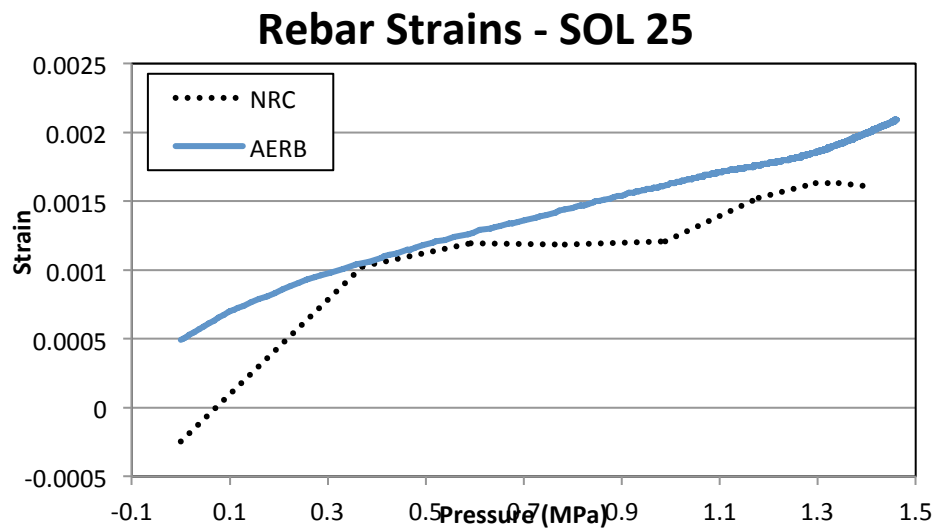


Figure 111: Rebar Strain Versus Pressure at SOL #25 (Meridional Strain of Inner Rebar at Springline)

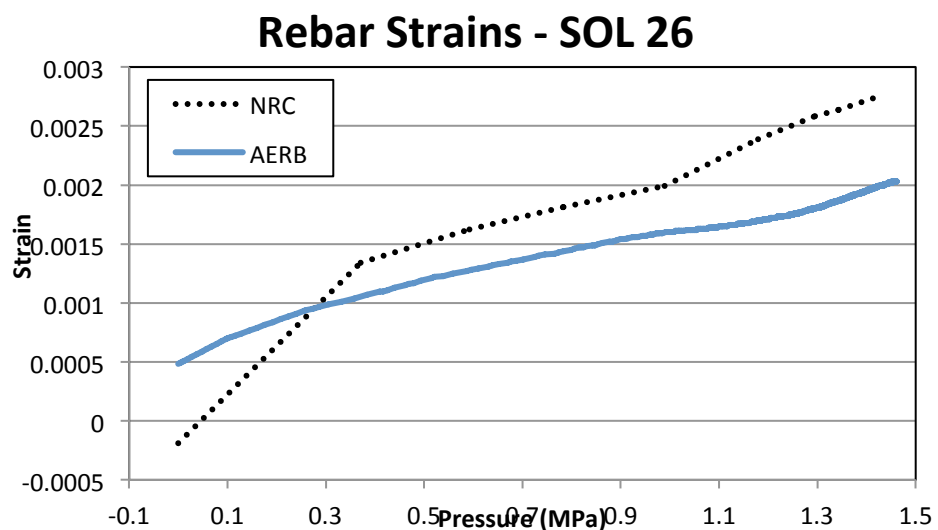


Figure 112: Rebar Strain Versus Pressure at SOL #26 (Meridional Strain of Outer Rebar at Springline)

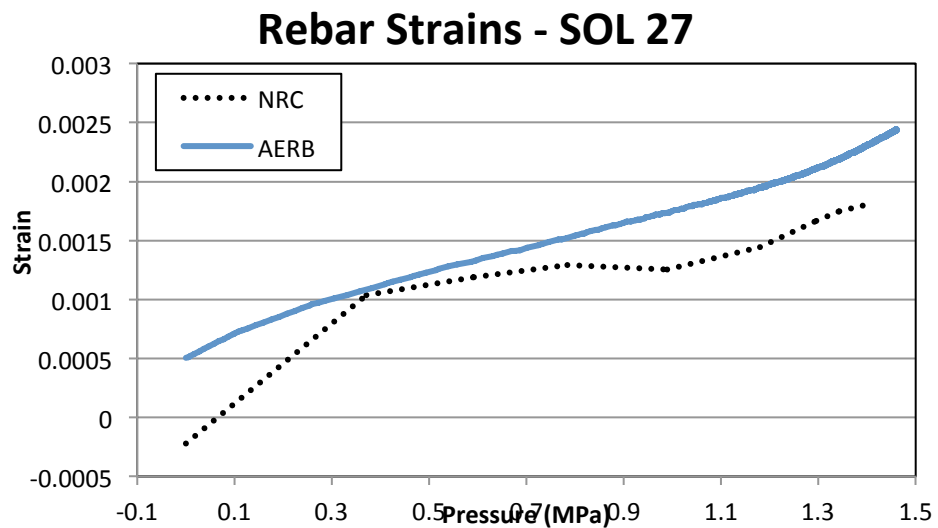


Figure 113: Rebar Strain Versus Pressure at SOL #27 (Hoop Strain of Outer Rebar at Dome 45°)

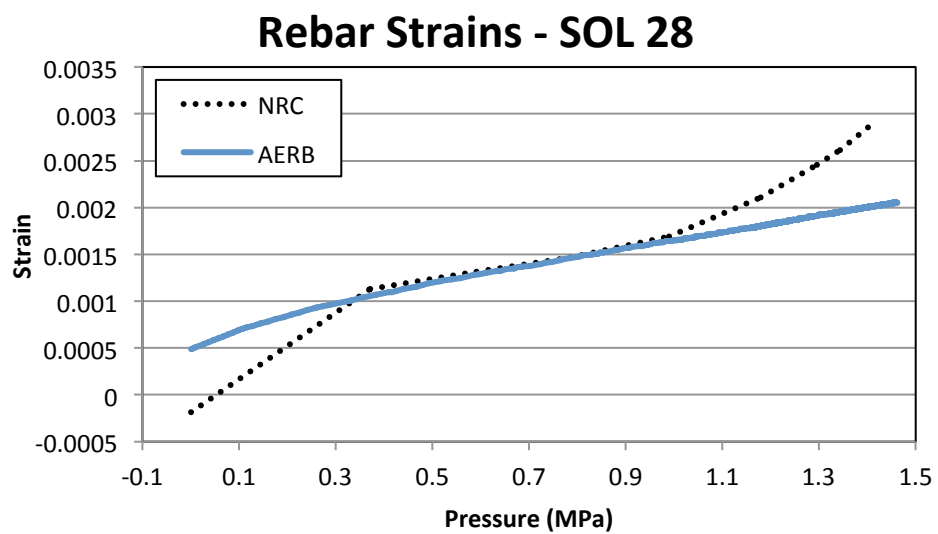


Figure 114: Rebar Strain Versus Pressure at SOL #28 (Meridional Strain of Inner Rebar at Dome 45°)

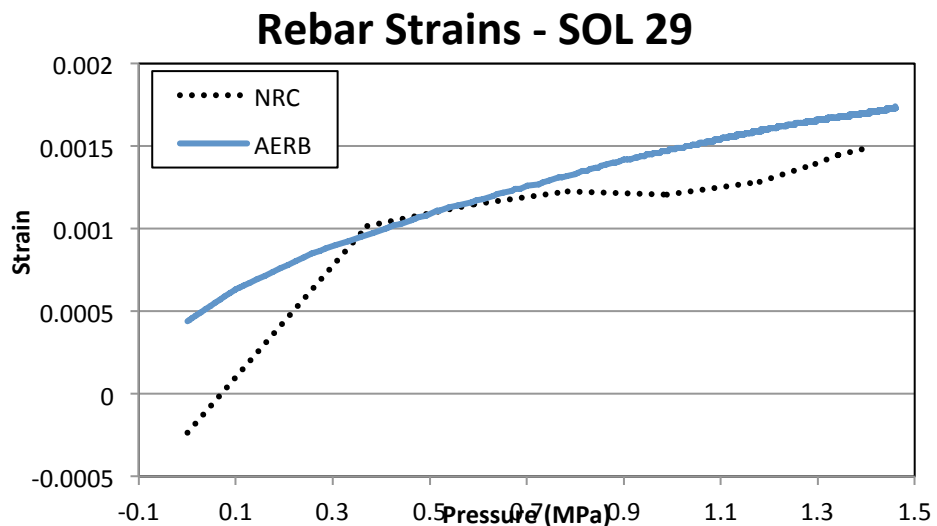


Figure 115: Rebar Strain Versus Pressure at SOL #29 (Meridional Strain of Outer Rebar at Dome 45°)

3.4.3 *Liner Strains*

The participants were asked to report liner strains at locations SOL 36-42. The comparison plots for the liner strain data and for the modeled results are presented in Figure 116 through Figure 122.

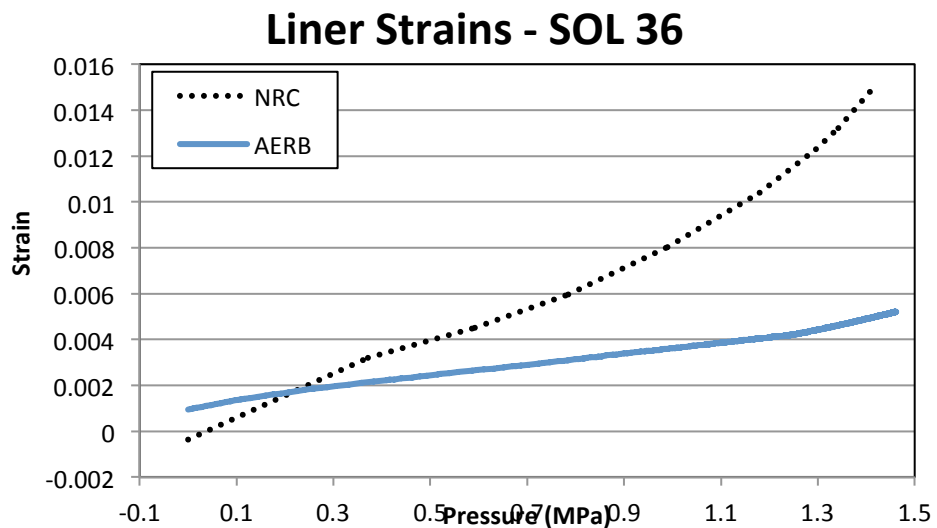


Figure 116: Liner Strain Versus Pressure at SOL #36 (Meridional Strain of Inside of Liner at Base of Cylinder)

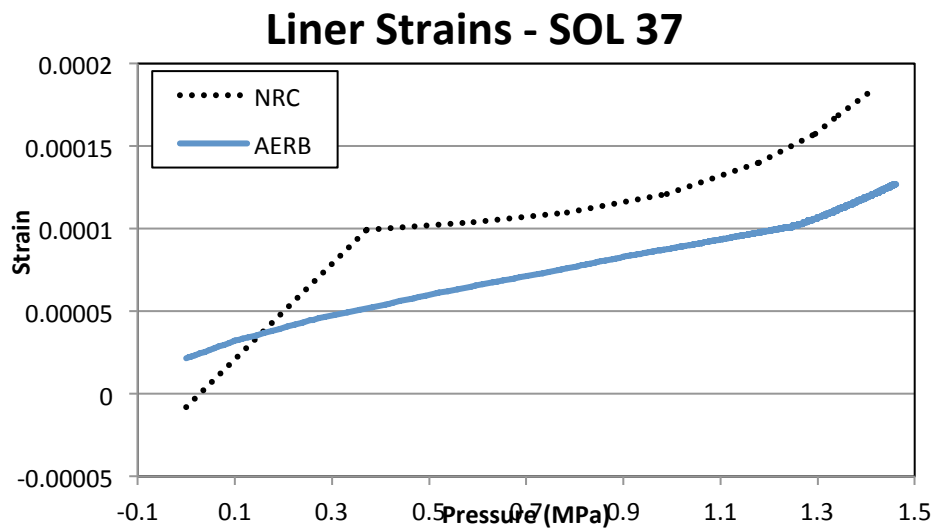


Figure 117: Liner Strain Versus Pressure at SOL #37 (Hoop Strain of Inside of Liner at Base of Cylinder)

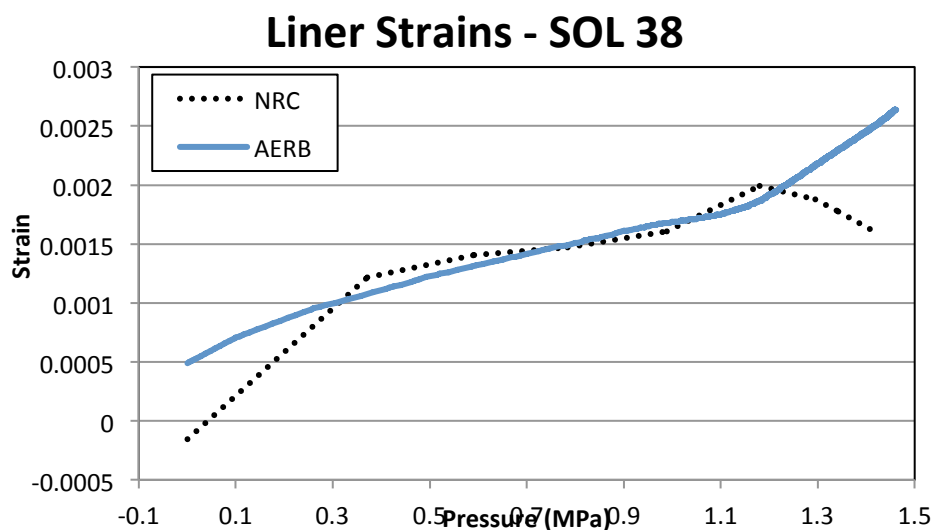


Figure 118: Liner Strain Versus Pressure at SOL #38 (Meridional Strain of Inside of Liner at Midheight)

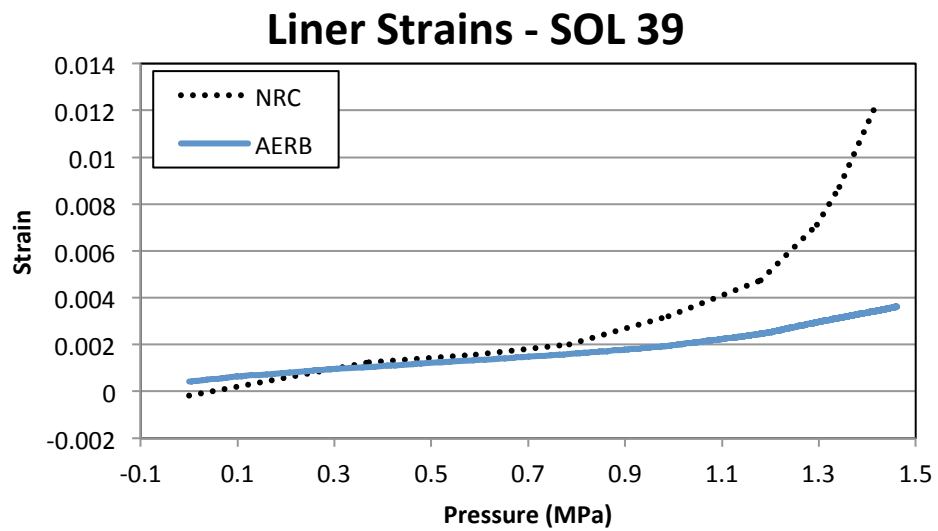


Figure 119: Liner Strain Versus Pressure at SOL #39 (Hoop Strain of Inside of Liner at Midheight)

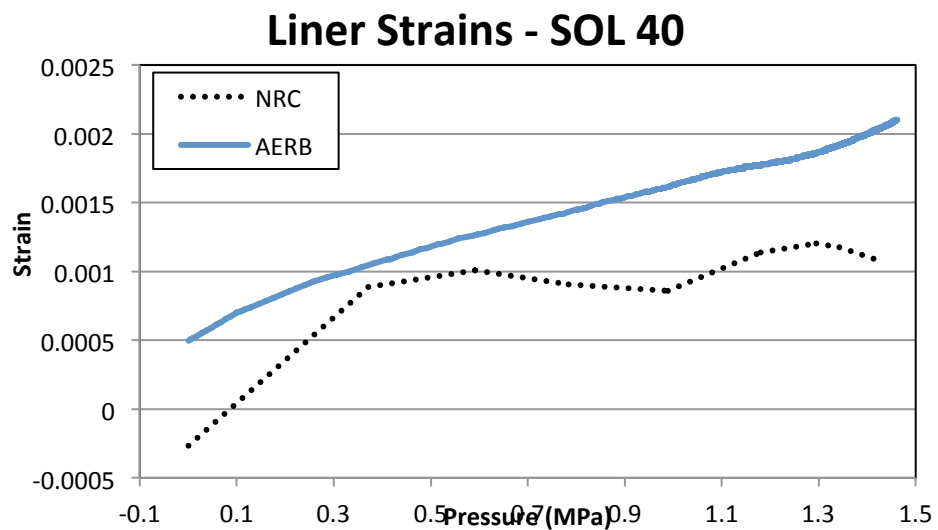


Figure 120: Liner Strain Versus Pressure at SOL #40 (Meridional Strain of Inside of Liner at Springline)

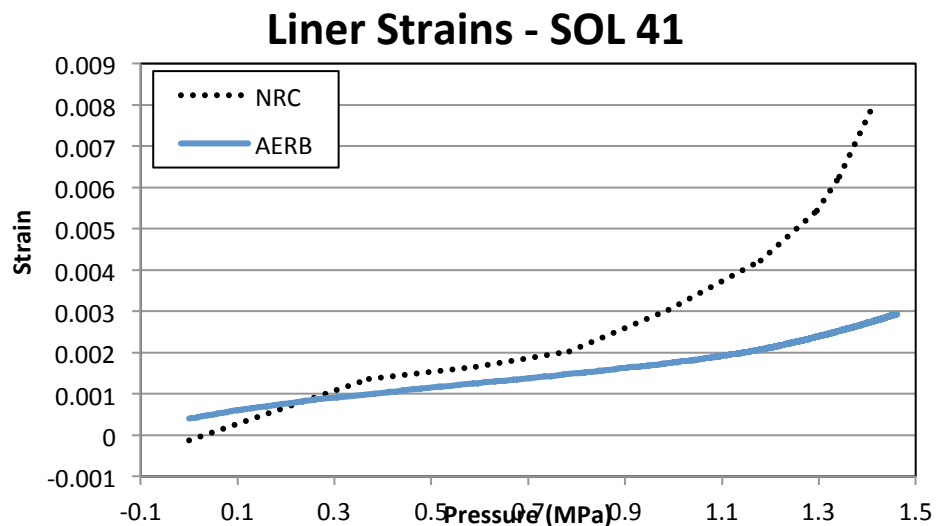


Figure 121: Liner Strain Versus Pressure at SOL #41 (Hoop Strain of Inside of Liner at Springline)

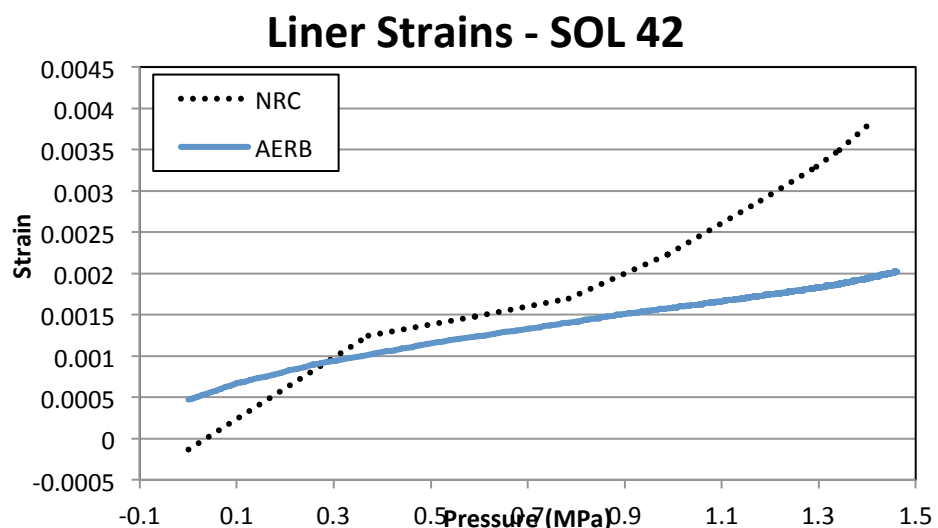


Figure 122: Liner Strain Versus Pressure at SOL #42 (Meridional Strain of Inside of Liner at Dome Apex)

3.4.4 Tendon Strains

Participants were requested to provide results at SOLs 48-53 for the tendon strains. The tendon strain data comparison plots can be found in Figure 123 through Figure 128.

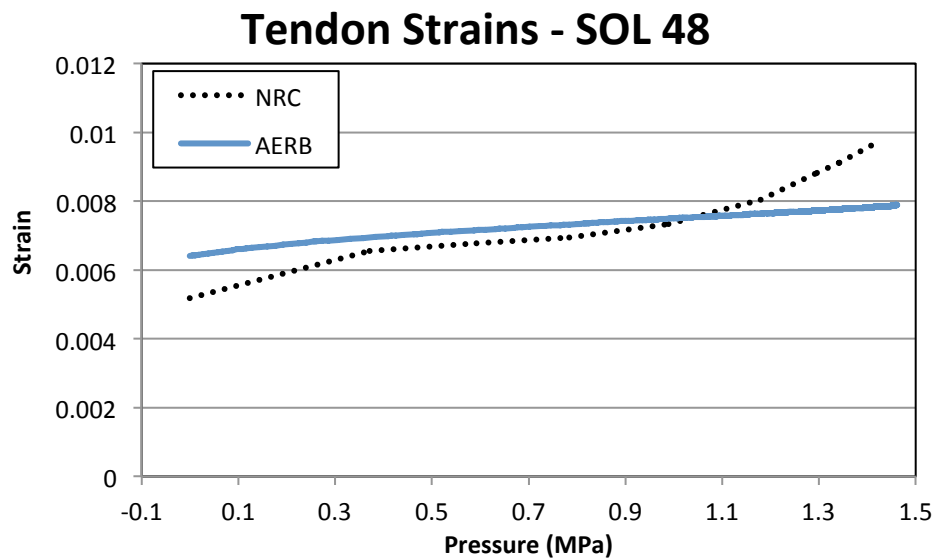


Figure 123: Tendon Strain Versus Pressure at SOL #48 (Hairpin, Tendon V37 at Tendon Apex)

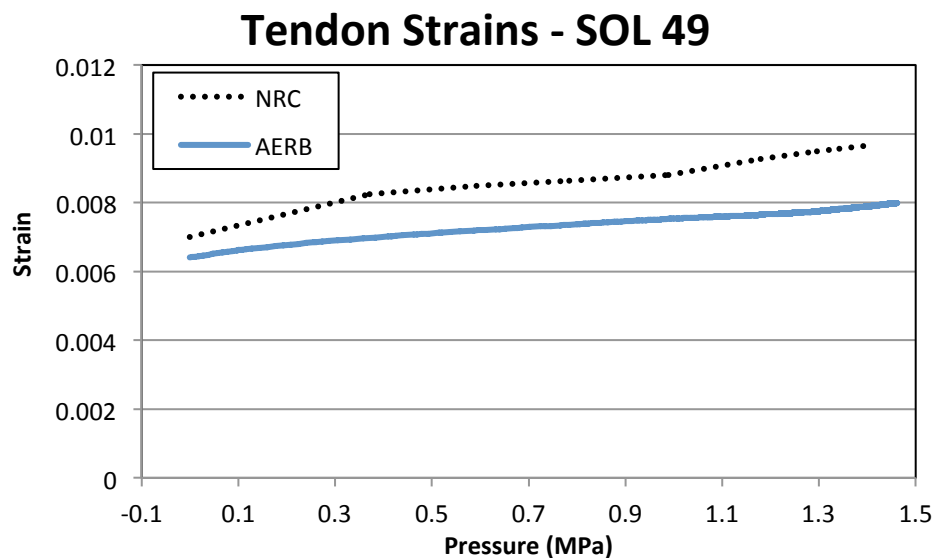


Figure 124: Tendon Strain Versus Pressure at SOL #49 (Hairpin, Tendon V46 at Tendon Springline)

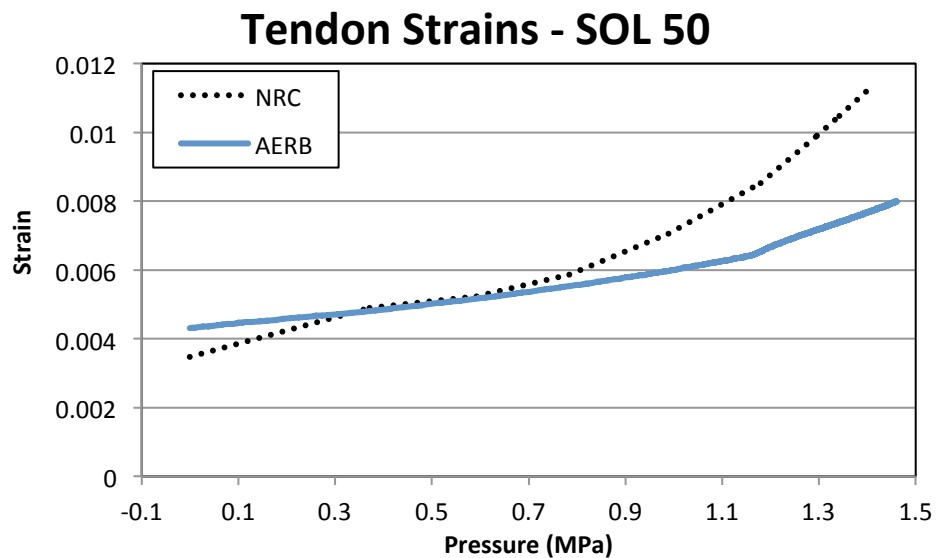


Figure 125: Tendon Strain Versus Pressure at SOL #50 (Hoop, Tendon H53 at Mid-Tendon)

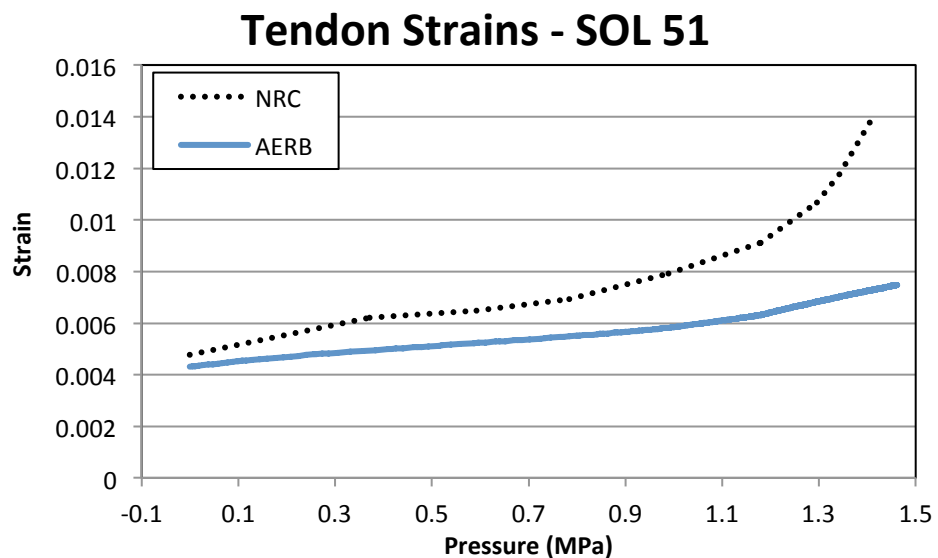


Figure 126: Tendon Strain Versus Pressure at SOL #51 (Hoop, Tendon H53 at $\frac{1}{4}$ Tendon)

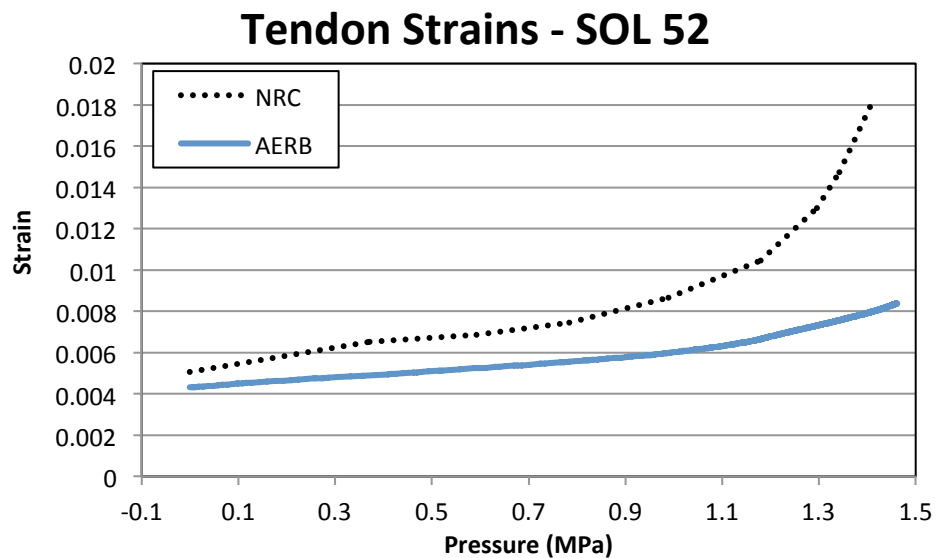


Figure 127: Tendon Strain Versus Pressure at SOL #52 (Hoop, Tendon H53 Near Buttress)

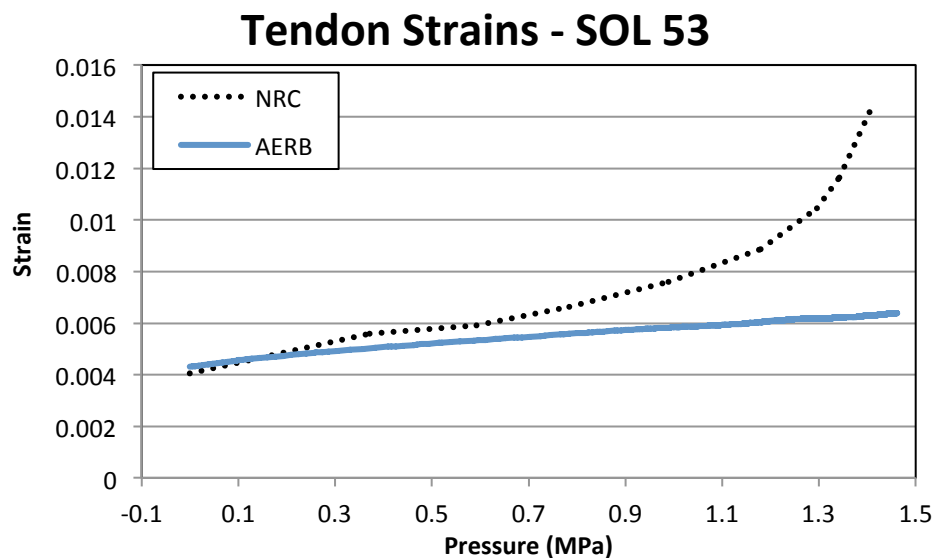


Figure 128: Tendon Strain Versus Pressure at SOL #53 (Hoop, Tendon H35 Between E/H and A/L)

3.4.5 Tendon Forces

The final SOLs measure tendon force and the comparison plots can be found in Figure 129 and Figure 130. None of the other participants provided these results, so we have compared to the NRC Model 3 results from Phase 1.

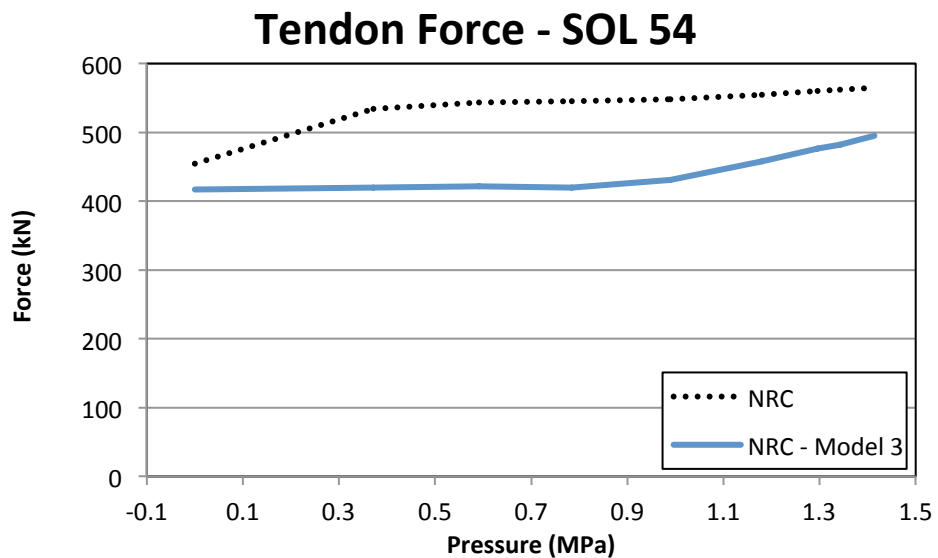


Figure 129: Tendon Force Versus Pressure at SOL #54 (Hairpin, Tendon V37 at Tendon Gallery)

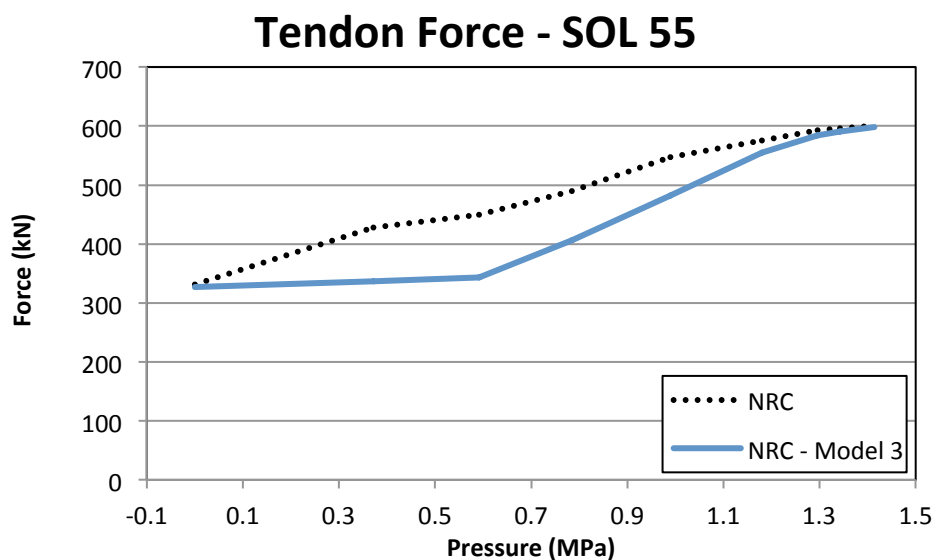


Figure 130: Tendon Strain Versus Pressure at SOL #55 (Hoop, Tendon H53 at Buttress)

4 CASE 2: STATION BLACKOUT RESULTS

4.1 Deformed Shape

Several participants provided deformed shape plots for Model 3 at the usual pressure milestones. These deformed shape plots can be found in Figure 131 through Figure 139. Similar to the deformed shape plots from Model 1, the different scaling factors used by the various participants limit the initial comparability of the figures. Nonetheless, the general shape of the deformed models does indicate some difference between the participants.

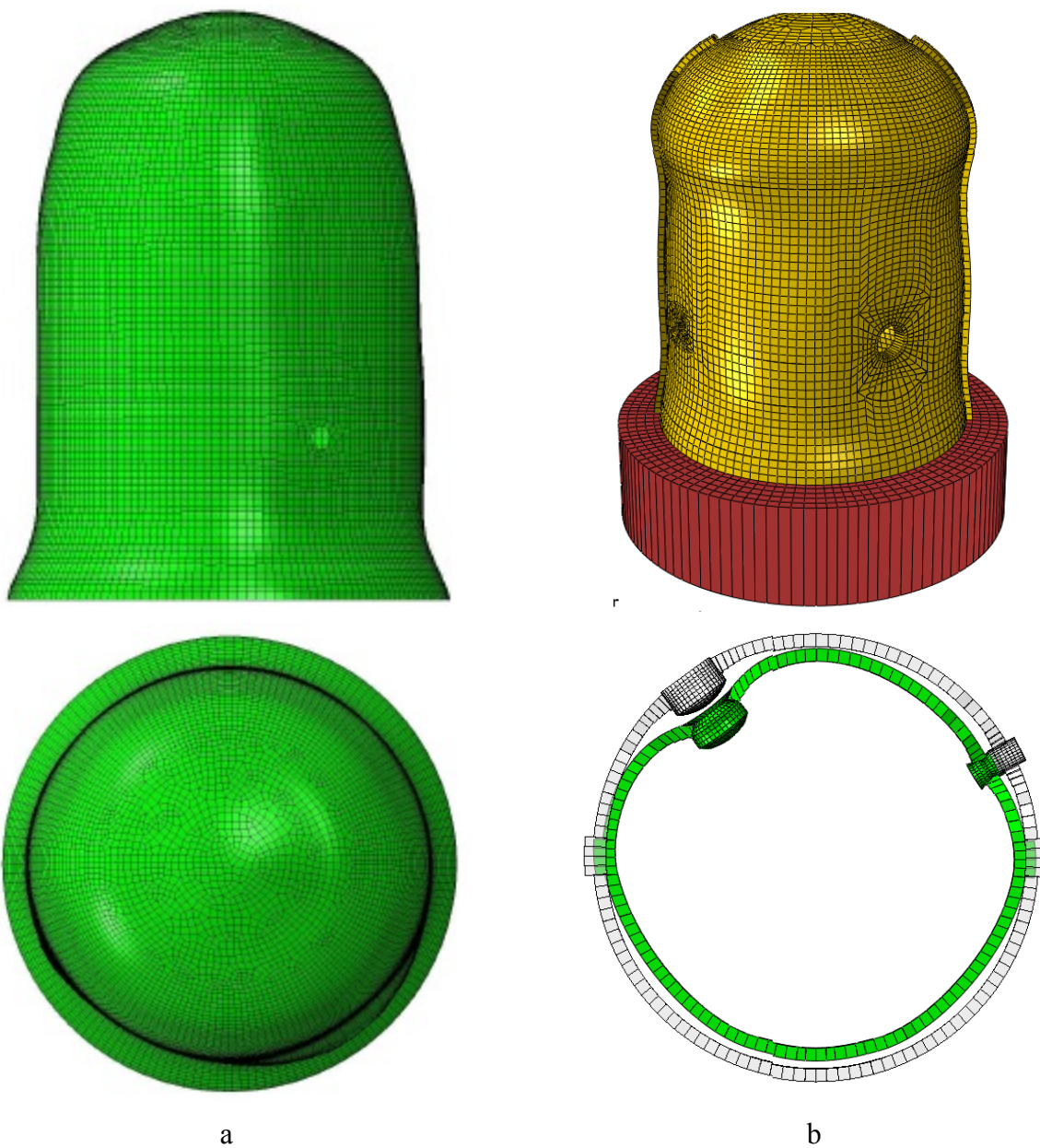


Figure 131: Deformed Shape after Tendon Anchorage (a) AERB (b) NRC (x500)

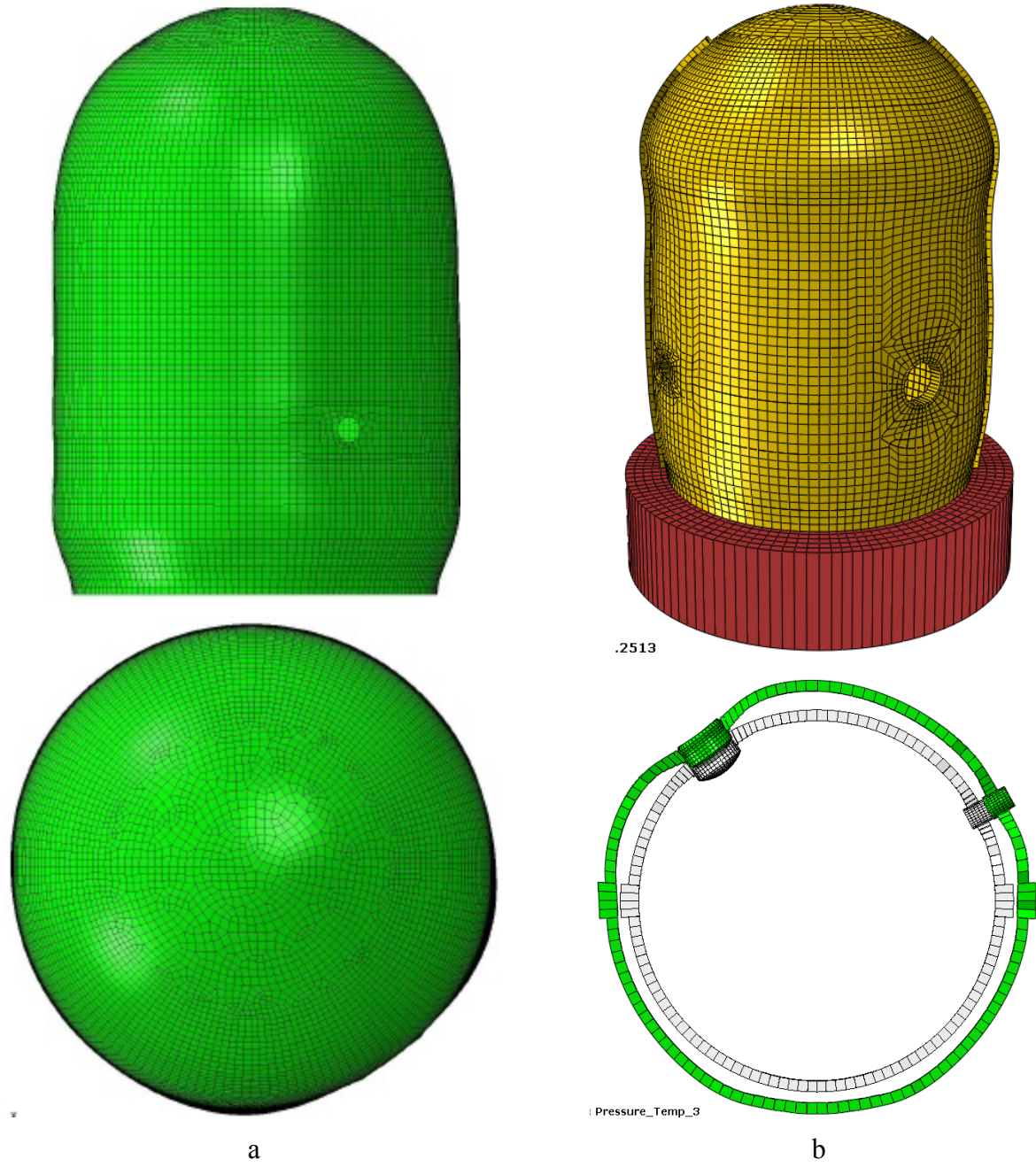


Figure 132: Deformed Shape at $1.0 \times P_d$ (a) AERB (b) NRC (x100)

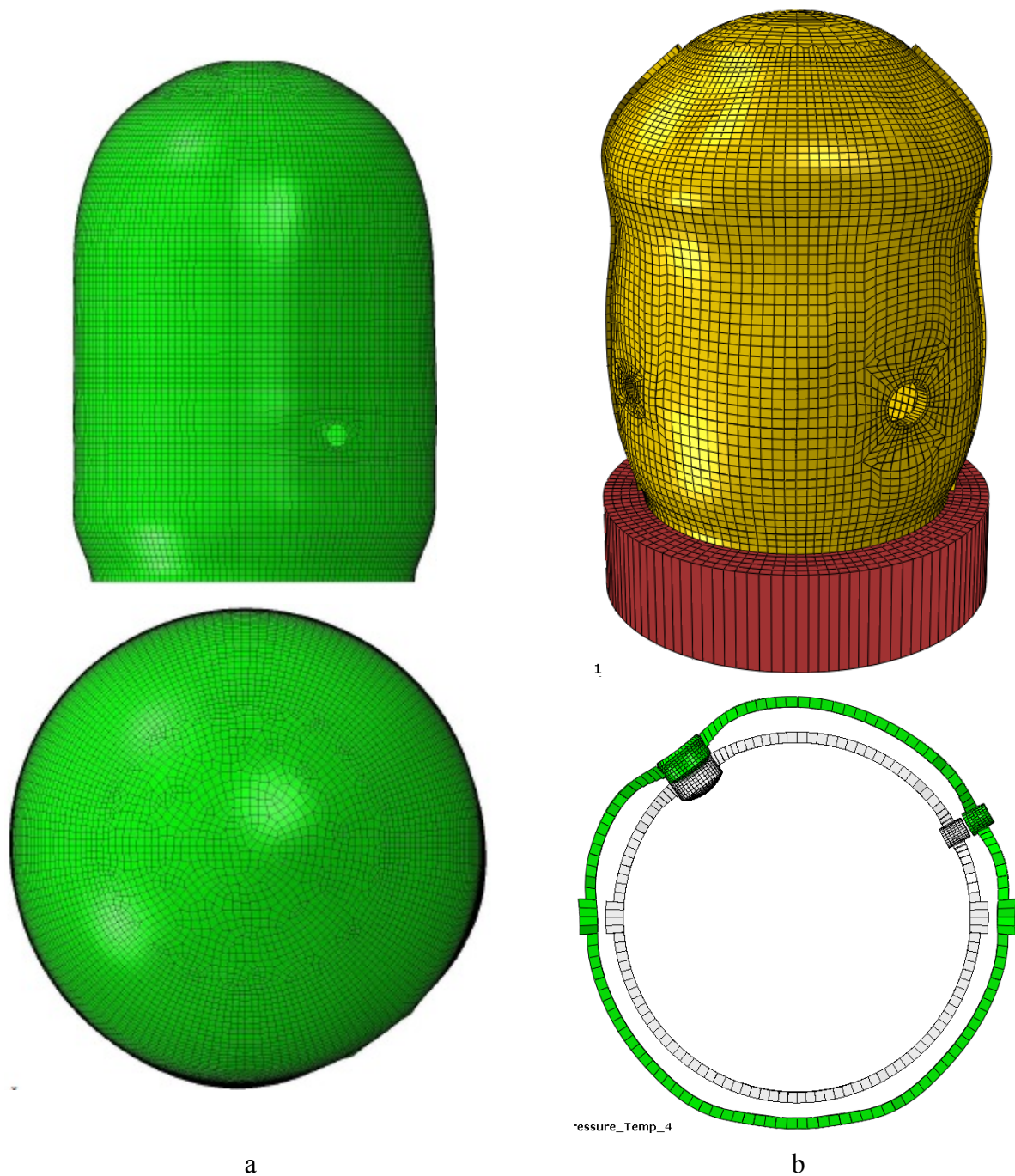
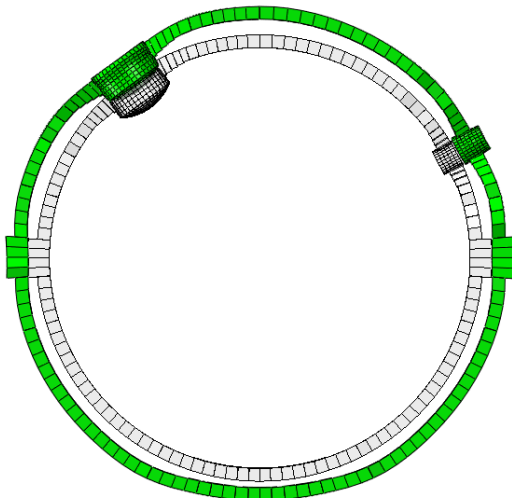
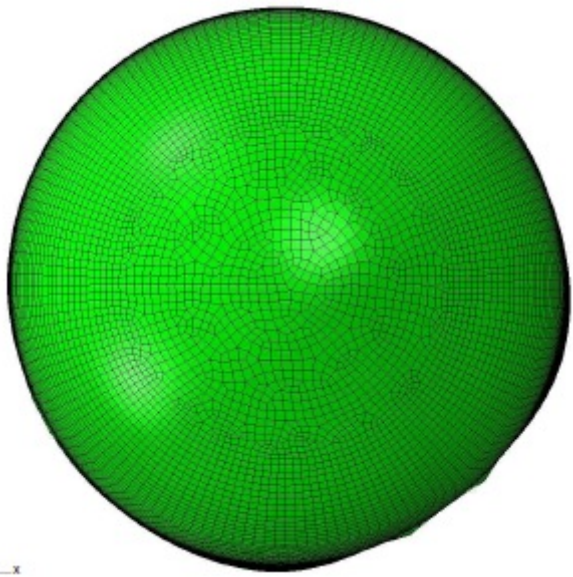
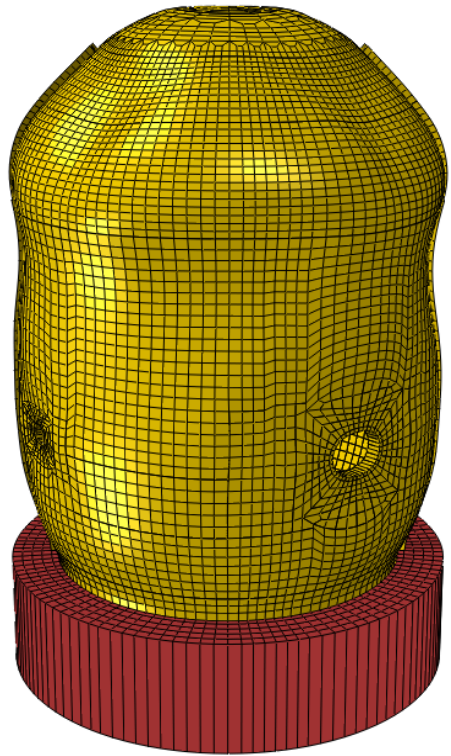
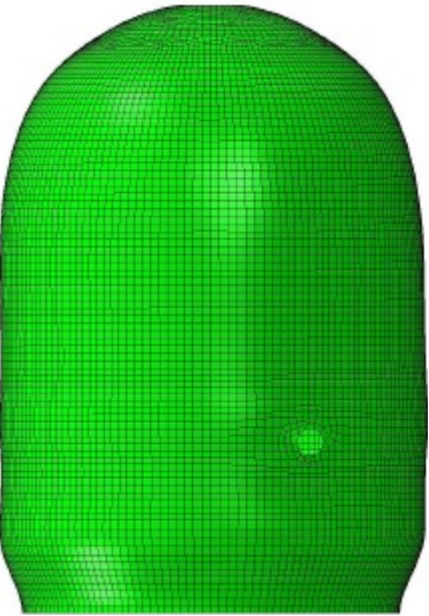


Figure 133: Deformed Shape at $1.5 \times P_d$ (a) AERB (b) NRC (x100)



a

b

Figure 134: Deformed Shape at $2.0 \times P_d$ (a) AERB (b) NRC (x50)

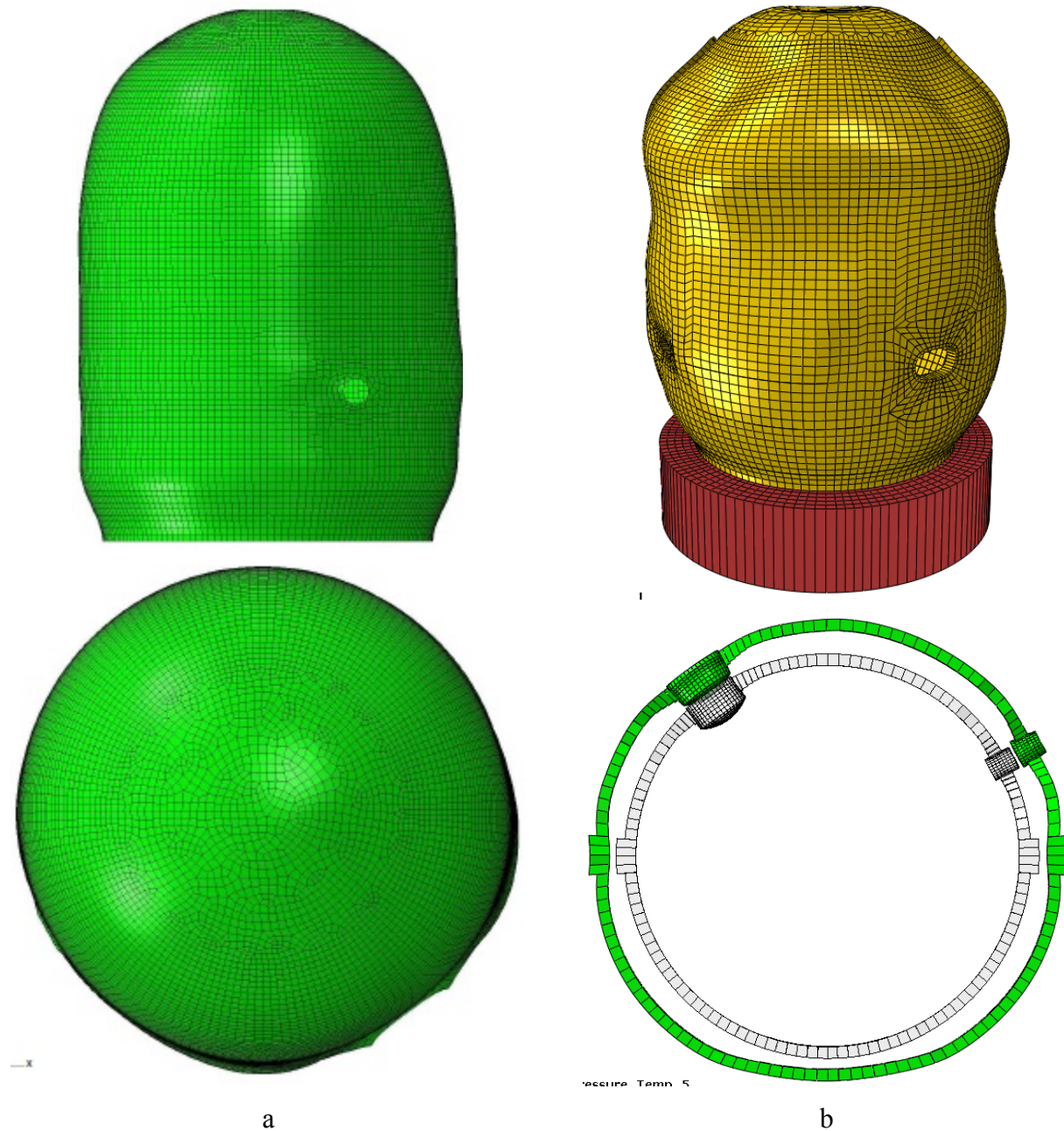


Figure 135: Deformed Shape at $2.5 \times P_d$ for (a) AERB (b) NRC (x50)

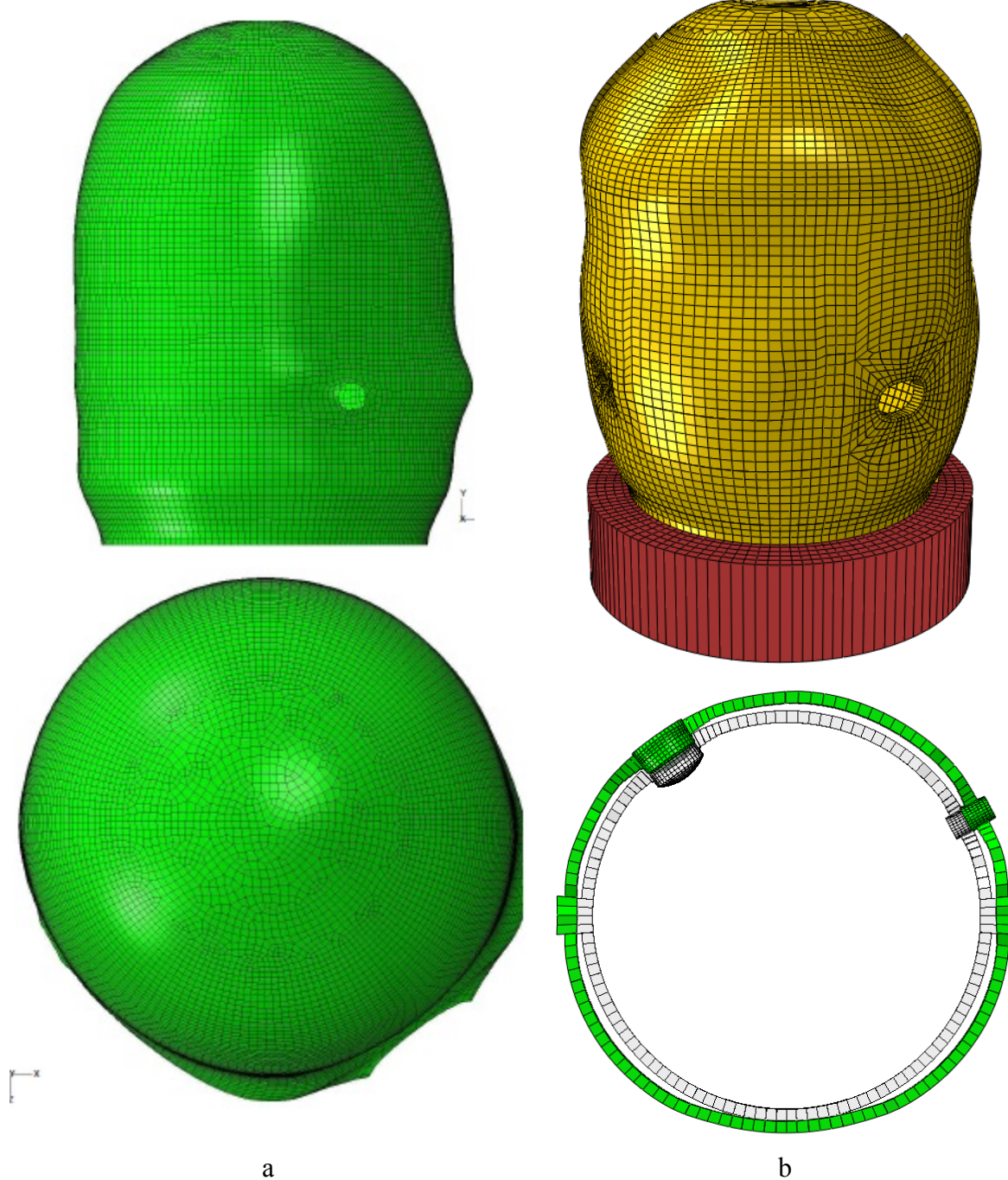


Figure 136: Deformed Shape at $3.0 \times P_d$ (a) AERB (b) NRC (x20)

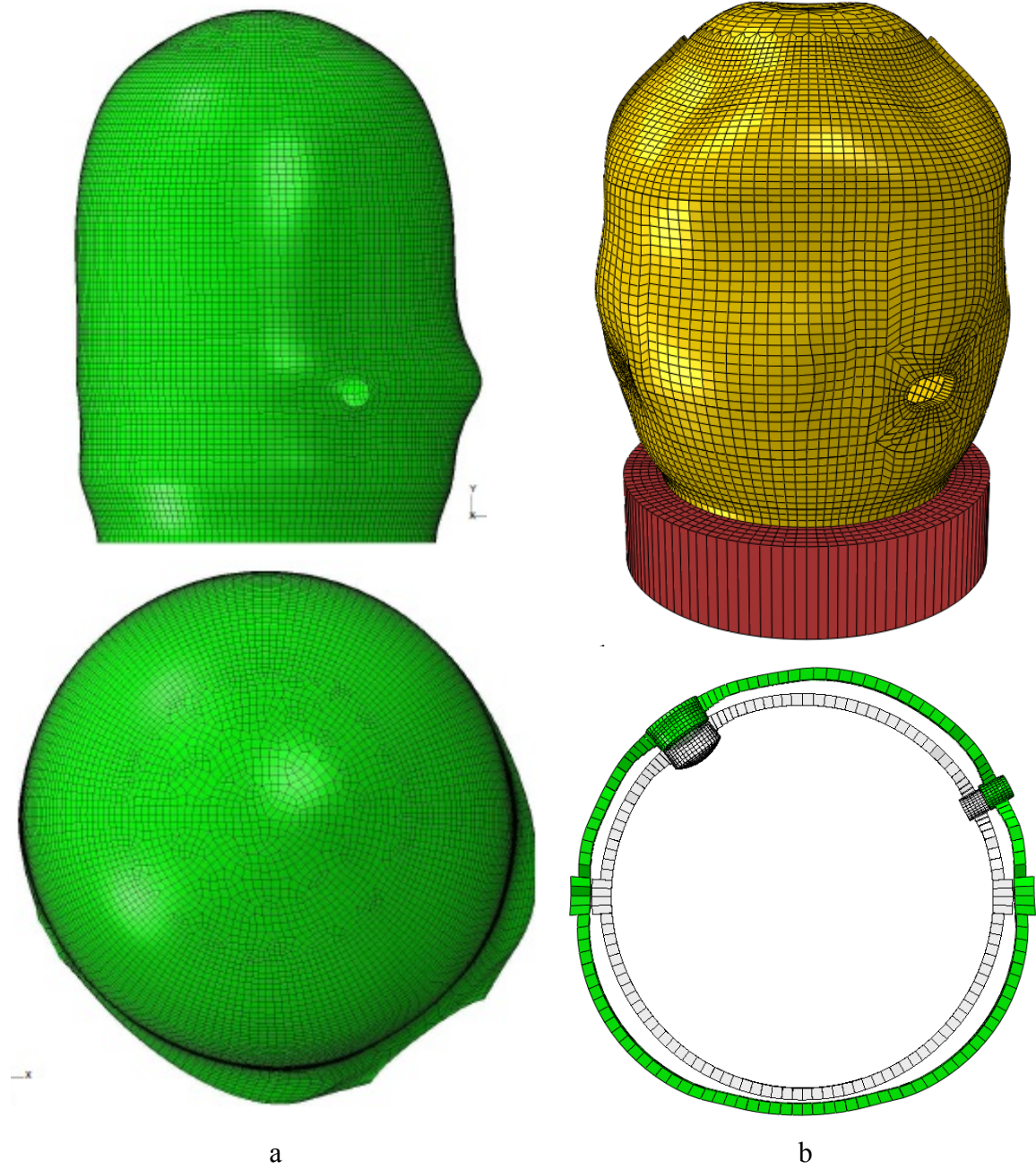


Figure 137: Deformed Shape at (a) $3.25 \times P_d$ AERB (b) $3.3 \times P_d$ NRC (x20)

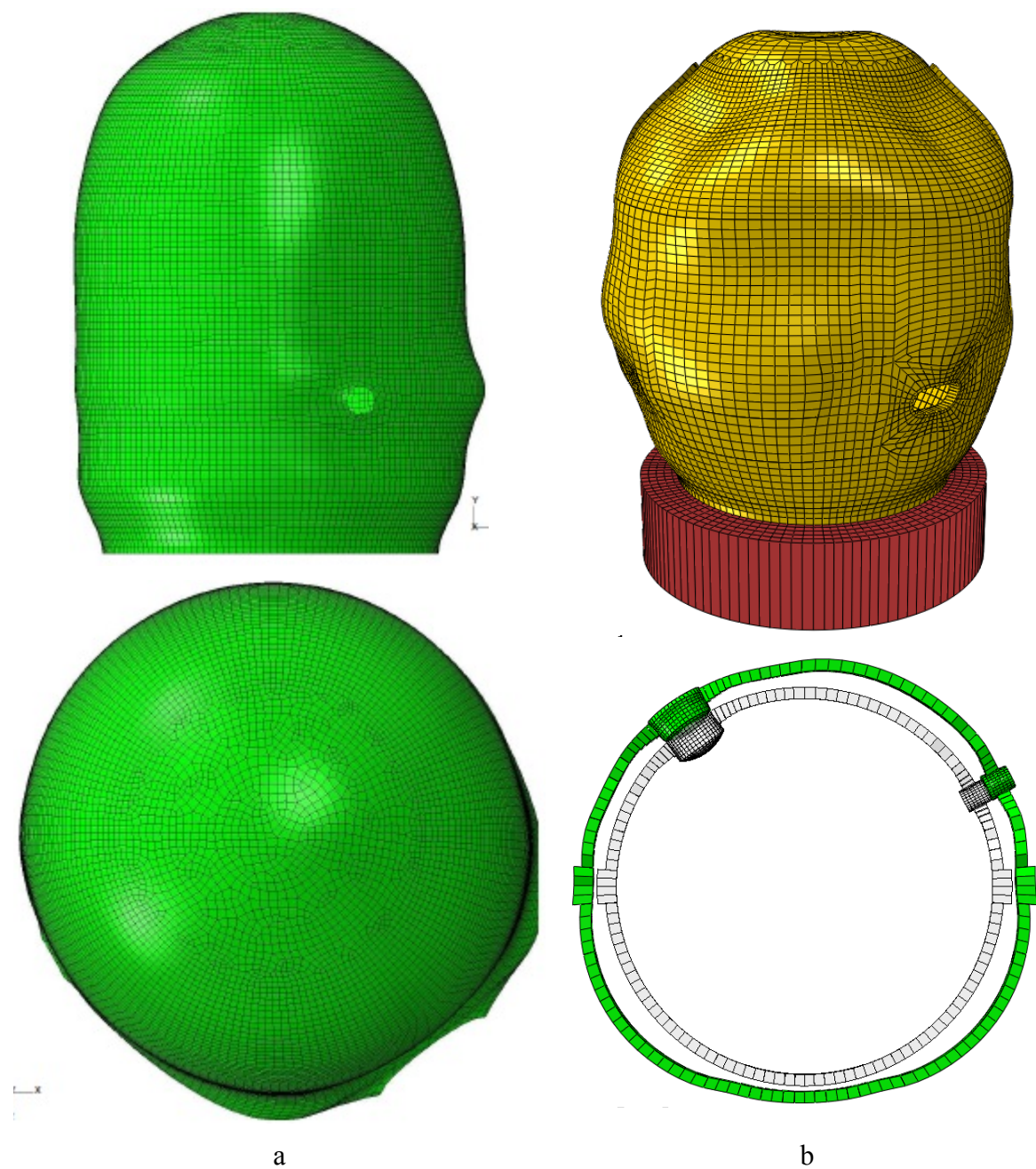


Figure 138: Deformed Shape at $3.4 \times P_d$ (a) AERB (b) NRC (x20)

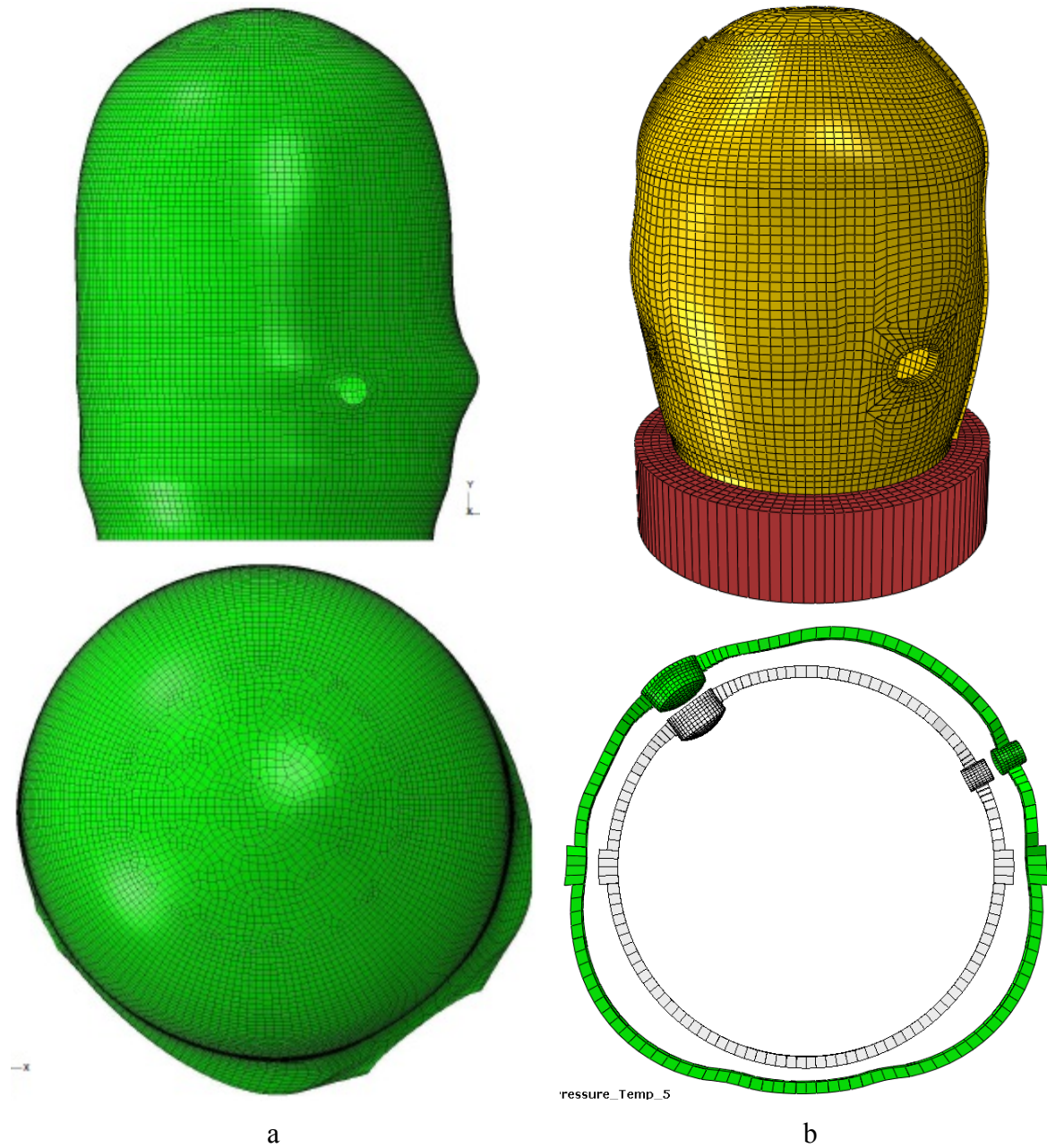
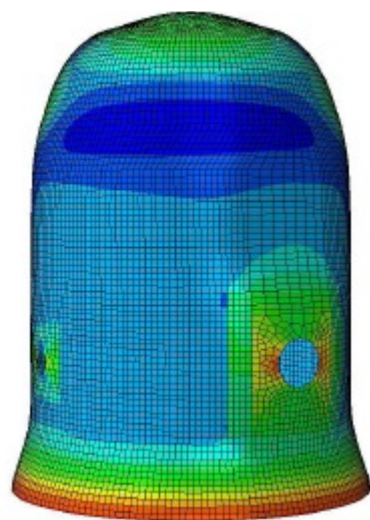


Figure 139: Deformed Shape at Ultimate Pressure (a) AERB - $3.46 \times P_d$ (b) NRC $3.6 \times P_d$, Deformation Scale x 20

4.2 Liner Strains

4.2.1 Peak Strains of Entire Liner

Contour plots of peak strains in the liner at the pressure milestones can be found in Figure 140 through Figure 148. Perhaps of greatest interest in the peak strain plots, are the general frequency and locations of the “hot spots” in the liner. The peak strains occur near the various discontinuities in the model. This is in agreement with the experimental testing from the PCCV test.



(Hoop, Peak Scale Strain = 1.2e-5)



(In Plane Principal)



(Meridional, Peak Scale Strain = -6.7e-5)

a

b

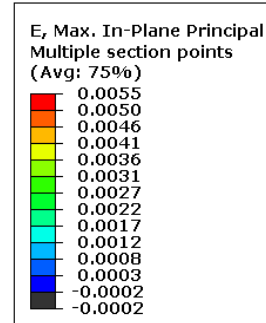
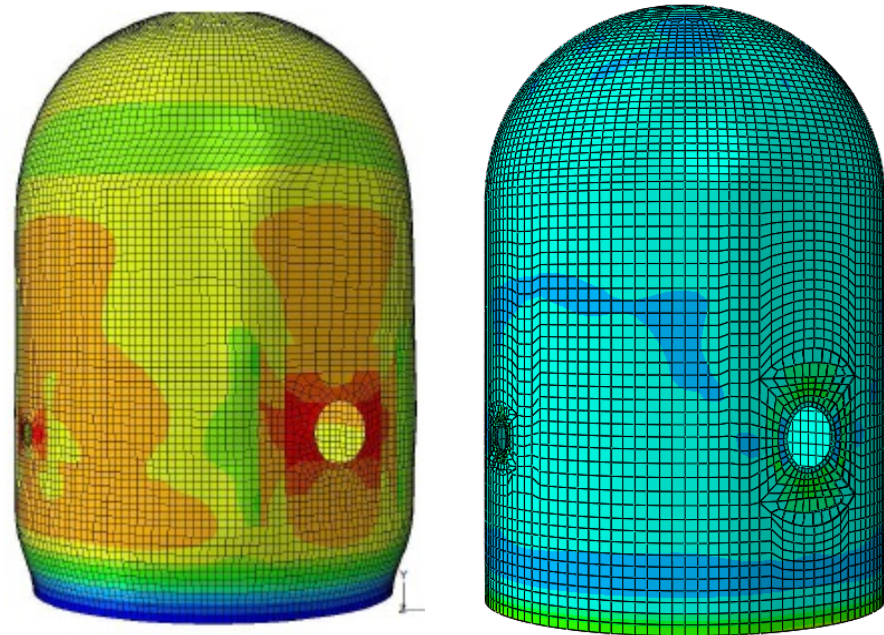
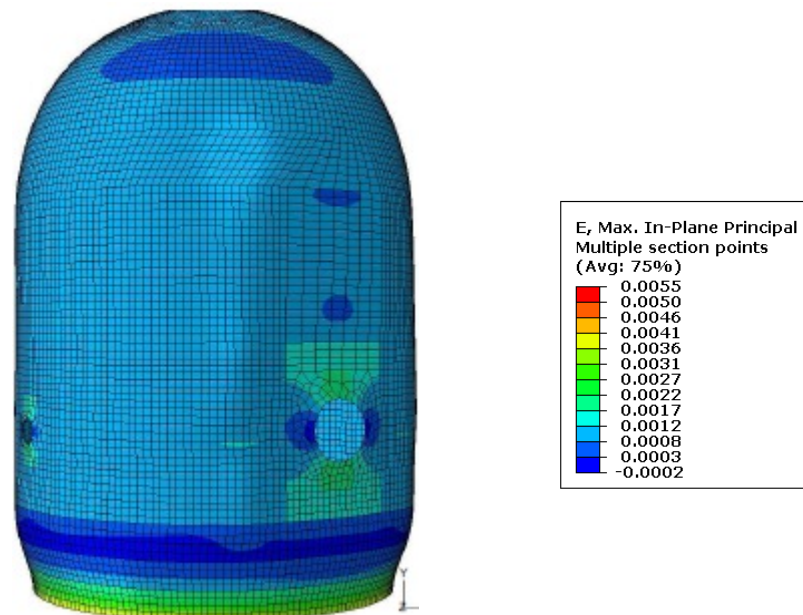


Figure 140: Peak Strain at 0 x P_d (a) AERB (b) NRC



(Hoop, Peak Scale Strain = 1.8e-3)

(In Plane Principal)



(Meridional, Peak Scale Strain = 3.8e-3)

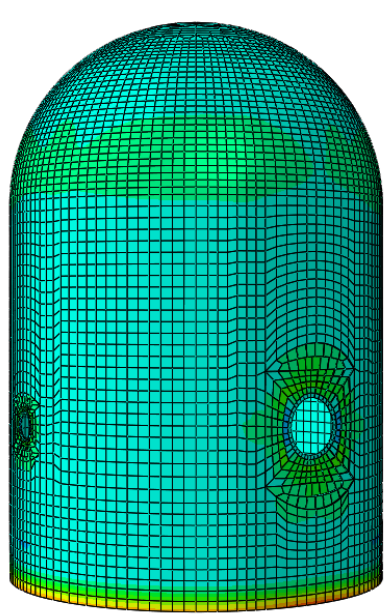
a

b

Figure 141: Peak Strain at $1.0 \times P_d$ (a) AERB (b) NRC



(Hoop, Peak Scale Strain = 2.0e-3)



(In Plane Principal)



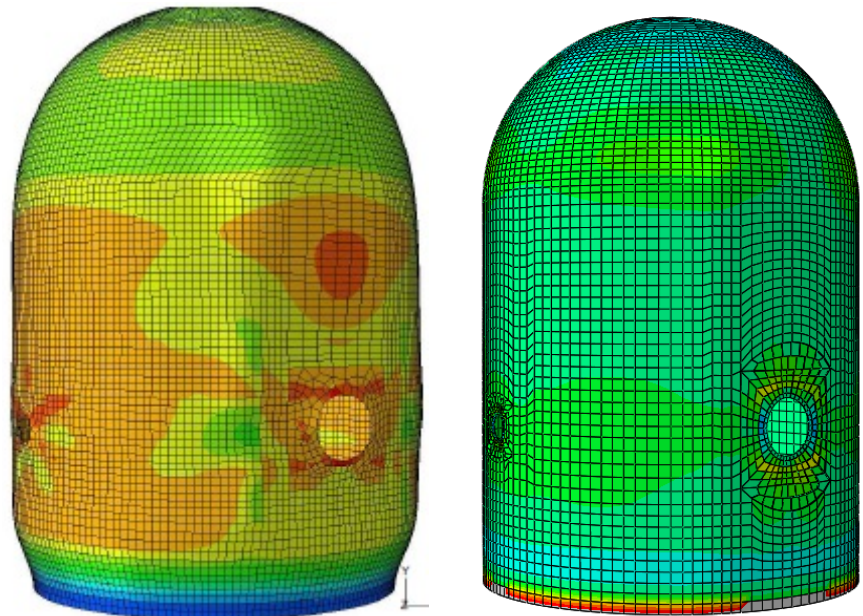
(Meridional, Peak Scale Strain = 4.8e-3)

a

b

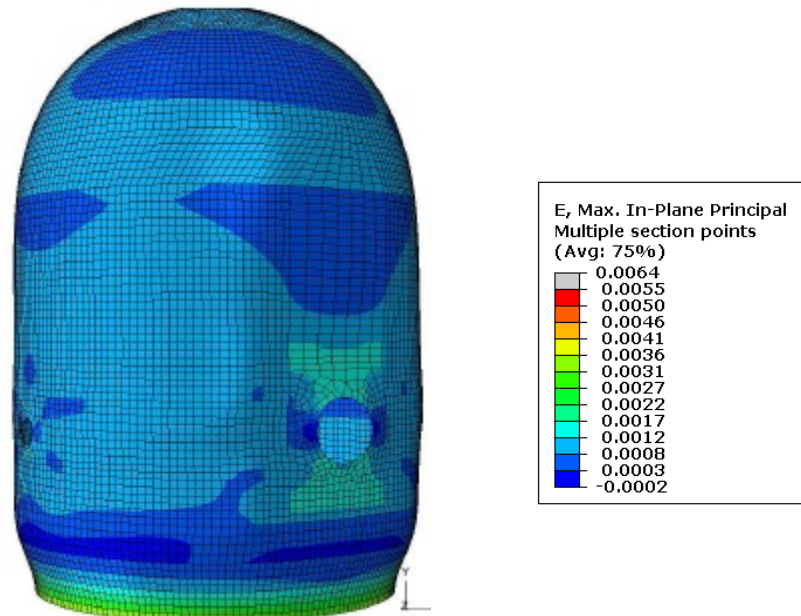
E, Max. In-Plane Principal Multiple section points (Avg: 75%)	
0.0055	
0.0050	
0.0046	
0.0041	
0.0036	
0.0031	
0.0027	
0.0022	
0.0017	
0.0012	
0.0008	
0.0003	
-0.0002	

Figure 142: Peak Strain at $1.5 \times P_d$ (a) AERB (b) NRC



(Hoop, Peak Scale Strain = 2.6e-3)

(In Plane Principal)

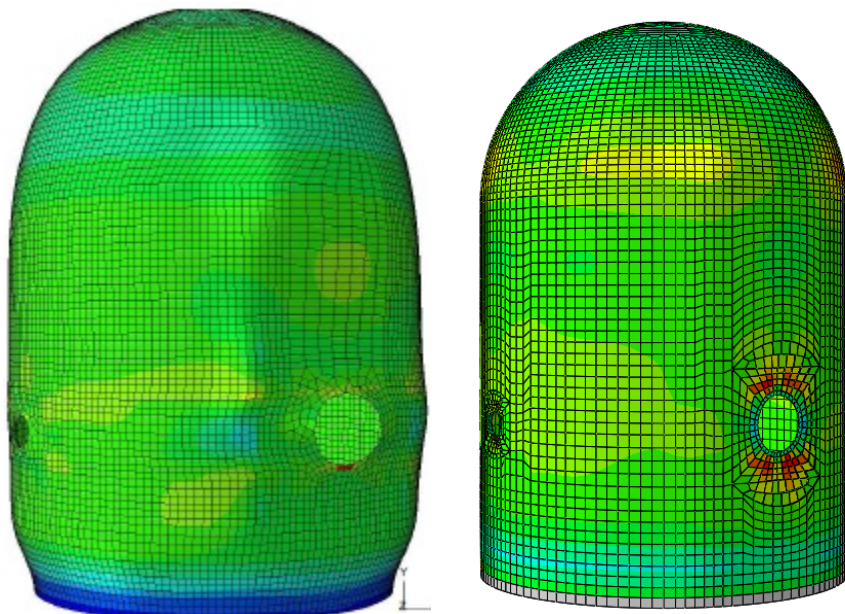


(Meridional, Peak Scale Strain = 5.8e-3)

a

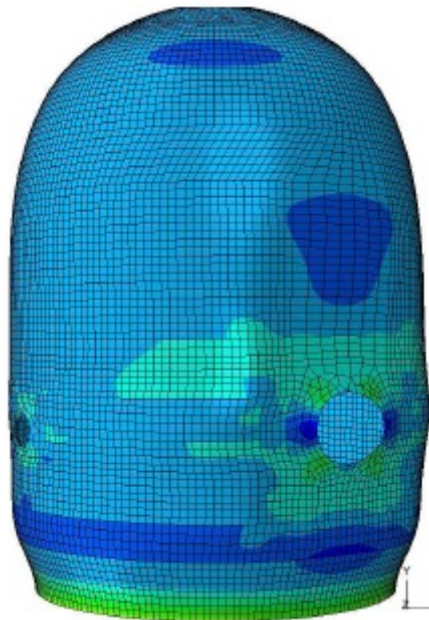
b

Figure 143: Peak Strain at $2.0 \times P_d$ (a) AERB (b) NRC



(Hoop, Peak Scale Strain = 4.7e-3)

(In Plane Principal)



(Meridional, Peak Scale Strain = 7.1e-3)

a

b

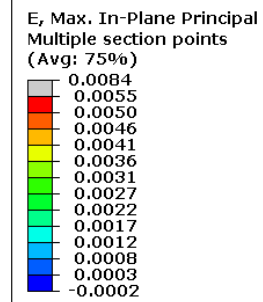
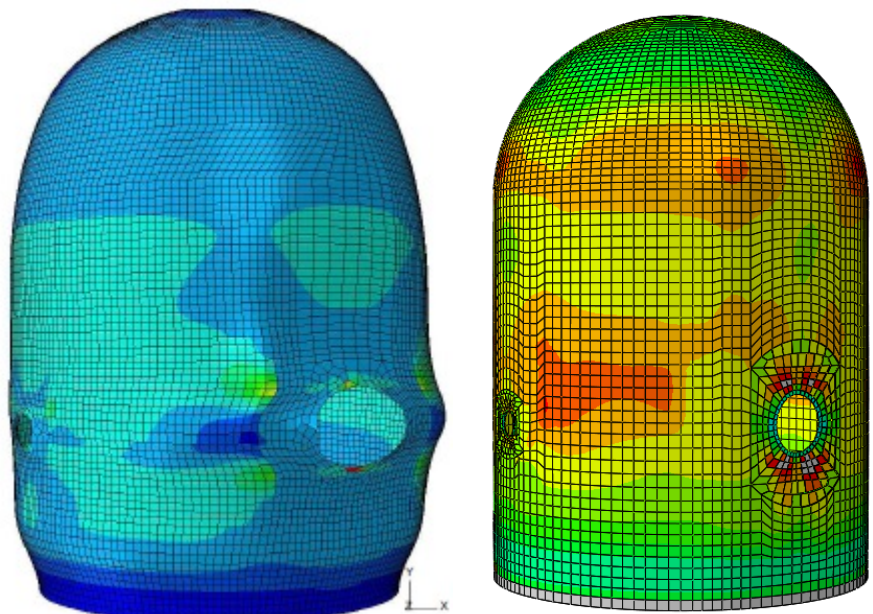
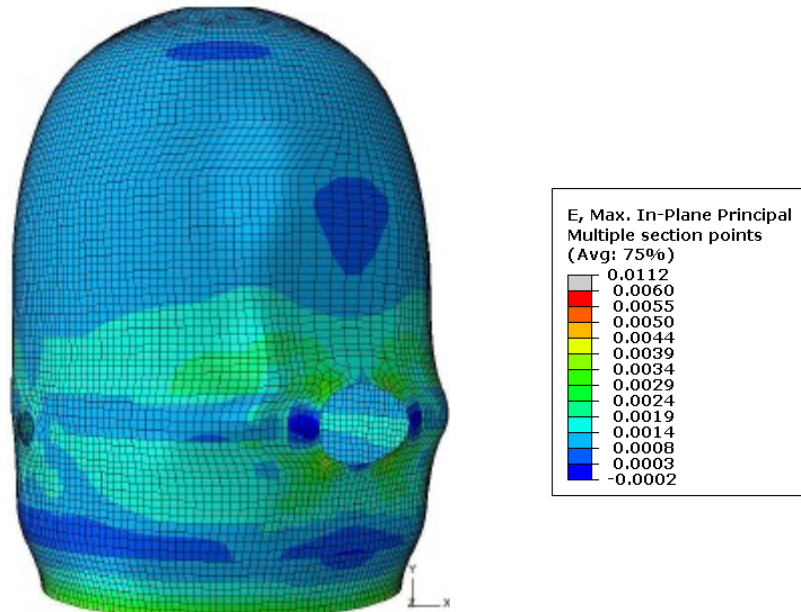


Figure 144: Peak Strain at $2.5 \times P_d$ (a) AERB (b) NRC



(Hoop, Peak Scale Strain = 1.3e-2)

(In Plane Principal)

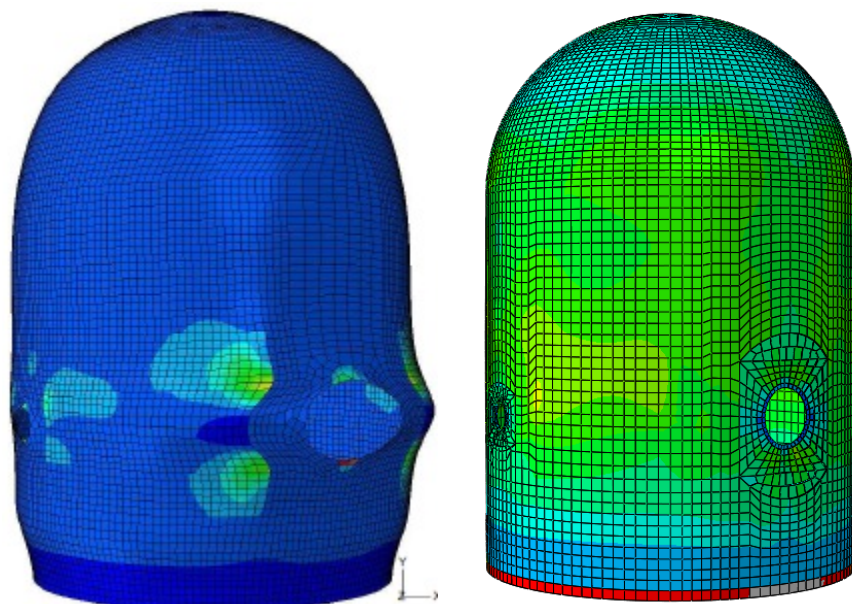


(Meridional, Peak Scale Strain = 8.7e-3)

a

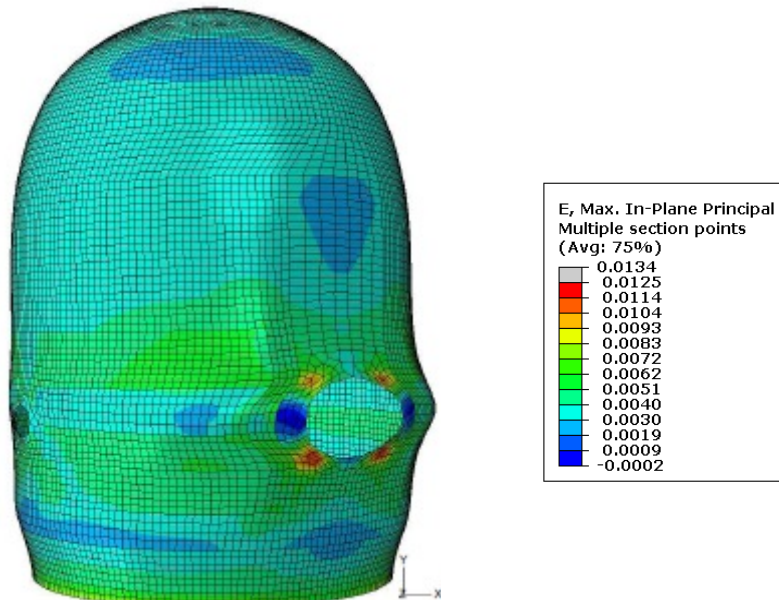
b

Figure 145: Peak Strain at $3.0 \times P_d$ (a) AERB (b) NRC



(Hoop, Peak Scale Strain = $2.7\text{e-}2$)

(In Plane Principal)

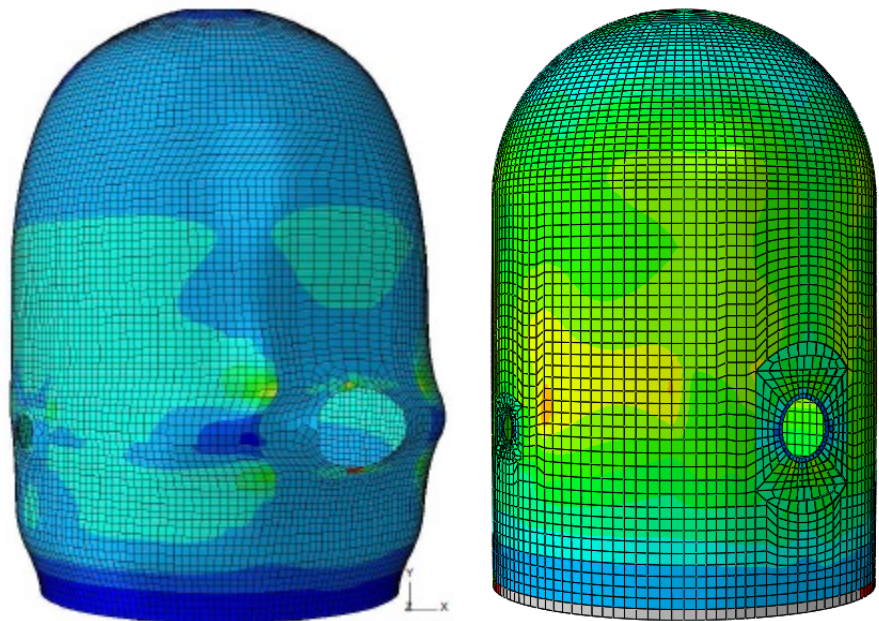


(Meridional, Peak Scale Strain = $1.0\text{e-}2$)

a

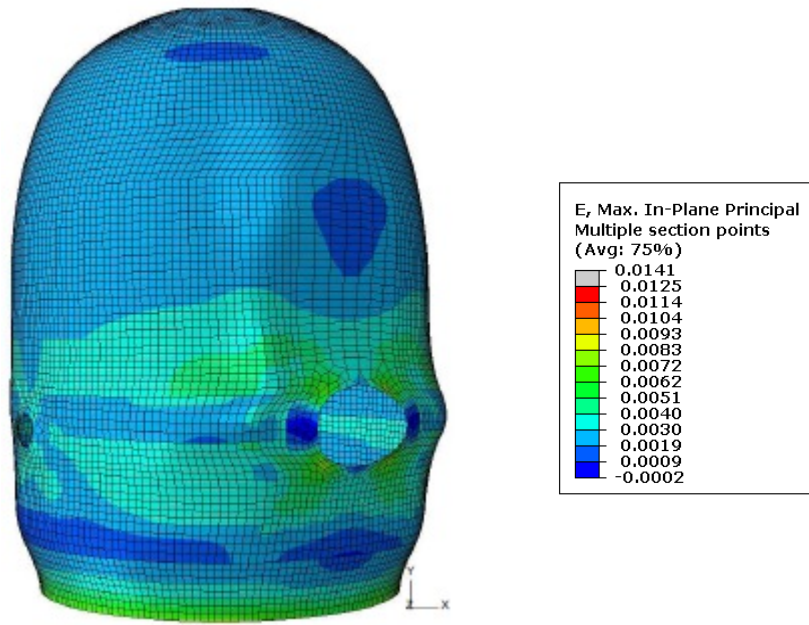
b

Figure 146: Peak Strain at (a) $3.25 \times P_d$ AERB (b) $3.3 \times P_d$ NRC



(Hoop, Peak Scale Strain = 1.3e-2)

(In Plane Principal)

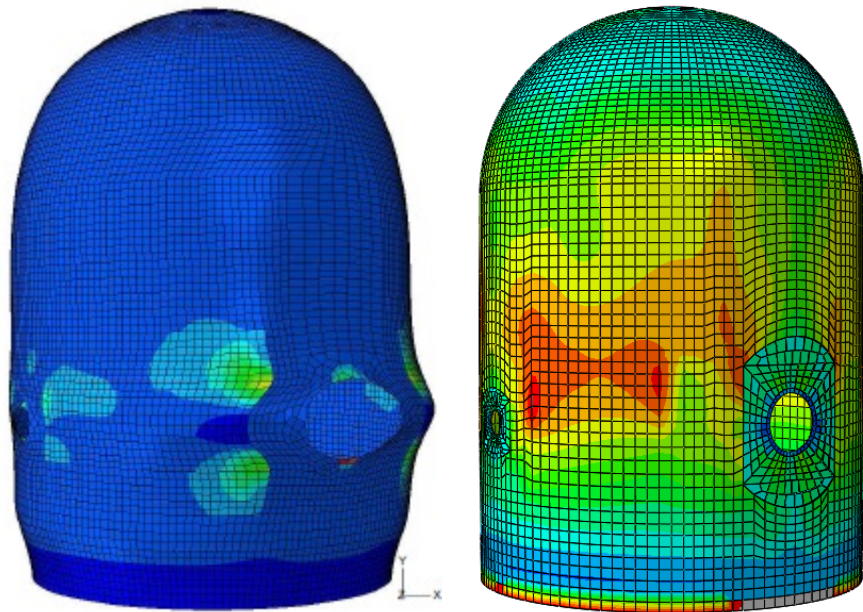


(Meridional, Peak Scale Strain = 8.7e-3)

a

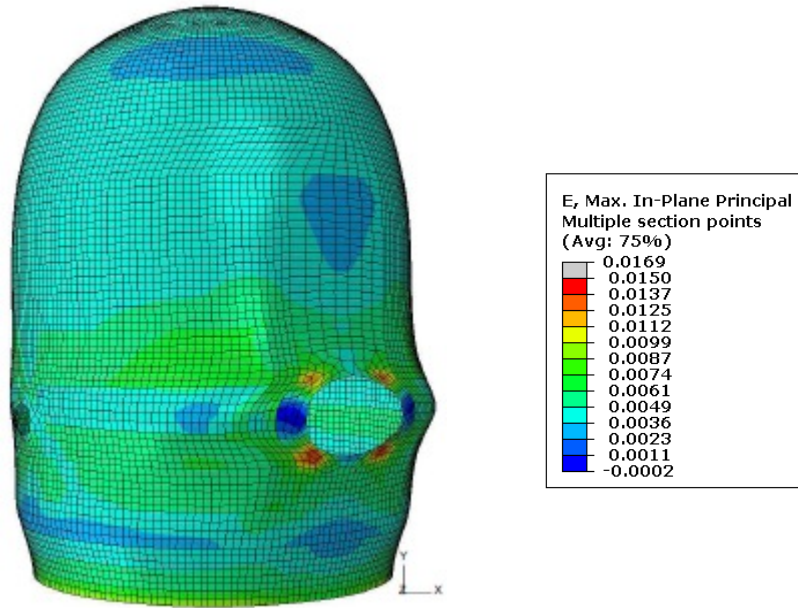
b

Figure 147: Peak Strain at $3.40 \times P_d$ (a) AERB (b) NRC



(Hoop, Peak Scale Strain = 2.7e-2)

(In Plane Principal)



(Meridional, Peak Scale Strain = 1.0e-2)

a

b

Figure 148: Peak Strain at Ultimate Pressure (a) 3.46 x P_d AERB (b) 3.6 x P_d NRC

4.2.2 Average Strains at Selected Locations

As was requested for Case 1, the participants were asked to provide strain data at the locations shown in Figure 37 for Case 2. These strain results are shown in Figure 149 through Figure 158.

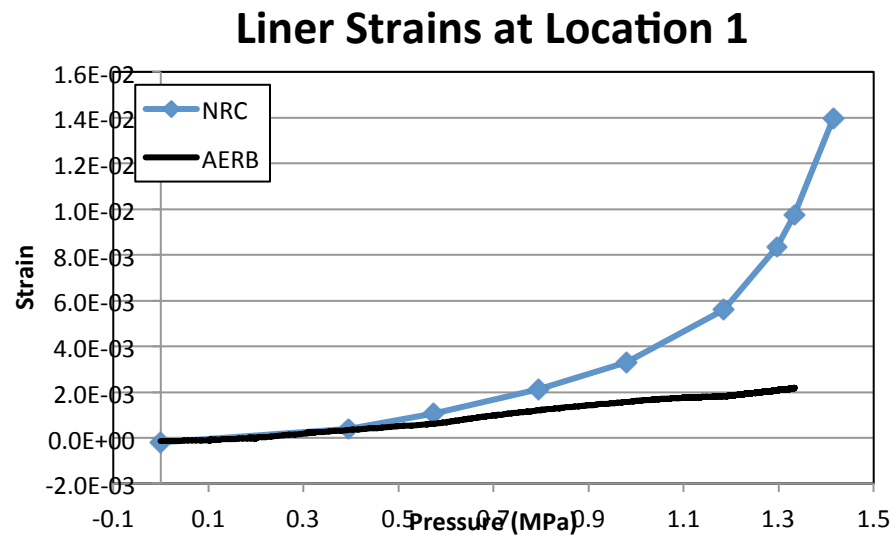


Figure 149: Strain over Gauge Length at Location 1 Near Equipment Hatch

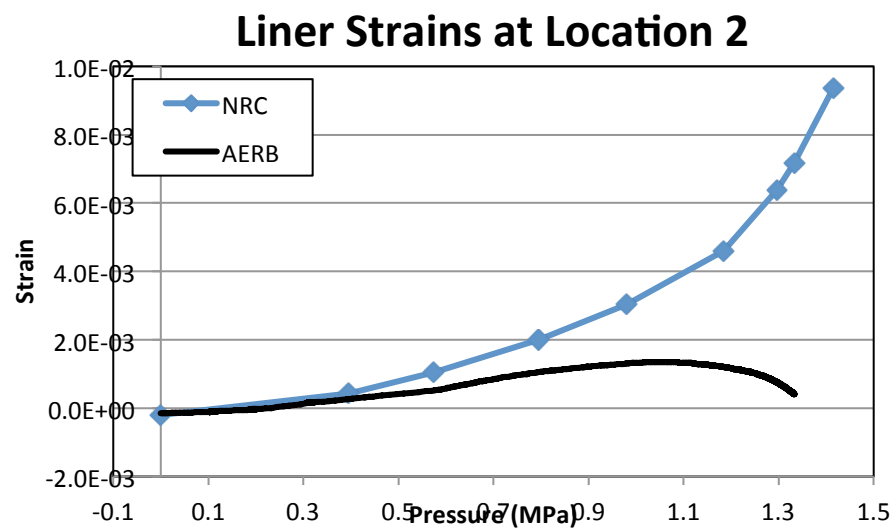


Figure 150: Strain over Gauge Length at Location 2 Near Equipment Hatch

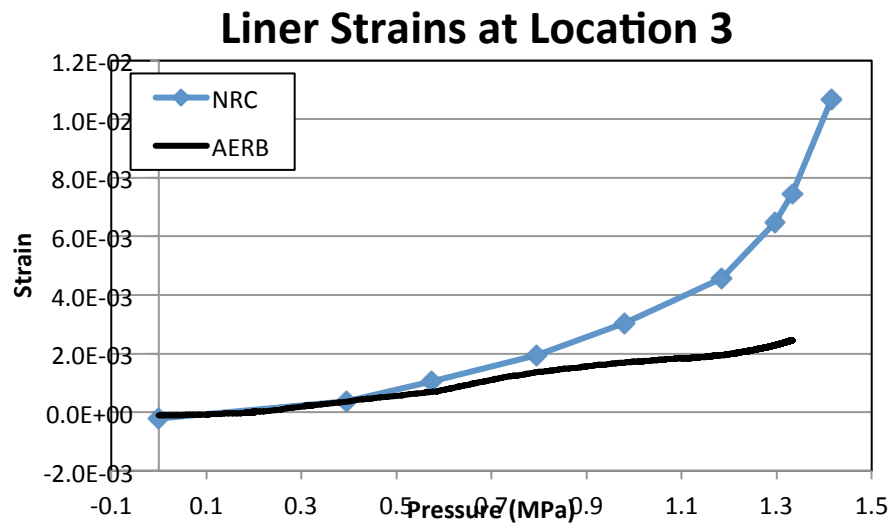


Figure 151: Strain over Gauge Length at Location 3 Near Equipment Hatch

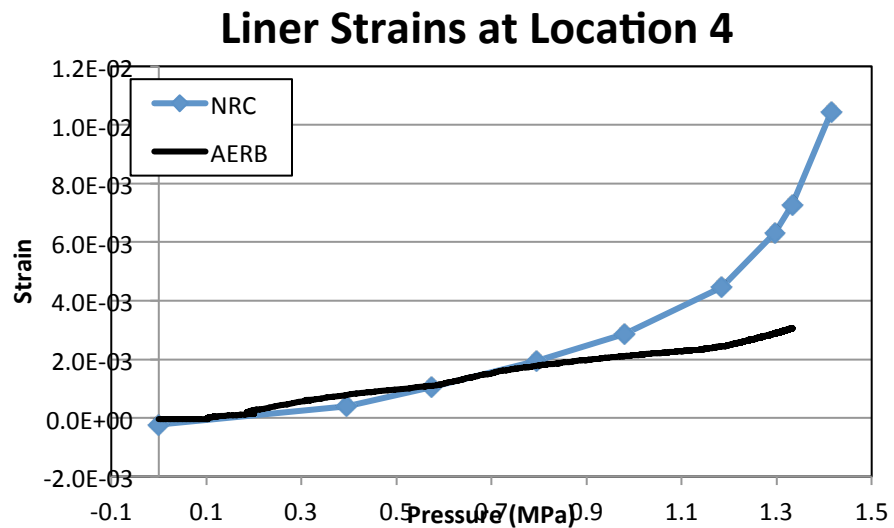


Figure 152: Strain over Gauge Length at Location 4 Near Equipment Hatch

Liner Strains at Location 5

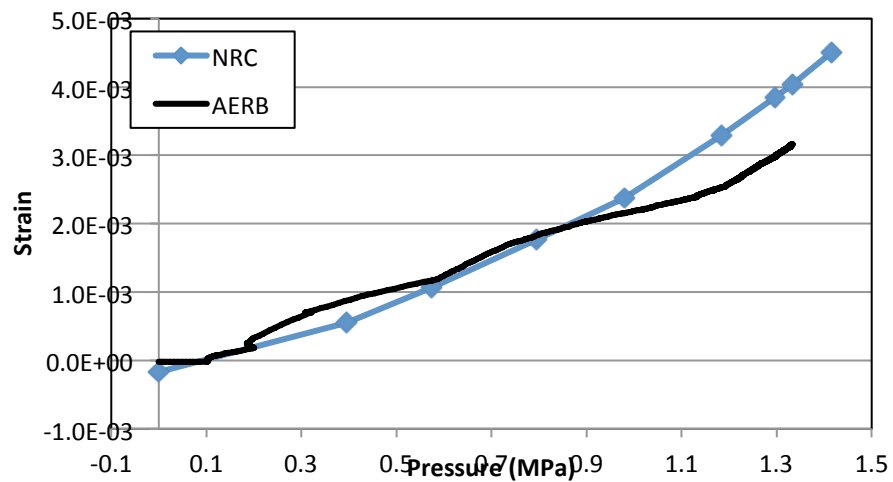


Figure 153: Strain over Gauge Length at Location 5 Near Equipment Hatch

Liner Strains at Location 6

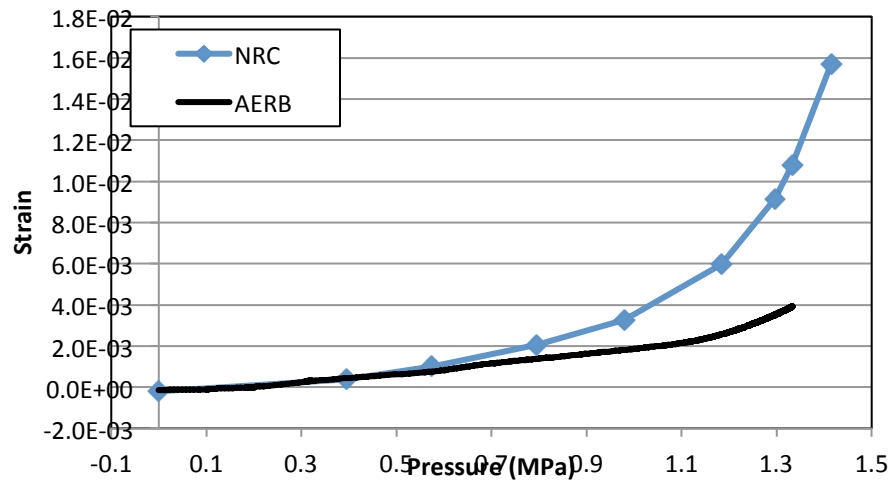


Figure 154: Strain over Gauge Length at Location 6 Near Equipment Hatch

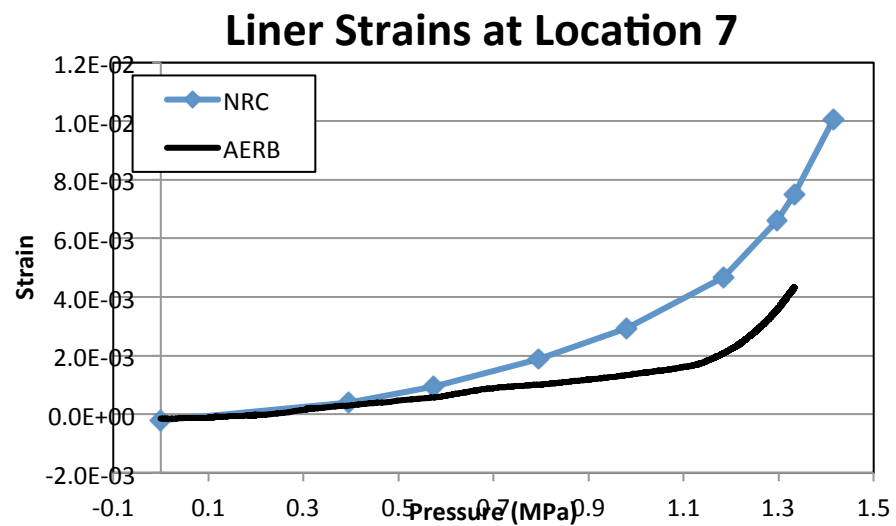


Figure 155: Strain over Gauge Length at Location 7 Near Equipment Hatch

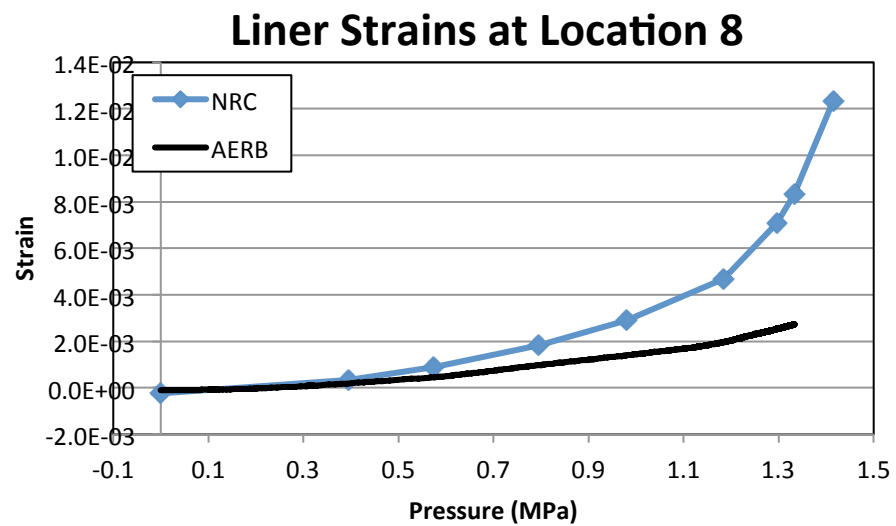


Figure 156: Strain over Gauge Length at Location 8 Near Equipment Hatch

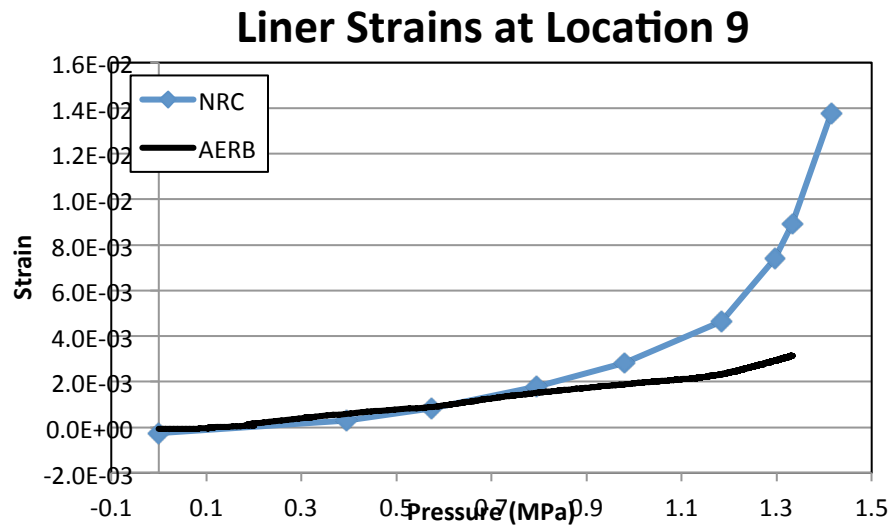


Figure 157: Strain over Gauge Length at Location 9 Near Equipment Hatch

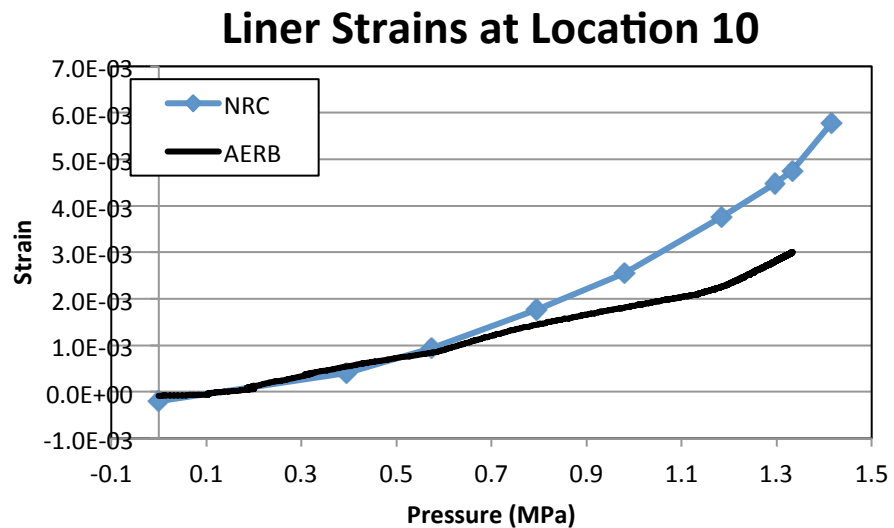


Figure 158: Strain over Gauge Length at Location 10 Near Equipment Hatch

4.3 Tendon Stress Distribution

The tendon stress distribution plots from the participants are presented in Figure 48 through Figure 92. As was the case in previous sections, the abscissa and ordinate are plotted on constant scales through this subsection in order to facilitate comparison between the plots.

4.3.1 Hoop Tendons

The hoop tendons plotted in this subsection correspond to tendons #H35, H53, and H68 from the PCCV test. The selection of these tendons for analysis will help to facilitate comparison with the most instrumented tendons from the 1:4 scale test. The hoop tendon stress profiles can be found in Figure 159 through Figure 185. In general the tendon stress distributions from the participants

agree reasonably well with the exception of the AERB provided data which seems to deviate from the shape of the other participant's data. AERB did not provide data for the horizontal tendons at ultimate pressure, so the NRC results for Case 2 are compared to the Case 1 results in Figure 167, Figure 176, and Figure 185. Interestingly, the results are quite comparable.

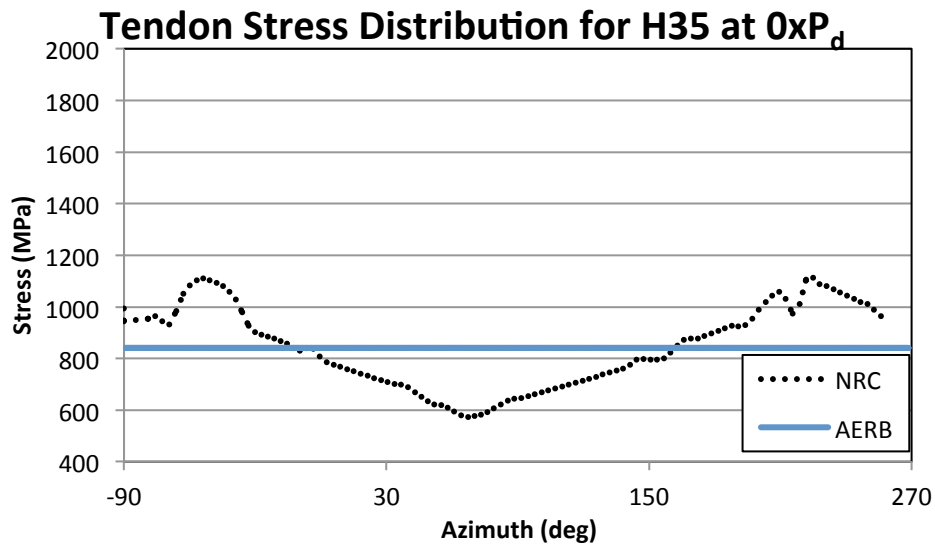


Figure 159: Tendon Stress Distribution for Tendon #H35 at $0 \times P_d$

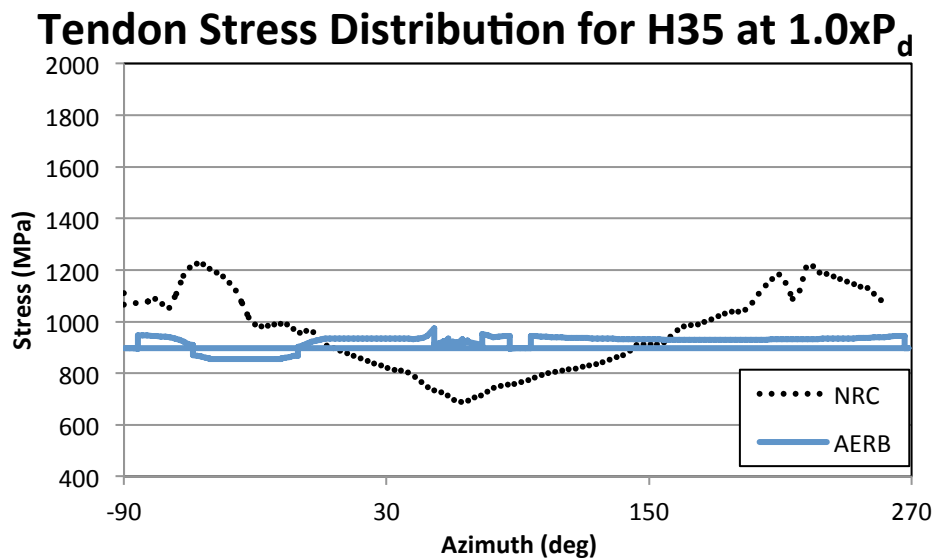


Figure 160: Tendon Stress Distribution for Tendon #H35 at $1.0 \times P_d$

Tendon Stress Distribution for H35 at $1.5 \times P_d$

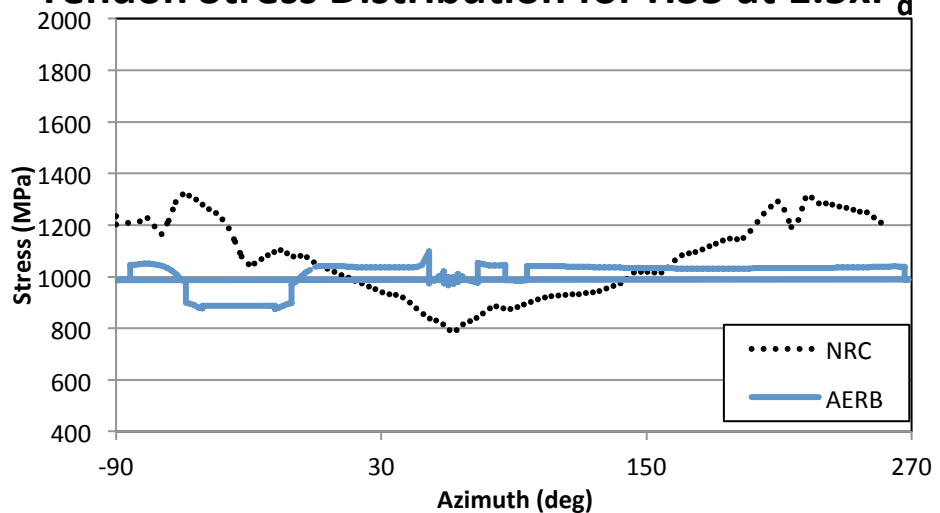


Figure 161: Tendon Stress Distribution for Tendon #H35 at $1.5 \times P_d$

Tendon Stress Distribution for H35 at $2.0 \times P_d$

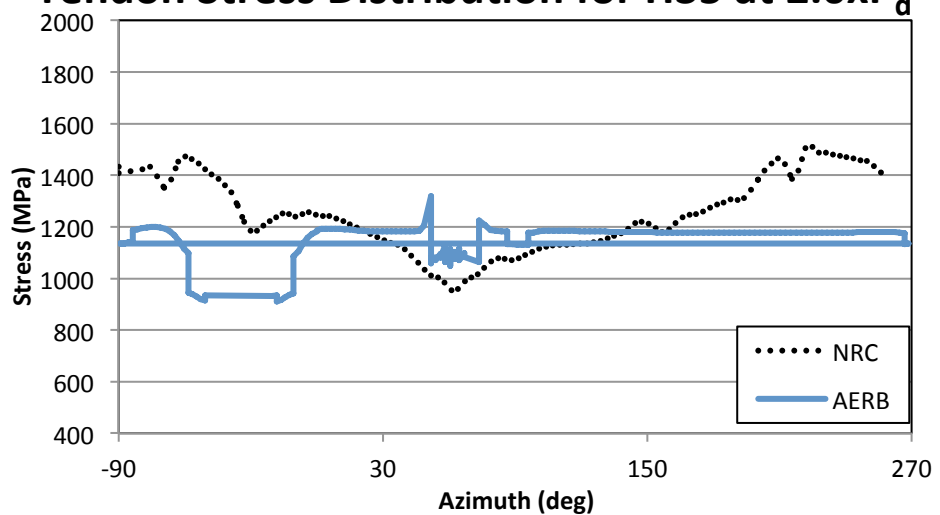


Figure 162: Tendon Stress Distribution for Tendon #H35 at $2.0 \times P_d$

Tendon Stress Distribution for H35 at $2.5 \times P_d$

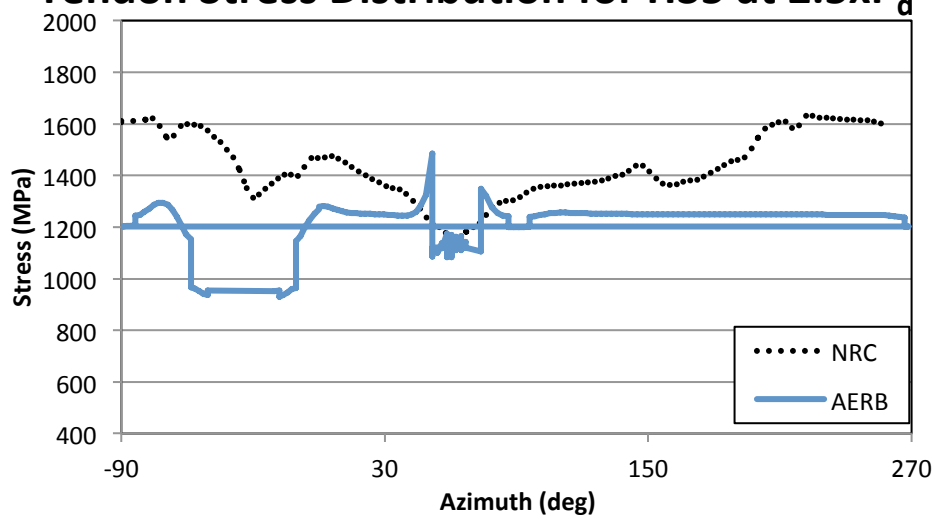


Figure 163: Tendon Stress Distribution for Tendon #H35 at $2.5 \times P_d$

Tendon Stress Distribution for H35 at $3.0 \times P_d$

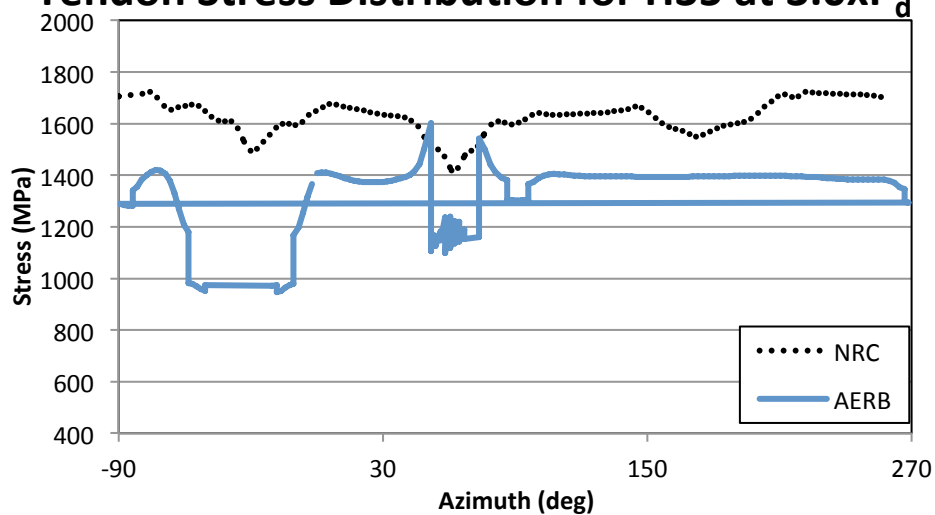


Figure 164: Tendon Stress Distribution for Tendon #H35 at $3.0 \times P_d$

Tendon Stress Distribution for H35 at $3.3 \times P_d$

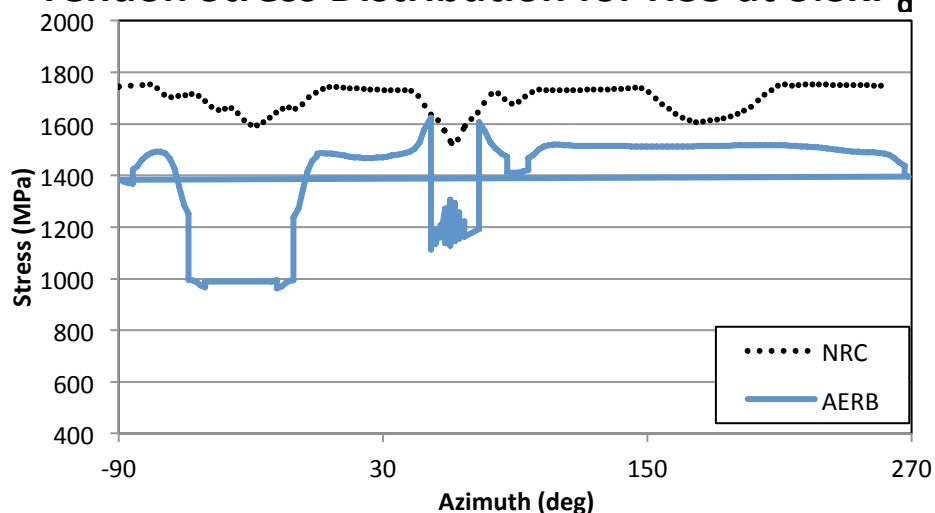


Figure 165: Tendon Stress Distribution for Tendon #H35 at $3.3 \times P_d$

Tendon Stress Distribution for H35 at $3.4 \times P_d$

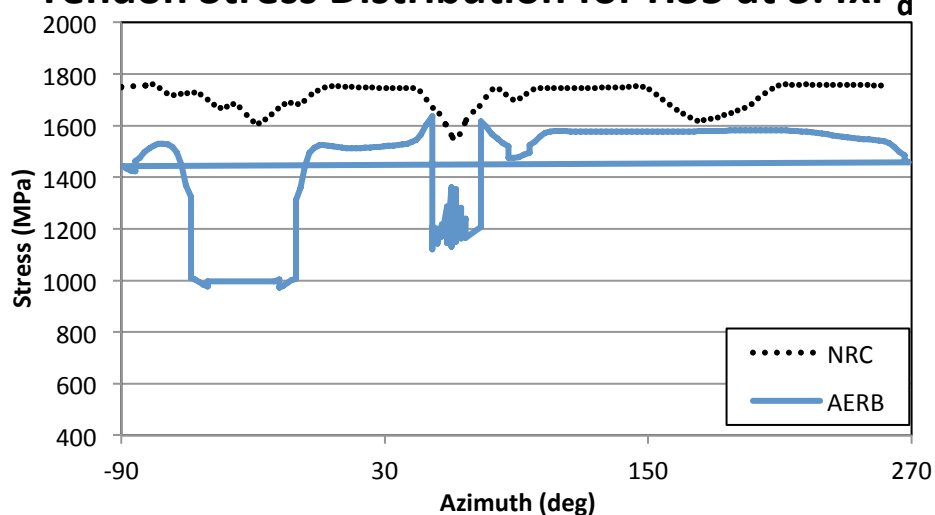


Figure 166: Tendon Stress Distribution for Tendon #H35 at $3.4 \times P_d$

Tendon Stress Distribution for Ultimate Pressure

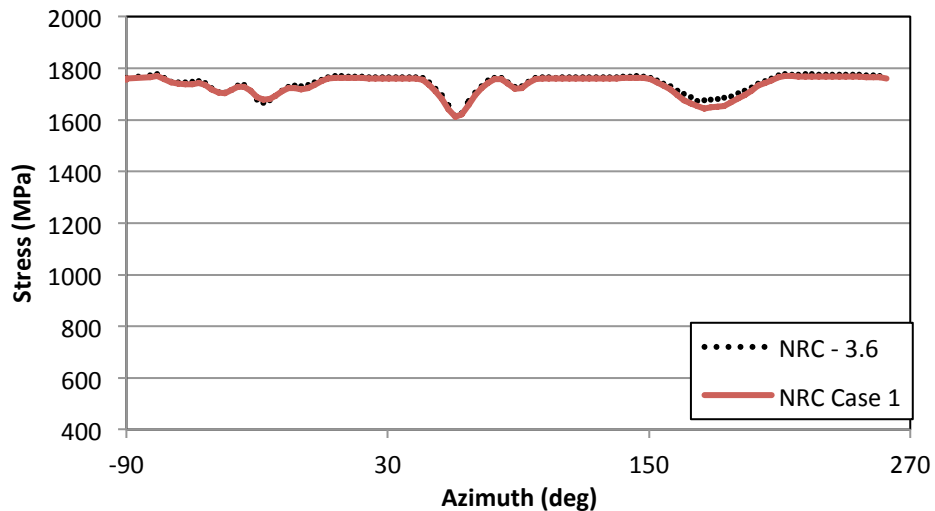


Figure 167: Tendon Stress Distribution for Tendon #H35 at Ultimate Pressure

Tendon Stress Distribution for H53 at $0 \times P_d$

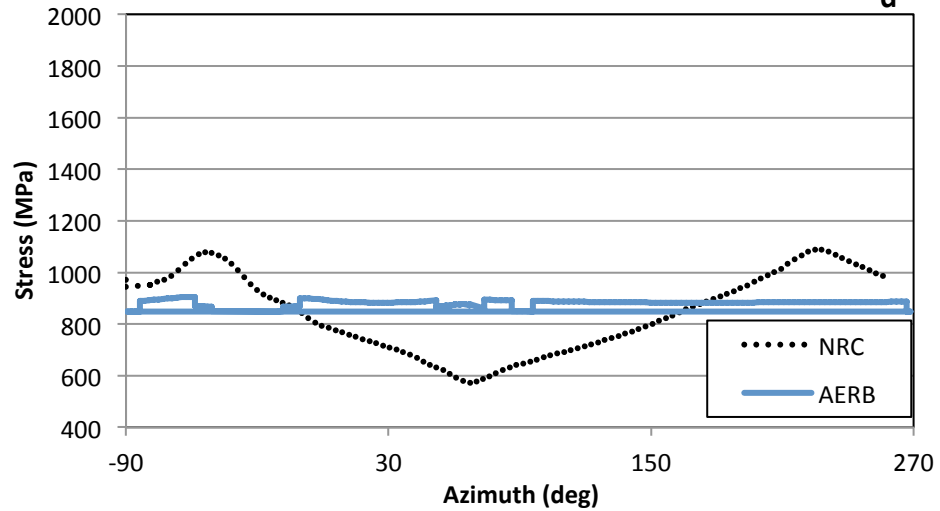


Figure 168: Tendon Stress Distribution for Tendon #H53 at $0 \times P_d$

Tendon Stress Distribution for H53 at $1.0 \times P_d$

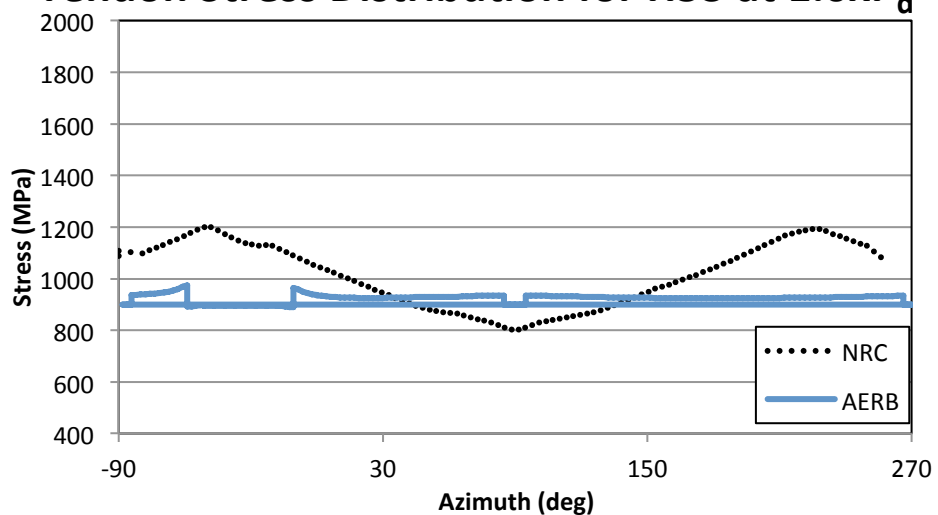


Figure 169: Tendon Stress Distribution for Tendon #H53 at $1.0 \times P_d$

Tendon Stress Distribution for H53 at $1.5 \times P_d$

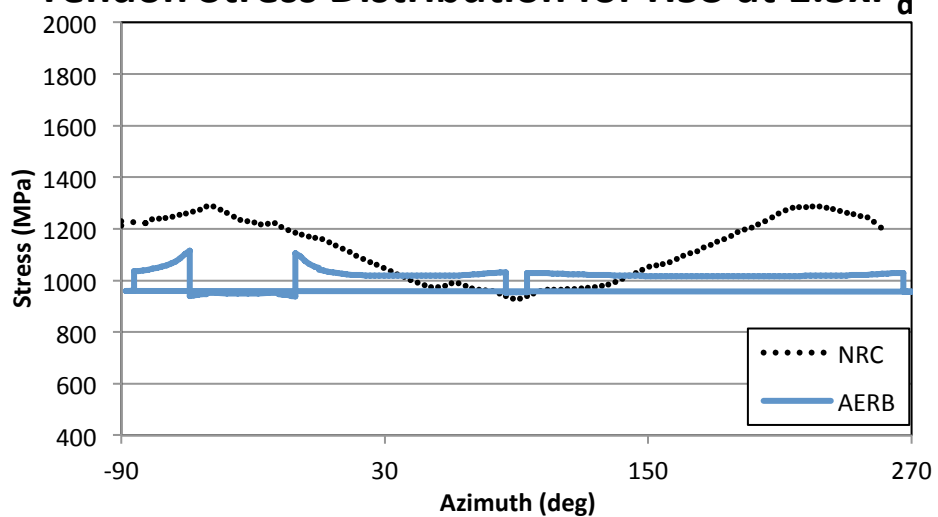


Figure 170: Tendon Stress Distribution for Tendon #H53 at $1.5 \times P_d$

Tendon Stress Distribution for H53 at $2.0 \times P_d$

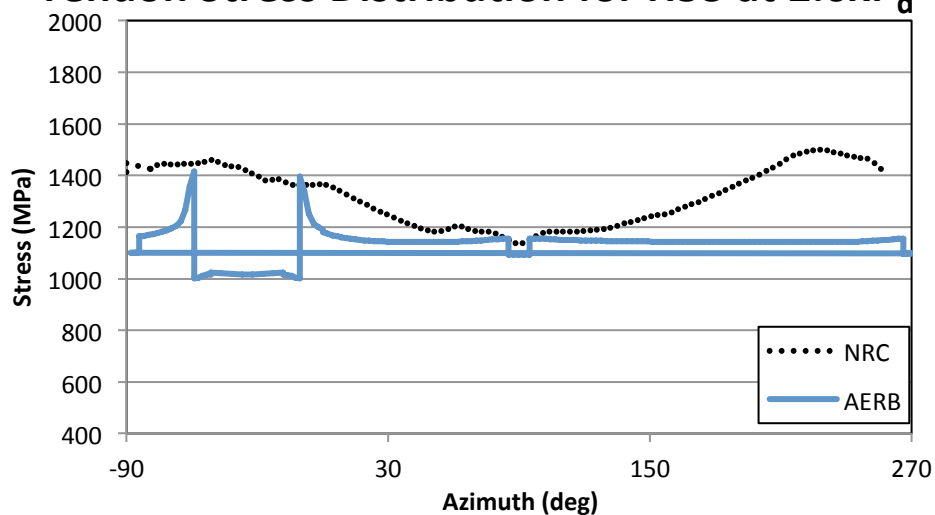


Figure 171: Tendon Stress Distribution for Tendon #H53 at $2.0 \times P_d$

Tendon Stress Distribution for H53 at $2.5 \times P_d$

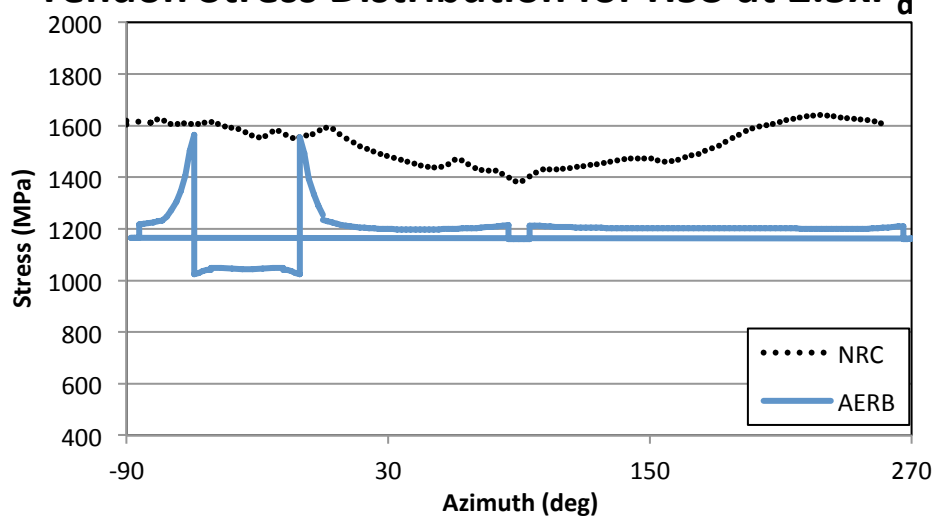


Figure 172: Tendon Stress Distribution for Tendon #H53 at $2.5 \times P_d$

Tendon Stress Distribution for H53 at $3.0 \times P_d$

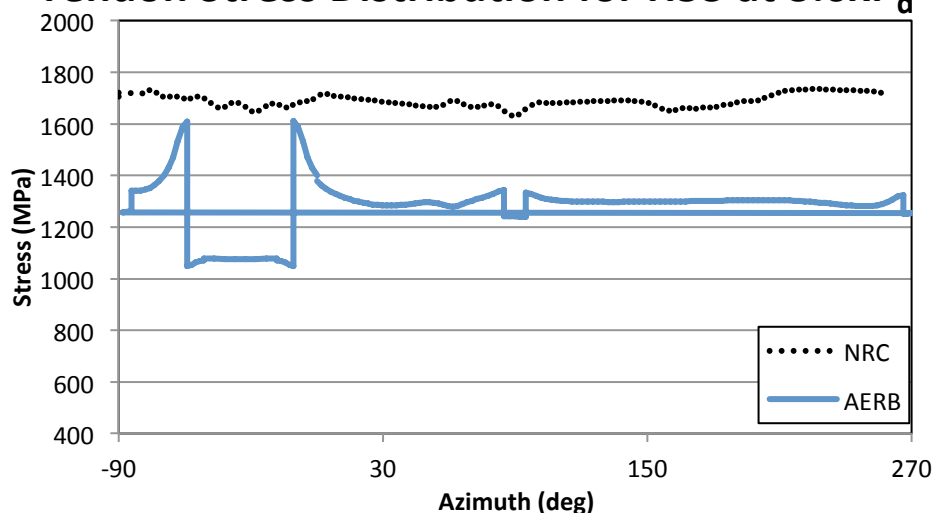


Figure 173: Tendon Stress Distribution for Tendon #H53 at $3.0 \times P_d$

Tendon Stress Distribution for H53 at $3.3 \times P_d$

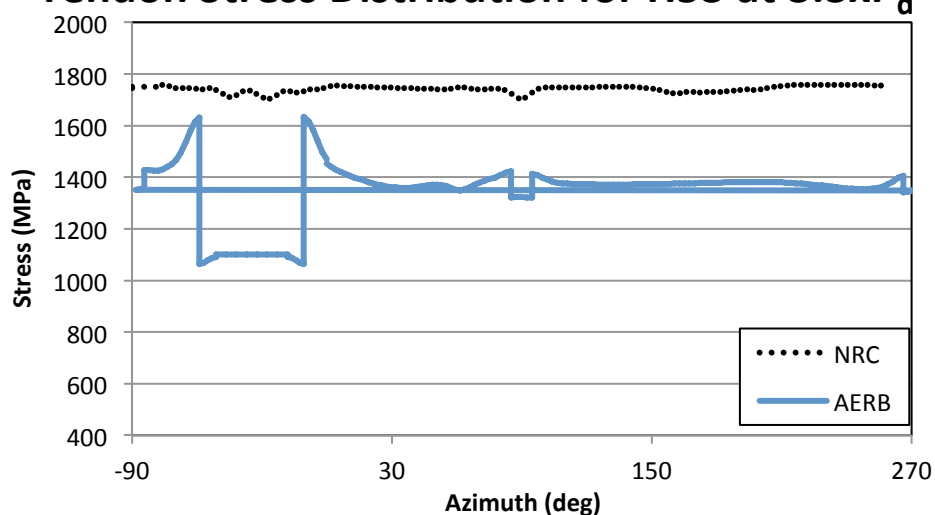


Figure 174: Tendon Stress Distribution for Tendon #H53 at $3.3 \times P_d$

Tendon Stress Distribution for H53 at $3.4 \times P_d$

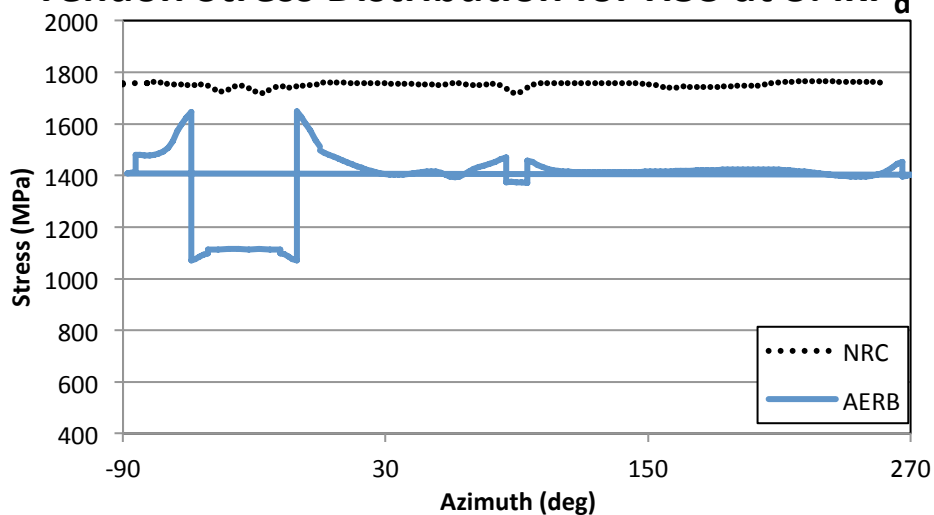


Figure 175: Tendon Stress Distribution for Tendon #H53 at $3.4 \times P_d$

Tendon Stress Distribution for H53 at Ultimate Pressure

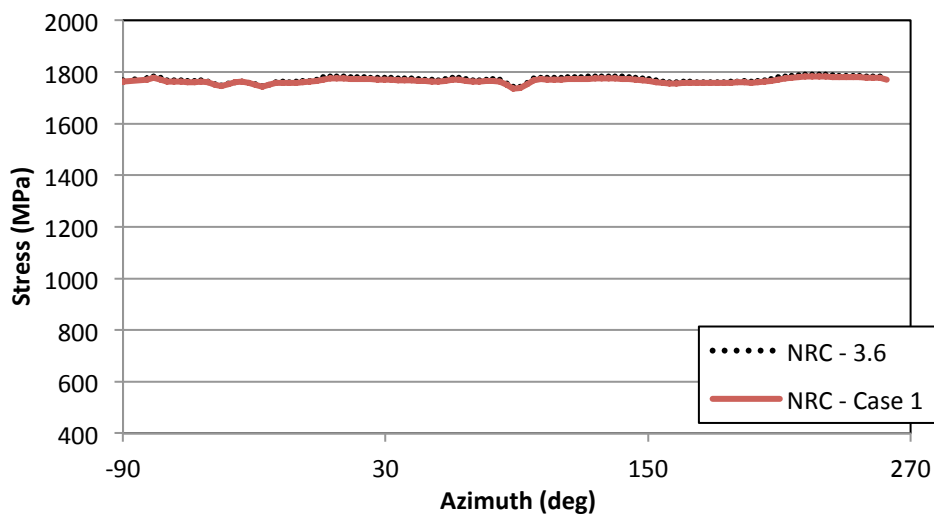


Figure 176: Tendon Stress Distribution for Tendon #H53 at Ultimate Pressure

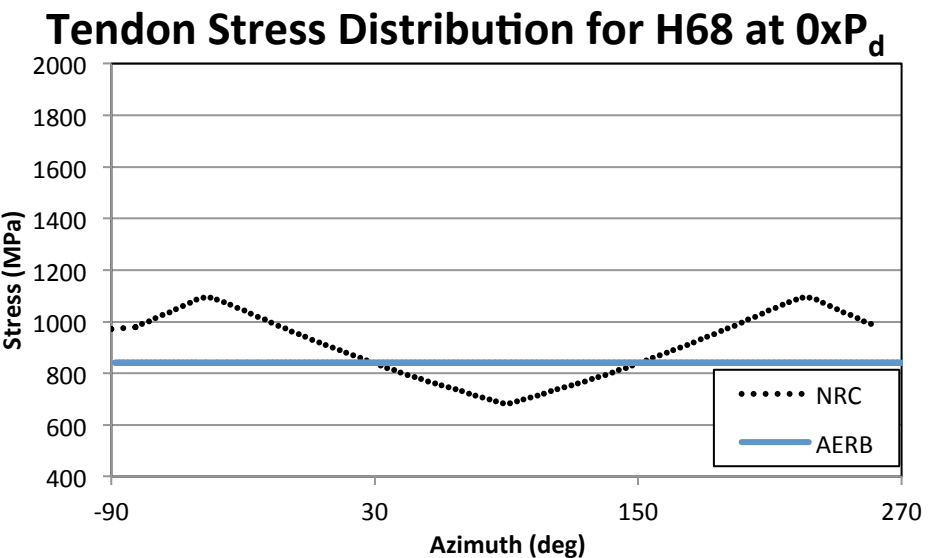


Figure 177: Tendon Stress Distribution for Tendon #H68 at 0 x P_d

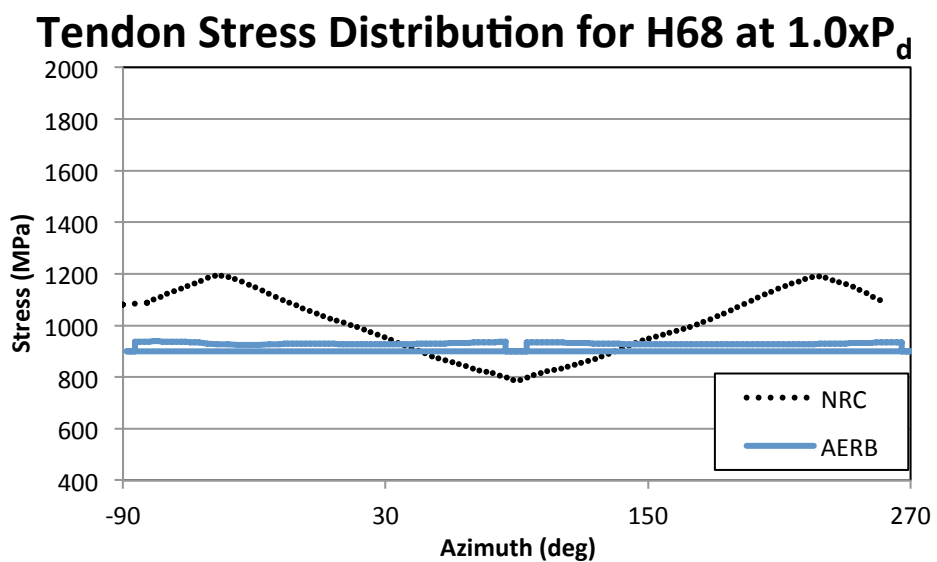


Figure 178: Tendon Stress Distribution for Tendon #H68 at 1.0 x P_d

Tendon Stress Distribution for H68 at $1.5 \times P_d$

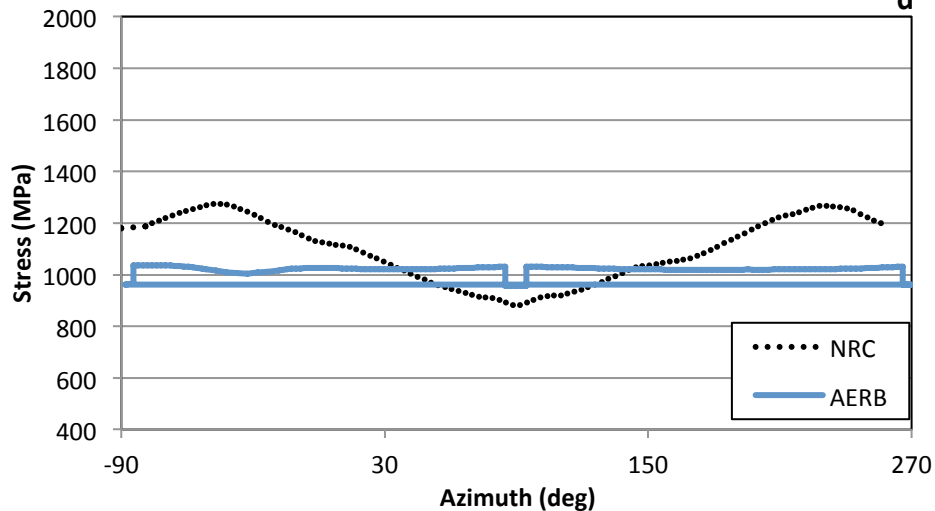


Figure 179: Tendon Stress Distribution for Tendon #H68 at $1.5 \times P_d$

Tendon Stress Distribution for H68 at $2.0 \times P_d$

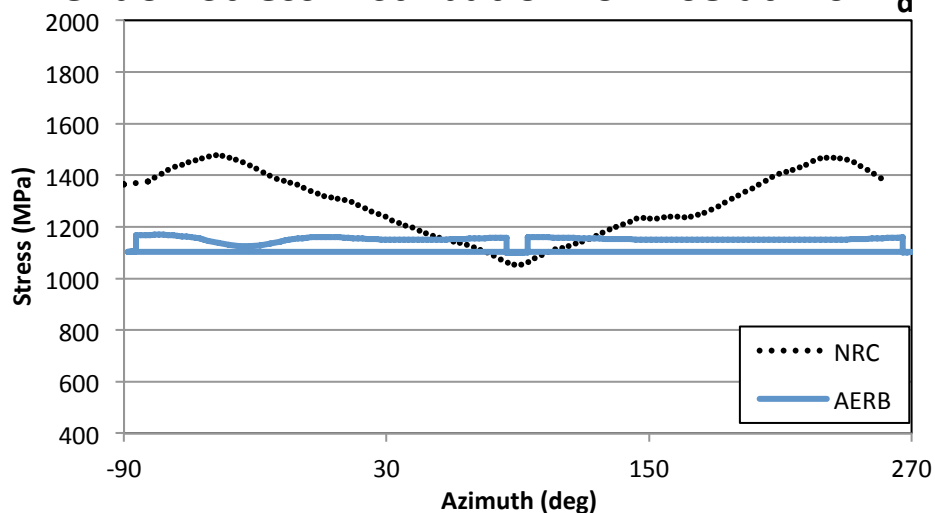


Figure 180: Tendon Stress Distribution for Tendon #H68 at $2.0 \times P_d$

Tendon Stress Distribution for H68 at $2.5 \times P_d$

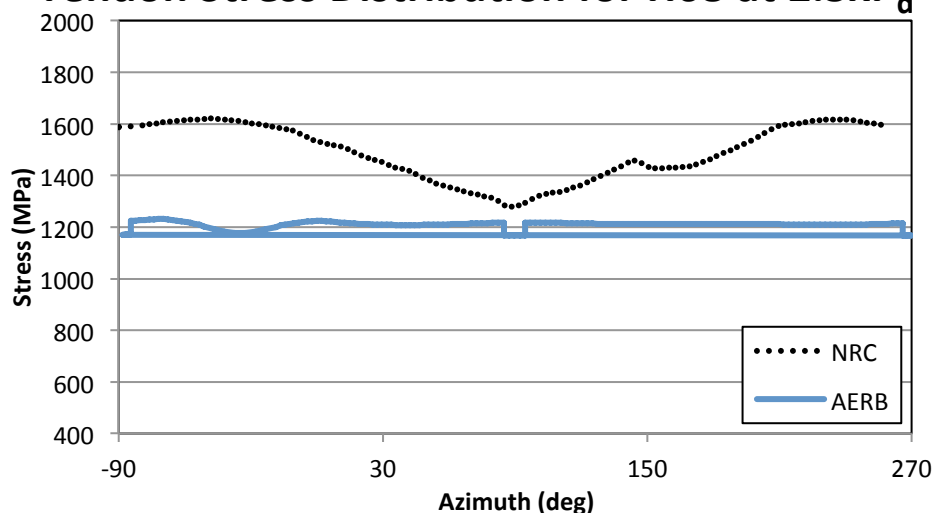


Figure 181: Tendon Stress Distribution for Tendon #H68 at $2.5 \times P_d$

Tendon Stress Distribution for H68 at $3.0 \times P_d$

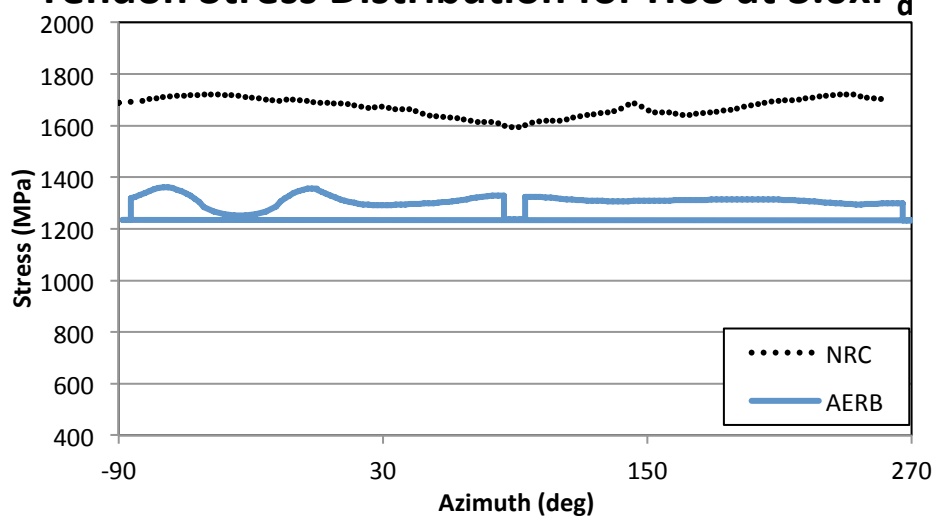


Figure 182: Tendon Stress Distribution for Tendon #H68 at $3.0 \times P_d$

Tendon Stress Distribution for H68 at $3.3 \times P_d$

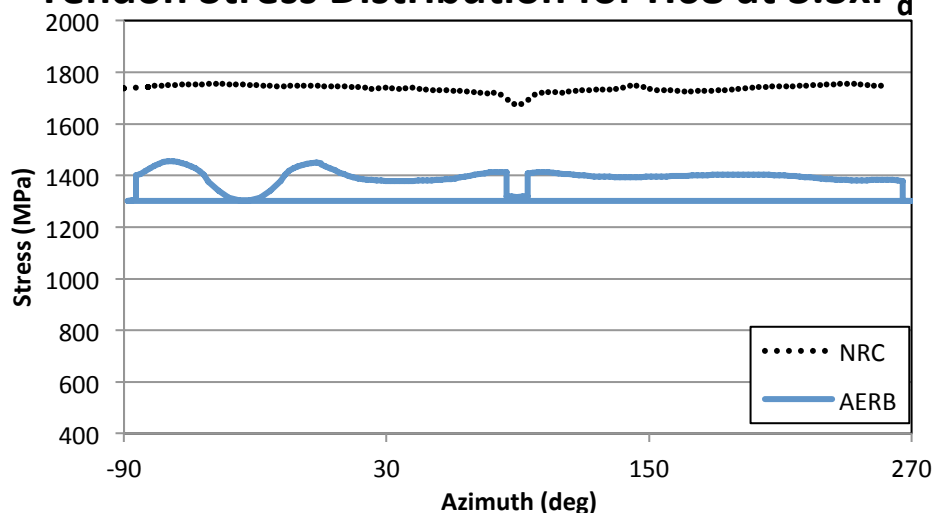


Figure 183: Tendon Stress Distribution for Tendon #H68 at $3.3 \times P_d$

Tendon Stress Distribution for H68 at $3.4 \times P_d$

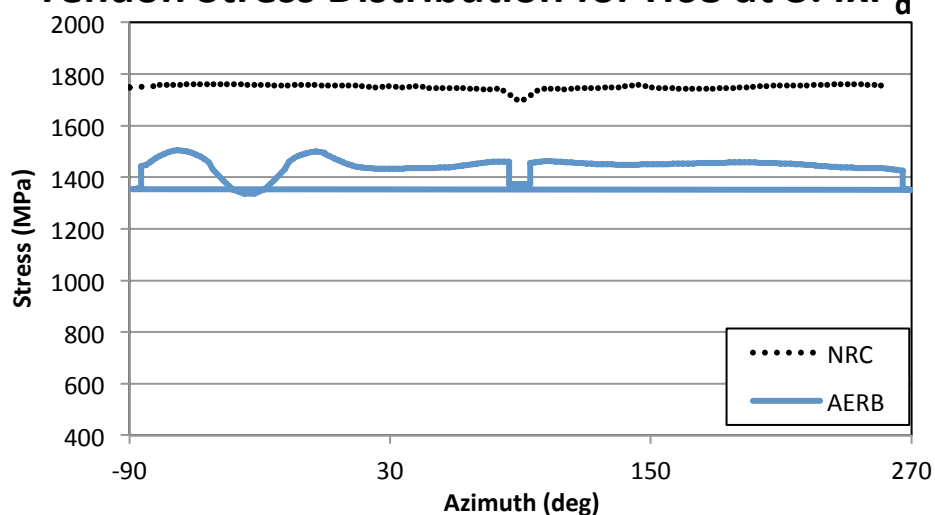


Figure 184: Tendon Stress Distribution for Tendon #H68 at $3.4 \times P_d$

Tendon Stress Distribution for H68 at Ultimate Pressure

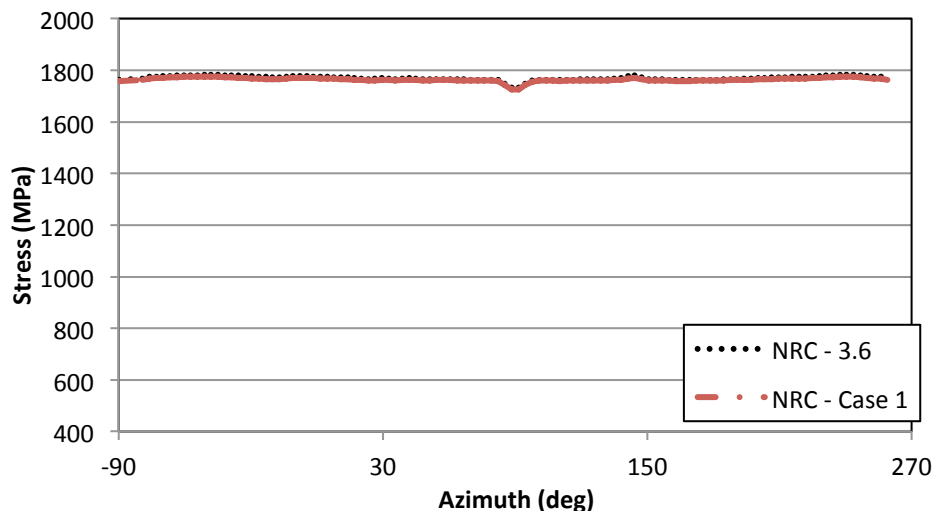


Figure 185: Tendon Stress Distribution for Tendon #H68 at Ultimate Pressure

4.3.2 Vertical Tendons

The vertical tendons selected for analysis correspond with tendons #V37, V46 from the PCCV test, and as stated earlier, this selection facilitates comparison with the most instrumented tendons from the test. There appears to be less agreement between the participants for the vertical tendons when compared with the hoop tendons in the previous section. The source of this deviation is not immediately known. The tendon stress versus location plots for the vertical tendons can be found in Figure 186 through Figure 203. AERB did not provide data for V46 at ultimate pressure, so the NRC results for Case 2 are compared to the Case 1 results in Figure 203. Interestingly, the results are quite comparable.

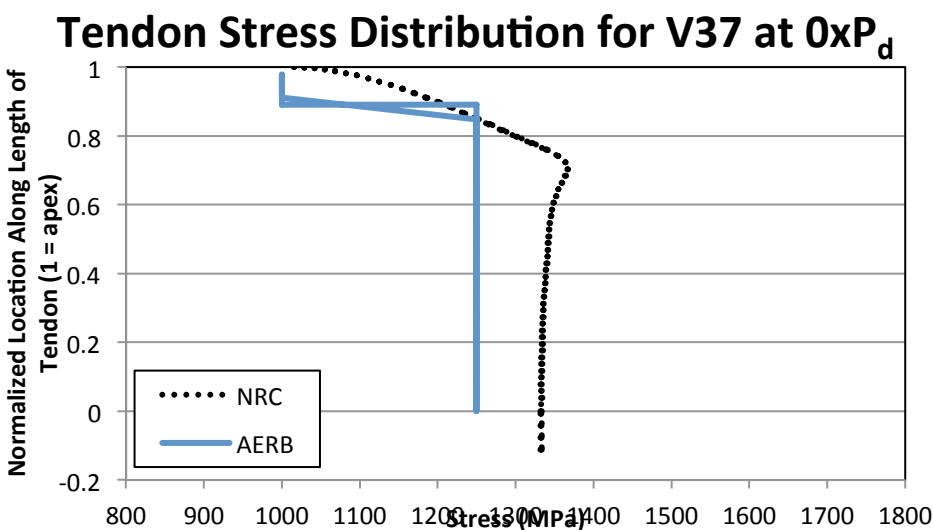


Figure 186: Tendon Stress Distribution for Tendon #V37 at $0 \times P_d$

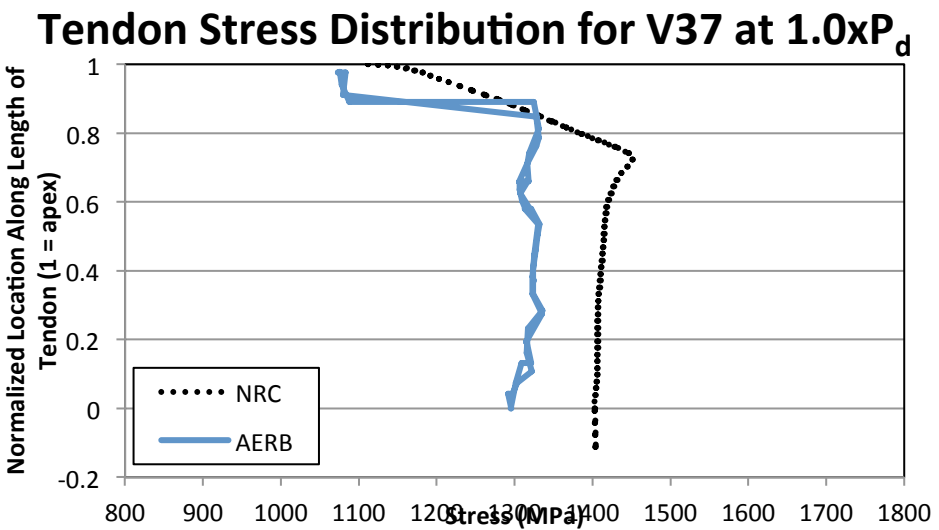


Figure 187: Tendon Stress Distribution for Tendon #V37 at $1.0 \times P_d$

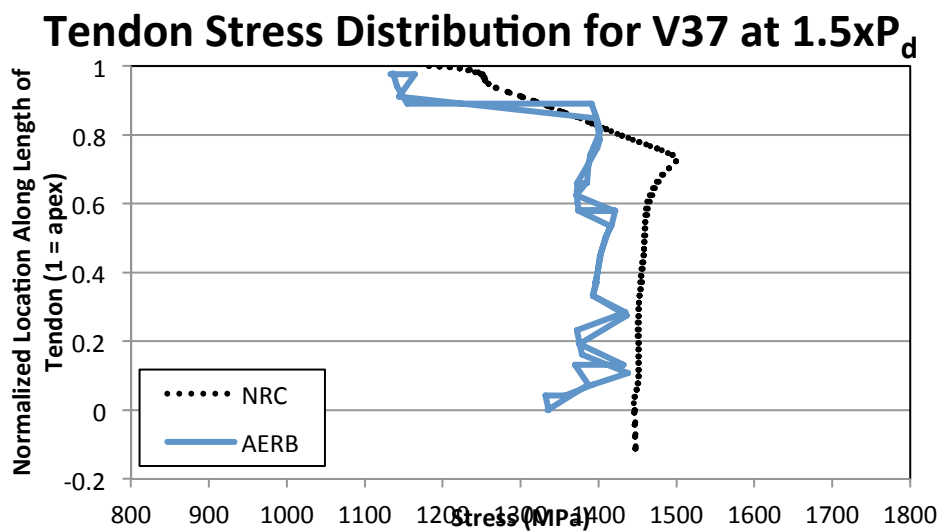


Figure 188: Tendon Stress Distribution for Tendon #V37 at $1.5 \times P_d$

Tendon Stress Distribution for V37 at $2.0 \times P_d$

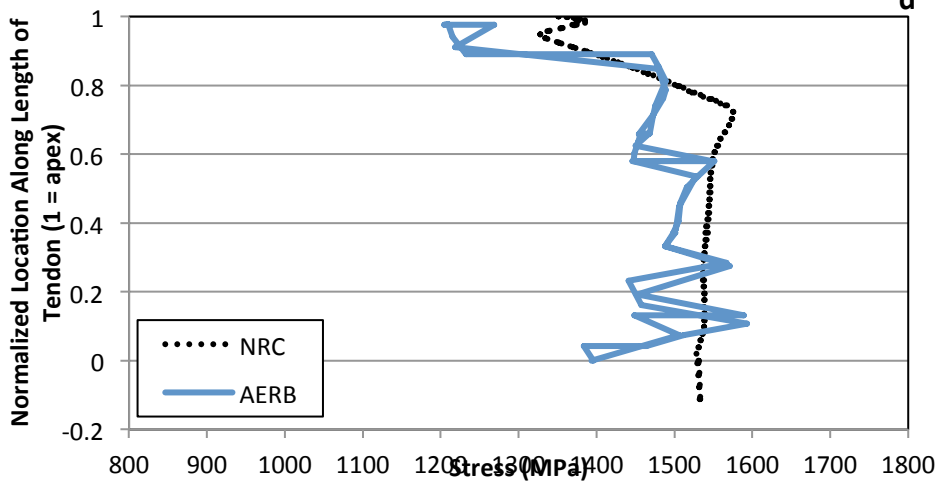


Figure 189: Tendon Stress Distribution for Tendon #V37 at $2.0 \times P_d$

Tendon Stress Distribution for V37 at $2.5 \times P_d$

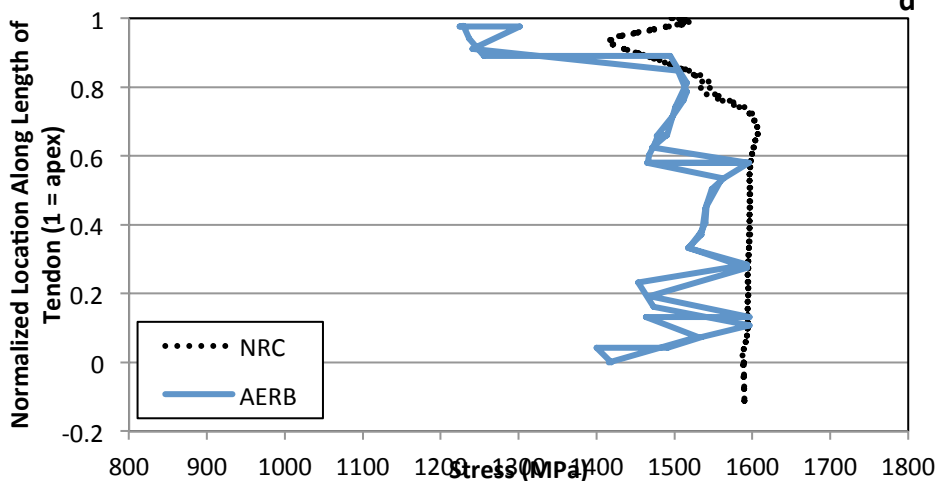


Figure 190: Tendon Stress Distribution for Tendon #V37 at $2.5 \times P_d$

Tendon Stress Distribution for V37 at $3.0 \times P_d$

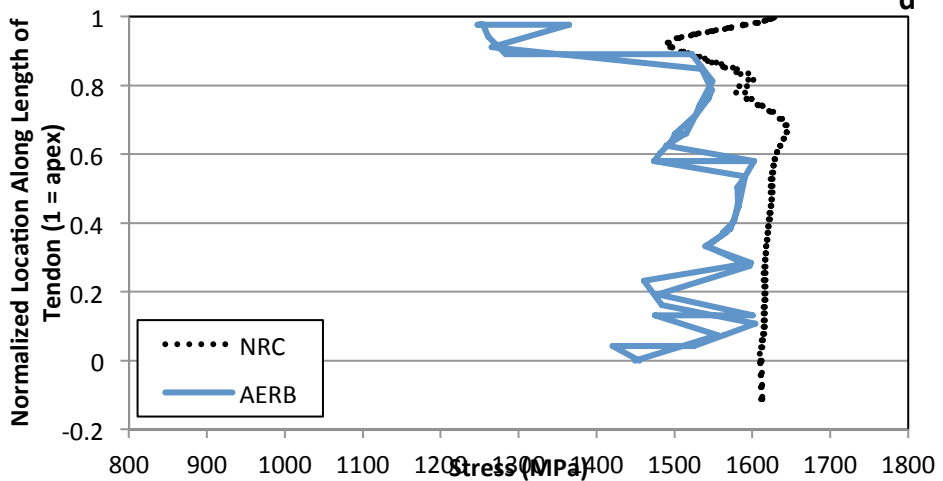


Figure 191: Tendon Stress Distribution for Tendon #V37 at $3.0 \times P_d$

Tendon Stress Distribution for V37 at $3.3 \times P_d$

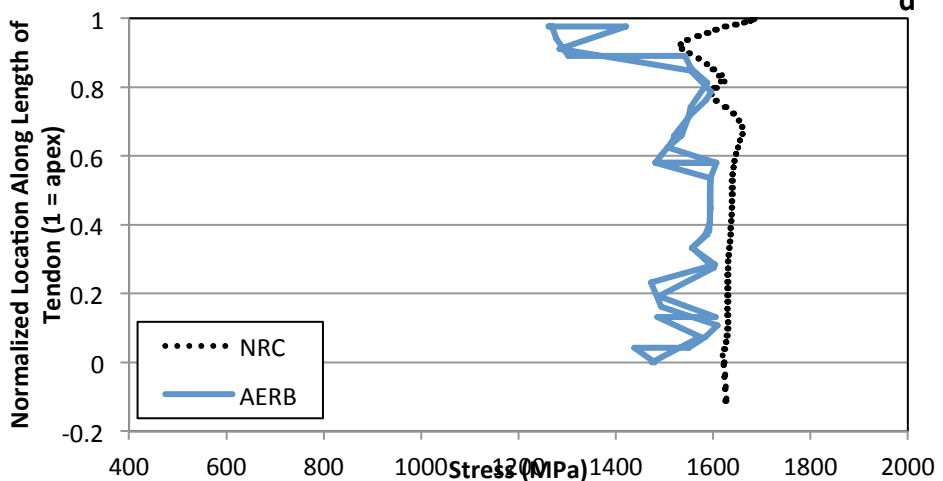


Figure 192: Tendon Stress Distribution for Tendon #V37 at $3.3 \times P_d$

Tendon Stress Distribution for V37 at $3.4 \times P_d$

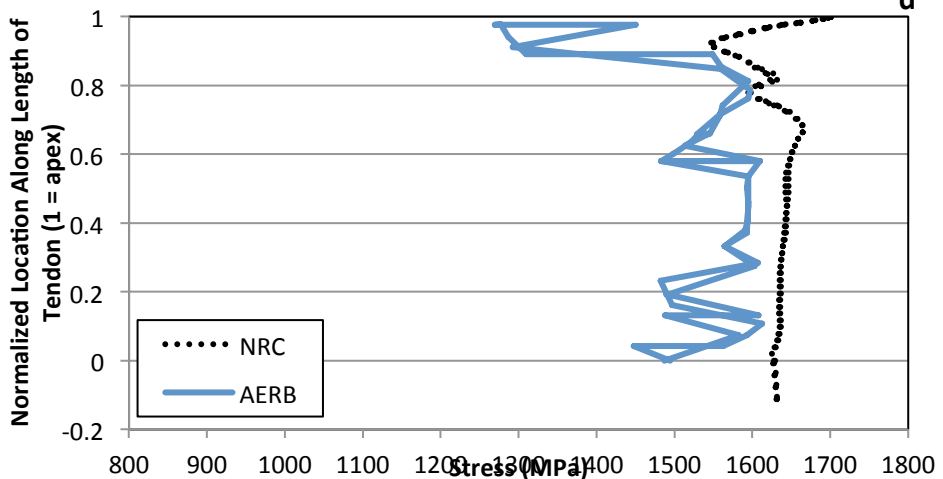


Figure 193: Tendon Stress Distribution for Tendon #V37 at $3.4 \times P_d$

Tendon Stress Distribution for V37 at Ultimate Pressure

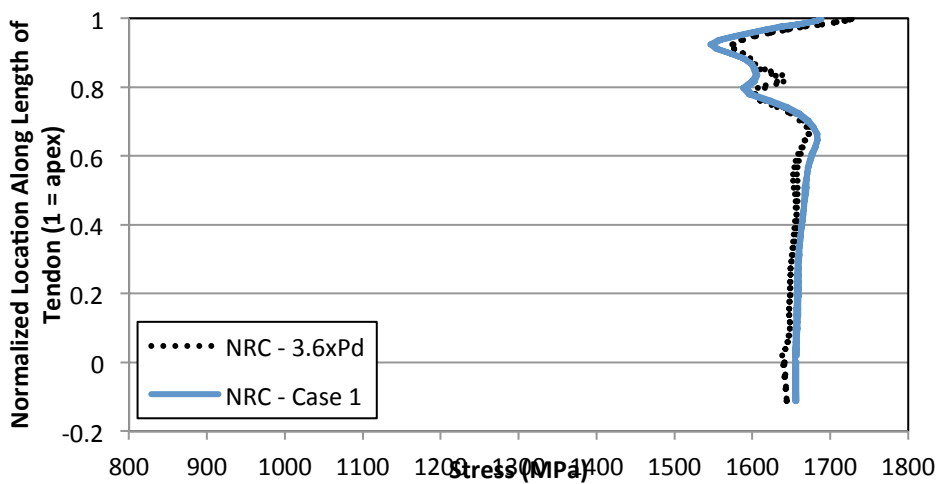


Figure 194: Tendon Stress Distribution for Tendon #V37 at Ultimate Pressure

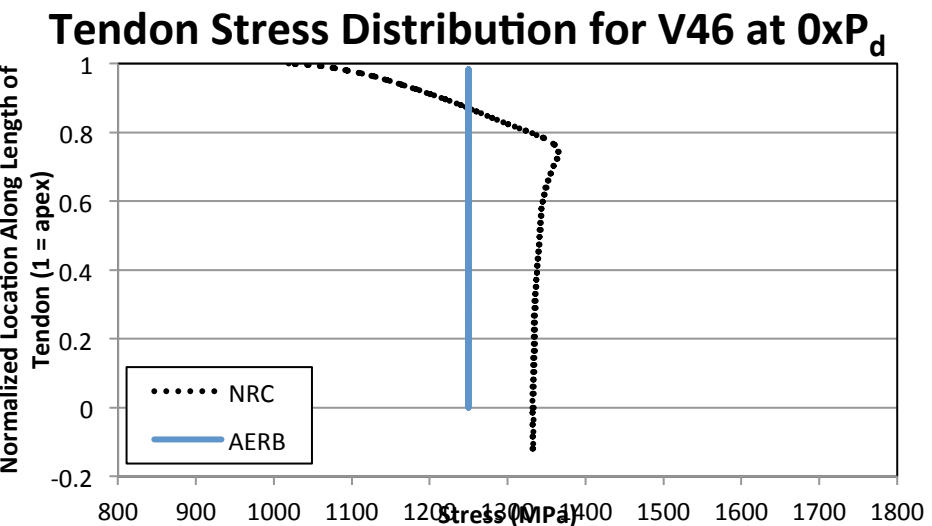


Figure 195: Tendon Stress Distribution for Tendon #V46 at 0 x P_d

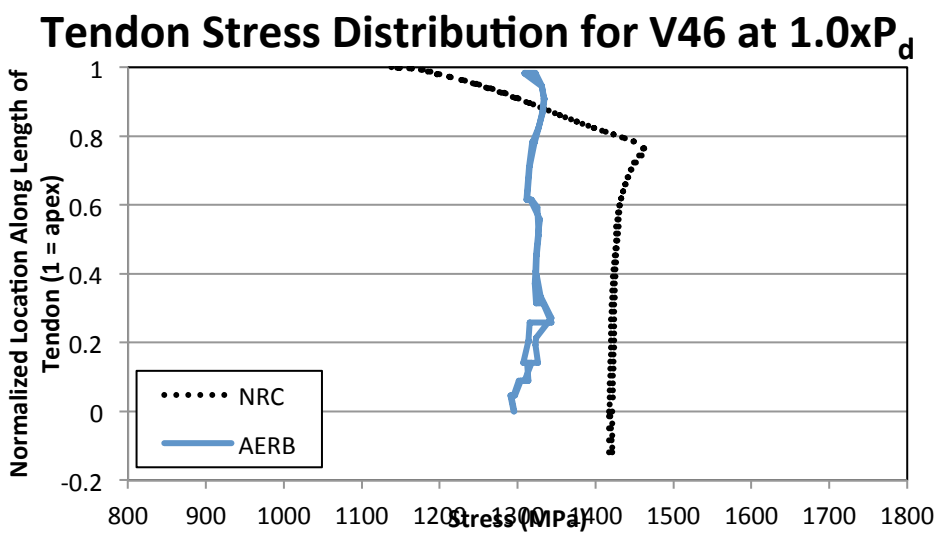


Figure 196: Tendon Stress Distribution for Tendon #V46 at 1.0 x P_d

Tendon Stress Distribution for V46 at $1.5 \times P_d$

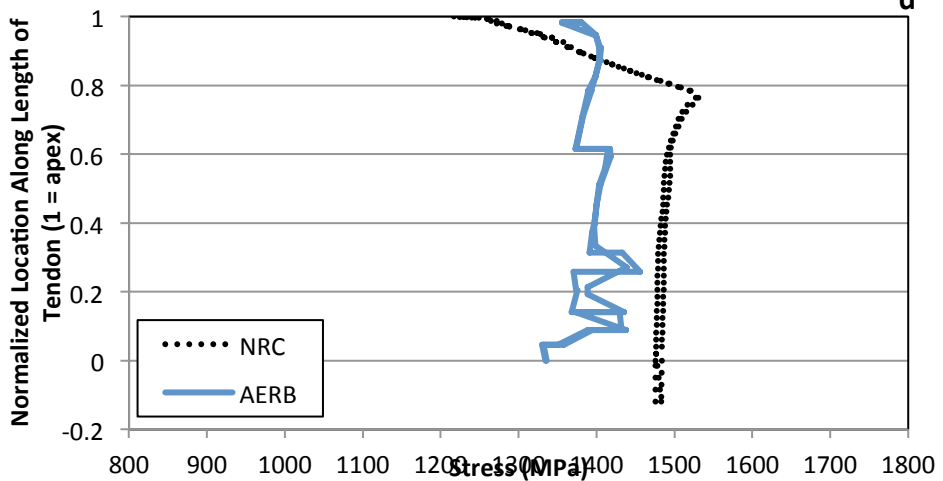


Figure 197: Tendon Stress Distribution for Tendon #V46 at $1.5 \times P_d$

Tendon Stress Distribution for V46 at $2.0 \times P_d$

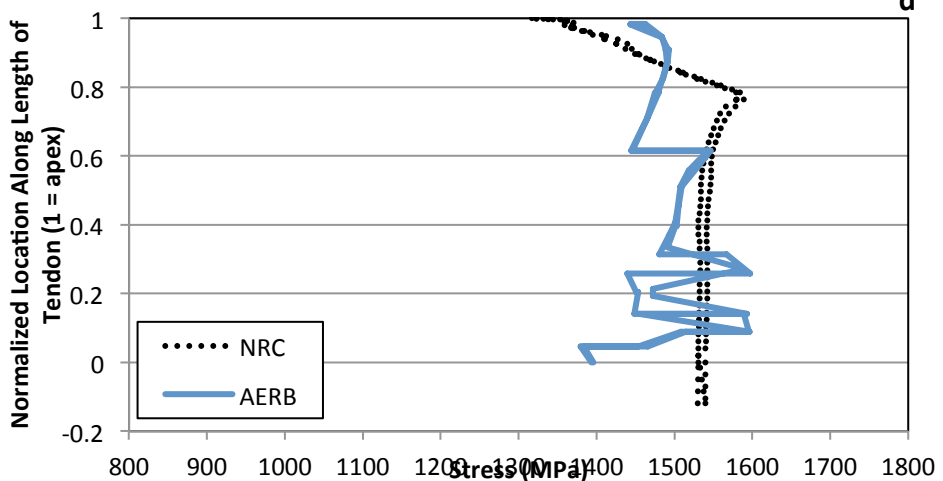


Figure 198: Tendon Stress Distribution for Tendon #V46 at $2.0 \times P_d$

Tendon Stress Distribution for V46 at $2.5 \times P_d$

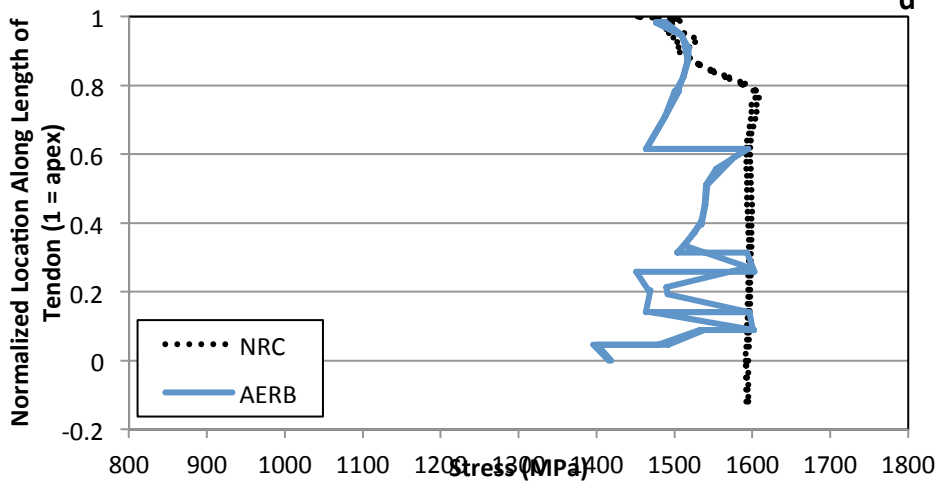


Figure 199: Tendon Stress Distribution for Tendon #V46 at $2.5 \times P_d$

Tendon Stress Distribution for V46 at $3.0 \times P_d$

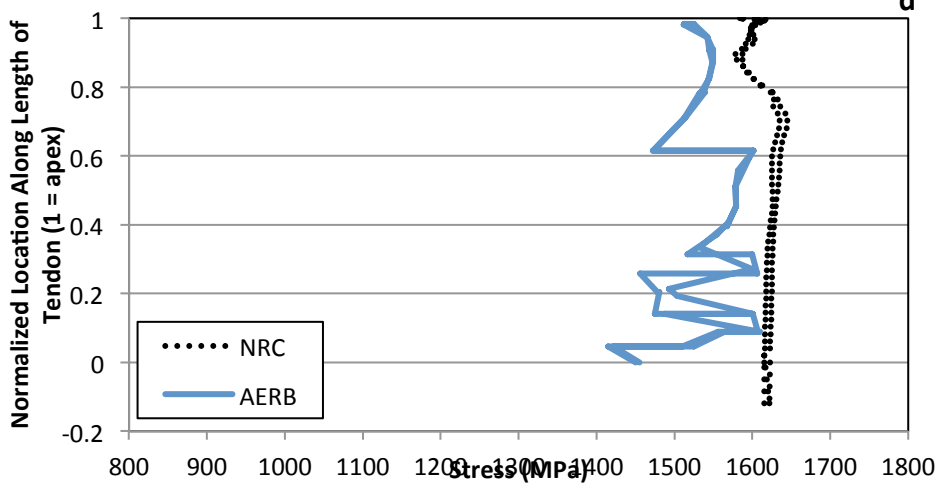


Figure 200: Tendon Stress Distribution for Tendon #V46 at $3.0 \times P_d$

Tendon Stress Distribution for V46 at $3.3 \times P_d$

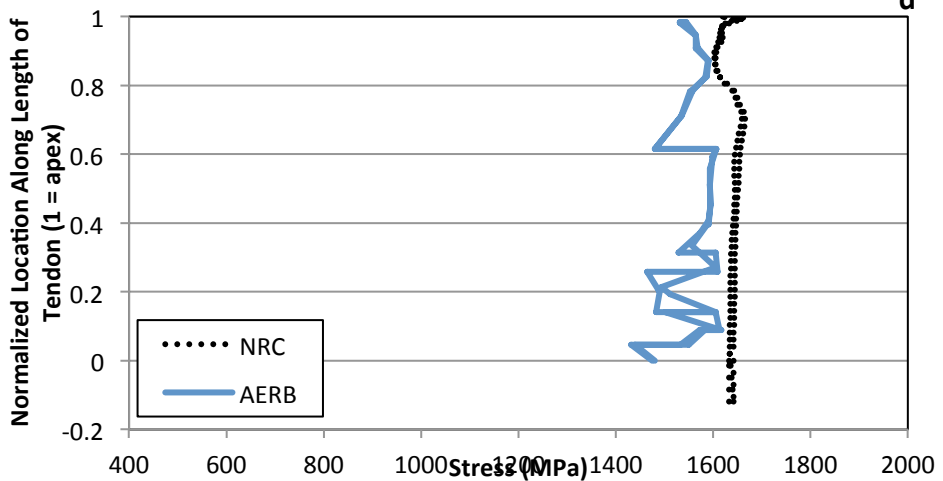


Figure 201: Tendon Stress Distribution for Tendon #V46 at $3.3 \times P_d$

Tendon Stress Distribution for V46 at $3.4 \times P_d$

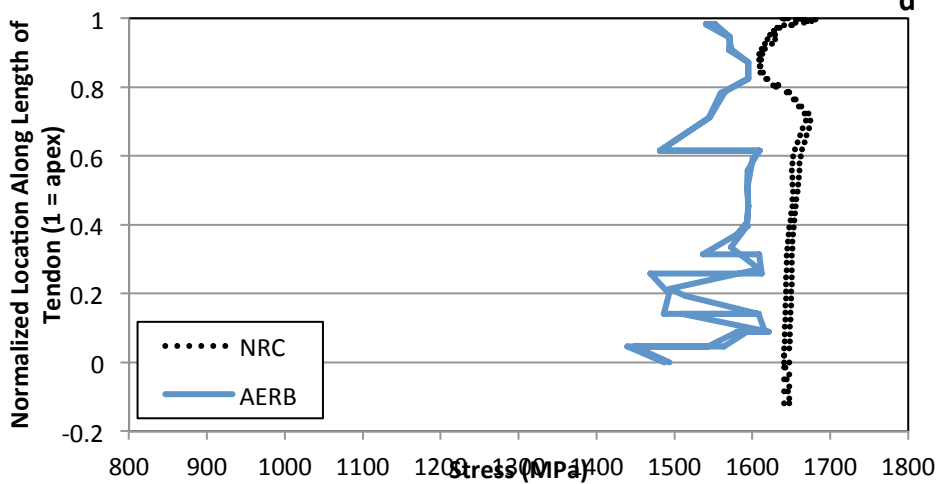


Figure 202: Tendon Stress Distribution for Tendon #V46 at $3.4 \times P_d$

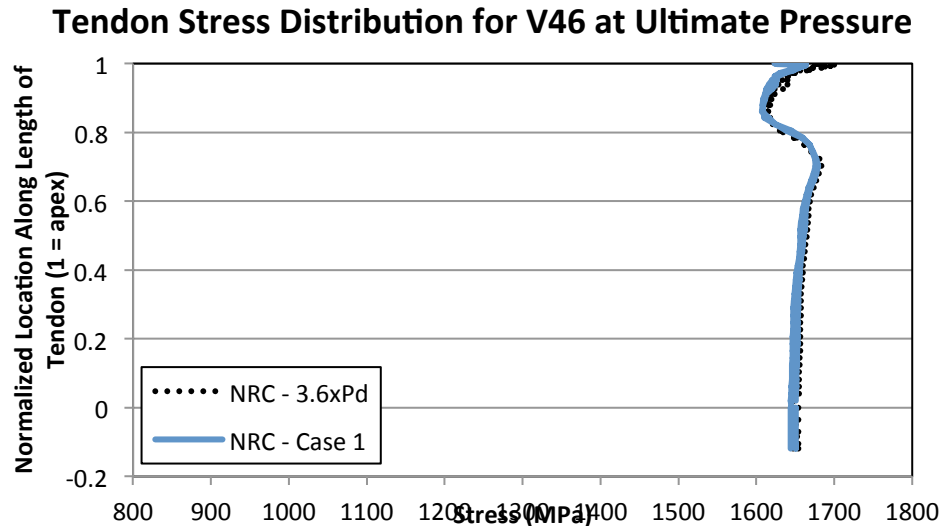


Figure 203: Tendon Stress Distribution for Tendon #V46 at Ultimate Pressure

4.4 Standard Output Location Comparisons

This section of the report compares the modeled results from the participants with the standard output locations (SOLs) from the PCCV test. This section serves to provide the most direct comparison to the experimental results and is therefore considered very valuable for evaluating the modeling of the participants.

4.4.1 Displacements

The first 15 SOLs involve displacement measurements both in the radial and meridional directions. The nature of the displacement is indicated in the figure caption for each figure in this section and the plots comparing the participants' data with test data for SOLs 1-15 can be found in Figure 204 through Figure 218. As before, the participants' data agree well with test data, particularly well at the lower pressure levels. As the internal pressure approaches the failure level more divergence both between the participants and between the modeled and test data is noted.

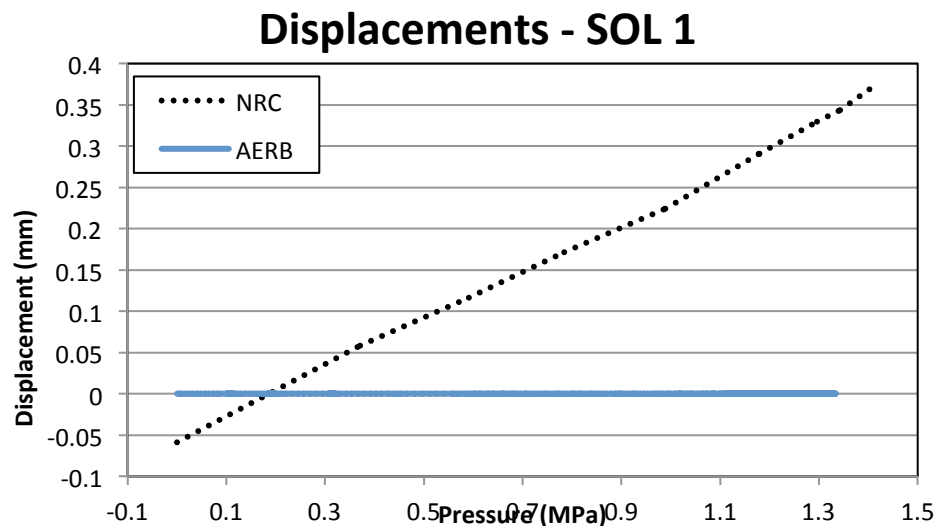


Figure 204: Displacement Versus Pressure at SOL #1 (Vertical Displacement at Top of Basemat)

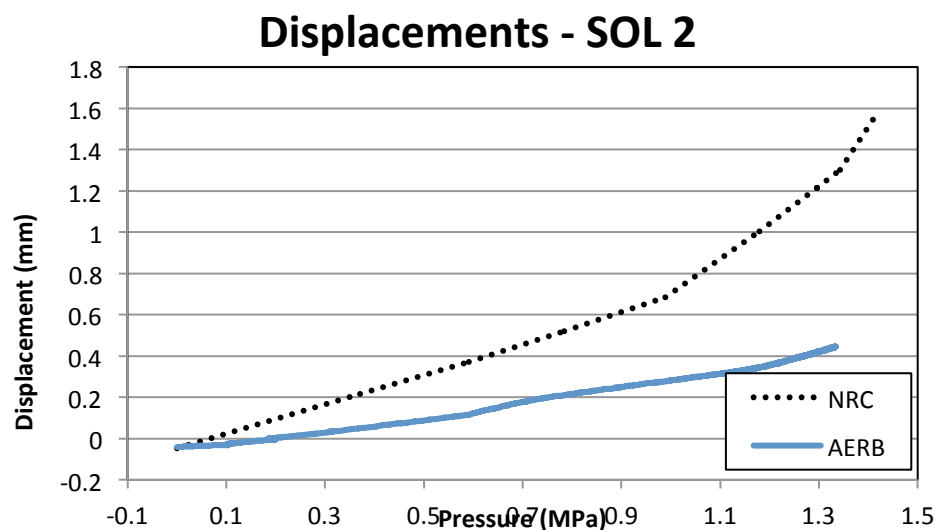


Figure 205: Displacement Versus Pressure at SOL #2 (Radial Displacement at Base of Cylinder)

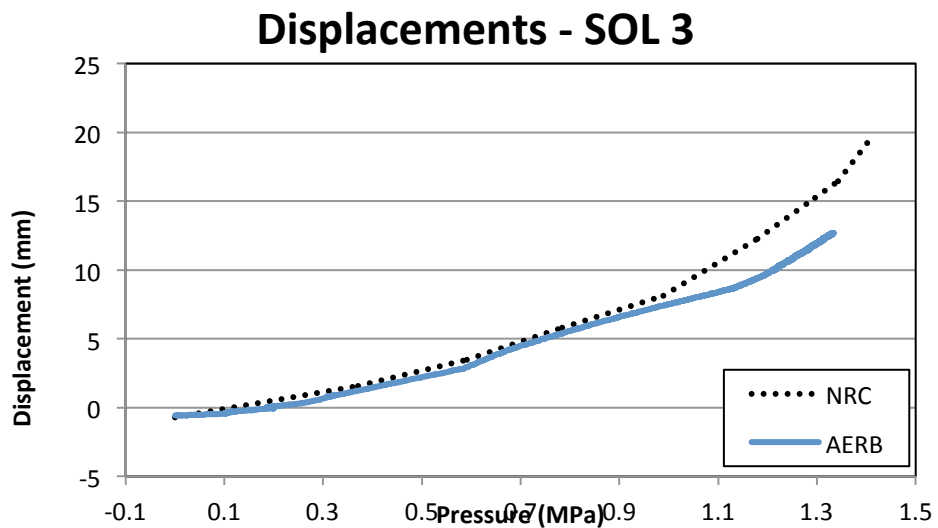


Figure 206: Displacement Versus Pressure at SOL #3 (Radial Displacement at Base of Cylinder)

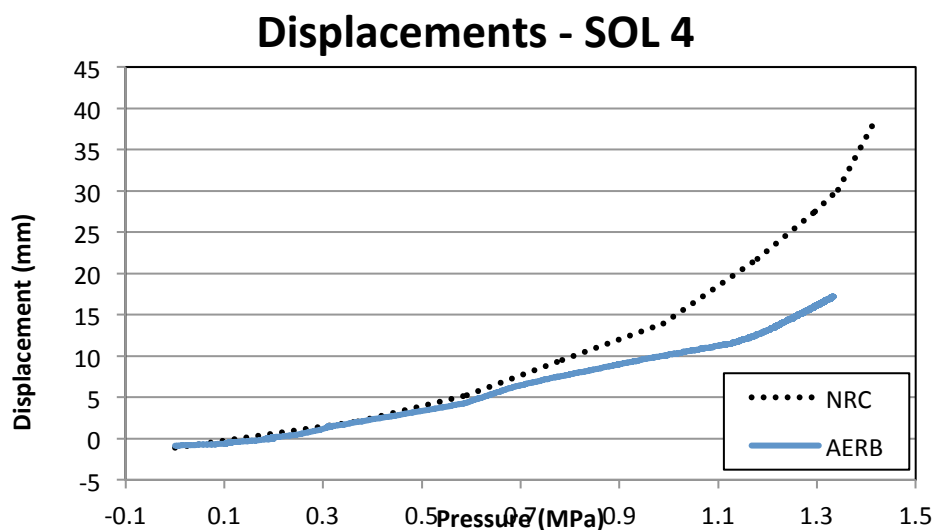


Figure 207: Displacement Versus Pressure at SOL #4 (Radial Displacement at Base of Cylinder)

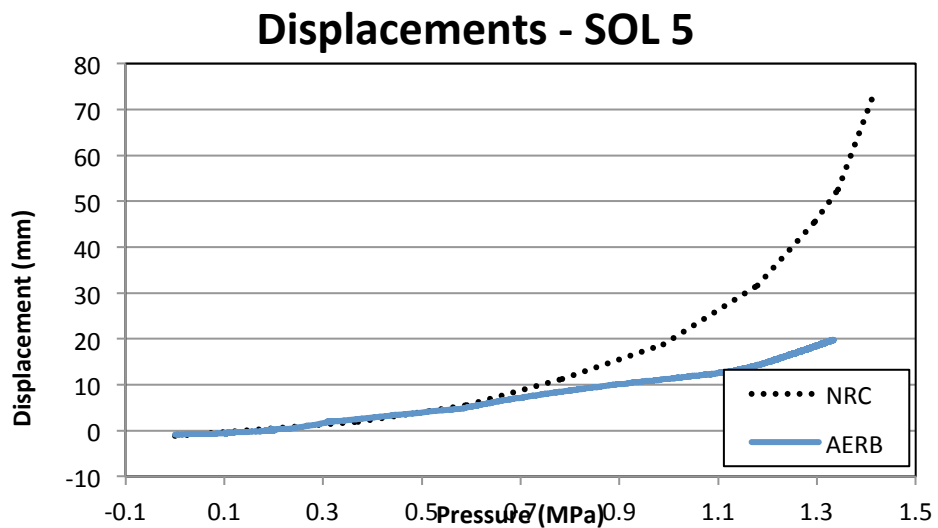


Figure 208: Displacement Versus Pressure at SOL #5 (Radial Displacement at E/H Elevation)

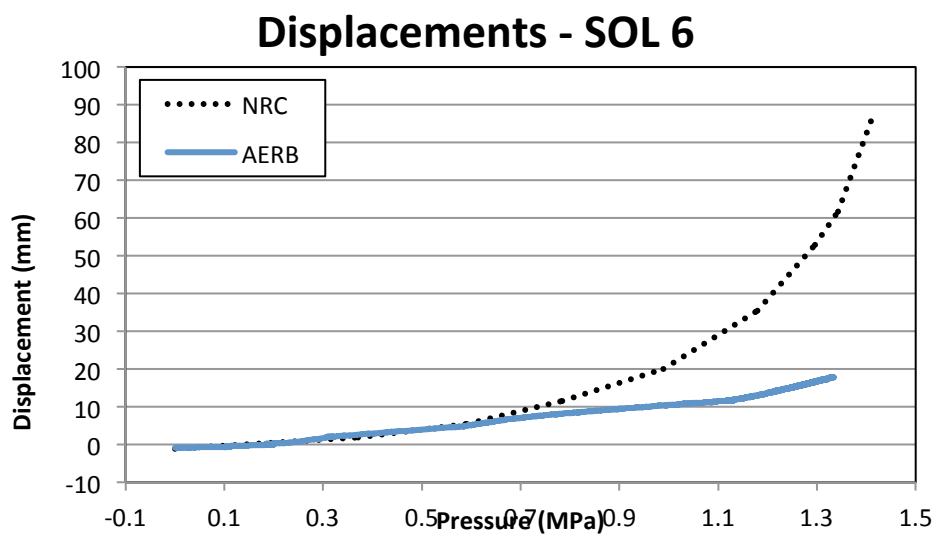


Figure 209: Displacement Versus Pressure at SOL #6 (Radial Displacement at Midheight)

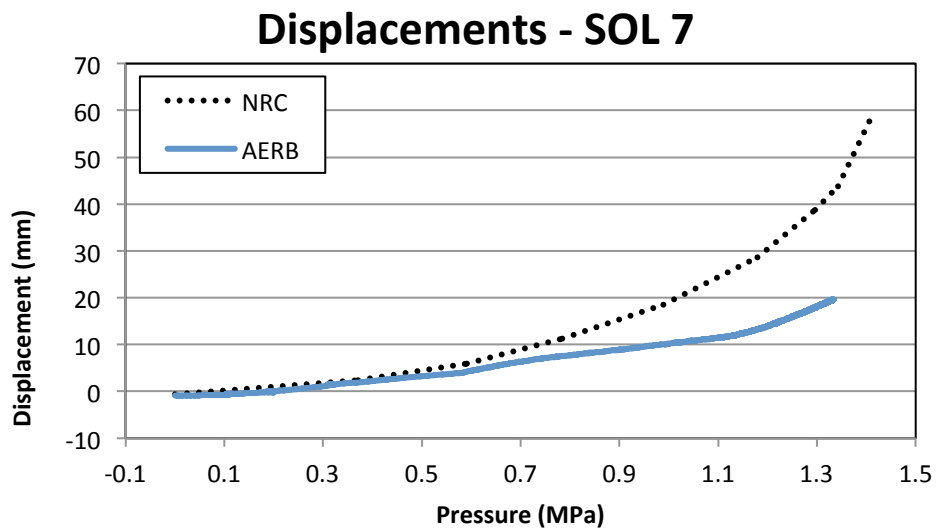


Figure 210: Displacement Versus Pressure at SOL #7 (Radial Displacement at Springline)

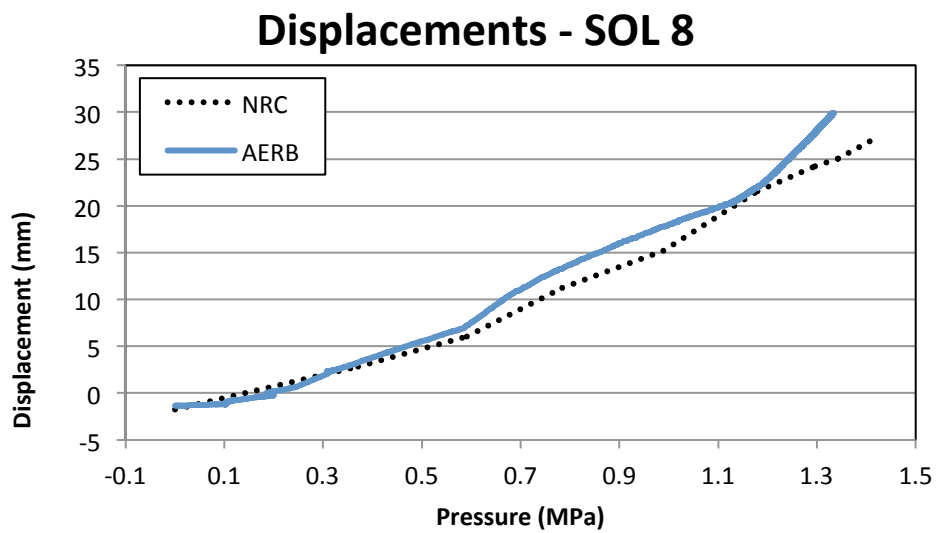


Figure 211: Displacement Versus Pressure at SOL #8 (Vertical Displacement at Springline)

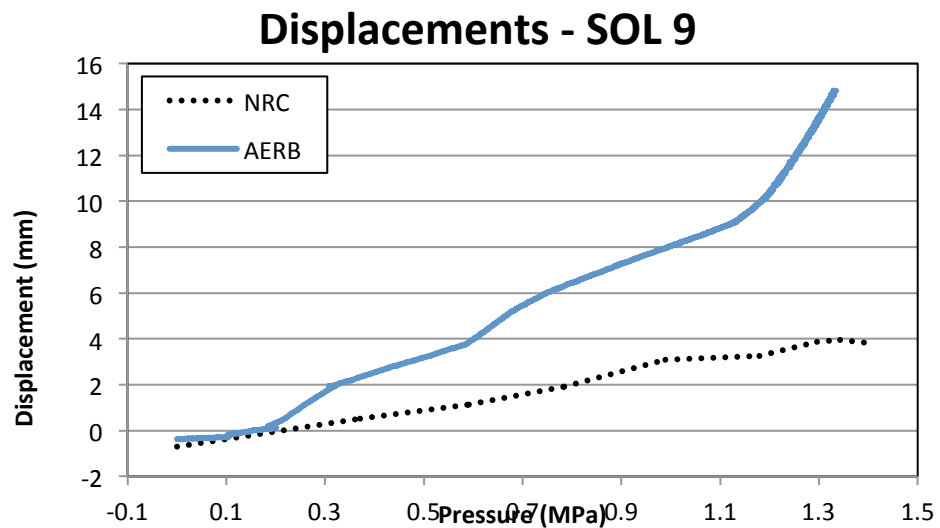


Figure 212: Displacement Versus Pressure at SOL #9 (Radial Displacement at Dome 45°)

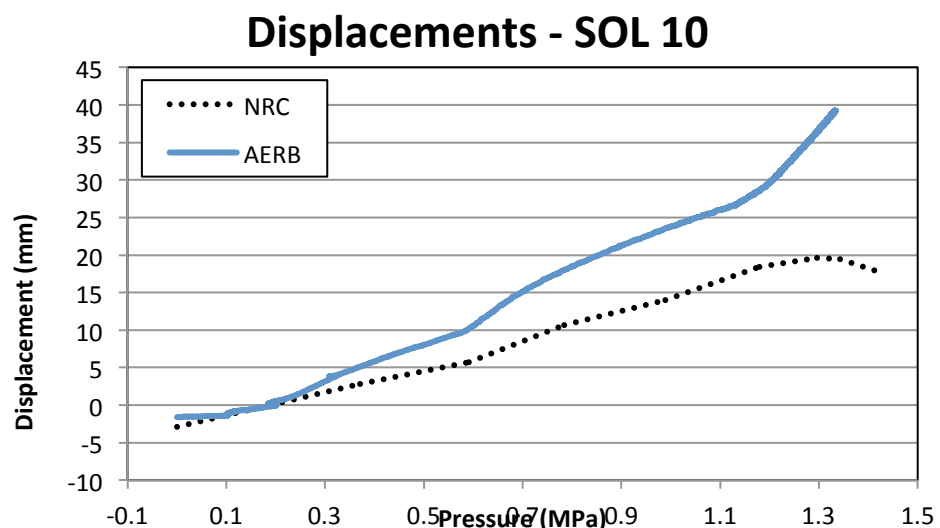


Figure 213: Displacement Versus Pressure at SOL #10 (Vertical Displacement at Dome 45°)

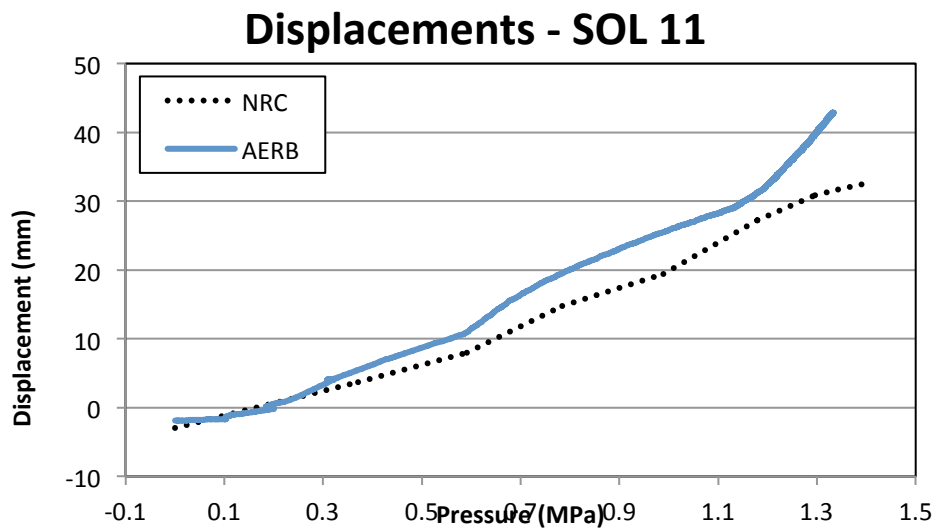


Figure 214: Displacement Versus Pressure at SOL #11 (Vertical Displacement at Dome Apex)

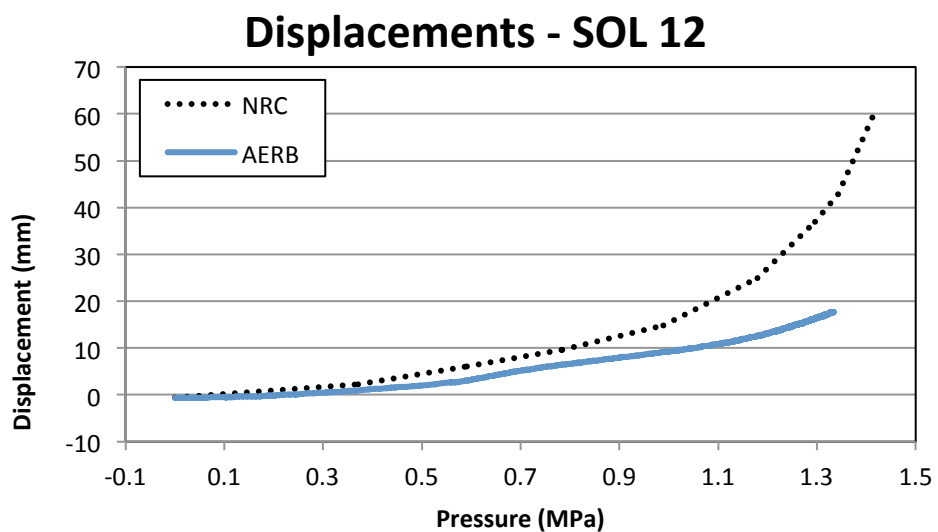


Figure 215: Displacement Versus Pressure at SOL #12 (Radial Displacement at Midheight of Buttress)

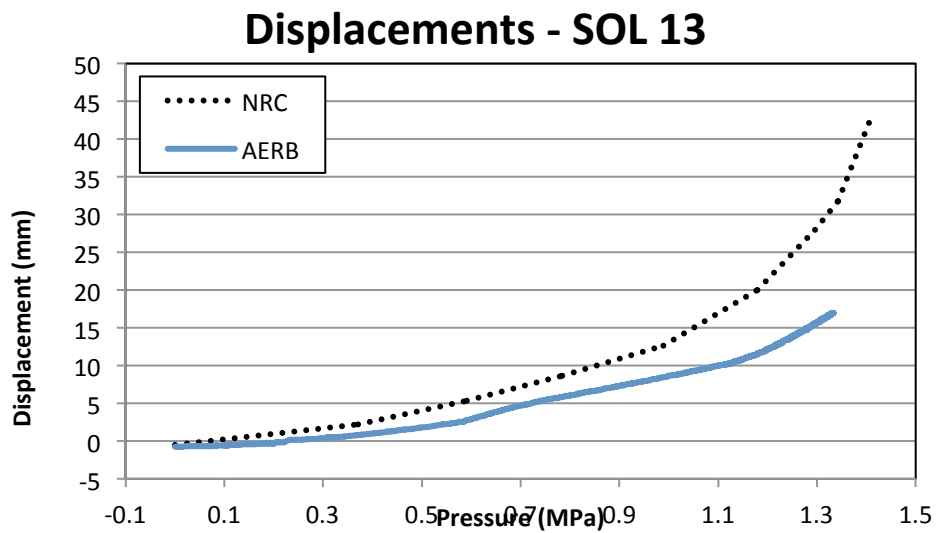


Figure 216: Displacement Versus Pressure at SOL #13 (Radial Displacement at Springline of Buttress)

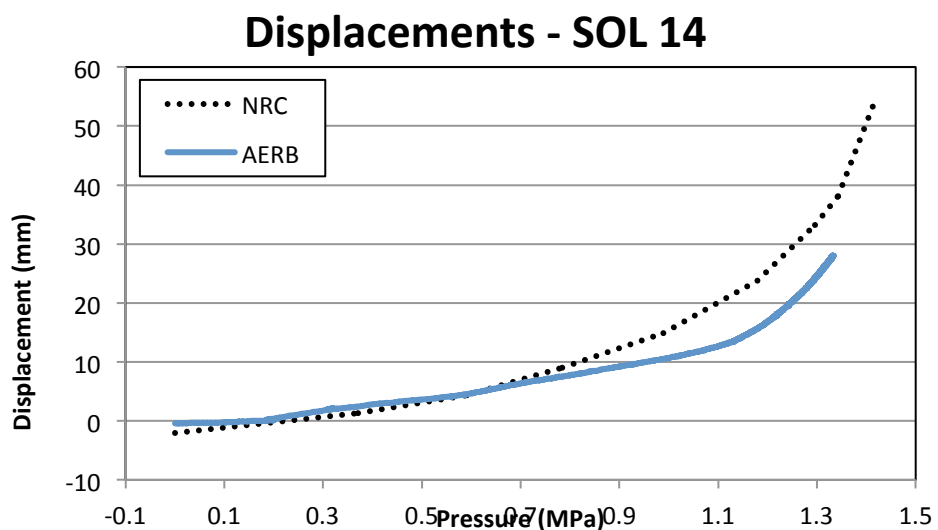


Figure 217: Displacement Versus Pressure at SOL #14 (Radial Displacement at Center of E/H)

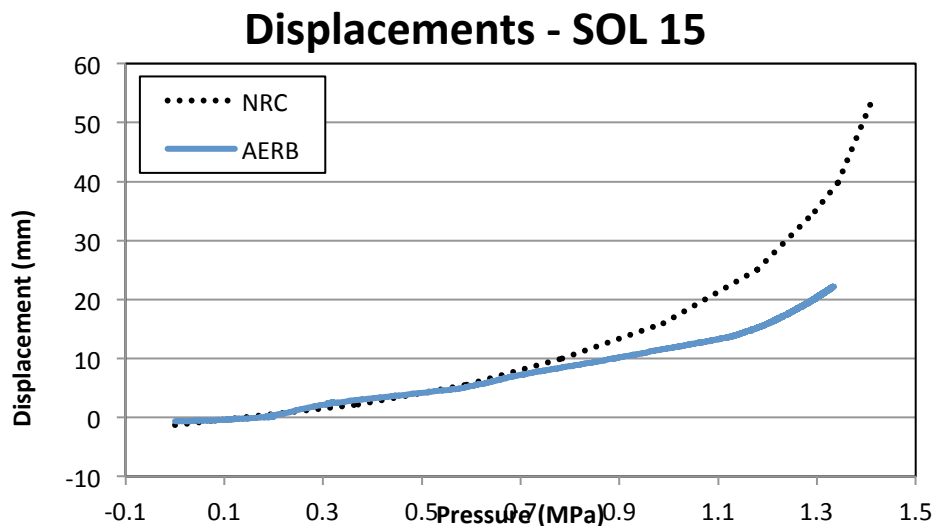


Figure 218: Displacement Versus Pressure at SOL #15 (Radial Displacement at Center of A/L)

4.4.2 Rebar Strains

The participants were asked to report results for rebar strains at locations SOL 22-29. The rebar SOL comparison plots can be found in Figure 219 through Figure 226.

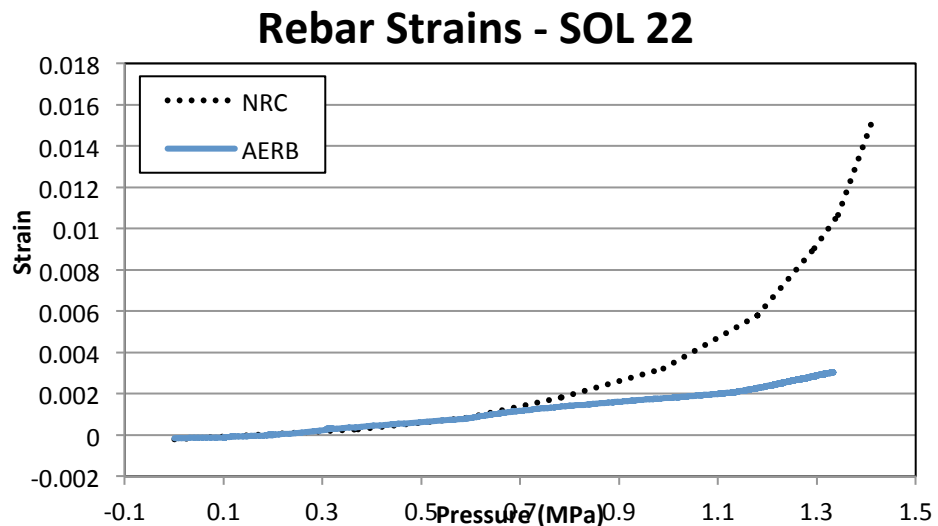


Figure 219: Rebar Strain Versus Pressure at SOL #22 (Hoop Strain of Outer Rebar at Midheight and Azimuth 135)

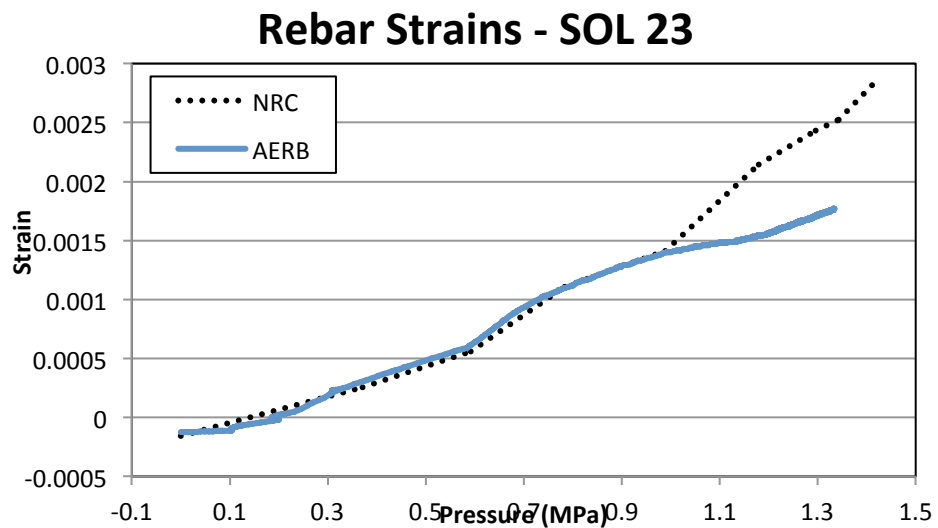


Figure 220: Rebar Strain Versus Pressure at SOL #23 (Meridional Strain of Outer Rebar at Midheight and Azimuth 135)

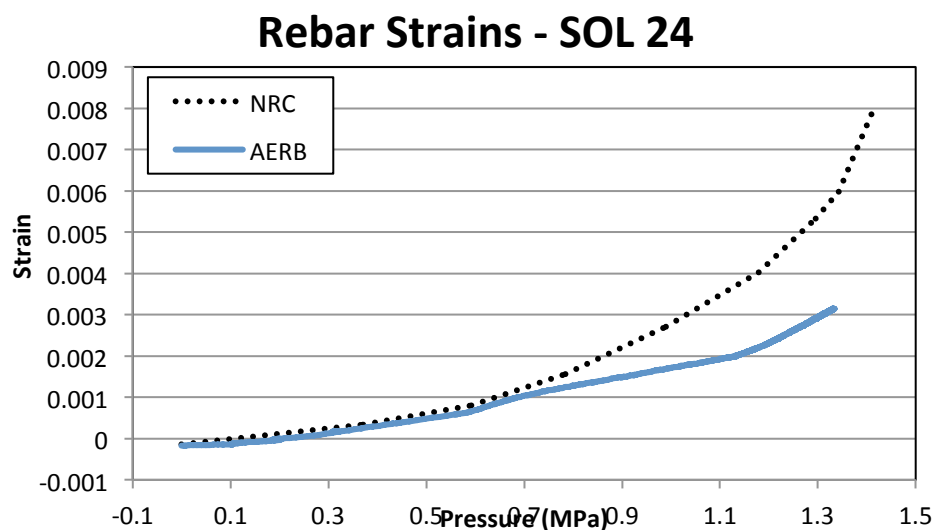


Figure 221: Rebar Strain Versus Pressure at SOL #24 (Hoop Strain of Outer Rebar at Springline)

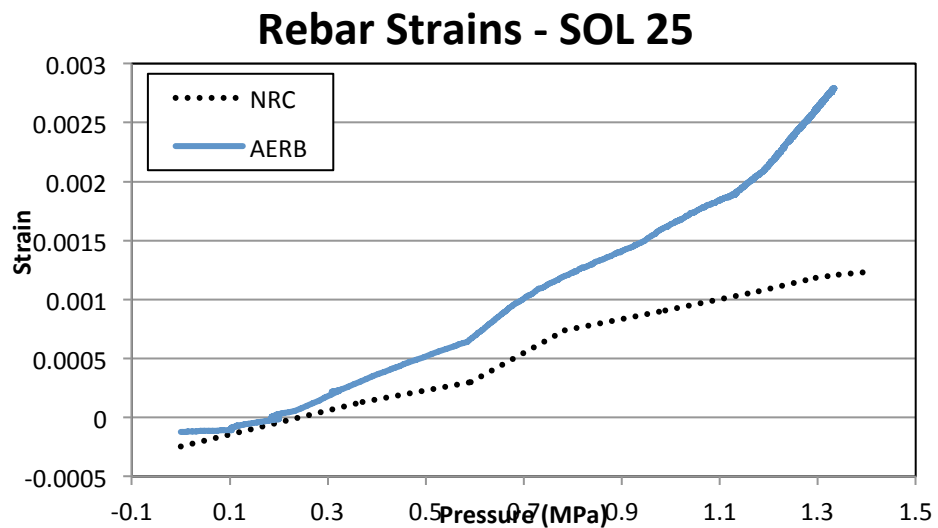


Figure 222: Rebar Strain Versus Pressure at SOL #25 (Meridional Strain of Inner Rebar at Springline)

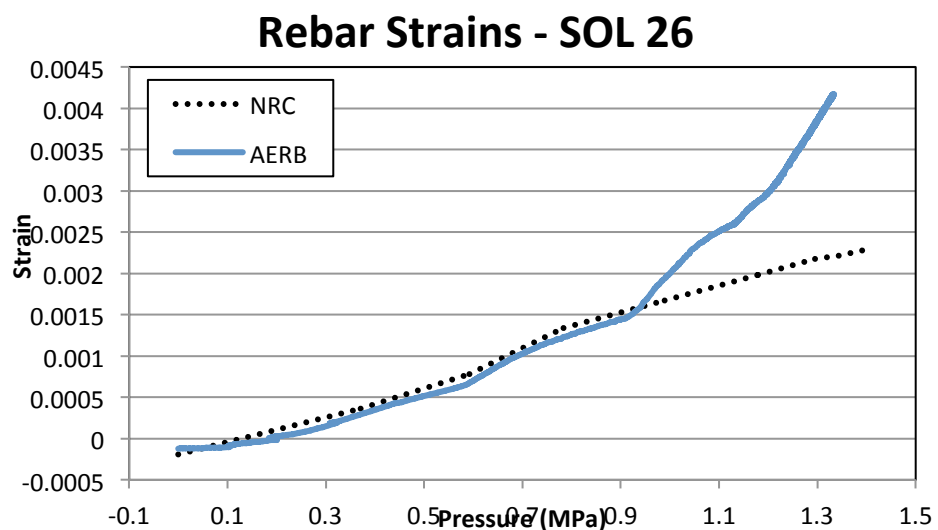


Figure 223: Rebar Strain Versus Pressure at SOL #26 (Meridional Strain of Outer Rebar at Springline)

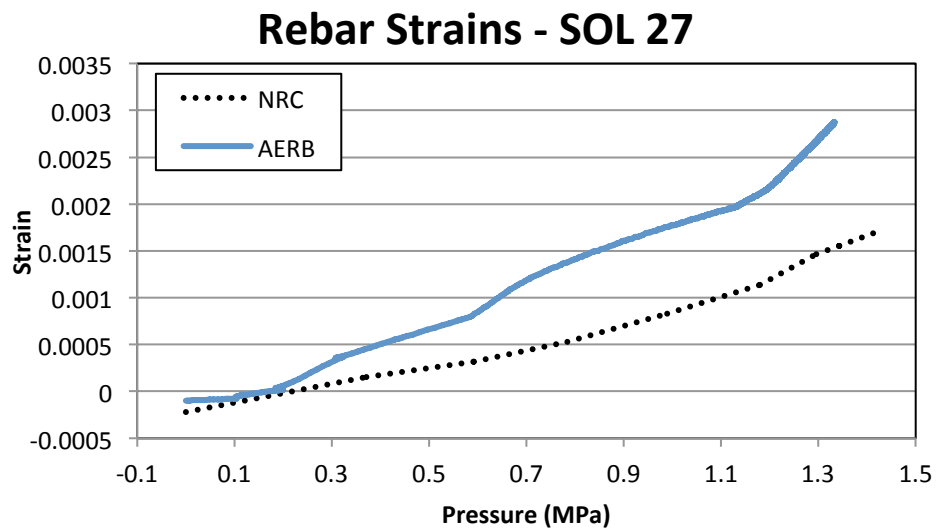


Figure 224: Rebar Strain Versus Pressure at SOL #27 (Hoop Strain of Outer Rebar at Dome 45°)

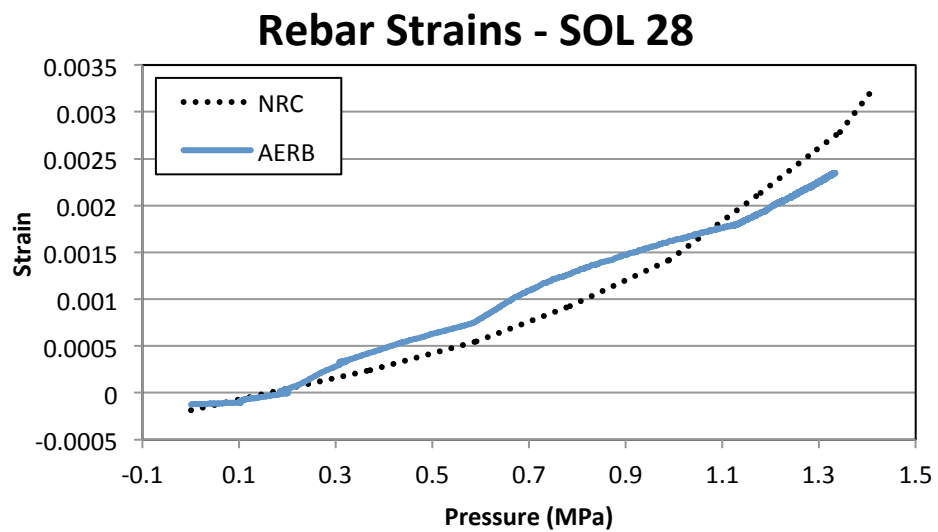


Figure 225: Rebar Strain Versus Pressure at SOL #28 (Meridional Strain of Inner Rebar at Dome 45°)

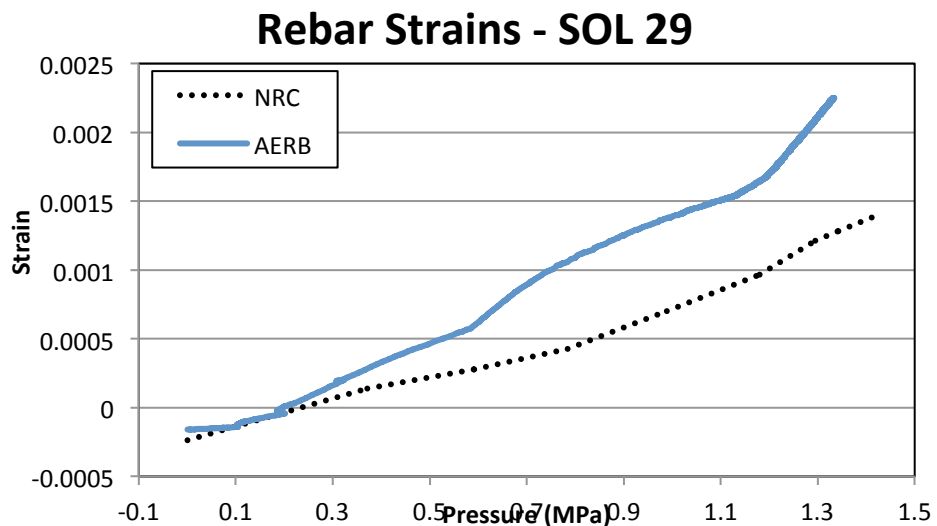


Figure 226: Rebar Strain Versus Pressure at SOL #29 (Meridional Strain of Outer Rebar at Dome 45°)

4.4.3 *Liner Strains*

The participants were asked to report liner strains at locations SOL 36-42. The comparison plots for the liner strain data and for the modeled results are presented in Figure 227 through Figure 233.

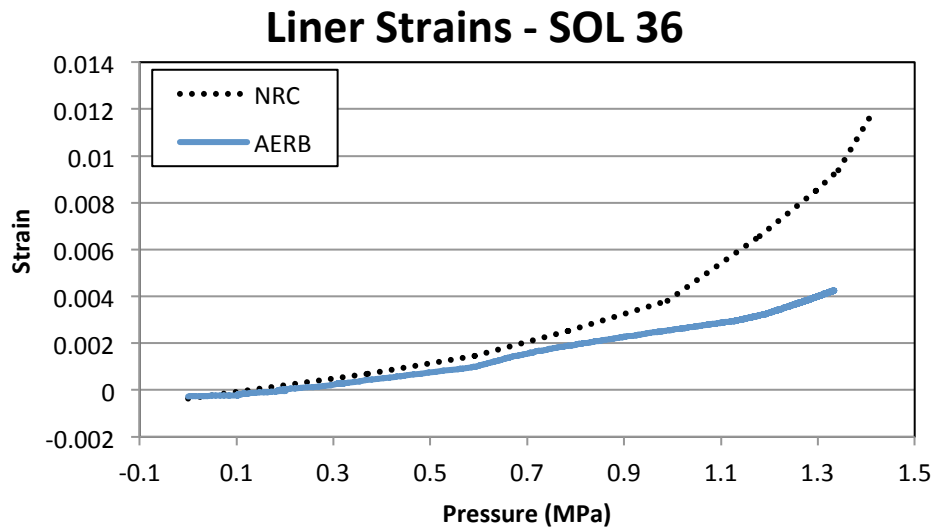


Figure 227: Liner Strain Versus Pressure at SOL #36 (Meridional Strain of Inside of Liner at Base of Cylinder)

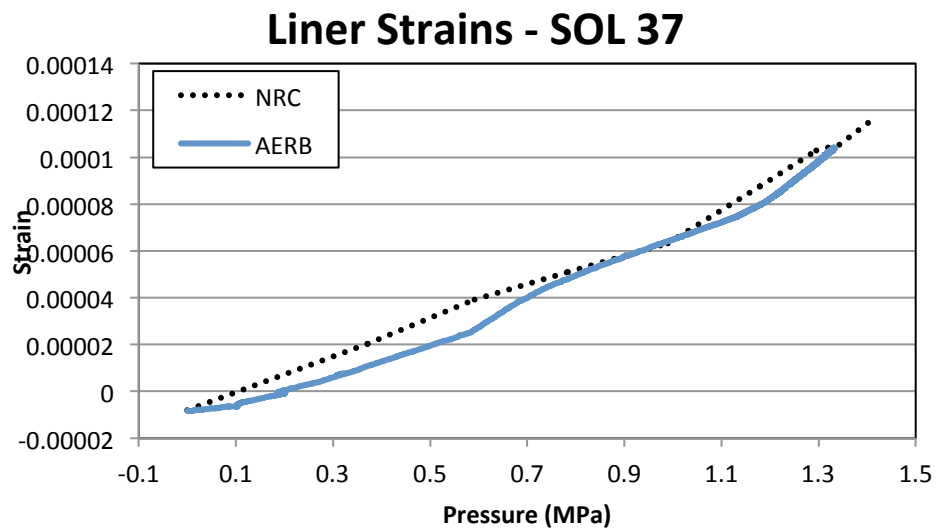


Figure 228: Liner Strain Versus Pressure at SOL #37 (Hoop Strain of Inside of Liner at Base of Cylinder)

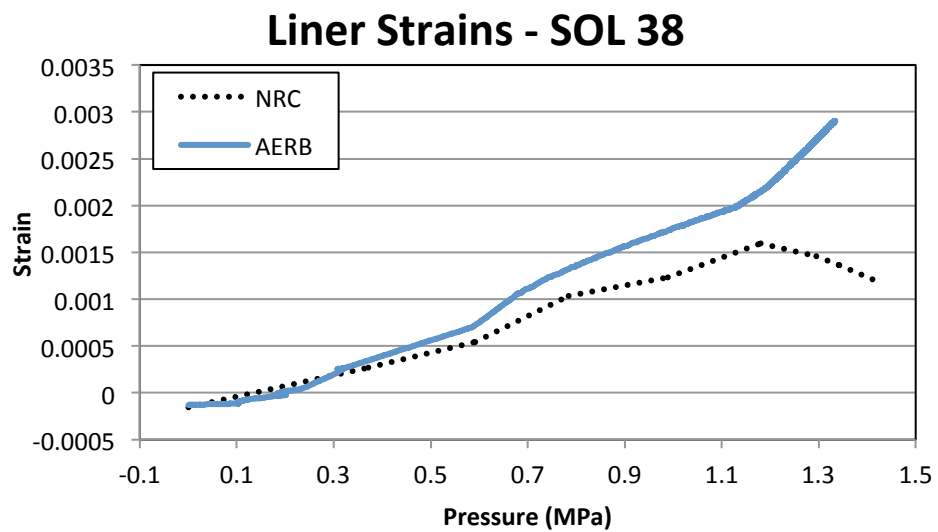


Figure 229: Liner Strain Versus Pressure at SOL #38 (Meridional Strain of Inside of Liner at Midheight)

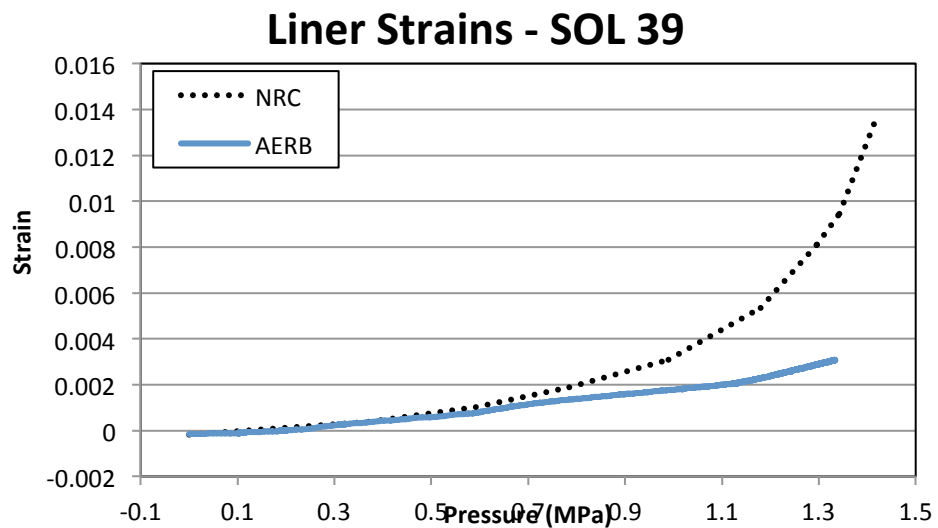


Figure 230: Liner Strain Versus Pressure at SOL #39 (Hoop Strain of Inside of Liner at Midheight)

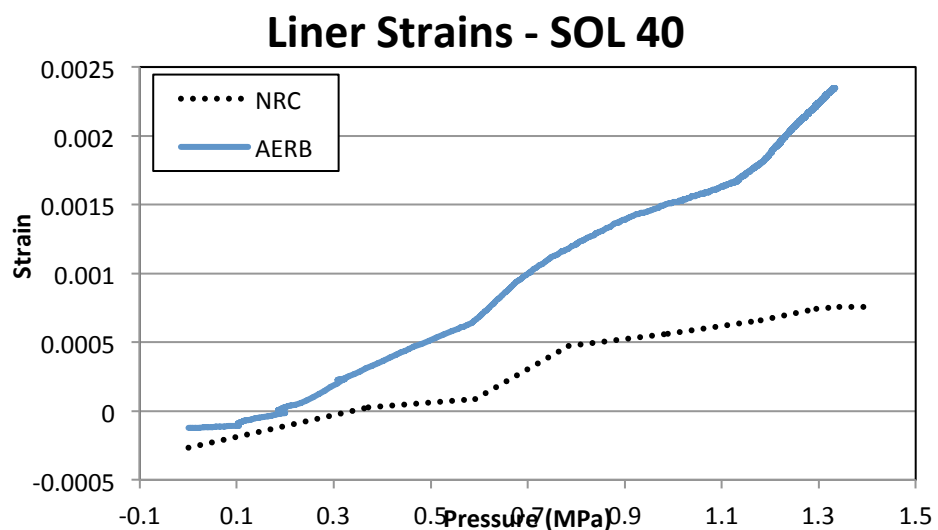


Figure 231: Liner Strain Versus Pressure at SOL #40 (Meridional Strain of Inside of Liner at Springline)

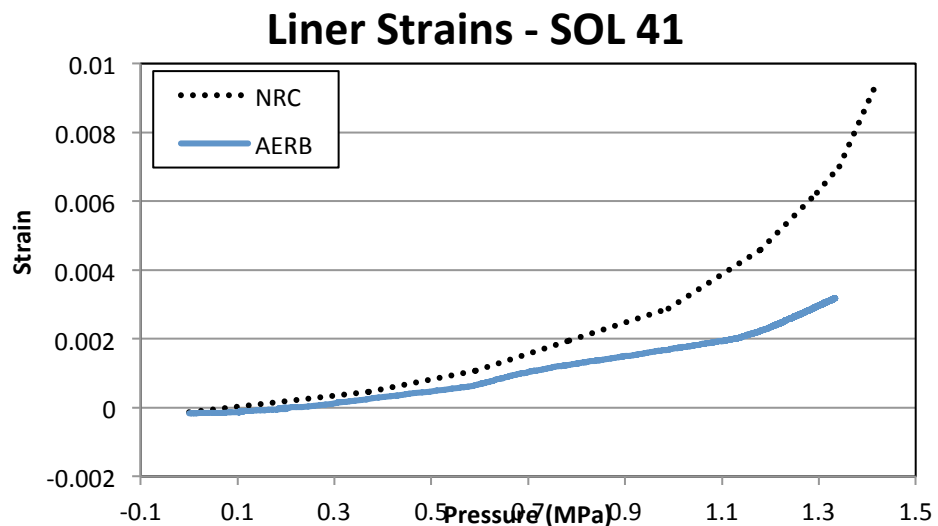


Figure 232: Liner Strain Versus Pressure at SOL #41 (Hoop Strain of Inside of Liner at Springline)

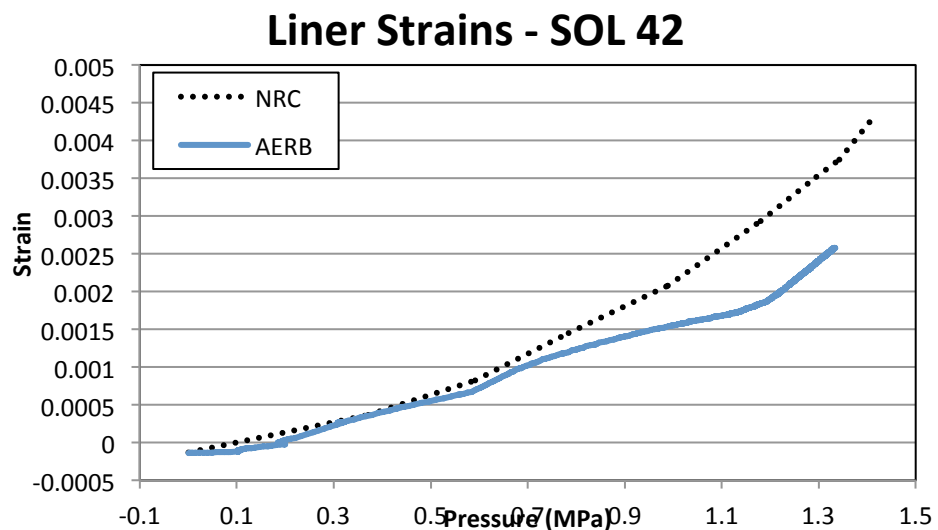


Figure 233: Liner Strain Versus Pressure at SOL #42 (Meridional Strain of Inside of Liner at Dome Apex)

4.4.4 Tendon Strains

Participants were requested to provide results at SOLs 48-53 for the tendon strains. The tendon strain data comparison plots can be found in Figure 234 through Figure 239.

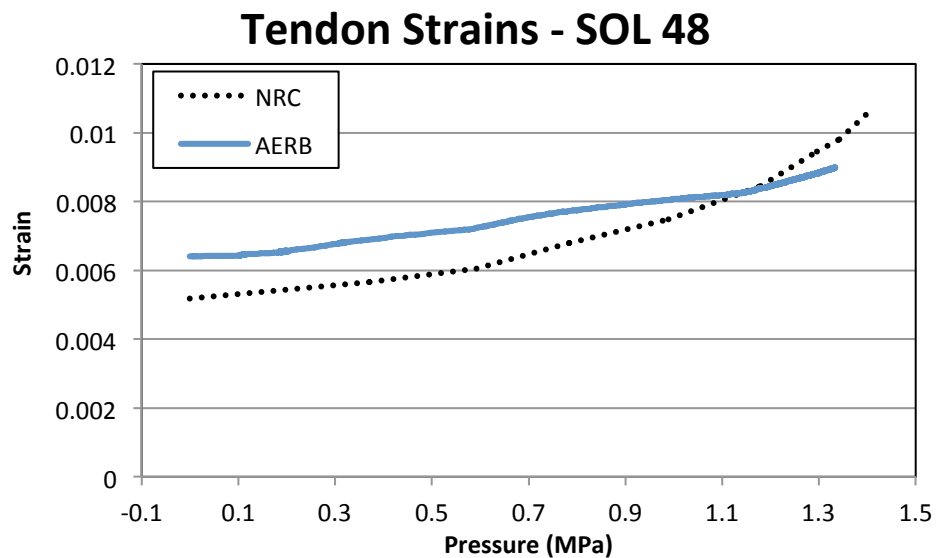


Figure 234: Tendon Strain Versus Pressure at SOL #48 (Hairpin, Tendon V37 at Tendon Apex)

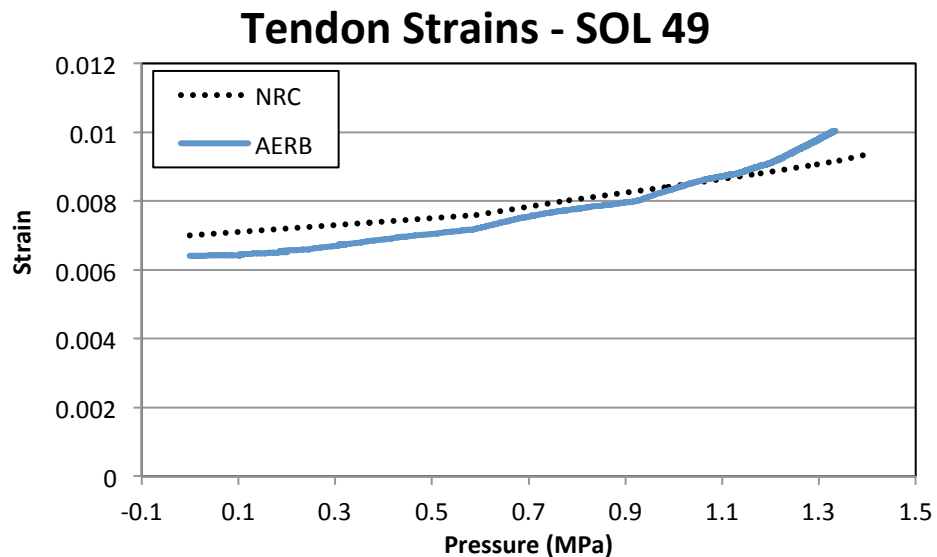


Figure 235: Tendon Strain Versus Pressure at SOL #49 (Hairpin, Tendon V46 at Tendon Springline)

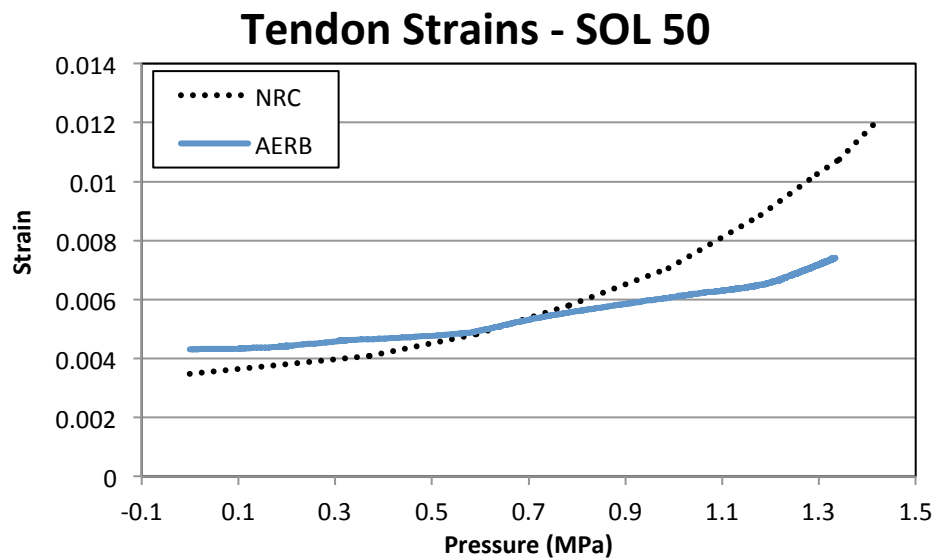


Figure 236: Tendon Strain Versus Pressure at SOL #50 (Hoop, Tendon H53 at Mid-Tendon)

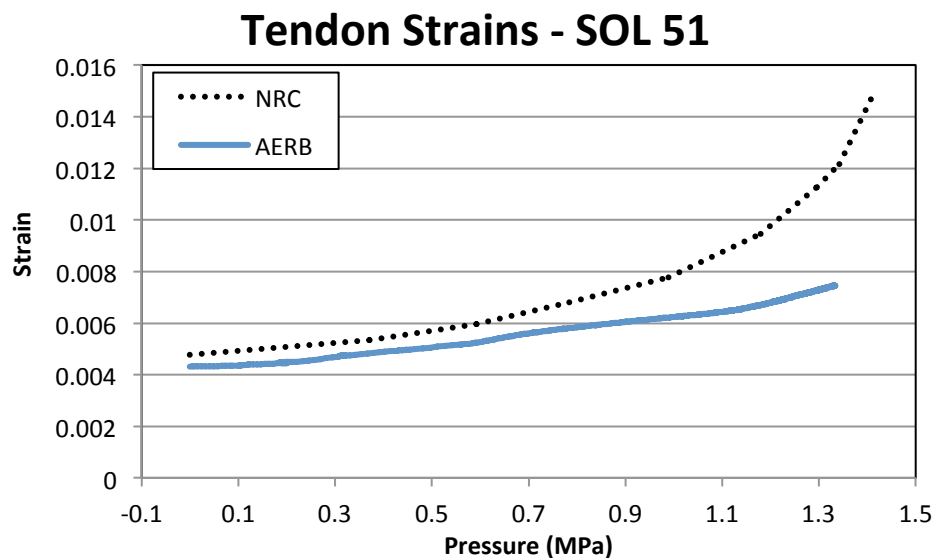


Figure 237: Tendon Strain Versus Pressure at SOL #51 (Hoop, Tendon H53 at $\frac{1}{4}$ Tendon)

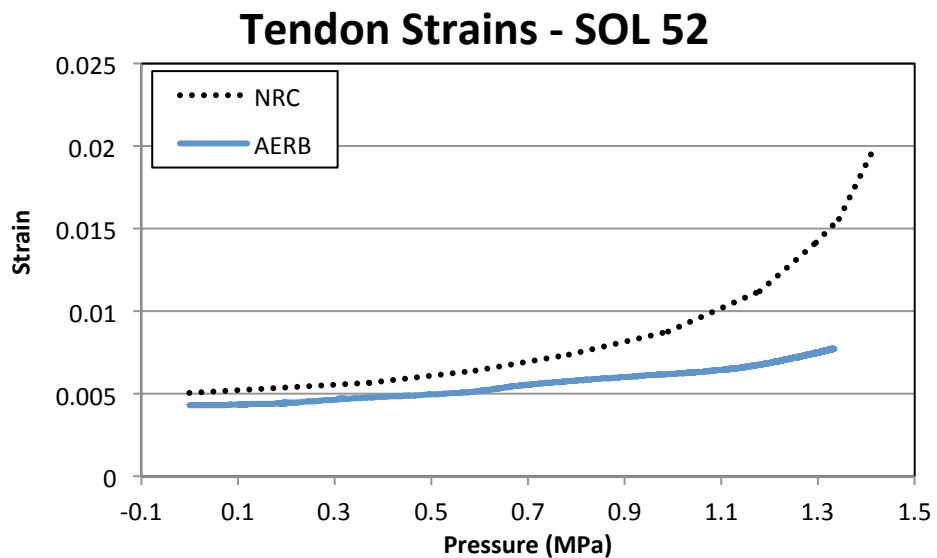


Figure 238: Tendon Strain Versus Pressure at SOL #52 (Hoop, Tendon H53 Near Buttress)

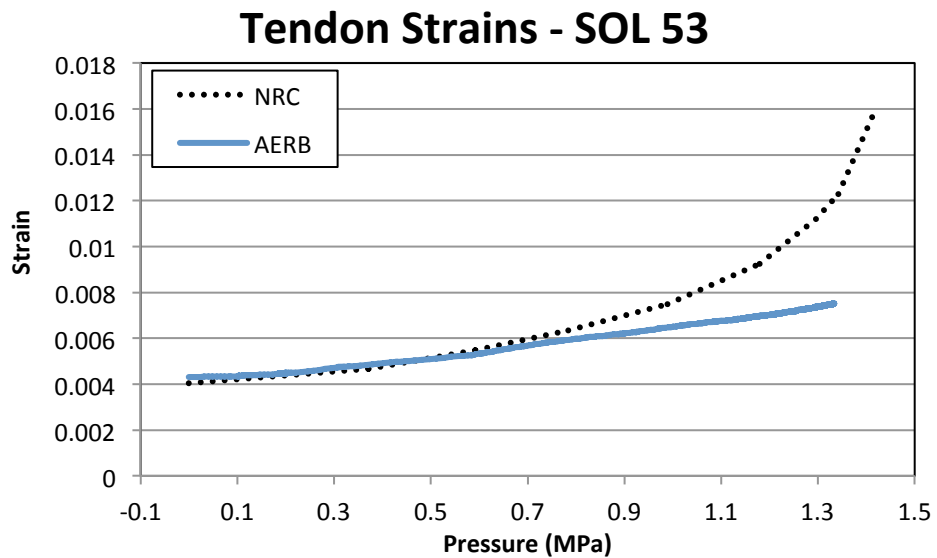


Figure 239: Tendon Strain Versus Pressure at SOL #53 (Hoop, Tendon H35 Between E/H and A/L)

4.4.5 Tendon Forces

The final SOLs measure tendon force and the comparison plots can be found in Figure 240 and Figure 241. None of the other participants provided these results, so we have compared to the NRC Model 3 results.

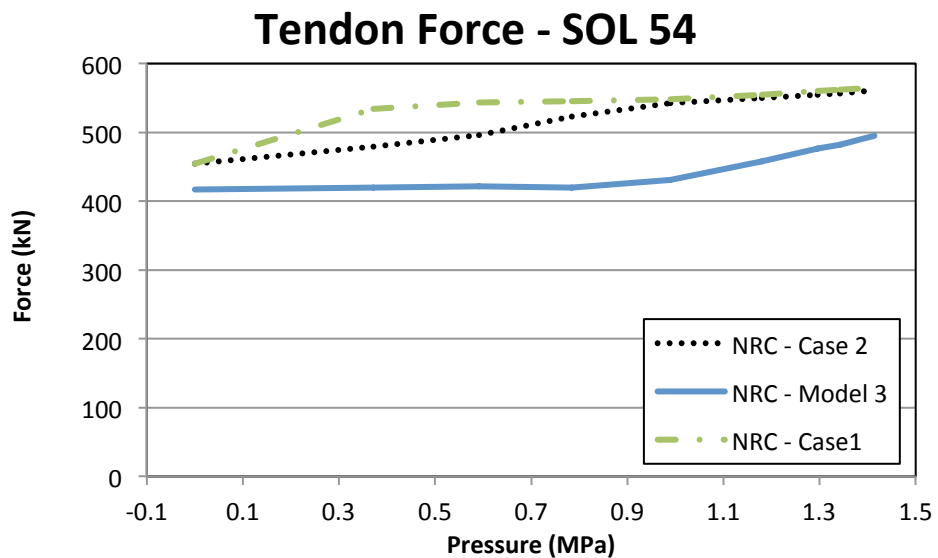


Figure 240: Tendon Force Versus Pressure at SOL #54 (Hairpin, Tendon V37 at Tendon Gallery)

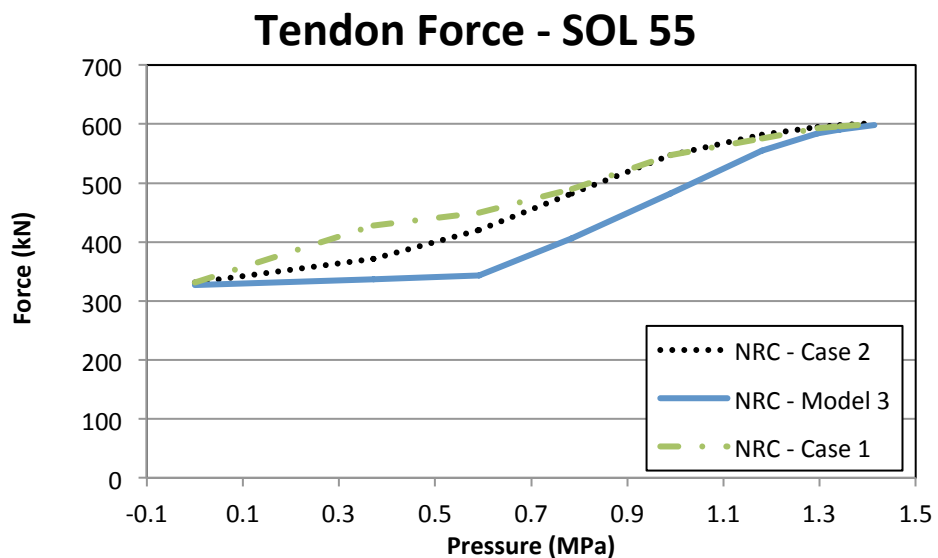


Figure 241: Tendon Strain Versus Pressure at SOL #55 (Hoop, Tendon H53 at Buttress)

5 LEAK RATE COMPARISON

This chapter compares the methods that each participant used to calculate leak rate. Additionally, the results of applying the leak rate calculation methods to the results from Phase 1, as well as to the Case 1 and Case 2 loading conditions are compared.

5.1 Methods Used To Calculate Leak Rate

5.1.1 Leakage Rate Methods Provided by AERB

The participants from AERB provided a description of two models from literature to calculate the leakage rate through various materials. They focused on the Rizkalla et al. [6, 7] method, and the Suzuki et al. [8, 9] method. A summary of the two methods, as provided by AERB is included. Both methods provide leak rate as a function of crack size to estimate leakage rate with respect to internal pressure.

A description of the crack, as used in both models, is shown below in Figure 242.

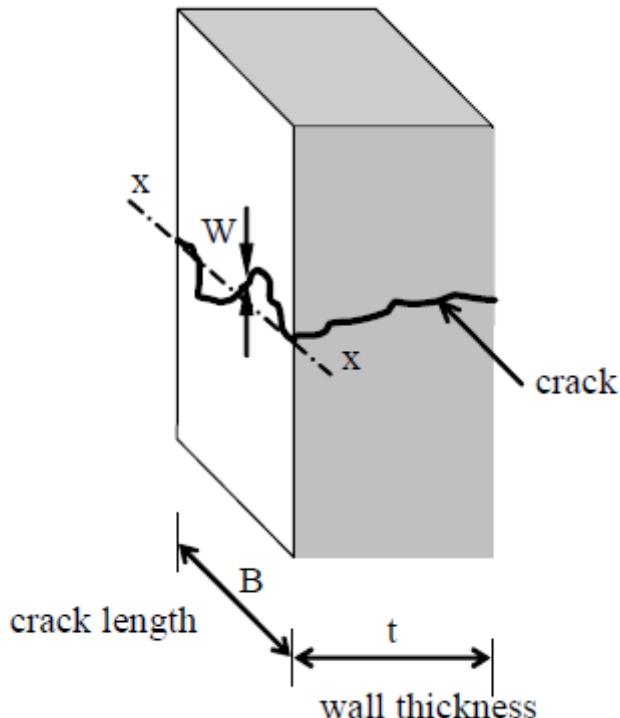


Figure 242: Definition of Crack Length and Crack Width

The formulas suggested by Rizkalla et al are applicable for a wide range of pressures, whereas the Suzuki et al formulas tend to provide reasonable estimates of leakage for lower pressures with small differences. The formulas are as follows:

Rizkalla et al:

$$\frac{p_1^2 - p_2^2}{t} = \left(\frac{k}{2}\right)^n \left(\frac{\mu}{2}\right)^n (RT)^{n-1} \left| \frac{p_2 Q}{B} \right|^{2-n} \frac{1}{\sum_{i=1,j} W_j^3}$$

where:

$$\sum_{i=1,j} W_j^3 = 1.42 NW_{av}^3$$

N = number of cracks

W_{av} = average crack width

$$n = \frac{0.133}{(\sum W_i^3)^{0.81}} = \frac{0.195}{(NW_{av}^3)^{0.063}}$$

$$k = 2.907 \times 10^7 (\sum W_i^3)^{0.428} = 8.702 \times 10^6 (NW_{av}^3)^{0.367}$$

Q = flux through the wall (ft³/s)

B = crack length (ft)

W = crack width (ft)

t = wall thickness

p₁ = upstream pressure (lb/ft²)

p₂ = downstream pressure (lb/ft²)

μ = dynamic viscosity of air or gas used (lb s/ft²) (typical value is 1.8x10⁻⁵ Pa-s)

T = absolute temperature (°R)

R = gas constant (ft²/s² °R) (typical value is 1716 ft²/s² °R)

Suzuki et al:

$$Q^2 = \frac{W^3(p_1^2 - p_2^2)}{2\rho_o p_o t [a(W)\frac{12\mu}{\rho_o Q} + b(W)]}$$

where:

$$\bar{a}(W) = \frac{4.33 \times 10^{-5}}{W^{1.5}} + 1$$

$$b(W) = \frac{3.41 \times 10^{-4}}{W}$$

For p ≈ 1 (atm) and Δp ≤ 0.2 (atm):

$$Q = \bar{a}(W) \frac{W^3(p_1 - p_2)}{\mu t}$$

Where $\bar{a}(W) = 15.3W + 7.56 \times 10^{-3}$

W, t have units of meters

p₁, p₂, p_o have units of Pa

ρ_o has units of kg/m³

μ_o has units of Pa s

Q has units of $\text{m}^3/\text{s}/\text{m}$ and is calculated for unit crack length. To get the total leakage, the Q should be multiplied with the crack length (B).

Each participant could use one of the aforementioned methods, or any method of their choosing.

5.1.2 Comparison of Methods Used by Participants

The leakage rate formulas used by each participant to transition from crack width to leakage rate as a function of pressure are listed in Table 10.

Table 10: Leakage Rate Formulations Used

Organization	Leakage Rate Method Used
AERB	Rizkalla
FORTUM	Rizkalla
NRC	Rizkalla
SCANSBOT	Vennard & Street [10] (frictionless gas flow through a convergent nozzle)

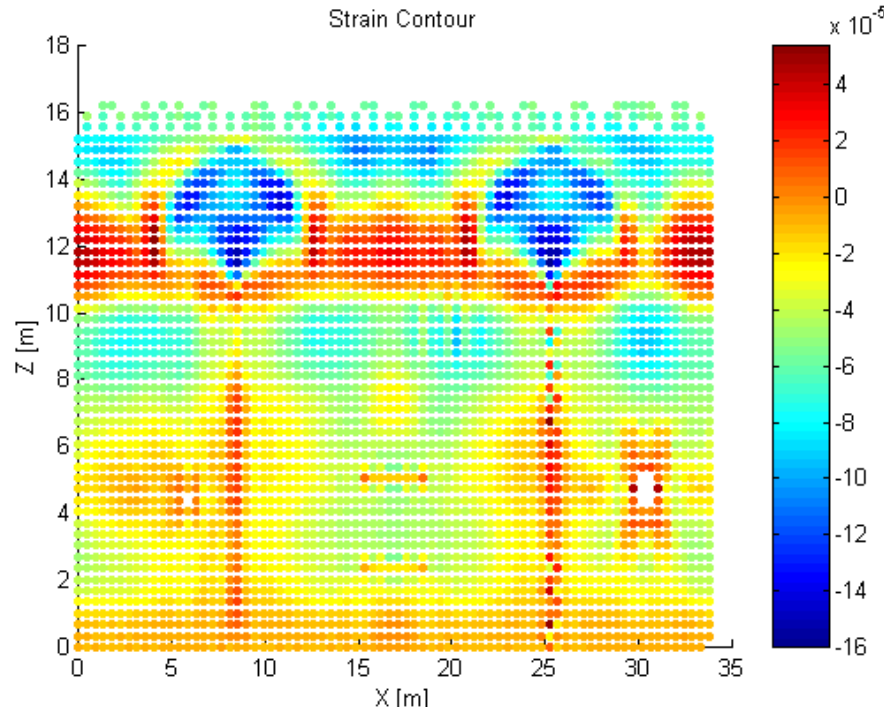
Each participant had the freedom to use any method desired to transition from FEM strains to subsequent crack widths. For a detailed discussion of the methods used by each participant, refer to the individual participant reports in the appendices. A list of the different methods used is provided in Table 11.

Table 11: Methods Used to Calculate Crack Width

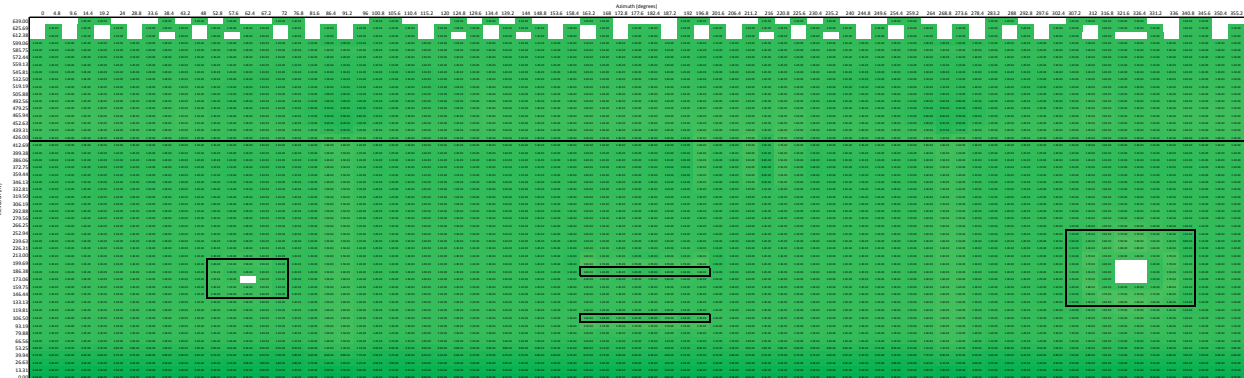
Organization	Crack Width Calculation
AERB	J-Critical Combined with Rizkalla: number of through wall cracks = N $N = N_{twc} \left[\frac{\varepsilon_{s2} - \varepsilon_{s2,cr}}{0.002 - \varepsilon_{s2,cr}} \right]$
FORTUM	Optimization of Fit to Experimental Data Using Rizkalla $w = w(L_e, \varepsilon_\theta) = L_e(c_1\varepsilon_\theta + c_2\varepsilon_\theta^2)$
NRC	average crack width equals peak equivalent uniaxial strain times spacing between anchors where equivalent peak strain is equal to global strain times strain concentration factor times stress biaxiality factor
SCANSOT	Fracture Mechanics, J-Integral

5.2 Comparison of Model 3 Liner Strains and Leak Rates

A comparison of the Model 3 liner strains is shown in Figure 243 through Figure 247.



(a)

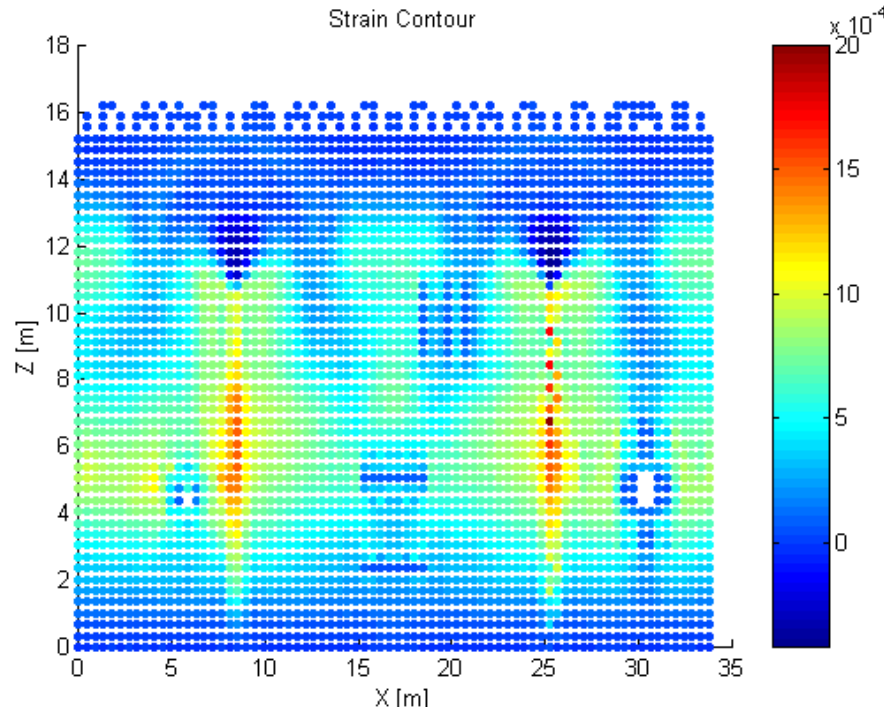


(b)

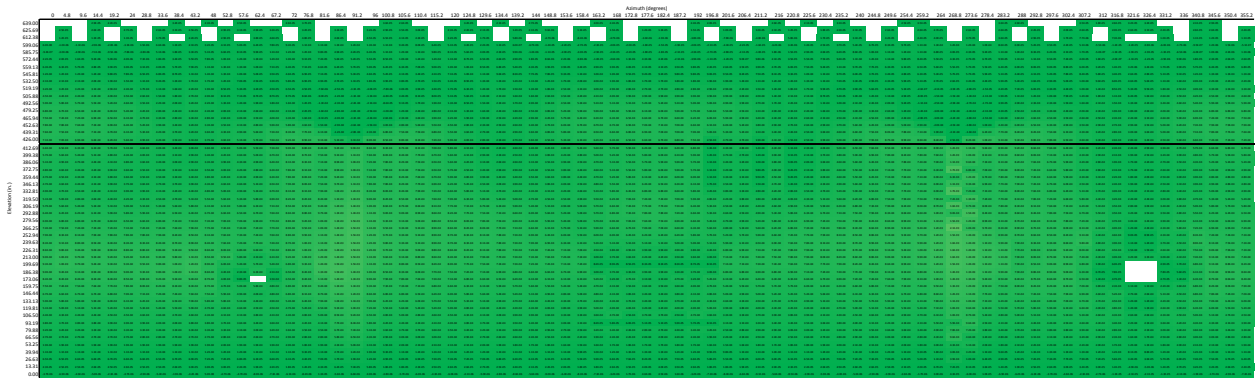
Color codes	
Strain	Color
$0 \leq \epsilon < 0.006$	green
$0.006 \leq \epsilon < 0.012$	yellow
$\epsilon \geq 0.012$	red

(c)

Figure 243: Liner Strains in Model 3 at $1.0 \times P_d$ for (a) FORTUM, and (b) NRC with (c) Scale for NRC



(a)

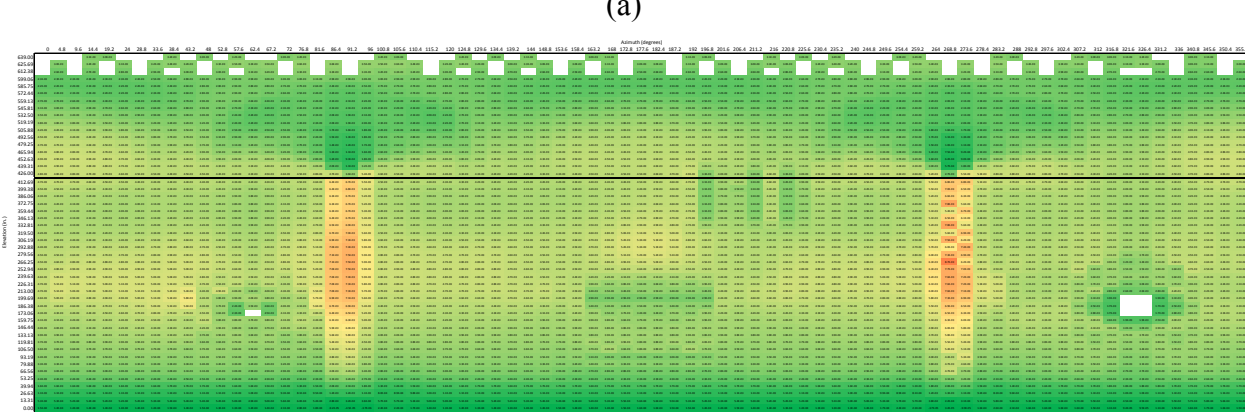
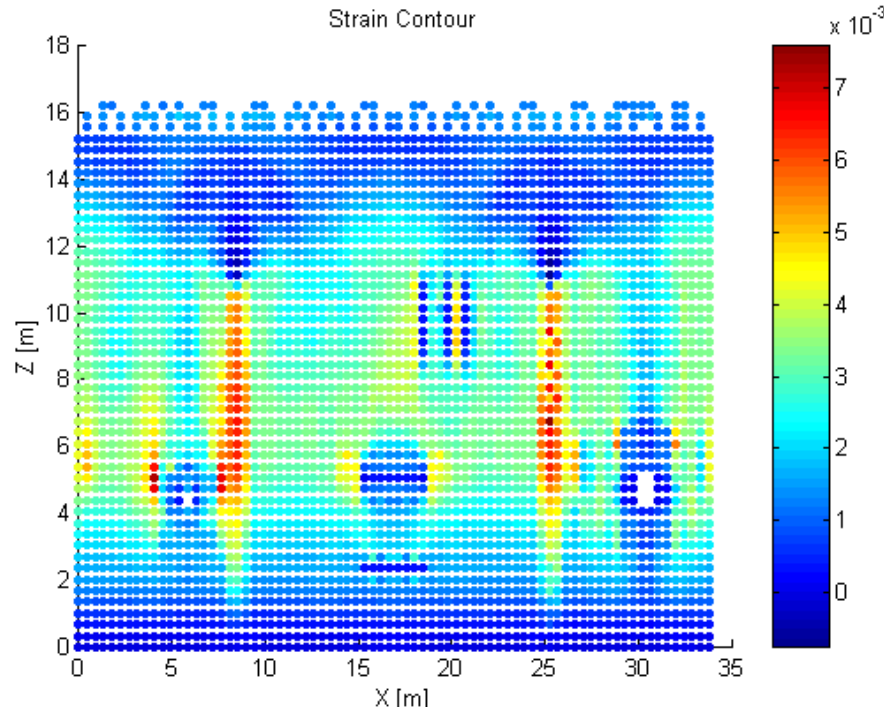


(b)

Color codes	
Strain	Color
$0 \leq \epsilon < 0.006$	green
$0.006 \leq \epsilon < 0.012$	yellow
$\epsilon \geq 0.012$	red

(c)

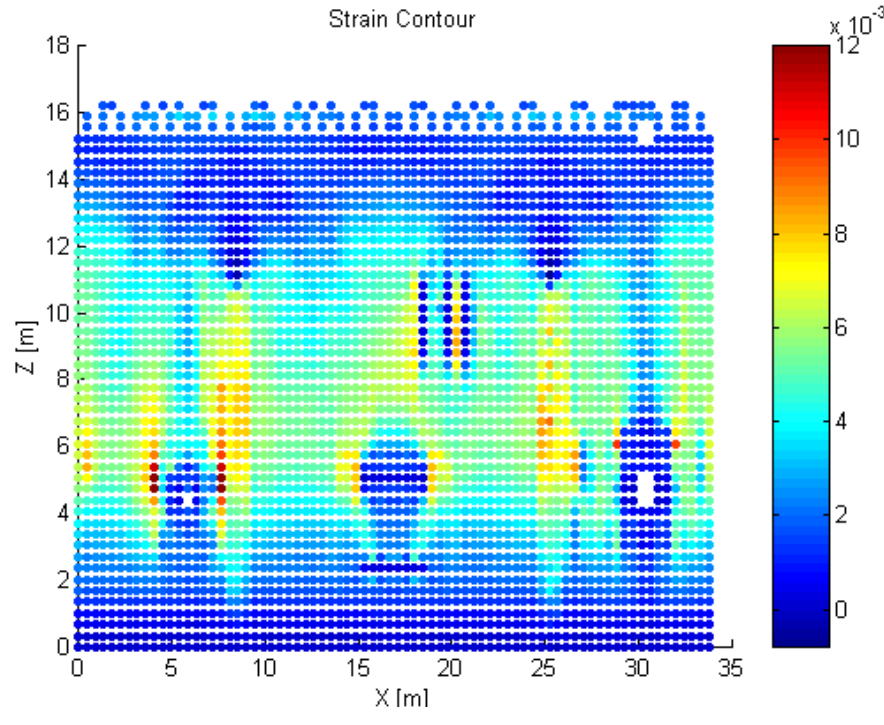
Figure 244: Liner Strains in Model 3 at $2.0 \times P_d$ for (a) FORTUM, and (b) NRC with (c) Scale for NRC



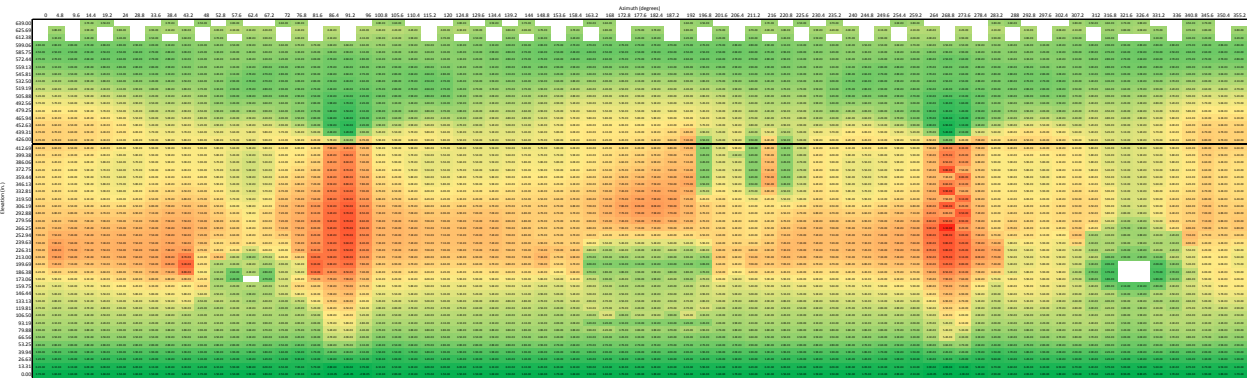
Color codes	
Strain	Color
$0 \leq \epsilon < 0.006$	green
$0.006 \leq \epsilon < 0.012$	yellow
$\epsilon \geq 0.012$	red

(c)

Figure 245: Liner Strains in Model 3 at $3.0 \times P_d$ for (a) FORTUM, and (b) NRC with (c) Scale for NRC



(a)

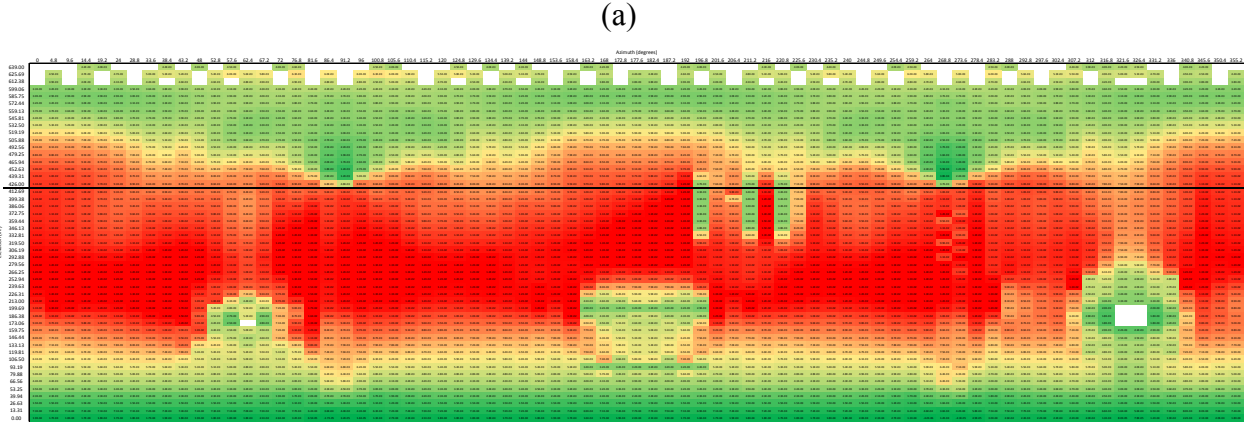
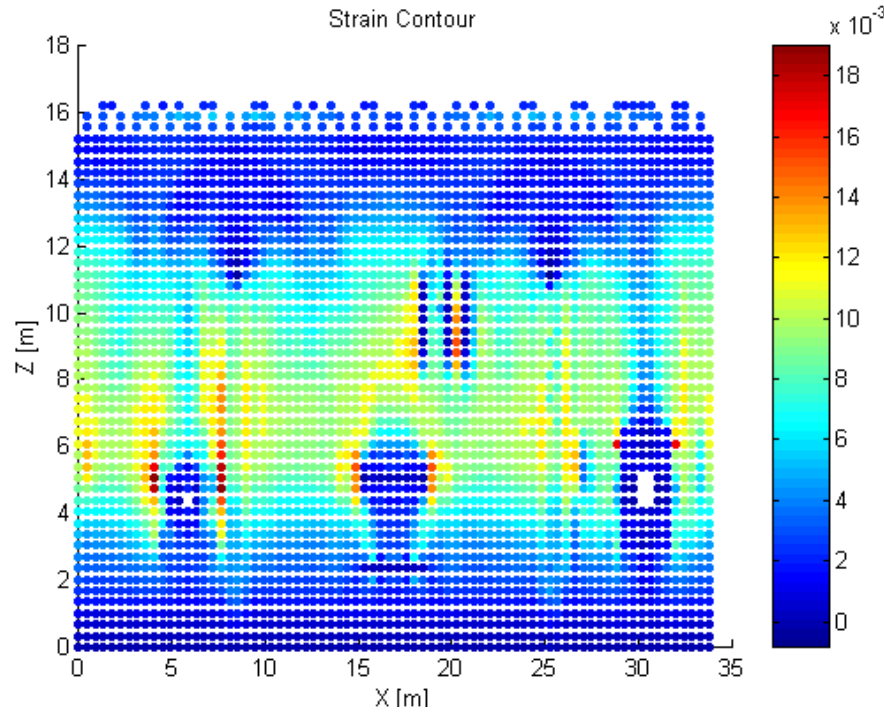


(b)

Color codes	
Strain	Color
$0 \leq \epsilon < 0.006$	green
$0.006 \leq \epsilon < 0.012$	yellow
$\epsilon \geq 0.012$	red

(c)

Figure 246: Liner Strains in Model 3 at $3.3 \times P_d$ for (a) FORTUM, and (b) NRC with (c) Scale for NRC

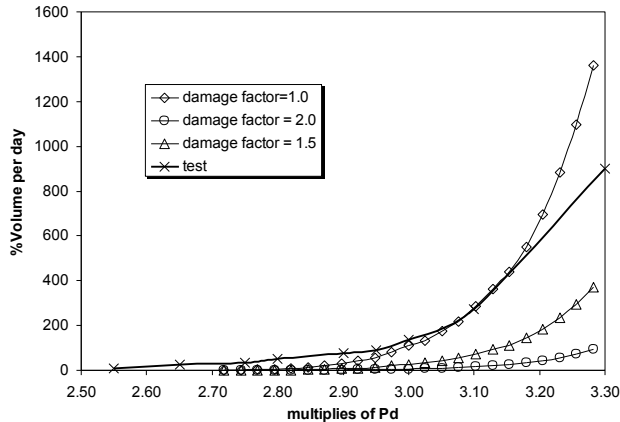


Color codes	
Strain	Color
$0 \leq \epsilon < 0.006$	green
$0.006 \leq \epsilon < 0.012$	yellow
$\epsilon \geq 0.012$	red

(c)

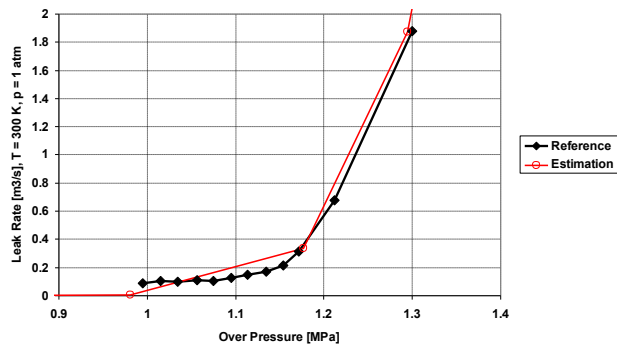
Figure 247: Liner Strains in Model 3 at Ultimate Pressure for (a) FORTUM ($3.5 \times P_d$), and (b) NRC ($3.6 \times P_d$) with (c) Scale for NRC

The comparisons that each participant made to the test data are shown in Figure 248. Scanscot did not provide a figure comparing this, but reported that their method overpredicted leakage by approximately 45%. As discussed in Appendix B, AERB considered three damage initiation criteria corresponding to the critical fracture toughness values suggested in the organizational white paper and reproduced in § 1.2.7. These damage initiation criteria are referred to as damage factor 1.0, 1.5, and 2.0 in Figure 248 (a).



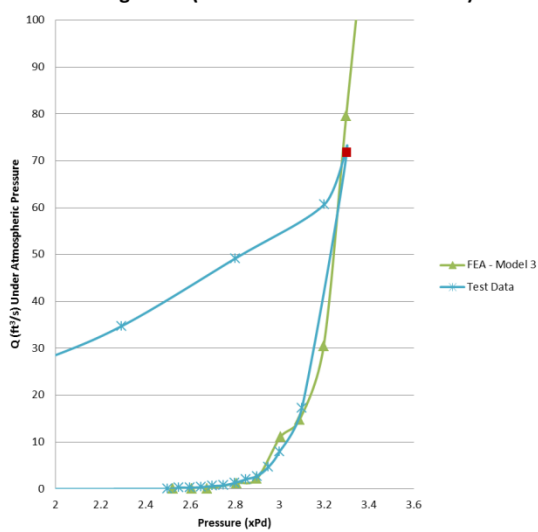
(a)

ISP48-LST, Leak rate estimation.
Reference curve based on pressure measurements.



(b)

Leakage Rate (Rizkalla Method vs. Test Data)



(c)

Figure 248: Comparison of Model 3 Leak Rates vs Experimental Data for (a) AERB (b) FORTUM and (c) NRC

5.3 Comparison of Model 4, Case 1 and 2 Leak Rates

A comparison of the resulting leak rates for Case 1 and 2 from the participants is shown in Figure 249.

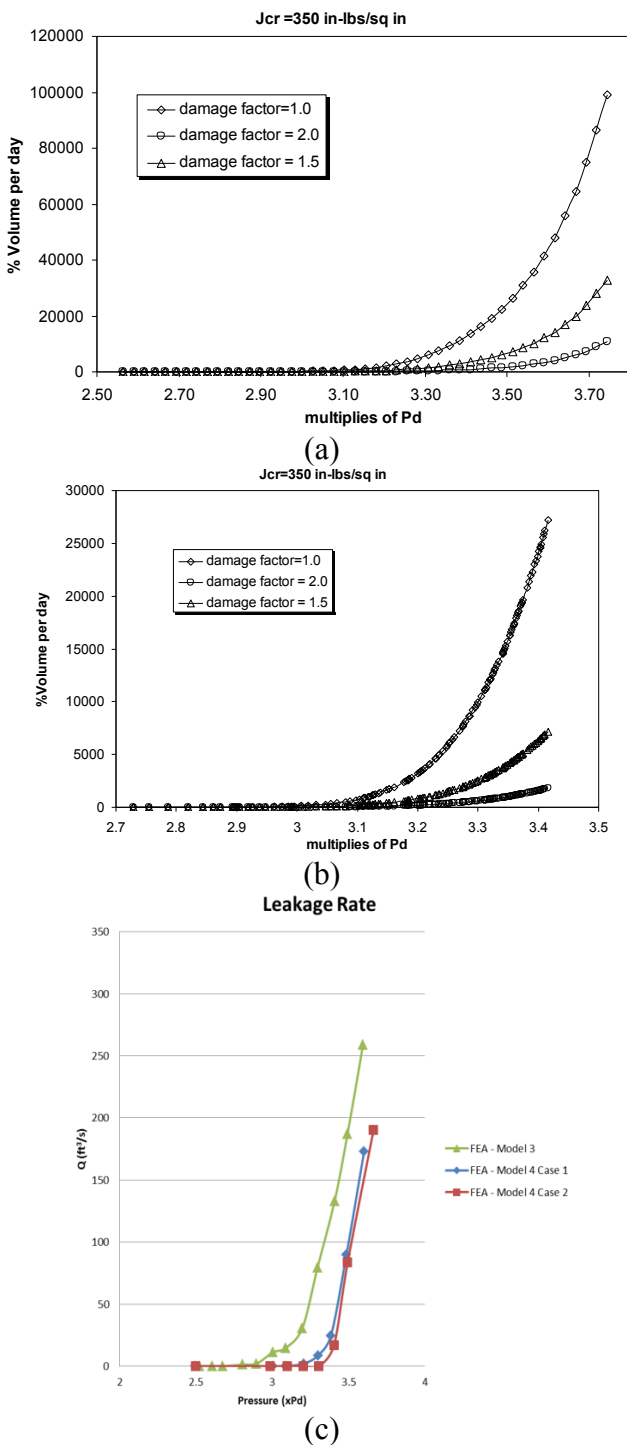


Figure 249: Calculated Model 4 Leak Rates for (a) AERB (case 1) (b) AERB (case 2) and (c) NRC

6 TRANSITION TO PROBABILISTIC SPACE

Each participant treated the transition to probabilistic space differently, and there is no easy way to compare the different approaches that the participants took. We ask the reader to refer to each participant's report, included in the appendices, for the various discussions on a transition to probabilistic space.

7 CONCLUSIONS

Six international organizations have participated in the round robin Standard Problem Exercise #3, by using the 1:4 Scale PCCV Model as a starting point. These organizations include:

- Atomic Energy Regulatory Board of India (AERB),
- Électricité de France (EDF)
- FORTUM (Finland)
- Gesellschaft für Anlagen und Reaktorsicherheit (GRS), (German Agency for Reactor Safety)
- Nuclear Power Corporation of India Limited (NPCIL)
- US Nuclear Regulatory Commission (NRC)

This analysis involved the structural analysis of a prestressed concrete containment vessel (PCCV). Phase 1 Results and Discussion were completed in 2011. Phase 2 requires participants to re-investigate Model 3 from Phase 1, with two distinct objectives.

1. The participants were asked to examine the methods to estimate leakage rate as a function of pressure. These methods were evaluated relative to the PCCV test results, and incorporated lessons learned from Phase 1 of the round robin analysis;
2. Temperature effects modifications were implemented into Model 3. SPE refers to this additional investigation as Model 4. The participants applied two different temperature loading cases to the global Model 4. The two thermal analysis cases under consideration in Part 2 were selected based on the participant's agreement to use the ISP-48 cases, which are considered as representative challenges to typical containments.

The response to the temperature and pressure loadings have been provided herein, including comparison of Standard Output Location information between the two pressure-and-temperature cases among the participants. Unfortunately, requested output data was only provided by AERB and NRC so the value of this comparison is limited somewhat. For example, for incongruous results for only two data sets for any one metric, it is difficult to say which data set is more valid.

For SPE Phase 2, a key objective of the work was to estimate crack size and leak area. After consideration of alternative methods, it was decided to use the strain-based methodology developed during EPRI research in the 1990s as the basis for the prediction of crack size and occurrence. This also leads to estimation of leakage versus pressure. Some refinements and simplifications to the methodology have been made and are described herein (especially, Appendix A). The Rizkalla formulation has been used by a plurality of participants to calculate leak rates through postulated liner tear areas. The formulation, when applied to the 1:4 Scale PCCV Model, produces leak rates which are reasonably close to those observed and measured during the test. A significant driver of the formulation is the strain concentration factor K; taking liner-weld-zone-defects into account by increasing the effective "K" might improve predictions of leak rate versus pressure.

A general observation and conclusion can be drawn with respect to temperature response combined with pressure. For the temperature cases considered, while the overall deformation of the PCCV cylinder is larger at a given pressure with the addition of temperature, "failure", i.e. tearing of the liner and significant leakage, is not reached until a somewhat greater pressure. This conclusion is supported by the following observations:

1. For the liner, which has radial displacement constrained by the concrete to which it is attached, temperature tends to induce compressive mechanical strains. Mechanical strains are used in the liner tear prediction formulation, thus at the same pressure, analysis with internal temperature shows liner tears at higher pressures.
2. The temperatures do not climb high enough to substantially degrade the material strengths of the concrete/rebar containment wall. If they did, then pressure + temperature would likely pose a more severe challenge (with lower failure pressure) than with pressure alone.

A final goal of the SPE-3 program was to introduce a probability component to the leakage prediction versus pressure. While work-scope and schedule constraints have limited the detailed pursuit, a general framework for this is laid out in the EPRI methodology summarized in [11]. AERB and NRC have produced a few results in the context of this framework. The method consists of the following steps:

1. Assume that prediction of liner strains from a global model, K-factors, B-factors, and liner ductility limit have a lognormal distribution.
2. Through statistical sampling of actual data, use of judgment, or an expert panel, assign parameters of i). Randomness and ii). Uncertainty to liner strains from a global model, K-factors, B-factors, liner ductility limit, and leak rate formula versus leak area.
3. Apply the randomness and Uncertainty parameters to each step of the liner tear prediction versus pressure, and sum these as has been done in the calculations herein. This produces leak rate versus pressure with a lognormal distribution associated with every point on the leak rate versus pressure curve.
4. For any specific plant, other probabilistic aspects related to construction variations (liner thickness variations, weld quality, liner ductility variations, etc.) could also be introduced.

Fortum has taken a similar approach by varying the input parameters of the Rizkalla model to encompass the realistically expected range of values indicated by the containment experiments and simulations.

It is believed that much knowledge was gained by all the round robin participants, though participation in phase 2 was somewhat varied. The prediction of leakage coupled with the structural modeling insights gained in Phase 1 represent a great step forward for the state of the practice in containment analysis. Similarly, the framework for a probabilistic “containment performance model” constitutes a logical next step for the containment research community.

8 REFERENCES

1. Hessheimer, M.F. and E. Mathet, International Standard Problem No. 48, Containment Capacity, NEA/CSNI/R(2005)5, OECD Nuclear Energy Agency, Paris, France, 2005.
2. Callister, W.D. and D.G. Rethwisch, Fundamentals of materials science and engineering: an integrated approach2012: Wiley. com.
3. Lamont, S., The behaviour of multi-storey composite steel framed structures in response to compartment fires, 2001, University of Edinburgh: Edinburgh, UK.
4. Eurocodes, Part 2 and 3, in Concrete and Steel Material Behaviors at Elevated Temperatures2005.
5. Hessheimer, M.F., E.W. Klamerus, G. Rightley, L. Lambert, and R. Dameron, Overpressurization Test of a 1:4-Scale Prestressed Concrete Containment Vessel Model, NUREG/CR-6810, SAND2003-0840P, Sandia National Laboratories, Albuquerque, NM, 2003.
6. Tinkler, J., R. Del Frate, and S. Rizkalla, The prediction of air leakage rates through cracks in pressurized reinforced concrete containment vessels. International journal of pressure vessels and piping, 1987. 29(1): p. 33-46.
7. Rizkalla, S.H., B.L. Lau, and S.H. Simmonds, Air leakage characteristics in reinforced concrete. Journal of Structural Engineering, 1984. 110(5): p. 1149-1162.
8. Suzuki, T., K. Takiguchi, and H. Hotta, Leakage of gas through concrete cracks. Nuclear engineering and design, 1992. 133(1): p. 121-130.
9. Suzuki, T., K. Takiguchi, H. Hotta, N.K.M. Fukuhara, and K. Kimura. Experimental study on the leakage of gas through cracked concrete walls. in Structural Mechanics in Reactor Technology. 1989. Anaheim.
10. Vennard, J.K. and R.L. Street, Elementary fluid mechanics. John Wiley & Sons, Inc., 605 Third Ave., N. Y., NY 10158, USA, 1982, 7041982.
11. Dameron, R., R. Dunham, Y. Rashid, and H. Tang, Conclusions of the EPRI Concrete Containment Research Program. Nuclear Engineering and Design, 1991. 125(1): p. 41-55.

DISTRIBUTION

4 Nuclear Regulatory Commission
Attn: Madhumita Sircar
U.S. Nuclear Regulatory Commission
Washington, DC 20555-0001

2 Moffatt and Nichol
Attn: Robert Dameron
1660 Hotel Circle North, Suite 500
San Diego, CA 92108

1	MS0349	Lili A. Heitman	1523
2	MS0744	Christopher A. Jones	6233
1	MS0899	Technical Library	9536 (electronic copy)

